Computational modeling of thermal interfaces in graphene based nanostructures

Doctoral Dissertation
Doctoral Program in Science and technology of materials (31th Cycle)

Computational modeling of thermal interfaces in graphene based nanostructures

Alessandro Di Pierro

* * * * * *

Supervisors
Prof. A. Fina, Supervisor
Dr. B. Mortazavi, Co-Supervisor, Bauhaus Universität Weimar

Doctoral Examination Committee:

Prof. Luiz Felipe Cavalcanti Pereira - Universidade Federal do Rio Grande do Norte
Prof. Luciano Colombo – Università di Cagliari
Prof. Maurizio Cossi – Amedeo Avogadro – Università del Piemonte Orientale
Prof. Alberto Frache - Politecnico di Torino
Prof. Claudio Gerbaldi - Politecnico di Torino

Politecnico di Torino
June 27, 2019

I hereby declare that, the contents and organization of this dissertation constitute my own original work and does not compromise in any way the rights of third parties, including those relating to the security of personal data.

…….....

Alessandro Di Pierro

June 27, 2019

Summary

Since first investigations, nanostructured materials exhibited new and promising chemical and physical properties, opening new opportunities to enhance the performance of conventional materials leading research and industry demand. Two-dimensional materials and particularly carbon-based materials, including graphene, have attracted tremendous attention owing to their outstanding physical properties, especially concerning thermal and electrical conductivity.

The exploitation of the outstanding properties of graphene and other 2D materials into tridimensional bulk materials is traditionally done via the simple dispersion of nanoparticles into a continuous matrix, to produce nanocomposite materials. When aiming at thermally efficient nanostructured materials, one of the most important factors dominating the thermal transport in nanocomposites is the thermal contact resistance that exists across the interfaces when coupling different materials. To manufacture efficient nanocomposite materials with high thermal conduction properties, it is therefore crucial to properly design and control thermal interfaces, thus combining knowledge in physics, materials science and engineering. In this field, a precious support comes from computational modelling or interfaces and bulk materials. Indeed, in the last decades, several different computational methods became popular and powerful tools to investigate material properties. This consideration is particularly true when dealing with materials close to the atomic scale, where the limited complexity and consequently limited computational demand can be satisfied by relatively small systems.

In this PhD work, Molecular Dynamics (MD) and Finite Element Method (FEM) were employed to calculate the thermal properties of nanostructured materials. In particular, MD was adopted to investigate parameters that could improve heat transfer among graphene-based materials, and FEM was applied to upscale MD results from the nano-scale level to bulk nanocomposites. By

employing this approach, the thermal transports in composites materials were analyzed and some important conclusions were drawn.

The largest investigation was focused on the thermal boundary conductance (TBC) in edge-to-edge interfaces between suspended graphene nanoplatelets. The purpose of this work was to discover and tune the key parameters that affects the heat transfer across the interfaces when molecules were employed as thermal junctions. The simulation of chemical functionalization was carried out systematically, either with covalently bonded molecules or with non-bonded ones, focusing the following efforts on the covalently bounded species, revealed as the most efficient linkers.

The design of thermally conductive interfaces paid attention to the actual chemical feasibility by selecting molecules that already demonstrated capable to be grafted to graphene edges. Both thermal conductance and vibrational density of states were calculated to determine the match of phonons as heat carriers in interface constituents and the overall efficiency. Moreover, the mechanical stiffness of the junction was correlated to the thermal properties, finding some proportionalities, depending on the constituent chemistry.

The findings from thermal properties of suspended junctions drove the following investigations to a step-up in modeling, more representative of an actual nanocomposite material. The contribution of molecular linkers acting as heat carriers inside a complex polymer matrix was indeed addressed by embedding the graphene flakes and the molecular junctions inside bulk polymer. The contribution in thermal transport from molecular linkers was found significant even within the surrounding polymeric matrix. Thus, covalently bound molecular junctions demonstrated to be a promising method to drive the enhancement in thermal conductivity for graphene-based polymer nanocomposites.

Beside graphene-graphene junction, the effect of interfacial thermal conductance (ITC) between nanoparticles and the polymer matrix was also addressed, for both graphene and borophene. ITC values calculated by MD were fitted in a FEM model, able to predict the bulk composite thermal conductivity as a function of volume fraction and aspect ratio of the conductive nanoparticles.

Acknowledgment

I would like to thank my supervisor, Prof. Alberto Fina, for his guidance and patience in a novel field for me. His ideas and work attitude provided me the basis for a structured professional growth in the organization of the scientific research. This work would have been impossible without the financial support of the European Research Council (ERC) under the European Union's Horizon 2020, the EU Framework *Programme* for research and innovation, grant agreement 639495 — INTHERM — ERC-2014-STG.

Great thanks are also due to Dr. Bohayra Mortazavi from for the kindness to transmit his knowledge about computational modelling, with LAMMPS at the beginning and Abaqus in the time spent in Bauhaus-Universität Weimar.

Lastly, and most important, I want to express gratitude to my family and my friends, whom patiently understood how much time this cause needed.

Ai buoni esempi

A zio Giovanni
A Piera

Contents

List of Tables

List of Figures

Chapter 1

State of the art

In last decades, computational modelling has established as a powerful tool to investigate materials properties. In the computational environment, many different techniques were developed to satisfy proper compromises between results accuracy, in terms of simulation object size, computational load in as needed resources and simulation time, considered as the time where investigated phenomenon takes place. Nowadays, the popularity of these techniques is rising, as their applications benefits from the continuously growing computational power-price ratio, thanks to the progresses in electronics. A popular scheme, which places these techniques in terms of simulation time as a function of model size, is represented in Figure 1.

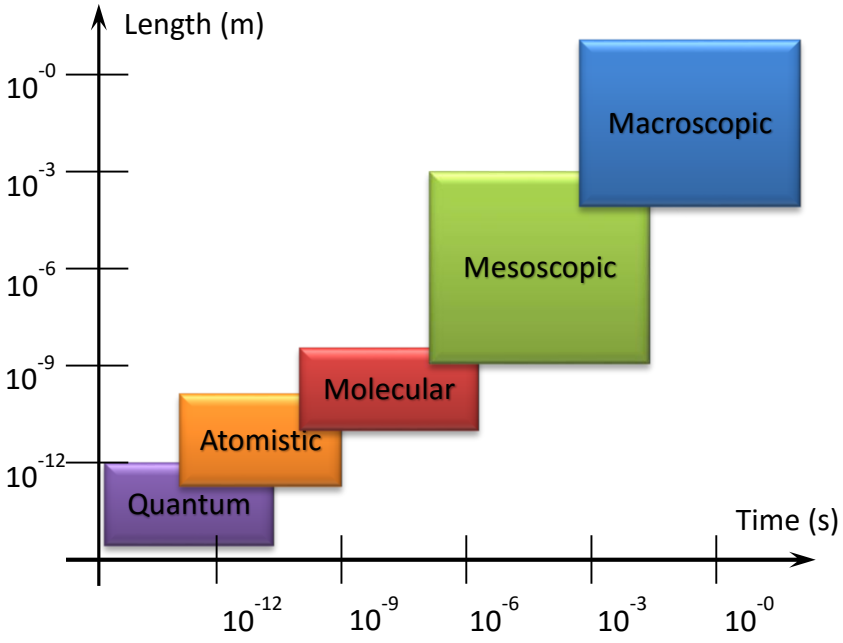

Figure 1. Computational Methods for materials simulations.

This scheme, scales up the methods from first principles ones, referred as *Quantum* methods, where the elementary electronic structure is investigated to address phenomenon lasting up to a few picoseconds (ps). Among these methods, is noteworthy to remember Quantum Mechanics/Molecular mechanics (QM/MM) [1] developed for biological systems, Density Functional Theory (DFT) [2] and Car-Parrinello-Molecular Dynamics (CPMD) [3]. On a slightly larger scale, *Atomistic* dynamics are investigated; the most common methods are Monte Carlo (MC) and Classical Molecular Dynamics (MD) [4]. In MD, Newton equation of motion simulates dynamics of single atoms and molecules. On a larger scale, the same dynamics are applied to groups of atoms, called beads, and considered as a single unit for Coarse Grained (or United Atoms) Molecular Dynamics [5]. Coarse Grained MD is popular for polymer-based simulations, where a single bead corresponds to an entire monomeric unit. Within the *mesoscopic* scale methods, it is possible to group methods capable to investigate fluidodynamics phenomenon as Brownian, Dissipative and Multi-particle collision Dynamics, Lattice Boltzmann methods to Computational Fluid Dynamics, where transport phenomenon, collision and mixtures in fluids are investigated. In the *Macroscopic* scale are grouped methods used in the continuum. Within the continuum methods, Finite Element Method (FEM) and Isogeometric Analysis are the most popular representatives and widely used in engineering simulations for thermal and mass transport, mechanical analysis and electromagnetic fields simulations.

Depending on the properties that need to be evaluated, one or more of the above techniques may be used. Indeed, when addressing macro-scale properties and phenomenon, it is most often convenient to combine different techniques into a so-called multiscale modelling, in which the outcomes of a lower scale computation method are used as parameters to feed the higher scale method.

This thesis addresses thermal transfer phenomenon at the nanoscale: therefore, the main technique exploited in this work is MD. However, as the properties of interfaces between graphene nanosheets directly affect the thermal conductivity at the nanoscale, FEM analysis of graphene-based nanostructure are also addressed.

1.1. Thermal transport in condensed matter

Heat transfer is a physical phenomenon that affects massively life on earth, from sun irradiation to everyday cooking. Heat could be transferred in three modes [6]:

- Radiation, in media where thermal radiation can be transmitted
- Convection, typical of liquids and gases
- Conduction, in solids and soft matter, driven by contact.

Heat transfers by radiation occurs when electromagnetic waves are emitted by from a body, propagates through a compatible medium and hits a second body acting as a target. All bodies with a temperature greater than the absolute zero convert part of the internal thermal motion in electromagnetic radiation, this happens when electrons in a higher atomic level moves to lower energy levels. The thermal radiation spectrum falls is in the wavelength range between 0.1 to 100 μm comprehending part of the ultraviolet spectrum, the visible light and largest part of the infrared region. Most of the materials absorb or reflects thermal wavelengths and only few solids allows the transmission of thermal radiation, in limited ranges. Such materials operate as infrared windows materials, this class of material includes only some glasses and few covalent and ionic crystals. When wavelength transmission is allowed, the transferred power by thermal radiation scales following the Equation 1 [6],

$$P = \epsilon \cdot \sigma \cdot A \cdot (T_1^4 - T_2^4) \qquad 1$$

where P is the radiative power (W), ϵ is the emissivity factor, σ is the Stefan-Boltzmann constant (5.67×10^{-8} W m^{-2} K^{-4}), A is the surface area, and T_1 and T_2 are the absolute temperatures of the radiation emitter and the receiver, respectively. The emissivity factor describes the capability of a material to emit and absorb thermal radiation; it is a dimensionless coefficient ranging from 0 to 1, which depends on material type and surface state.

In this work, the thermal properties of carbon-based nanostructures are investigated aiming at application in graphene nanostructures and nanostructured polymer composites. Inside such materials, the transmission of thermal radiation is close to zero and even in case of voids for highly porous materials, where theoretically radiation occurs, the difference of operating temperatures between polymeric surfaces is still low to make radiation contribution significant. Convection occurs in fluids (liquids, gases and melts) and it is negligible in solids, where the low degrees of freedom does not allow the cooperative motion of atoms and molecules. The nanostructures and the composites investigated here are assumed to be in the condensed state where matter flow is not allowed.

The focus of this work is thermal conduction transfer mode, which occurs when a thermal gradient is applied to solid matter. Thermal conduction is driven by two carriers: electrons and phonons. In metals, both carriers are responsible for heat transfer but electrons represent the main contribution, due to higher mobility. In metals, the contribution of electrons in thermal conductivity is so consistent that the Wiedemann-Franz law (Equation 2), with few exceptions, relates those two properties:

$$\frac{k_e}{\sigma} = L \cdot T \qquad 2$$

Where k_e is the thermal conductivity of the electrons, σ the electrical conductivity, L the Lorentz number ($2.44 \cdot 10^{-8}\, W\Omega K^{-2}$) and T the absolute

temperature. In ceramics and in polymeric materials, the heat conduction is almost all cases carried by phonons.
The description of a phonons starts with the Einstein-Debye model. Can be assumed that the thermal energy of a solid crystal is distributed amongst the normal modes of vibration of the atoms as a whole. Each normal mode is represented by a standing wave, independent and incapable of interacting with surrounding ones. n normal modes can be analyzed into n-1 travelling waves in opposite directions[7]. A simple 1D lattice is shown in Figure 2, where the short wavelength represents the standing waves from the oscillating atoms and the long wavelength is a lattice wave. Only lattice waves with wavelength longer than a complete period of standing waves can represent the motion [8].

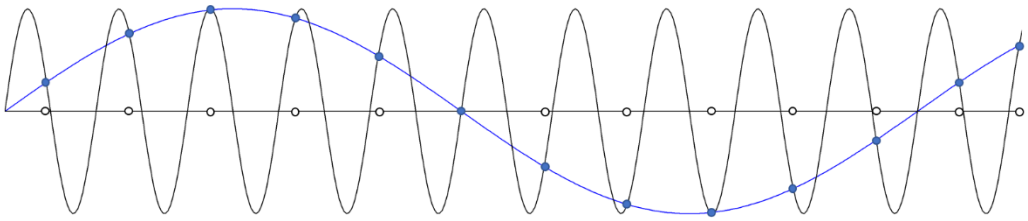

Figure 2. Standing waves from the atoms (black line) and a phonon wave (blue line) from the lattice.

Such lattice waves are energy carriers, with velocity of the same magnitude to the velocity of sound and, when longitudinally polarized are called sound waves. Similarly to the photons inside the electromagnetic field, the *quanta* of lattice vibrational field are called phonons [7]. Following the similarity between phonons and photons, the lattice became an empty volume with a "gas" of phonons, like if these were particles. All these analogies allowed to derive the understanding from classical kinetic theory, for example velocity distribution, mean free path, collisions between the phonons and more [7].
Phonons are featured by the polarization direction for each lattice coordinate into acoustic modes (A) and optical modes (O). In the acoustic modes, the wavelength are ordinary waves of a continuum lattice while the optical modes are featured by vibration frequencies that correspond to electromagnetic radiation in infrared, absorbed by dipole moment. Assuming a linear chain as one dimensional lattice, in the acoustic mode the displacement of both atom of the unit cell is coherent for amplitude, direction and phase, whereas in the optical mode the two atoms move opposite to each other and the amplitude is greater [9, 10]. Figure 3 depicts the polarization directions for a simple linear chain.

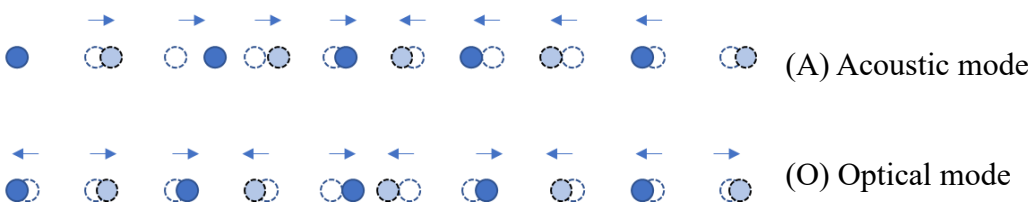

Figure 3. Polarization directions for acoustic mode (up) and optical mode (down) of a 1-dimension lattice.

In a three dimensional crystal, the allowed frequencies of propagation wave are reported by dispersion curves, where the phonon frequency is a function of coordinates in the first Brillouin zone (the primitive cell of the reciprocal lattice). In these curves, the phonon propagation is split into upper optical branches, and the lower acoustic branches. The number of those curves depends on the number of the atoms belonging to the first Brillouin zone and the three perpendicular directions of phonon motion: in a three dimensional system, a longitudinal (L) and two transversal (T_1, T_2) direction are expected for each atom of the cell. The density distribution of the available frequencies is the phonon (or vibrational) density of states (PDOS, VDOS). Such function describes the number of states as a function of the energy at each energy level available to be occupied. In small isolated systems, the number of available states is limited, deriving a VDOS with a neat discrete behavior. The VDOS is usually expressed in arbitrary units (count) as a function of wavelength (usually expressed in cm^{-1}) of frequency (THz), where 1000 $cm^{-1} \approx 29.98$ THz.

The mechanism of phonon propagation is illustrated in Figure 4 for a crystalline material (Figure 4A) and amorphous polymeric chain (Figure 4B). In both cases, the first step is the heating of the atoms that constitutes the surface on the left, it may take place by radiation, conduction or convection. What follows depends on materials behavior, in crystalline materials, the incoming heat is transformed into vibrational energy of particles. This vibrational energy is then gradually transferred to the high coordinated adjacent atoms, forming a planar wave from the cumulative displacement of equilibrium positions. The thermal energy in waveform, then, diffuses with a common phonon mode to the whole crystal. When the heat reaches the opposite end, it is transferred to the environment via conduction, convection or radiation. When a polymer is exposed to a heat source, the heat does not propagate as a planar wave among chains as happens in traditional crystals. In polymers heat diffuses slowly through disordered local atomic motions and rotations of repetitive units, cumulating the contribution of the freedom degrees of the molecule, as schematically reported in Figure 4 from B’ to B’’’.

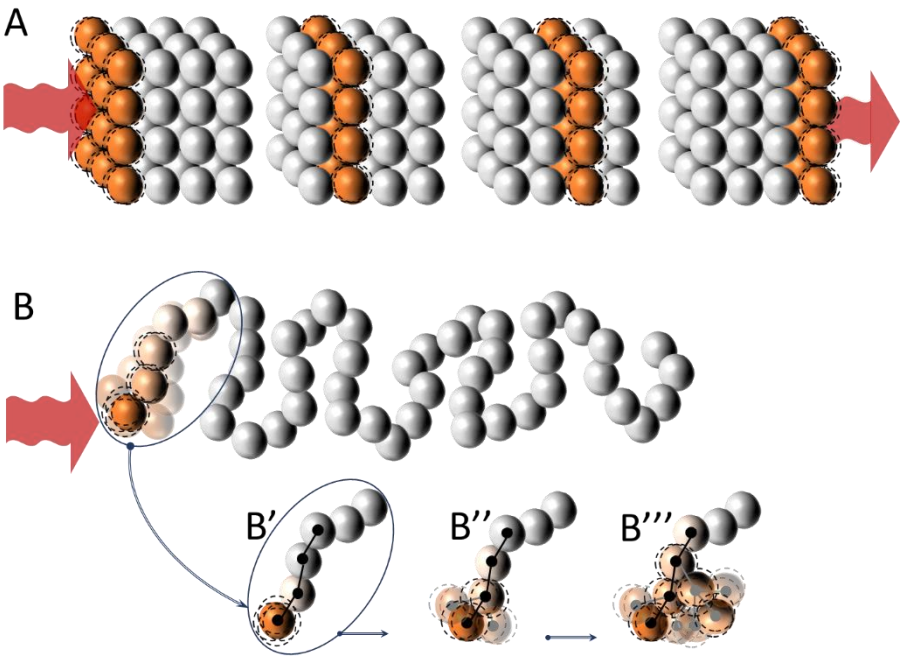

Figure 4. Thermal conductivity mechanisms in (A) rigid lattice, where phonon propagation waves are represented by dashed orange atoms and (B) amorphous polymer diffusion mechanism (in B, a sphere represent a monomer). Reprinted with modifications from [11]. Copyright (2016), with permission from Elsevier.

The thermal conductivity is the unit of measure of the heat conduction, and it is an intensive property typical of the material. The general formulation for thermal conductivity in three dimensions is represented from Fourier expression, which assumes a linear temperature profile inside the material, as reported for three-dimensional case in Equation 3, where $\vec{q}$ is the heat flux density ($\frac{W}{m^2}$), k is the thermal conductivity ($\frac{W}{m \cdot K}$) and $\vec{\nabla} T$ the temperature gradient.

$$\vec{q} = -k\vec{\nabla}T \qquad 3$$

However, a large number of systems can even be approximated to the one-dimensional formulation reported in Equation 4, which reduces the temperature gradient to $\frac{dT}{dx}$.

$$\vec{q}_x = -k\frac{\partial T}{\partial x} \qquad 4$$

Such transport equation derives from a typical non-equilibrium condition, schematically depicted in Figure 5, when a temperature difference is applied to the ends.

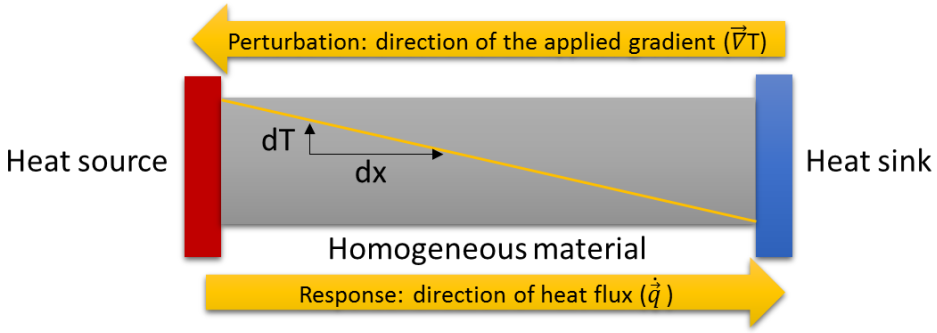

Figure 5. Conceptual scheme representing a typical non-equilibrium process, where a perturbation (the temperature gradient $\vec{\nabla}$T) is applied to a homogeneous material and the response of the material a steady-state heat flux.

When a material reached the equilibrium temperature T, its phonon population $n_{\vec{q}j}^{(eq)}(T)$ describes the number of phonons for each vibrational mode $\omega_{\vec{q}j}(T)$ with wave vector k_k and branch index j found at energy $\hbar\omega_{\vec{q}j}$. By the application of a temperature gradient, as briefly depicted in Figure 5, a corresponding heat flux is generated following Fourier's equation (4). This heat flux can be written in terms of phonon group velocities $\vec{v}_{qj} = \frac{\partial\omega_{\vec{q}j}}{\partial\vec{q}}$, phonon energies $\hbar\omega_{\vec{q}j}$, and perturbed population $n_{\vec{q}j}$ from equation 7, where Ω_c is the volume of unit cell in crystal and N the number of cells of the system [12].

$$q_x = \frac{1}{N\Omega_c}\sum_{\vec{q}j}\hbar\omega_{\vec{q}j}\ \vec{v}_{qj}n_{\vec{q}j} = -k\frac{\partial T}{\partial x} \qquad 5$$

Inside an ideal crystal, free from defect, impurities and boundaries the energy content of lattice waves is a constant of motion, meaning that the mean free path of the phonon is almost infinite and thus the thermal conductivity goes up to infinite levels. In real crystals, the energy between energy waves is exchanged with high power, thus reducing the mean free path of the phonons and the thermal conductivity too.

Equation 7 is not enough to predict transport properties inside from a theoretical point of view. An accurate description of the role of the perturbation, balanced by the phonon population, was formulated from Peierls in 1929, the Boltzmann Transport Equation (BTE) and it is reported in equation 6.

$$\left.\frac{\partial n_{\vec{q}j}}{\partial t}\right]_{scatt} = \vec{v}_{qj}\frac{\partial T}{\partial x}\frac{n_{\vec{q}j}}{\partial T} \qquad 6$$

The solution of the BTE is not a trivial issue, because requires a deep knowledge in phonon properties, interaction and lifetime of the system, moreover it requires a large amount of computational resources. Despite this premise, some simplifications were made to handle a reduced number of information, like the single mode

approximation (SMA) by Klemens in 1951, which uses only the diagonal term of the scattering matrix, and further developments. To solve the BTE, the Density Functional Theory (DFT) represent one of the most used approach, moreover with the addition of some perturbing potential in the density functional perturbation theory DFPT, it is possible to investigate the consequential system responses [12].

When the phonon picture is unfeasible, for example in translational variant or atomic vibrations out of collective modes systems, Molecular Dynamics approach can be used, thus calculating the actual atomic trajectories in the real space. In this case, the accuracy is strongly dependent on the force-field accuracy, where parameters obtained from ab-initio calculations are to prefer to empirical ones [12] (paragraph 1.3. includes an in-depth presentation of force fields and their parameters).

The comparison made in Figure 4, among A and B cases, highlights that the crystal nature of a material is fundamental to achieve high thermal conductivity when phonons are the thermal carriers. Indeed, more than a crystalline structure itself is the binding energy, the high atoms coordination and stiffness of the structure that matters. As a matter of comparison, the thermal conductivity of pure diamond, having a very regular crystalline structure made of four coordinated identical carbon atoms, it is about ~2000 W m^{-1} K^{-1}[13] whereas two engineering ceramic materials as boron nitride and silicon carbide reports values one order of magnitude lower (Table 1). On the other hand, one of the semi-crystalline polymer with the higher crystallinity grade and ordered lamellae, such as High-Density Polyethylene HDPE (Table 2) exhibits a thermal conductivity four order of magnitude lower, about 0.5 W m^{-1} K^{-1}. Most of this discrepancy can be explained by the coordination of identical atoms in diamond that allows phonon motion through the whole crystal coordinates. On the opposite, in HDPE molecules, the unbounded degrees of freedom attenuates phonon motion.

Table 1. Thermal conductivity of metals, ceramics and carbon based materials commonly adopted as composite fillers.

Material	**Thermal conductivity at 25°C (W m^{-1} K^{-1})**	**Reference**
Graphene	[2000, 6000]	[14, 15]
Carbon nanotubes (CNT)	[2000, 4000]	[14]
Diamond	2000	[13]
Silver	427	[16]
Copper	386	[13]
Gold	315	[13]
Hexagonal boron nitride (h-BN)	[185, 300]	[14, 17]
Silicon carbide (SiC)	[120, 270]	[13, 14]
Aluminum	[234, 247]	[13, 14]
Silicon nitride (β-Si3N4)	[103, 200]	[14]

Graphite	[100, 400]	[14]
Alumina	30	[14]

Table 2. Thermal conductivity of various polymers.

Material	Thermal conductivity at 25°C ($W\ m^{-1}\ K^{-1}$)	Reference
High density polyethylene (HDPE)	[0.33, 0.53]	[14, 15]
Low density polyethylene (LDPE)	[0.30, 0.34]	[14, 15]
Polyamide 6.6 (PA66)	[0.24, 0.33]	[14, 15]
Polycarbonate (PC)	[0.19, 0.21]	[14, 15]
Epoxy resin	0.19	[15]
Poly(dimethylsiloxane) (PDMS)	[0.15, 0.25]	[15]
Poly(ethylene terephthalate) (PET)	0.15	[14, 15]

From the previously cited similarity between phonons and photons, where the lattice is represented by an empty volume filled with a phonon gas, as if these were particles [7], the contribution in thermal conductivity of a phonon can be estimated through Debye approximations [18], by the kinetic theory of gas [19, 20], briefly reported in Equation 7.

$$k_p = \frac{1}{3} c_p v l \qquad 7$$

Where k_p is the thermal conductivity of a single phonon, c_p is the heat capacity, v the speed of the phonon and l is the mean free path (MFP). The MFP represents the average propagation distance for a phonon before a scattering event.

In crystalline matter, all lattice imperfections scatter lattice waves to some degree and thus contribute to the rise of thermal resistance [10]. The types of imperfections are usually classified by their dimensionality, from 0D to 3D, and the correspondingly scattering power occurring between each imperfection and phonon (or electron) can be calculated [7]. Thus, phonon scattering occurs in lattice imperfections in case of:

- 0D defects are isolated point defects, such as vacancies, interstitials, atomic substitutions and isotopes [7].
- 1D defects or line defects are typically dislocations [7]
- 2D defects or surface defects comprehends grain boundaries, twin boundaries or stacking faults [7, 11]
- 3D imperfections occurring in substitutional alloys and glasses, caused by volume disorder [7, 11].

Moreover, phonon/phonon scattering could occur. Ideally all atoms vibrates with the same frequency, harmonically, but actually several vibrational modes are allowed in phonon motion [11]. These colliding anharmonic vibrations can generate a reverse wave in overall vibrations called Umklapp scattering [9, 10]. This phenomenon shortens the MFP, affecting k_p as calculated by Equation 7.
In polymer matrix composites, the inefficiency of phonon transfer from a conductive particle to another has been related to the "soft" interface, which does not allow transfer of efficient vibrational modes of phonons [11, 21].

1.1.1. Thermal transport across interfaces

Figure 6 qualitatively illustrates the perturbation and response applied to two different systems, a homogeneous material and two-coupled materials featured by an interface. If we assume that the heat sink and the heat source are at the same temperature for both the systems, the presence of an interface interferes with heat carriers (phonons), generating a thermal resistance and thus, the rise of a temperature difference $\Delta T = (T_1 - T_2)$ across the interface [22, 23].

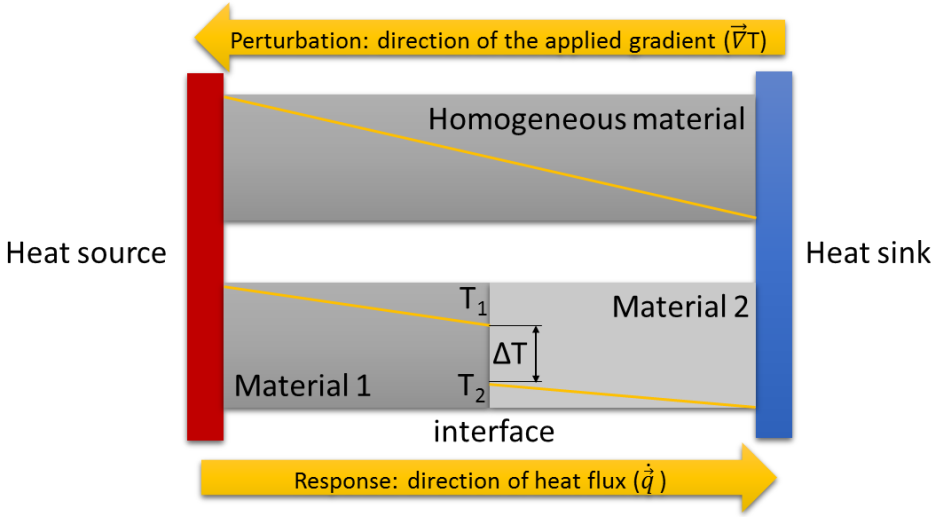

Figure 6. Conceptual scheme representing a typical non-equilibrium process, where a perturbation (the temperature gradient $\vec{\nabla}$T) is applied to a homogeneous material (up) and two-coupled materials featured by the presence of an interface (down). The response of both systems is a steady-state heat flux, featured by a thermal resistance across the interface, where present.

A phonon incident to an interface has only two options, being transmitted or not. In the following description, the transmission probability it is named α and it is a function of phonon mode, wave vector, frequency and system temperature. We assume that the system is isotropic, thus, no temperature effect will be considered in the following description.

The total heat current density from side *1* to side *2*, $\frac{1}{A}\dot{q}_{1\xrightarrow{total}2}(T)$, it is the sum over all frequencies and incident angles of the phonons with frequency and angles incident over the area unit A times the phonon energy $\hbar\omega = \hbar c_{1,j} k_k$ times the probability of transmission $\alpha_{1\to2}(\theta, j, \omega)$.

The letter *j* represent the phonon mode, k_k the wave vector of the phonon and $c_{1,j}$ is the phonon propagation velocity in side *1* for phonons owing mode *j* of propagation and frequency ω. Incident angles are, φ azimuthal and θ, between incident phonon and wave vector normal to the interface. If $c_{1,j}cos\theta$ it is the normal component of the velocity, $d\Omega = d\varphi sin\theta\, d\theta$ and $N_{1,j}(\omega, T)$ the product of the phonon states density with angles φ and θ given, times the Bose occupation factor. Then, the number of phonons incident to the surface with given frequency and incidence angle on *A* per time unit is $\frac{N_{1,j}(\omega,T)}{4\pi} d\Omega c_{1,j} cos\theta$. Integrating all over the angles, we obtain $c_{1,j}N_{1,j}(\omega, T)$. Thus, the total heat current is reported by equation 8

$$\frac{1}{A}\dot{q}_{1\xrightarrow{total}2}(T) = \frac{1}{2}\sum_j \int_0^{\frac{\pi}{2}} \int_0^{\omega_1^{max}} N_{1,j}(\omega, T)\, \hbar c_{1,j} \times \alpha_{1\to2}(\theta, j, \omega) \times cos\theta sin\theta\, d\theta\, d\omega \qquad 8$$

Where ω_1^{max} is the maximum frequency of phonons allowed on side 1. For small difference in tempertures $\frac{(T_1 - T_2)}{2}$, the thermal boundary conductivity becomes as reported by equation 9:

$$G = \frac{\dot{q}_{1\xrightarrow{total}2}(T_2) - \dot{q}_{1\xrightarrow{total}2}(T_1)}{A(T_2 - T_1)} \qquad 9$$

Which it is solved by knowing the transmission probabilities α. To estimate the transmission probability mainly two models were developed. In the acoustic mismatch model (AMM) no scattering occurs at the interface, despite this phenomenon has been observed in several cases. In diffuse mismatch model (DMM), it is assumed that all phonons are scattered at the interface.

Within AMM phonons are treated as plane waves and the lattices as the continuum. Such approximation is therefore accurate where the phonon wavelength is much longer than the interatomic spacing. In this picture, the incident phonon can be reflected, reflected and converted, refract or refract and converted, similarly to what happens in electromagnetic wavers for Schnell's law. Despite this simplification, the transmission of phonons across the interfaces is much more complicated than the transmission of signals, because there are three phonon modes, because solid are anisotropic, and phonon transmission depends on angle of incidence. The simplest mode to calculate the transmission probability is that for each material is attributed an acoustic impedance equal to $Z_i = \rho_i c_i$ where ρ_i is the mass density and c_i is the phonon velocity. In case of phonon with normal incidence, for example, the energy transmission probability becomes as reported from equation 10:

$$\alpha_{1\to2} = \frac{4Z_1Z_2}{(Z_1+Z_2)^2} \qquad 10$$

On the opposite, in DMM the probability of transmission is nonetheless determined by a mismatch between the density of states. According with DMM theory, two solids with identical acoustic properties should reflect a transmission of half while in case of AMM it will be unity. In this case, thus, DMM estimates the thermal boundary resistance as double. In case of very different materials, such as liquid gases and metals, as Kapitza did in 1941 [24], measuring the thermal resistance in solid/liquid helium interface, DMM underestimates the thermal boundary resistance. In DMM, the parameter α is independent from wave vector and mode as described in equation 11.

$$\alpha_{i,j}(\omega, j) = \alpha_i(\omega) \qquad 11$$

From the definition of AMM, where the transmission and reflection probability are equals, follows equation 12

$$\alpha_i(\omega) = 1 - \alpha_{3-i}(\omega) \qquad 12$$

Moreover, the density of phonons of energy $\hbar\omega$ leaving side i corresponds to equation 13

$$\sum_j \int_0^{2\pi} \int_0^{\frac{\pi}{2}} d\theta cos\theta d\varphi c_{i,j} N_{i,j}(\omega, T)\, \alpha_i(\omega) \qquad 13$$

Where $N_{1,j}(\omega, T)$ is the density of phonons with energy $\hbar\omega$ at temperature T. The angular integral is reported in equation 13

$$\frac{1}{4}\sum_j \left[c_{i,j} N_{i,j}(\omega, T)\right] \alpha_i(\omega) \qquad 14$$

Balancing the phonon number leaving side *3-i* per unit area per unit time we get equation 15.

$$\sum_j \left[c_{i,j} N_{i,j}(\omega, T)\right] \alpha_i(\omega) = \sum_j \left[c_{3-i,j} N_{3-i,j}(\omega, T)\right] 1 - \alpha_i(\omega) \qquad 15$$

To obtain the transmission probabilities in eq.16

$$\alpha_i(\omega) = \frac{\sum_j c_{3-i,j} N_{3-i,j}(\omega, T)}{\sum_{i,j} c_{i,j} N_{i,j}(\omega, T)} \qquad 16$$

And with Debye approximation reduces to equation 17

$$\alpha_i(\omega) = \frac{\sum_j c_{3-i,j}^{-2}}{\sum_{i,j} c_{i,j}^{-2}} \qquad 17$$

Which allows to calculate the thermal boundary resistance from the application of equation 8. Despite AMM and DMM are actually based on antithetic hypothesis,

the thermal boundary conductivity calculated for several coupled materials differs of about ± 30% [23].

From measurements and calculations [22, 23, 25], thermal transport across interfaces is commonly proposed in terms of thermal boundary conductivity [26], i.e. the inverse of the interfacial thermal resistance, which formulation it is reported in Equation 18,

$$G_c = \frac{\dot{q}}{A \cdot \Delta T} \qquad 18$$

where G_c is the thermal boundary conductivity, $\dot{q}$ the heat flux flowing into the material, A the interface area and ΔT the temperature across the interface. The standard units of measurement is W m^{-2} K^{-1}. The thermal boundary conductance is geometry independent, meaning that doubling the contact area A will not affect the thermal boundary conductivity [23]. On the opposite, when dealing about defined object, such as heat spreaders, the thermal boundary conductance (TBC) is used and the conductance increases proportionally to the contact area [23]. TBC formulation is reported in Equation 19, where the thermal boundary conductance is expressed in W K^{-1}.

$$G = \frac{\dot{q}}{\Delta T} \qquad 19$$

1.1.2. Thermal conduction in polymers

Nowadays, polymers usage is incredibly wide: a large amount of different polymers are employed in almost all the industrial fields, from packaging for electronics, clothing, aerospace, automotive, buildings, adhesives and coatings and more, making polymers an incredibly versatile class of materials, where almost all the component of a modern product benefits from polymer adoption. Sometimes, industrial manufacturing limits polymeric materials to cost reduction idea, just as metal replacement or to reduce weight in non-structural parts. However, significant advantages from polymer adoption also include corrosion resistance, flexibility and the ability to be processed in complex geometries. The high corrosion resistance in polymer is intrinsic and mainly due to a general chemical inertia of polymers in acid ad alkaline environments. A typical application of polymeric corrosion resistance is protective coatings to preserve metals undergoing aggressive environment. Complex geometries objects can be industrially produced through the typical polymer manufacturing techniques for: injection molded objects, extruded products thin films, and foams. In smaller scale, polymeric additive manufacturing is currently a popular rapid prototyping method. The polymer flexibility, is related to the low Young modulus of polymers (usually well below 4 GPa), for the sake of comparison, metals such aluminum and steel reaches about 70 and 210 GPa, respectively. In the extreme case of rubbers and elastomers, this modulus falls down to 0.1 GPa and less, with no equals in other classes of materials for example in vibrations attenuation.

On one hand, polymers are known to be thermal insulators, as proven by the low thermal conductivity values previously reported in Table 2. In fact, many applications that involves polymers take advantage from the insulating properties: in clothing as textile fibers, in handles and handgrips for automotive and household appliances, to improve safety and comfort and overall where a warm touch is preferred. Such insulating properties are even enhanced in foams and expanded products, where the trapped air boost the thermal insulation with major applications in buildings and in packaging field. On the other hand, polymers with high thermal conductivity are desirable to gather the polymer properties of flexibility, corrosion resistance, molding techniques in heat removal applications. Examples of potential applications are found in electronics, where heat removal is crucial for chip packages, lighting devices, lithium batteries and where overheating can cause from device life shortening to potential hazard to users. Moreover, desirable application can be found in where chemical inertia is predominant as food processing industry, polymeric heat exchangers for corrosive fluids environments. To improve thermal conductivity of polymers, the common route is to introduce thermally conductive particles acting as a filler, inside a polymer matrix and thus generating a composite material.

The mechanism of heat propagation in polymers has been introduced in Figure 4B, where a single amorphous polymer chain was ideally exposed to heat. In this case, the lack of coordination in phonon motion (Figure 4 from B' to B''') is the cause of poor thermal conductivity in polymers. Following the Equation 7, the thermal conductivity of a phonon is proportional to the MFP, usually lower than 10 Å in polymers above 100 K [18]. Inside a real polymer, the phonon MFP is shortened by the unbounded degrees of freedom inside the molecules. Moreover, irregularities as crystalline and non-crystalline interfaces, entanglements, van der Waals (vdW) interactions, free volume, branches and other defects presents in the bulk affects thermal conductivity. Usually, the thermal conductivity of crystalline polymers is higher than the amorphous ones (Table 2). This trend, partially can be explained with a longer MFP for phonons, on the other hand, the boundaries among crystallites and amorphous regions behave as interfaces, thus inducing phonon scattering and the growth of a boundary resistance [18]. The equilibrium of these competitive phenomenon in semi-crystalline polymers is actually unclear, a comprehensive theory is still missing and contradictions in literature works exists [15].

The molecular orientation of a polymer can be modified by fiber drawing. The drawing operation of molten polymer creates a tensional state due to the speed difference inside the melt, which reduces entanglements and aligns the macromolecules, bringing to permanent molecular rearrangement once the melt cools down. The drawn polymer usually exhibits along the strong anisotropy, higher tensile strength, and thermal conductivity along the drawing axis [18]. Ultra-drawn HDPE fibers were reported thermal conductivities up to 104 W m^{-1} K^{-1} [27] along the drawing axis and standard values transversally, this finding was attributed to a longer MFP associated to a reduced scattering among oriented macromolecules. The thermal conductivity of single polymer chains has been deeply investigated by computational works, by theoretically perfect design of topological structures. computational findings usually achieves higher thermal conductivities compared to

the actual polymer [28]. Henry and Chen [29] adopted Green-Kubo MD calculations to calculate the thermal conductivity of a single stiff polyethylene chain. That work revealed that the velocities in longitudinal mode, within the HDPE chains, reached about 16000 m/s, determining about 350 W m^{-1} K^{-1} of thermal conductivity. For the sake of comparison, the calculate value corresponds about 700 times the bulk polymer one (as reported in Table 2).

In 2011, Luo *et al.* [30], investigated through reverse NEMD simulations various Polydimethylsiloxane (PDMS) configurations. The study covered from the single chain with ideal monomer orientation, a random-rotated monomers chain, a double chain, multiple parallel chains (defined as crystalline form), up to a bulky amorphous structure. The thermal conductivity was found strictly dependent from the polymer morphology, with a proportional decay as the complexity of the structure rise. That study reported values from 7 W m^{-1} K^{-1} for the ideal single chain to 0.2 W m^{-1} K^{-1} for the bulky polymer, a value very close to the actual one of about 0.15 W m^{-1} K^{-1} (Table 2). The discrepancy found by the authors with the previous work from Henry and Chen in terms of maximum thermal conductivity for the chain was attributed to the inner conformational disorder of PDMS. PDMS backbones atoms in fact, rotates easily, bringing to the lack of a long range order in single chain of ideal PDMS. To prove such thesis, the COMPASS Force Field was tuned to increase the dihedral angles stiffness (Figure 7) obtaining the suppression of rotations in simulation runtime.

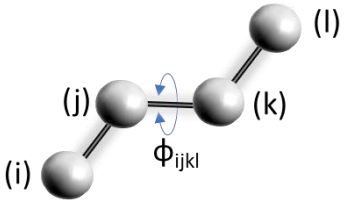

Figure 7. Dihedral angle in Molecular Dynamics Force Field.

This artifact worked and allowed the “stiff-ideal-chain” to reach a higher conductivity value. The same artifact was applied to the random-rotated monomer chain, but in this case, no significant improvement in conductivity was measured. This latter experiment confirmed the initial supposition made: temporal rotations of monomers exhibited a detrimental impact on PDMS thermal conductivity [20].

Also the temperature affects the thermal conductivity of polymers: in amorphous polymers, the thermal conductivity increases monotonically from 0 K [18] to the glass transition temperature (T_g) where a peak is observed [31, 32] even if the MFP monotonically reduces. Above the T_g, the chain mobility increases and the intermediate range order, which features amorphous polymers, loses allowing large conformational rotations. This condition increases scattering events due to the large defects propagations. The thermal conductivity in semicristalline polymers was observed from Choy [18] to increase at temperatures in the range between 2 K to 20 K, but later works reports a slightly decrease in thermal conductivity from room temperature up to the melting point. In this case, an accepted explanation of this behavior is still missing and different theories coexists [32].

1.1.3. Thermal conduction in graphene

Graphene is one of the most fascinating and extensively studied materials in this decade. The single layer graphene (SLG) is a planar sheet made of one-atom-thick, sp^2-bonded carbon atoms. It is also referred as a 2-dimensional material, due to the limited thickness (in the following text, the terms Graphene and SLG are adopted as synonyms). Graphene ideally forms a flat isolated honeycomb lattice (Figure 8), as opposite to its ancestor, graphite, which stacks several layers of the same structure.

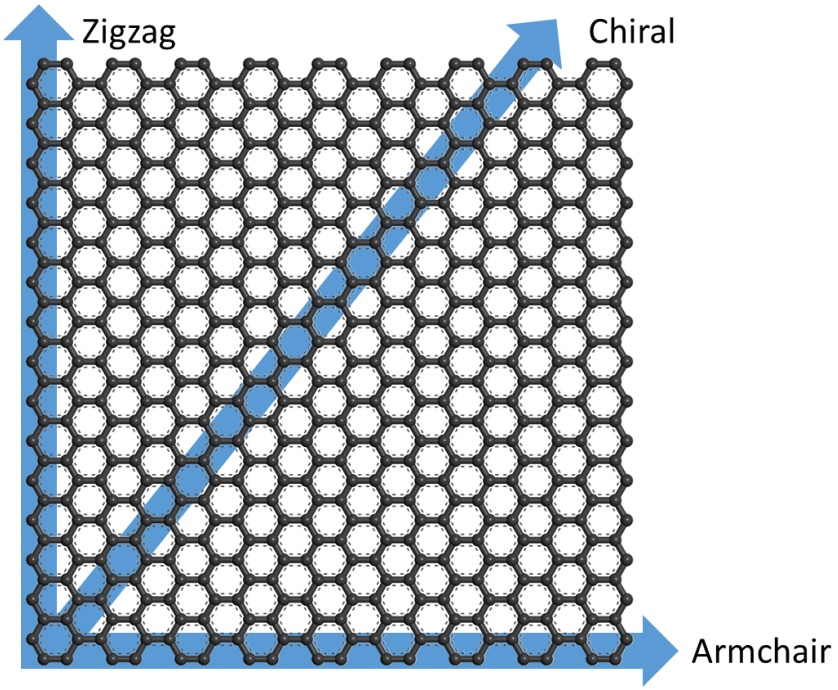

Figure 8. Graphene lattice structure. Zigzag on vertical axis, Armchair on horizontal axis and a chiral example in arbitraty angle (other Zigzag or Armchair configurations are tilted every 30°)

It was firstly isolated by Geim and Novosëlov in 2004 [33] which found advanced electronic properties. Graphene samples in the nanoscale exhibited top-known properties among materials for electronic structure [34], thermal conductivity [35], mechanical stiffness and modulus [36].

The production of a SLG similar to the ideal one is challenging and still belongs to highly specialized laboratory scale facilities, still far from industrial scale production, however many Graphene Related Materials (GRM) are available and employed in experimental studies. GRM is a family of graphene-based materials that comprehends a variety of materials which thickness is higher than the single layer, due to multiple sheets stacking and their oxidized derivations. In 2013, Bianco *et al.* [37] suggested a comprehensive nomenclature that is briefly reported as follows:

- Multilayer graphene (MLG), is a structure made of up to 10 stacked graphene layers and 34 Å of total thickness;

- Few layer graphene (FLG) is a subset of MLG where up to 5 layers are piled for an overall thickness of about 17Å;
- Graphite nanoplatelets/nanosheets/nanoflakes (GNP) are graphitic material with a thickness or a lateral size limited to a maximum of 100 nm.

As derivative version of above cited GRM, the oxides:

- graphene oxide (GO) is a SLG where extensive oxidation of the basal plane occurred;
- multilayer graphene oxide film (MGOF): a generic multilayer made of GO;
- reduced graphene oxide, (rGO): a bulky graphite, which underwent exfoliation trough oxidation, followed by chemical, thermal and/or other reduction processes to decrease the oxygen content.

Among its remarkable properties, the excellent thermal conductivity of SLG received great attention of materials researchers. MD calculations with the early version of Tersoff for carbon, revealed a theoretically thermal conductivity up to 10000 W m^{-1} K^{-1} in about 150Å defect less slab length [38], while experimental works based on Raman optothermal analysis measured up to 5000 W m^{-1} K^{-1} in suspended samples [39]. Nevertheless, the thermal properties of GRM are usually constricted when compared to SLG. The increase of thickness in GRM limits the thermal transport for a couple of reasons, the first it is due to the crystal anharmonicity typical of the lattice and the second reason it is the scattering of phonons at boundaries [40]. The studies on suspended FLG highlighted change in phonon dispersion [40]: firstly, in structures made up to four layers, a sharp decay was recorded in thermal conductivity and this was attributed to the availability of more phase-states while keeping zero the transverse component of velocity. In thicker MLG, the thermal conductivity exhibited a plateau, and then a decay of the thermal conductivity, even lower than graphite one, caused by a rise of boundary scattering [40].

Graphene has a semi-metal behavior [41] because it has a zero band-gap between valence and conduction bands [41]. As first consequence, despite the availability of mobile electrons in-plane, the thermal conductivity is attributed almost integrally to phonons [40, 42-44]. Both acoustic (A) and optical (O) modes (described in paragraph 1.1) contributes to thermal transport in graphene lattice, moreover, the phonon dispersion occurs longitudinally (L), transversally (T) or in out-of-plane coordinate (Z). The phonon dispersion calculated by Cocemasov and coworkers for of single layer graphene, calculated trough ab-initio methods, is depicted in Figure 9. From the same work, the density distribution of vibrational modes is reported as VDOS, Figure 10.

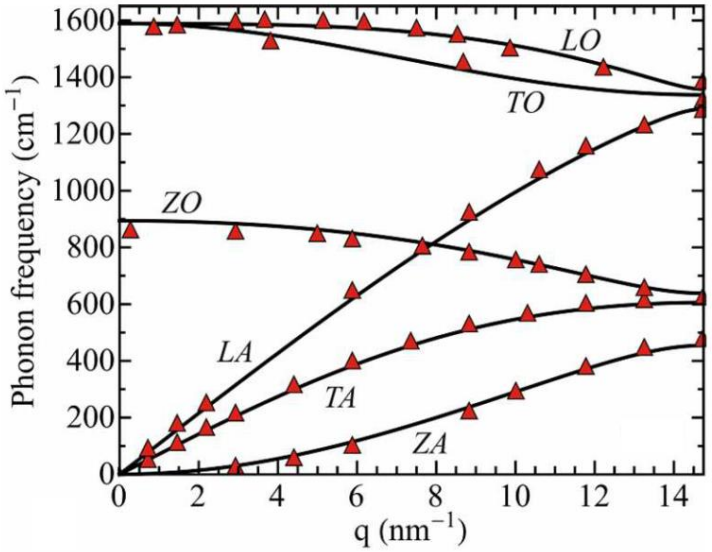

Figure 9. Phonon dispersion in single layer graphene. Reproduced from Ref. [45] with permission from the Royal Society of Chemistry.

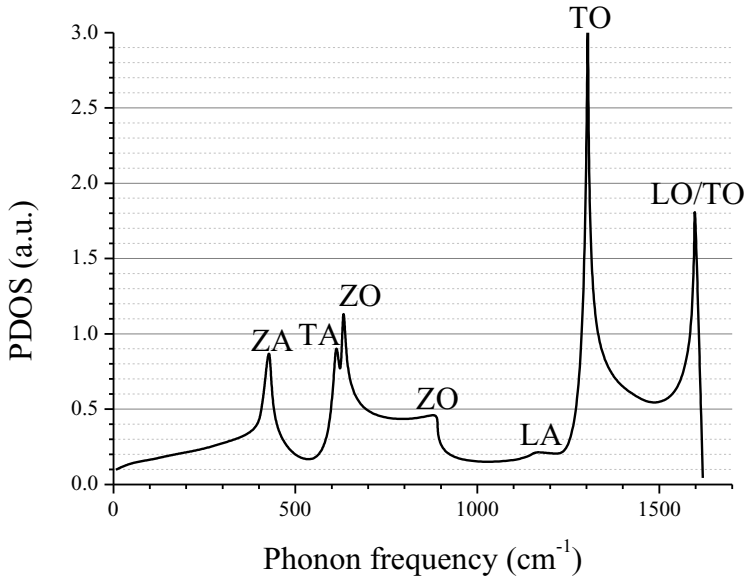

Figure 10. Phonon density of states (PDOS) in graphene monolayer as a function of frequency. Adapted from [45] with permission from the Royal Society of Chemistry.

In Graphene, the phonon MFP is extraordinary long, estimated of about 775nm at room temperature [35]. The MFP is also calculated as the product of phonon velocity and the relaxation time, as summarized by Equation 20:

$$MFP = v\tau \qquad 20$$

Where v is the phonon group velocity and τ the relaxation time of phonon, the time that occurs between two scattering events. In Graphene, the MFP is an important parameter, because phonon modes are affected by the ratio of flake length and MFP [46]. This assumption is valid both for experimental and computational analysis. If the MFP is longer than the sample length we can assume that no scattering occurs

[47], this condition is called ballistic regime. In graphene flake longer than the MFP, phonon scattering occurs and this condition brings the system to diffusive regime. Diffusive regime in graphene generates a plateau with the thermal conductivity that can be observed as the sample size grows. In 2014 Fugallo and coworkers [44], by solving the Boltzmann Transport Equation (BTE), through on ab-initio techniques, highlighted the underestimation for in-plane conductivity. This value was initially calculated about 500 $W\ m^{-1}\ K^{-1}$ by the Single Mode relaxation Approximation (SMA) of the BTE. By this new hypothesis, which evidenced that the collective nature of phonon excitation is neglected in SMA, attributed an even longer MFP to graphene. The collective excitation hypothesis, better agrees with experimental results, which reported in plane conductivity over 1000 $W\ m^{-1}\ K^{-1}$ for recently available longer flakes [44, 46]. Lattice orientation (Figure 8) is a parameter that affects thermal transport in graphene. From computational studies, it is known that, for finite size nanoribbons, the thermal conductivity of single layer graphene in Zigzag direction is about 30% higher than in armchair direction [48, 49]. The thermal conductivity difference between the two directions however flattens as the number of layer increases [40, 49]. The presence of defects in graphene lattice causes a rapid decay in thermal conductivity, this is due to the scattering of in-plane phonon modes [42]. Molecular dynamics investigations [50, 51] clearly demonstrated how a single defective site (stone wales, point vacancies, bivacancies) in 400 atoms can half the thermal conductivity of the graphene slab. The excess of oxidation in GO was also observed experimentally in nanocomposites, where the annealing process lead to a dramatic increase in thermal conductivity [52]. Analogously, a series of polycrystalline graphene sheet were simulated by Mortazavi and coworkers [53] through a multiscale study by coupling MD and FEM simulations. As a finding, the thermal conductivity decays became a small fraction of the pristine sheet due to diffuse scattering and consequently a reduction of available phonon modes.

1.1.4. Thermal conduction in polymer matrix composites

With the aim of improving the thermal conductivity (TC) of polymers, many efforts have been done by incorporating high thermally conductive fillers. Suitable thermally conductive fillers are metallic and ceramic particles or carbon based materials [15]. The resulting composite material were find strongly dependent from composite isotropy and filler dispersion, and usually best results were achieved with high filler loadings, typically more than 30% in weight [15]. Usually, as the filler loading increases, the polymer capability to being processed decreases [54]: a common drawback the of high filler loadings is represented by the increase of melt viscosity, inducing the use of plasticizers determining extra cost [54]. Moreover, in case of hard particles a three-body wear can occur in extruders, molds and other processing facilities.

In thermally conductive composite design, one of the challenges is to predict the final conductivity as a function of the filler loading. With this purpose, several predictive models are continuously developed [14, 15, 55-57]. In such models the thermal conductivity is predicted by knowing the thermal conductivity of the

constituents, the filler loading and other chemical or physical parameters as filler size, shape, aspect ratio and porosity and even more [14, 58]. Often, the practical fitting of experimental data in a theoretical equation is an awkward operation, due to the need of parameters hard to measure, as interfacial thermal resistance [59] or correcting terms as auxiliary constants in Rayleigh's model [56]. Nevertheless, a couple of predictive models can represent contemporary the ancestors and the upper and lower limits in thermal conductivity prediction models. The first one is defined as parallel model (right in Figure 11) where each phase contributes separately in thermal conductivity. The overall value is then assumed the weighted average to volume fractions, similarly to the composite density calculus.

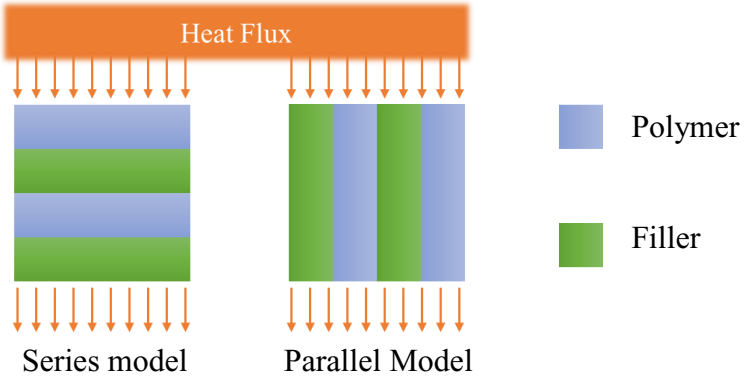

Figure 11. Series and parallel models for predicting thermal conductivity in composites.

In this model, each component is independent from the other. Following this hypothesis, the thermal conductivity can be calculated by Equation 21.

$$K_c = K_f \phi_f + K_p \phi_p \qquad 21$$

Where K_c is the composite TC, K_f is the filler TC, ϕ_f is the filler volume, K_p the polymer TC and ϕ_p the polymer volume fraction. This first model usually overestimates the final TC, behaving as an ideal upper limit of the property.
On the opposite, the series model, depicted on the left of in Figure 11 represents the lower limit in TC prediction. The series model, which formulation is reported in equation 22, is more accurate than the parallel model; however, the predicted values by the series model are often lower than the experimental ones.

$$K_c = \frac{1}{{K_f}^{-1}\phi_f + {K_p}^{-1}\phi_p} \qquad 22$$

Filling a polymer with metallic particles, typically results in enhancements in both thermal and electrical conductivity. Typical metals fillers particles includes: aluminum, silver, copper and nickel [15]. High filler loadings of metallic particles, however, makes the composite density to rise, thus reducing the applications where lightweight is desired [15]. Ceramic fillers allows improvements in polymer thermal

conductivity keeping an overall electrical insulation property. Among ceramic fillers, boron nitride (BN), silicon carbide (SiC), beryllium oxide (BeO) exhibited high thermal conductivity and electrical resistivity [15]. Carbon based fillers represent a promising family of fillers for polymers as they gather improved thermal and electrical conductivity, low density and mild processing [60]. The thermal conductivity of graphite can reach up to 400 W m^{-1} K^{-1} (Table 1), beside this, graphite can be dispersed uniformly in polymer matrix and exhibits even lubricant properties [61]. Some carbon fibers can reach a longitudinal thermal conductivity up to 2000 W m^{-1} K^{-1} but such fibers are characterized by high thermal anisotropy, which is reflects in composites. CNT (carbon nanotubes) and GRM, represent a modern challenging field in terms of thermal conductivity due to very high thermal conductivities of the fillers. In polymeric composite materials, to reach electrical conduction it is needed to reach a percolation network (Figure 12) which allows electrons to flow through it [15]. The minimum filler content, which allows electrical conduction, is defined as percolation threshold. In thermal transport, the beneficial properties from reaching a percolation network it is not sharply defined as in the electrical conduction case. This is due to the different carriers responsible for thermal transport, where phonons represents the major contributors compared to the electrons. Only few authors demonstrated the correlation of thermal conductivity and the reach of percolation [57]. Despite this premise, in 2015 Shtein and coworkers [62] found a bilinear trend in thermal conductivity for a threshold value and attribute it to the establishment of a percolation network. Nevertheless, high filler loadings promotes a diffuse filler-filler contact, which contributes preeminently to the thermal conductivity of the material [57] by reaching a good phonon coupling, thus, filler-filler thermal resistance limits thermal transport in composites materials.

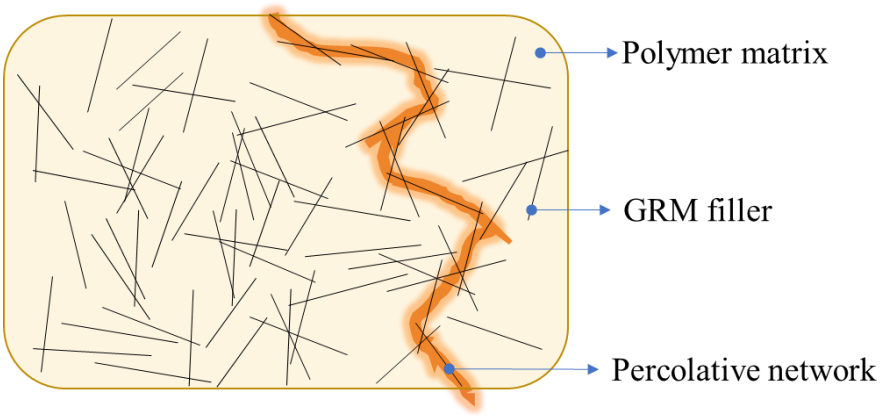

Figure 12. A schematic 2-Dimensional percolative network inside a polymer composite material.

The advantages in filler scale reduction from micro-scale to nano-scale were summarized by Kumar *et al.* [63]. As first, the adoption of nanofillers allows a reduction of the percolation threshold, measured from 0.1% to 2% of filler content in weight. This condition sums up a series of observations:

- the number of particles in composite is larger of about two orders of magnitude for nano-scale sized particles than micro-scale ones;
- the overall filler-polymer interface increases by a factor of 10 while reducing particle size, consequently, the importance of the interfacial resistance in composite conductivity rises;
- The thickness of the polymer among the particles in the nano-scale composites is reduced compared to micro-scale ones.

Zhi and coworkers [64], reported for a composite made of HDPE filled with 7% expanded of graphite the thermal conductivity. In that work, the nano-graphite more than doubled the thermal conductivity (1.59 W m^{-1} K^{-1}) when compared to micro-scale graphite at the same volume content. In 2015, in GnP-epoxy resin, thanks to an enhanced design of the interfaces, trough improvements of the wetting area, a 12.4 W m^{-1} K^{-1} thermal conductivity was reported experimentally [62].
As described in paragraph 1.1.3, the thermal properties of graphene were strongly correlated to its unique phonon transport modes. Indeed, graphene is recognized as an excellent candidate for the exploitation in thermally conductive materials. Nevertheless, thermal transport in nanocomposites is strongly limited by the low thermal boundary conductance between conductive particles in direct contact as well as between particles and the surrounding matrix [14, 57]. In 2018, to predict the thermal properties of graphene-polymer nanocomposites, Su and coworkers [57] developed a specific predictive model for graphene which clearly considers differently the thermal conductance between filler and matrix, and the thermal conductance in filler-filler contact. Despite this premise, the amount of parameters which knowledge is required to feed that model made it very complex to employ for a practical use.
The thermal conductance across different material has no univocal nomenclature, whereas the terms, interfacial thermal conductance (ITC) and thermal boundary conductance (TBC) are used for thermal conductance at any interface. From literature, it is common to use ITC between filler-matrix [65-68] but also for filler-filler interface [69, 70] and the term thermal boundary conductance (TBC) in filler-matrix [71, 72] but also filler-filler interfaces [73]. Moreover, the term contact conductance is used in unmodified filler-filler interface [15, 74] or a generic thermal conductance for various cases [75-78]. In this PhD work, with the only purpose to distinguish such different cases, the ITC acronym is used for filler-matrix case and TBC for the filler-filler case.

1.1.5. Functionalization of graphene

The covalent functionalization of pristine graphene with organic functional moieties has been developed for different purposes. The initial application of functionalized graphene was to solve dispersibility issues, due to the high hydrophobic behavior of pristine graphene. Nevertheless, new functionalities from graphene platelets can be obtained by the selection of proper moieties. This functionalization process allows the growth of selected molecules onto the graphene surface by chemical grafting. For

pristine graphene, the covalent grafting, by addition to sp^2 graphene atom bonds, can be achieved mainly by two routes: by free radicals addition or Dienophiles addition. Grafting molecules by free radicals addition was demonstrated by Tour through the employment of diazonium salt as precursor [79] and graphene nanoribbon obtained by unzipping nanotubes [80], obtaining pending nitro-phenyls groups on graphene surface, detected by X-ray photoelectron spectroscopy (XPS). Further, in 2009 Fang *et al.* [81] covalently grafted hydroxylated aryl moiety on graphene surface, acting as initiator in polymerization of polystyrene, allowing the growth of polymeric chains onto graphene platelets. The growth was determined from the increase of I_D/I_G ratio in Raman spectroscopy, where I_D and I_G are the peaks attributed to the sp^3 and sp^2 peaks, respectively at about 1350 and 1580 cm^{-1}. As alternative to free radicals, dienophiles addition to the c-c bond can occur, as reported by Georgakilas and coworkers [82], which grafted with dihydroxyl phenyl groups the graphene surface by the adoption of Azomethine ylide precursors. In this case, scanning probe techniques revealed an increase in graphene thickness, between 66 to 150 percent than literature values [83], indicating the presence of functional groups grafted onto the surface. By the choice of different precursors, several authors [84-87] introduced other species onto graphene by covalent grafting. A particular case is represented by Edge-grafting of carboxylic acid moiety (COOH) achieved by Salzmann and coworkers [88]. In this latter case, the edges of the graphene were decorated with carboxylic acid groups, which increased the dispersion properties in water and allowed the graphene to be further functionalized using carboxylate chemistry. Indeed, a higher reactivity of graphene edges has been reported [89], allowing in principle to preferentially locate chemical functionalization on the graphene edges, rather than on graphene surface. The improved chemical reactivity properties of this material made it ideally suitable to create junctions to the edges of the oxidized graphene. Similarly to graphene, also GRMs undergo covalent functionalization by chemical grafting. The larger availability of such materials than SLG quickly drove scientific interest on them. Compared to pristine graphene, GO and RGO can exploit the chemistry of epoxy, carboxyl and hydroxyl groups, granting more possibilities for the formation of derivatives trough covalent bonding onto the surface [90]. On the other hand, the thermal properties of such materials, which lattice is featured by a large number of defects, are poorer than SLG. The functionalization of GRM includes the addition of chromophores [91, 92] to implement the use in optoelectrocic devices, while a second opportunity comes from covalent linkage to polymers as polyethylene-glycol [93] in life sciences applications, polyallylamine cross-links for nanopapers production [94], are few examples.

Non-covalent interaction in graphene occurs onto the aromatic plane and strongly adsorbed molecules. The advantage of exploiting non-covalent functionalization is to add functionality without interfere with the lattice structure of graphene. The coupling with hydrogen-rich aliphatic molecules can be exploited and determines to a high polarizable interaction, which nature in terms of geometry of the interaction and binding energy it is strictly related to the electronegativity of each species [95]. A stronger interaction occurs trough aromatic-aromatic coupling onto graphene surface quantified in about 1 Kcal $Kmol^{-1}$ in 50% offset parallel-stacked

conformation [96]. Such interaction, responsible for the stacking of the layers in graphite, is an appealing synthetic method to attach functional groups. The term π-π interaction is commonly used as synonym to indicate the aromatic-aromatic coupling, despite the attribution of such force to the sp^2 π orbitals in carbon is not exhaustive [96]. Several authors investigated the nature of such interaction [96-98], which was determined by the electronic nature of the molecules by cumulative energy contribution: van der Waals, electrostatic, electron availability and electron polarization, finding that every coupled system balances the sum of the contributions differently.

Recently, the phonon transport in molecular junctions made of aromatic stacked systems was investigated by Li and coworkers [99], adopting DFT and non-equilibrium Green's functions. Figure 13 b, c, d reports the molecular junctions made of stacked aromatic rings molecules analyzed from Li and coworkers. For the sake of comparison, a covalent molecular junction (a in Figure 13) was used as example. The phonon transmission was calculated in the range between 0 and 50 THz and for aromatic stacked molecules only few vibrational modes were found at low frequencies (up to 5 THz), while the covalent bonded molecule exhibited several ranges up to 50 THz. The phononic thermal conductance reflected the transmission results, finding values one order of magnitude lower compared to the covalent junction. Overall, a complete attenuation was found in phonon transmission adopting non-bonded aromatic stacking junctions, with a residual contribution from vibrational modes in z direction.

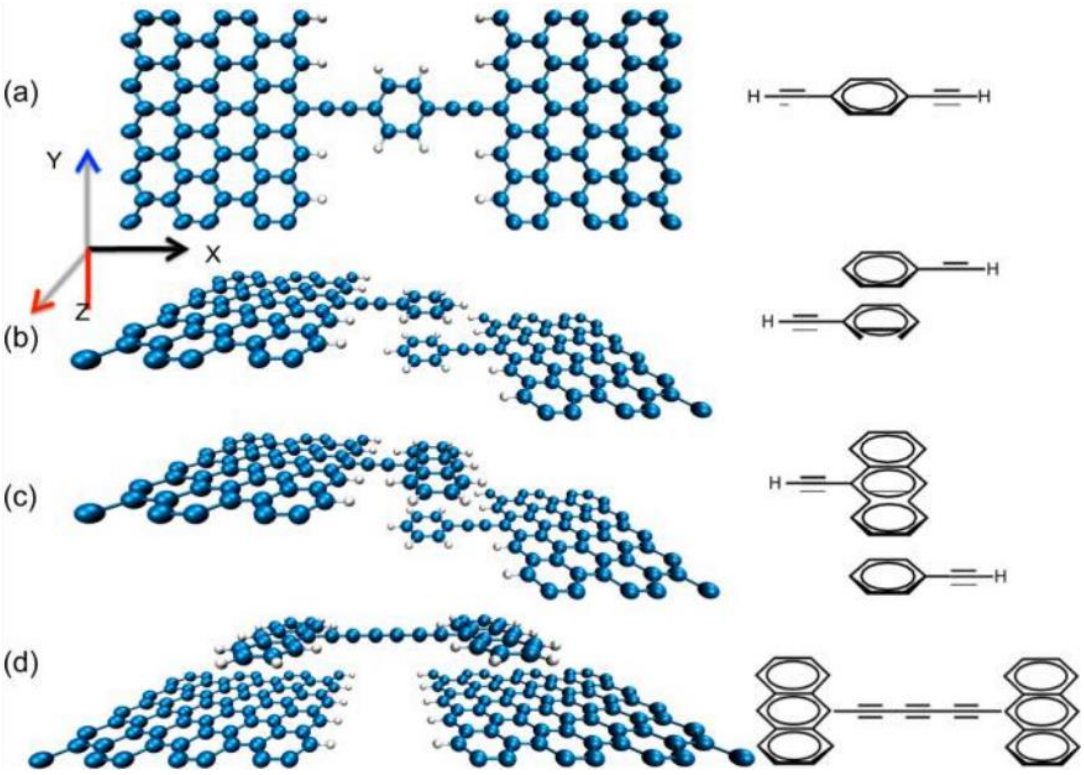

Figure 13. Molecular junctions for thermal transport (a) the covalent junction taken as example, (b) two overlapped aromatic rings bound by carbon atoms (c) stacked benzene and anthracene moieties (d) a suspended structure made of two anthracenes

bonded by a carbon filament. Reprinted with permission from [99] . Copyright (2017) American Chemical Society.

The work from Li and coworkers demonstrated how unbound molecular junction are poorly suitable for thermal transport across interfaces due to phonon suppression. This finding is important both in filler-matrix and in filler-filler interface design, to drive efforts in more efficient thermal interfaces, as covalent ones.

1.1.6. Particle-matrix interfacial resistance

Inside a composite material and even more in nanocomposites, contact surfaces between matrix and filler generates the largest amount of interfaces, thus most of the literature is focused on such interfaces. Both experimentally and computational studies were conducted to improve the thermal properties of nanocomposite materials. However, on the atomistic scale only computational tools provides the capability of fine-tuning of the nanostructures.

To calculate the thermal conductance of an interface at atomistic scale, few computational techniques are suitable. Non-Equilibrium Molecular Dynamics (NEMD) and Reverse NEMD (RNEMD) [100] represents the well-established techniques, while the equilibrium method is usually not suitable to deal with interfaces and quantum coupled methods are currently too heavy to compute. Recently, for a perfect super-lattice made of Si-Ge, an equilibrium method [101] was find in agreement with other experimental and computational studies for the overall conductivity, however no further application of this technique in composite materials followed.

In the literature, several layouts were designed with the aim of building representative scenario for graphene and GRM polymer interface. In 2011, Hu and coworkers [102] developed three different layouts for the same graphene and phenolic resin matrix. In these models, the graphene flakes were placed perpendicularly to the heat flux and the thermal reservoir regions were set in various positions along the sample either in graphene or in polymer, as depicted in Figure 14.

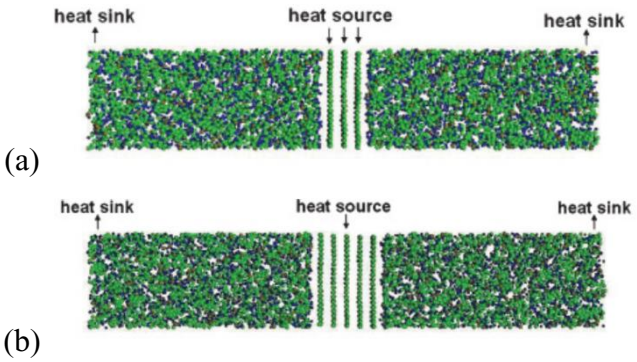

(a)

(b)

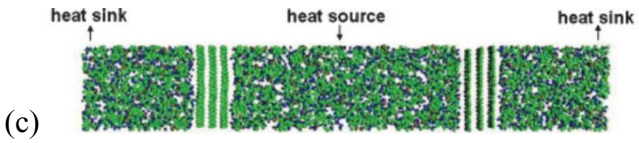

(c)

Figure 14. Model structures with (a) three and (b) six graphene flakes, in this case polymer ends acts as heat sinks and graphene flakes acting as heat source, only the central one in (b). (c) Heat sink and source in phenolic resin. Reprinted figures with permission from [102] Copyright (2011) by the American Physical Society.

One of the purposes was to compare NEMD method with temperature relaxation technique in composites. The authors concluded that non-equilibrium method was the more realistic approach for direct calculation of ITC due to the better phonon distribution compared to thermal equilibrium method. The same research group also investigated the contribution of the graphene flakes orientation [103] by comparison of the above cited perpendicular heat flow models with a series of models in which the heat flux is generated longitudinally to the flakes (Figure 15). In this latter case, up to five layers of graphene were employed. The author evidenced the detrimental effect of boundary resistance in composites, suggesting longer aspect ratio fillers adoption to overcome this issue. Overall, in these works the ITC varied from 10 to 30 MW $m^{-2} K^{-1}$.

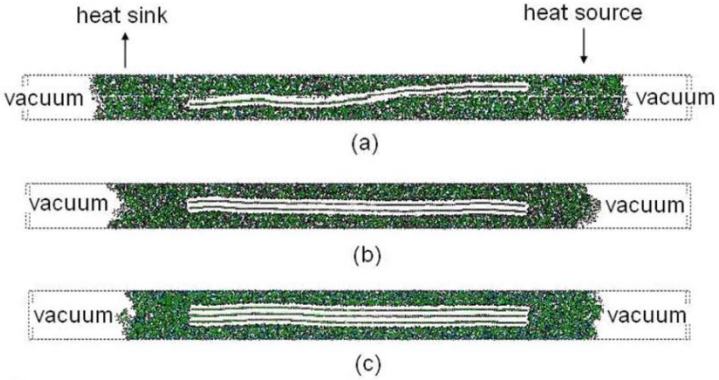

Figure 15. Phenolic resin matrix with (a) 1-layer-graphene, (b) 2-layer-graphene and (c) 3-layer-graphene in NEMD simulation, Reproduced with permission from: J. Appl. Phys. 110, 033517 (2011) Copyright 2011, American Chemical Society.

It is not surprising that many efforts have been spent in study and improvements of the ITC between graphene and polymer by chemical functionalization [15, 21, 67, 68]. Wang and coworkers [68] calculated an improvement in the thermal transport in polyethylene and SLG composite by covalent functionalization of graphene with long alkyl chains. The model setup was transversal to the heat flux and thermostats were located similarly to the layout made by Hu *et al.* [102], reported in Figure 14c, with both reservoirs placed in polymer center and ends. In this case, however, SLG was adopted and a series of alkyl chains were covalently bounded onto graphene surface, as reported in Figure 16.

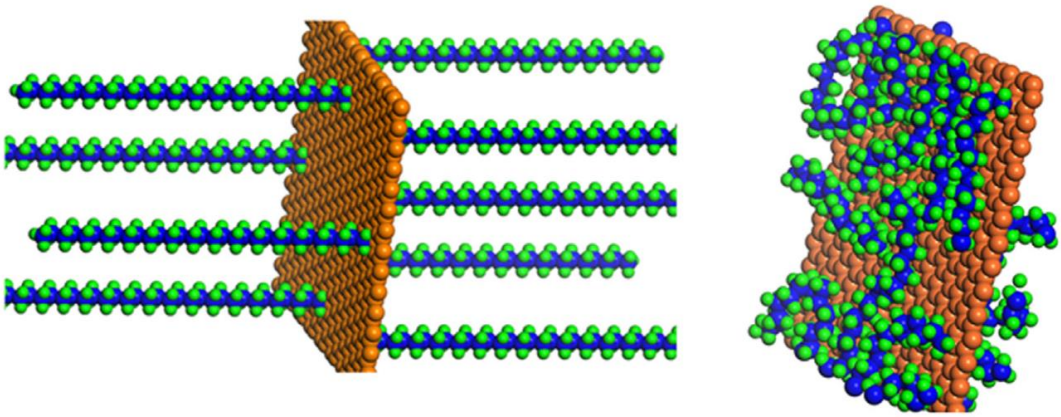

Figure 16. Graphene platelet covalently grafted by alkyl chain onto the surface, in “aligned” (left) and “relaxed” (right) morphology. Copyright © 2012 Carbon, Elsevier. Reproduced with permission from [68].

In that work, the amount of grafted chains, the length of such chains and the initial morphology were tuned, finding that the higher amount of chains, longer linkers and aligned morphology increases ITC from 56 to about 140 MW m^{-2} K^{-1}. This enhancement in ITC was explained by a shift in VDOS from high to medium frequency, where VDOS transmission between matrix and filler mainly occurs. The same NEMD layout was chosen by Wang and coworkers [104], who simulated a series of small moieties covalently bound as functional groups onto graphene surface. Such species were reported in Figure 17.

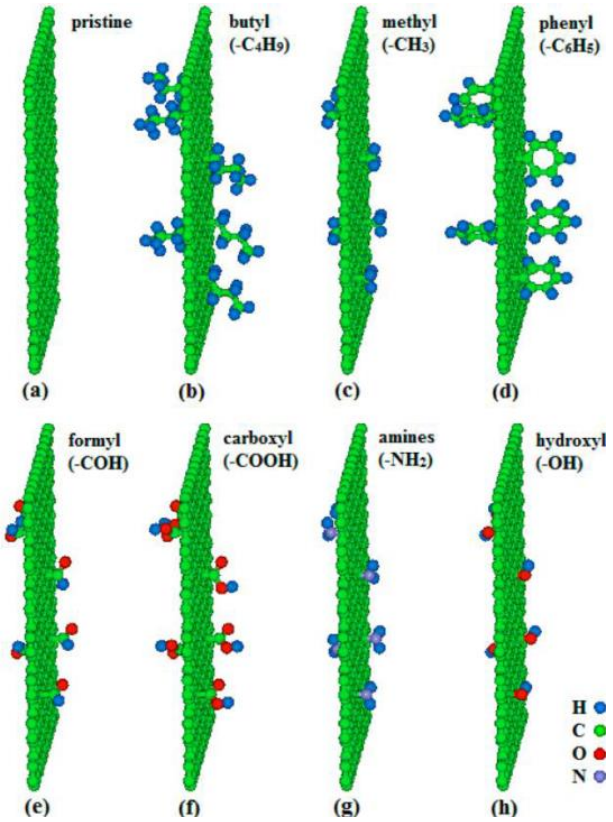

Figure 17. Pristine graphene (a) and functionalized graphene with various chemical moieties: (b) butyl, (c) methyl, (d) phenyl, (e) formyl, (f) carboxyl, (g) amines, and (h) hydroxyl. Reprinted with permission from [104]. Copyright (2015) American Chemical Society.

Among these moieties, butyl covalently functionalized graphene found to provide the best match in VDOS spectra with the paraffin polymer matrix, resulting in a remarkable ITC increase. In that study, the authors kept the coverage of functionalized moieties fixed at 5.36% of the graphene surface and obtained an increase of ITC up to about 57%. In 2016, Shen and coworkers [65] investigated the thermal transport at the nanoscale of an interface made of functionalized graphene and epoxy resin. The model is reported in Figure 18 and it is made by a functionalized graphene sheet between two thick layers of epoxy resin. In this work, four moieties were compared as functionalization for graphene: Hydroxyl group (b in Figure 18), fluorine (c in Figure 18), amine (d in Figure 18) and thriethylenetetramine (e in Figure 18). In this work, by thermal equilibration method, the interfacial thermal conductance between pristine graphene and epoxy resin was calculated of about 22 MW m^{-2} K^{-1}. Moreover, the role of the graphene surrounding matrix was highlighted because it halved the thermal conductivity from freestanding to embedded configuration in pristine graphene (about 1200 W m^{-1} K^{-1}), due to phonon energy damp by the matrix. The authors also introduced the critical size concept, corresponding to the maximum size of a functionalized flake where thermal conductance is improved compared to pristine graphene, until the number of defects in graphene lattice become a limiting factor in thermal transport. Overall, the covalent functionalization allowed an enhancement of ITC by one order of

magnitude with a peak of about 380 MW m^{-2} K^{-1} for the longest functionalized molecule, attributed to a deeper penetration of the phases.

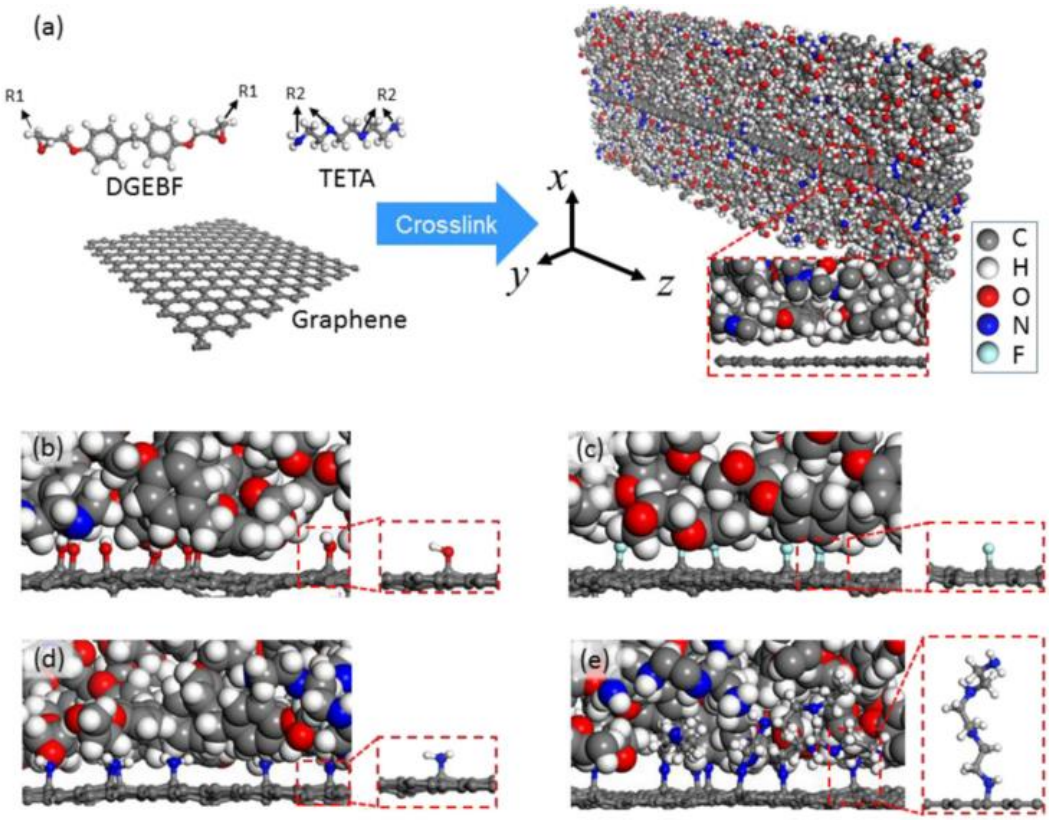

Figure 18. (a) Schematic representation of the graphene/epoxy resin model with hypothetical precursor. Functionalization with: (b) Hydroxyl group, (c) fluorine, (d) amine, and (e) thriethylenetetramine. Copyright © 2016 Carbon, Elsevier. Reproduced with permission from [65].

Gao and Müller-Plathe [67] employed Reverse Non-Equilibrium MD (RNEMD) approach to investigate thermal transport across functionalized graphene with bonded fragments of Polyamide 6,6 (PA66) in PA66 matrix. The ITC was evaluated as a function of grafting density and molecule length effect, finding an optimum density value and observing higher thermal conductance for longer penetrating molecules, as previously observed by other authors. Sun and coworkers [69] adopted alkyl chains in form of self-assembled monolayers (SAM) to improve phonon matching across gold and polyethylene interface. In this work, the role of wettability and chain length was pointed out and analyzed both experimentally and via MD simulations. MD simulations were carried out with via NEMD approach and highlighted an improvement in ITC for shorter SAM (with C2 and C6 backbones) and slightly lower improvement for longer ones (C12 and C16 backbones). Nevertheless, the authors demonstrated that the alkyl interlayer seven folded the ITC of the bare gold-polyethylene hard-soft interface. Luo and Lloyd [105] also investigated thermal transport in graphene and Paraffin wax by NEMD. The authors adopted various layouts to investigate thermal conductivity in VdW driven systems with graphene and paraffin wax, similar to the examples reported in Figure 14a and

Figure 15a, finding low thermal conductance values due to the poor strength of the VdW interaction at the interface. Despite this finding, the authors developed the model reported in Figure 19, where MLG edges creates the interface with polymer. The model depicted in Figure 19a, reported a thermal conductance of about 36 MW m^{-2} K^{-1}, a value close to the results of similar VdW driven configurations. However, simulating a high temperature thermal treatment, the reactive forcefield in use (AIREBO), allowed the creation of covalent bonds between MLG edges and paraffin wax (b in Figure 19). Such stronger interaction, by enhancing phonon transmission, determined a thermal conductance of about 536 MW m^{-2} K^{-1}, confirming the importance of strong bonds in thermal transport, even if from a chemical point of view it is not yet achieved experimentally.

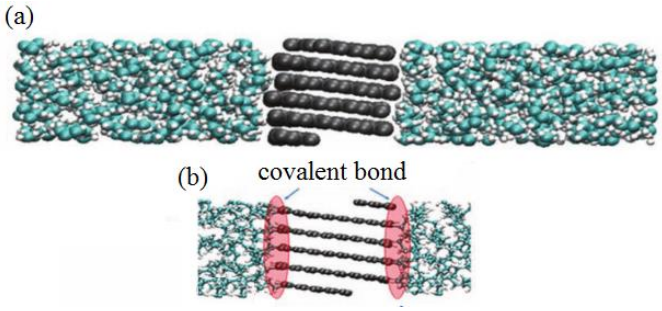

Figure 19. Simulation system setup of a MLG-polymer junction (a) unbound interfaces and (b) covalently bonded. From [105]. Copyright © 2012 by John Wiley Sons, Inc. Reprinted by permission of John Wiley & Sons, Inc.

1.1.7. Particle-particle contact resistance

Improving the thermal conductance between particle and matrix is not the only route to increase thermal transport in composites. This assumption is particularly true when dealing with materials at the nanoscale. In nanoscale fillers, the limited thickness allows very high form factors, thus the same filler loading generates a more efficient thermally conductive percolating network than at the micro-scale counterpart, as described in paragraph 1.1.4.

Inside a composite material, when the polymer wets completely the filler, the thermal conductivity between filler particles is limited by the coupled boundary resistance between polymer and filler and even by the poor thermal conductivity of the polymer. Thus, the design of high thermally conductive composites exploited the idea of reducing the polymer-filler interfaces, by creating percolative or three-dimensional networks, which exploits the contact between particles. Li and coworkers [106] reported that three dimensional structures are about five times more efficient in heat transfer than segregated structures typical of traditional blend composites. Despite this condition, between the flakes of materials used as thermally conductive fillers, the thermal resistance at the interfaces still limits heat transfer among particles thus limiting heat transport.

Macroscopically, the thermal resistance can be reduced by strengthening mechanical coupling. At the nano-scale, the experimental application of an external load is a challenging issue. By MD simulations, such investigation can be finely performed as was done in 2016 by Chen and coworkers [107]. In that work, the authors simulated the use of external force applied to a couple of perpendicular nanotubes and calculated the TBC across the interface by NEMD layout, as reported by Figure 20.

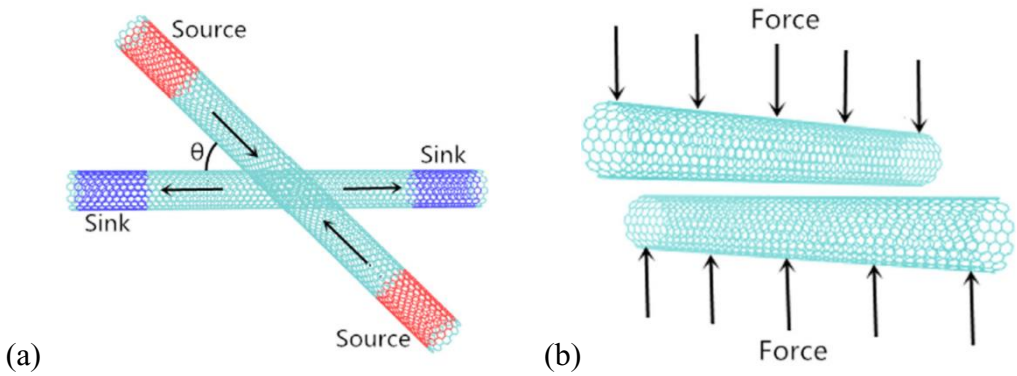

Figure 20. (a) Model topology of two stacked CNT with different contact angle θ where red and blue regions highlights hot and cold thermal reservoirs, respectively. (b) Scheme of the application of the external force, exerted in the normal direction, indicated by the arrows, Reprinted from [107], Copyright (2016), with permission from Elsevier.

The TBC in such system is driven by VdW interactions, as seen in several cases for the above-cited filler-matrix interface. The magnitude of the TBC was found proportional to the contact area and was calculated of about 28 pW K^{-1} without the application of external force. By tuning the external force, the TBC was found almost proportional to the force in the range -4 to 10 nN with a peak value of about 94 pW K^{-1} for the maximum applied load. The authors, also investigated also the use of molecular linkers, simulating a covalent functionalization of both nanotubes for θ=0 (a in Figure 20) with short methylene moieties. The TBC in this latter case revealed a proportionality with the density of linkers up to an optimum value, above which the TBC decreased. Such trend was attributed to the irregular structure of the functionalized CNT compared to the pristine one, which affected the thermal transport inside the CNT. Nevertheless, by covalent functionalization, the calculated thermal conductance in such system was about 4900 pW K^{-1}, approx. 50 times more effective than the application of the maximum external force. Such result confirmed that covalent functionalization is the theoretically optimal route to improve TBC across carbon-based materials acting as fillers in nanocomposites.

In 2014, Liu and coworkers [75] adopted a NEMD layout, to investigate the use of covalent linkers between graphene platelets. Such graphene platelets were partially overlapped and bonded by a variable number of ethylene cross-linkers, as depicted in Figure 21.

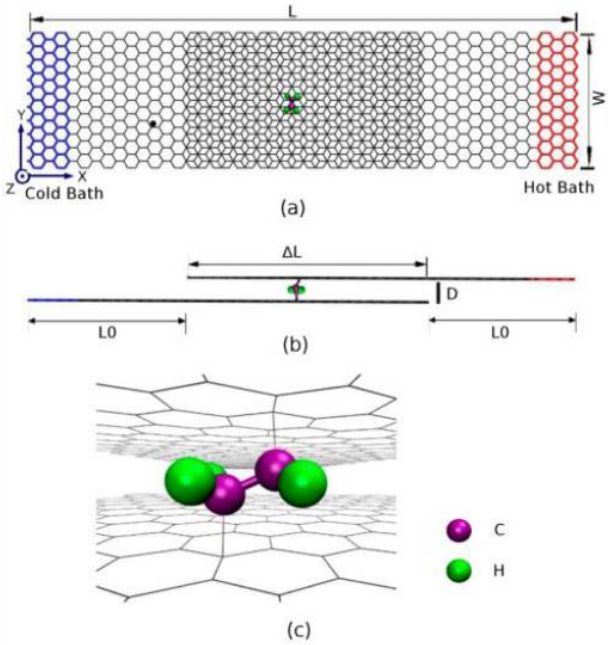

Figure 21. (a) Model layout of overlapped graphene with surface functionalized cross-linkers in classical NEMD layout. (b) Side view of the model. (c) Detail of the alkyl cross-linker. Reprinted with permission from [75]. Copyright (2014) American Chemical Society.

.

In that work, TBC and thermal jump across the junction were related to the position and amount of linkers used in the simulations. This oversimplified approach, from the chemical point of view, allowed to understand the role of chemical functionalization in heat transfer between graphene structures. An inversely proportional relation was found between the thermal jump and the number of cross-linkers. Moreover, the TBC was found proportional to the number of bounded cross-linkers independently from their spatial position finding a single linker thermal conductance of about 250 pW K^{-1}. The vibrational density of states was calculated both for the platelets and for the cross-linkers up to about 60 THz, following the classical acoustic mismatch model: a major contribution was found below in the low range frequencies (below 15 THz),. Such vibrational modes were attributed to the out of plane vibrational modes.

The experimental exploitation of covalent molecular junction was reported recently by Han *et al.* [78]. In that pioneering paper, three different organic amino-silane were employed to functionalize the interface between graphene platelets and a silica substrate. Such system adopted a heat-spreader-like layout where the silica substrate was warmed up and the free surface temperature, where graphene lays, was collected and analyzed. The temperatures were found up to about 40 K lower than the pristine interface by setting the same heat flux and the authors determined an overall 57% of heat spreading performance enhancement. Moreover, *ab initio* calculations combined with Green's functions were employed to calculate the single molecule thermal conductance, finding values between 1 and 2.7 pW K^{-1} at 300 K for the three species.

The thermal transport along molecular chains was experimentally quantified by Meier an coworkers [77] on self-assembled monolayers (SAM) made of alkane thiols lengths supported on gold substrate, as reported in Figure 22. The investigation was carried out with specifically designed scanning thermal microscope featured by a heated tip as probing tool. The authors focused the research on alkane thiols with carbon backbones varying from two to 18 finding out thermal conductances from 30 to 10 pW K^{-1} with higher values in shorter chains and an overall decaying trend of conductance versus chain length.

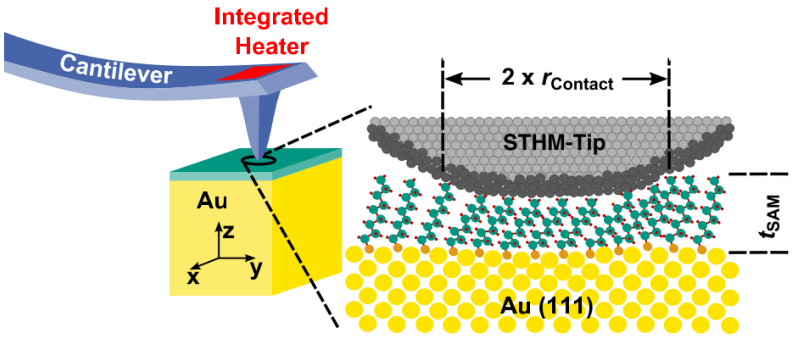

Figure 22. Experimental measurement of molecular thermal conductance by scanning probe technique, Reprinted figure with permission from [77]. Copyright (2014) by the American Physical Society.

Ab-initio quantum methods are preferred when quantum effects, which reasonably occurs approaching atom-sized devices. In 2007, Zhang [108] and coworkers introduced non-equilibrium Green's function (NEGF) as investigation method to calculate thermal transport properties, such as thermal conductance, in atomic size contact-device-contact setup. Two years later, Hopkins and coworkers [109] did a comparison between NEGF and the traditional acoustic mismatch model (AMM) of classical mechanics. In this latter work, the author analyzed the local density of states and transmission as a function of phonon angular frequency, finding a coincident behavior of AMM and NEGF for homogenous junctions and some discrepancies when heterogeneous atoms constitutes the molecular chains, finding that AMM underestimated the thermal conductance. Such discrepancies were attributed to the rough approximation of AMM which neglects the phonon wave behavior [109].

The dependence of the thermal conductance as a function of molecular length was studied theoretically, by Klöckner and coworkers [110] through a combination of NEGF and DFT methods. The authors simulated an even number of methylene and fluoroethylene substituted monomers ranging from 2 to 30 covalently bonded to a gold nanocrystal, as depicted in Figure 23. Moreover, the role of bonding elements of sulfur and nitrogen (ammonia) were compared. The obtained thermal conductances values were found in the range 15-45 pW K^{-1}, closer to the experimental work than other computational ones. The reported thermal conductance values followed different trends. For short molecules (up to 10 segments) both increase and decrease as function of chain length were found for different chemical

species, while for longer chains, different plateaus and decays were found. Overall, the authors ascribed ballistic regime of phonons as responsible for the thermal plateauing. Moreover, the ammonia moiety as anchoring species demonstrated a detrimental effect in thermal transport, particularly when coupled with fluoroethylene (depicted on the left in Figure 23). Such observations were confirmed in the calculated phonon transmission plots, where several modes were not allowed.

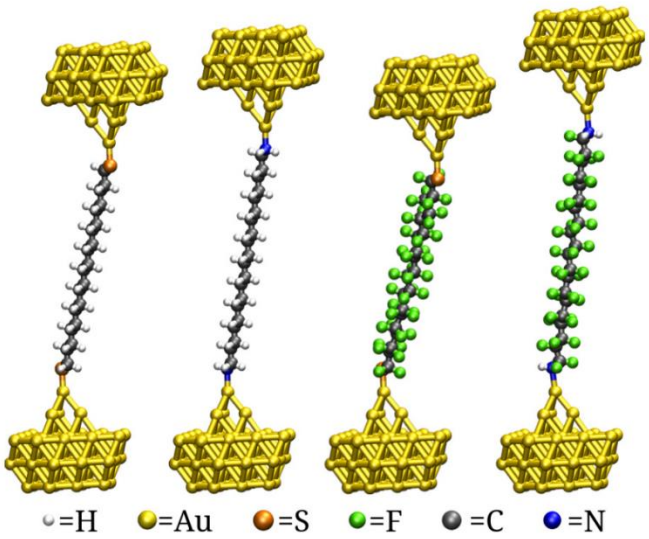

Figure 23. Examples of methylene and fluoroethylene molecular junctions covalently bonded to gold nanocrystals. Different anchoring groups were investigated. Reprinted figure with permission from [110]. Copyright (2016) by the American Physical Society.

By first-principles DFT calculations, Li *et al.* [111] investigated the thermal conductance of a single molecular junction as a function of the mechanical conformation. The model was composed by a couple of small thermal reservoirs, made of about 40 carbon atoms in graphene-like configuration with a covalently bonded alkyl chain with C11 backbone. The thermal conductance was calculated as a function of the molecule stretching in three different chain conformations (extended and with two levels of compression) as reported in Figure 24. The results highlighted that an extended junction almost doubles the thermal conductance compared to the compressed form. For the sake of comparison, at 300K the molecular conductance was reported of about 170 pW K^{-1} in stretched conformation and about from 70 to 75 pW K^{-1} for the compressed counterparts.

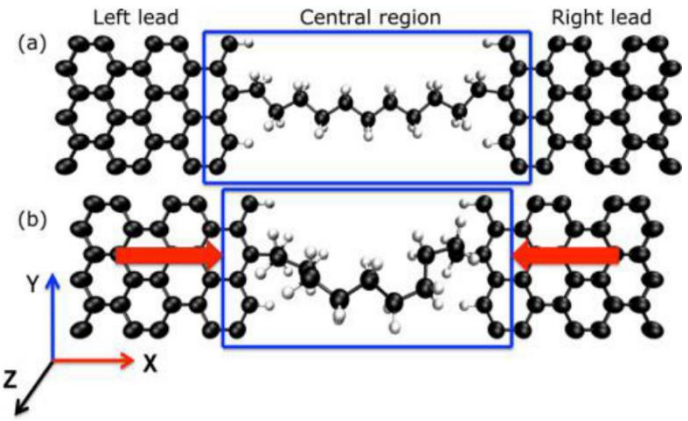

Figure 24. Molecular junction in (a) extended and (b) compressed configuration. Reprinted with permission from [111]. Copyright (2015) American Chemical Society.

A possible approach to decrease the contact resistance is by the use of molecular junctions [69] between contacting nanoparticles, to enhance the stiffness of the contact and increase the acoustic match [112], determining benefits in phonon transfer. However, controlled chemical functionalization of graphene is still challenging and presents drawbacks, as covalent bonding on graphene induces rehybridization [90], acting as lattice defects [113] and alters the in-plane phonon modes [42], affecting thermal properties of graphene [50, 114]. On the other hand, non-covalent functionalization is also possible, but the weaker secondary interactions [99, 105] are expected to deliver rather limited reductions in contact resistance.

1.2. Fundamentals of classical Molecular Dynamics for heat transfer

Classical Molecular Dynamics represents the state of the art of the deterministic theory, which featured physics up to the XX century, when quantum physics theories started being demonstrated. MD constitutes an important milestone in statistical mechanics theories which evolutions constitutes a fundamental branch of modern physics. The basic idea in Molecular Dynamics is to determine the continuous evolution of an atomistic system, by knowing atoms positions, interacting forces and velocities through the time integration of the equation of motion for a certain time.

While the motion of the atoms is determined via Newtonian dynamics, the interacting forces among atoms are calculated by the application of interatomic potentials, as set of equations and fitting data. The equation 23 describes the force $\vec{F_i}$ applied to the i^{th} atom, where r_{ij} is the interatomic distance between the atoms i and j, U is a simple pairwise potential. Further details about interatomic potentials are discussed in paragraph 1.3.

$$\vec{F_i} = \sum_{j>i} \nabla_{ri} U(r_{ij}) \qquad 23$$

The simulation takes place inside a virtual finite volume, named simulation domain or simulation box (from the shape of the simplest cubic volume). Inside the simulation domain, the positions of the atoms are initially defined by the user. For crystals, the simplest method is to define atomistic positions and lattice constraints at the same time. On the other hand, more complex system such as proteins or polymers requires a custom space arrangement. In this latter case, the atomistic coordinates may be imposed by script coding, spreadsheets, or through chemical design software. It is uncommon to start a MD simulation at absolute zero temperature (0 K), because at such temperatures, the quantum effect of sub-atomic particles is predominant. Usually, the potential parameters neglects quantum effect and this may determine a strong unphysical behavior. To overcome the 0 K velocity issue, the standard approach is to operate at higher temperatures and to assign from a pseudorandom algorithm the velocities to the atoms to reproduce a Maxwell-Boltzmann distribution as described in equation 24.

$$f_v(v_x, v_y, v_z) = \left(\frac{m}{2\pi k_b T}\right)^{\frac{3}{2}} e^{\left[-\frac{m\left({v_x}^2+{v_y}^2+{v_z}^2\right)}{2k_b T}\right]} \qquad 24$$

Where f_v is the Maxwell-Boltzmann probability function for velocities in three dimensions; v_x, v_y, v_z are the atom velocity component in *x*, *y*, and *z* coordinates; *m* is the atom mass; k_b is the Boltzmann constant and T the absolute temperature. Once each of the *N* atoms has been defined in terms of initial position, velocity and applied force, a *3N* set of differential equations continuously updates position, velocities and thus force among them through numerical integration. The most popular integration method to compute the equation of motion in MD is the velocity version of the Verlet algorithm [115, 116]. In this algorithm form[4], the positions ($\vec{r_i}$) and velocities ($\vec{v_i}$) are updated at the same *timestep* or time increment (dt) to allow the maximum energy conservation. Equation 25 represents the form to calculate position in velocity Verlet formulation for the i^{th} atom, here m_i is the mass of the i^{th} atom. Equation 26 is used to calculate velocity at midstep where forces are computed at the time *t+dt* and Equation 27 contains the form to compute the velocity of the same atom, when kinetic energy at time *t+dt* is available.

$$\vec{r_i}(t+dt) = \vec{r_i}(t) + \vec{v_i}(t)dt + \frac{dt^2}{2}\frac{\vec{F_i}(t)}{m_i} \qquad 25$$

$$\vec{v_i}\left(t+\frac{dt}{2}\right) = \vec{v}_i(t) + \frac{dt}{2}\frac{\vec{F_i}(t)}{m_i} \qquad 26$$

$$\vec{v_i}(t+dt) = \vec{v_i}\left(t+\frac{dt}{2}\right) + \frac{dt}{2}\frac{\vec{F_i}(t)}{m_i} \qquad 27$$

At the end of the simulation time, all the states of the dynamic system are determined. Now, the property subject of investigation (for example temperature, thermal

conductivity, adsorption energy or others) is evaluated through simulation convergence or time averaging of the property over the states, depending from the nature of the investigation.

Nowadays, High Performance Computing (HPC) allows to calculate nanoseconds of models made of few million atoms. Even if this number may appear to be very large, and from a computational side it actually is, on the chemical side it constitutes only a small fraction of a mole. This limitation in a three-dimensional system brings to a larger surface-over-bulk atoms ratio than in macroscopic world. This limitation complicates the study of bulk internal properties of the matter. Thus, Periodic Boundary Conditions (PBC) have been developed and applied to overcome artefacts from the presence of surface atoms.

1.2.1. Periodic Boundary Conditions

The virtual space where the dynamics takes place is a three-dimensional finite size cube along the x, y and z Cartesian coordinates called simulation domain or simulation box. The borders of the simulation box actually represents an interface between the matter and the empty space. In this classical design, the atoms, which are allowed to move freely inside the box, can easy get lost by crossing the domain borders as results of the interaction with the empty space.

Periodic Boundary Conditions (PBC) represents a method to remove the interface effect on the border of our system. Figure 25 depicts a hypothetical simulation box (in yellow) surrounded by identical replicas of it (in grey shade) along x and y Cartesian coordinates. When PBC are set, atoms and forces feels virtually no borders over the domain, meaning that an atom that crosses the border from a coordinate will appear on the opposite side of the domain without losing information about mass, charge and velocity. As well, the interatomic forces can cross the domain, feeling a virtual continuum condition. If PBC not correctly managed, unphysical results are generated, as the classical example of an atom that interacts with its own replica. The golden rule to avoid such self-interaction is by choosing simulation box size large enough to accommodate all the atoms and more than double the maximum cut-off distance. The cut-off distance is the threshold radius above which the interaction does not takes place and it is set arbitrary zero; in a three-dimensional system, it can be represented by a defined sphere surrounding every atom. The cut-off concept is an approximation developed to avoid to compute a large amount of infinitesimal forces, which scales with volume, bringing to the excess of computing demand. The application of cut-off concept is mostly related to the non-bonded interaction, but it is also used in internal potential formulation, as described in the following chapters.

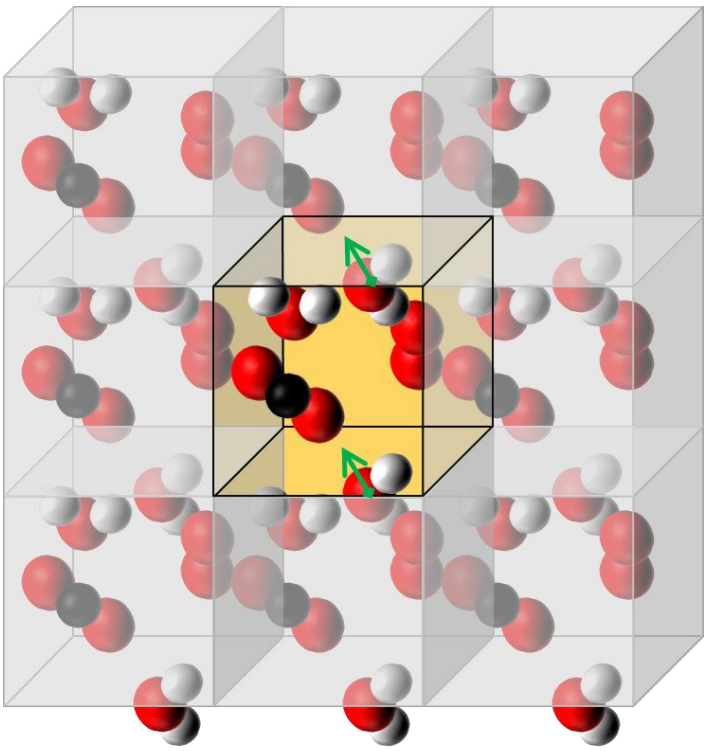

Figure 25. A representation of PBC: the simulation box (highlighted in yellow) among its replicas. A green arrow points out the motion mechanism of an escaping molecule out of the top of the domain readmitted from the bottom of it.

1.2.2. Statistical ensembles

A statistical ensemble is a cumulative set of representative microstates of a given system. Within this brief definition, the microcanonical ensemble is the native form of statistical ensemble that can be represented in classical MD simulations. This case is also referred as NVE and it represents an ideal isolated system with a fixed volume where no energy and matter is transferred. It is described as a statistical ensemble where the number of the atoms (N), the volume of the simulation box (V) and the Energy of the system (E) of the system are fixed.

Several statistical ensembles can be represented in MD simulations through the application of thermostats and barostats. The canonical ensemble, describes a closed system that reached the thermal equilibrium with large heat bath or thermostat. The canonical ensemble is also referred as constant NVT, because the number of particles / atoms (N), the volume of the simulation box (V) and the Temperature (T) of the system are constant. In classical MD, to keep the temperature of the simulation box constant, however, instead of allowing energy exchange at the simulation box surfaces as could happen inside an actual vessel, the surface effect is avoided by introducing a homogeneous energy exchange inside the simulation box. This condition is generated by superimposing of weighted microcanonical ensembles during numerical integration of position and velocities. The same methodology applies to isothermal-isobaric ensemble (NPT) where the number of the atoms (N), the pressure of the simulation box (P) and the Temperature (T) of the system are kept

constant. In NPT ensemble, the atomic coordinates are homogeneously scaled to simulate an external pressure applied to the simulation box and the temperature is fixed as discussed in NVT examples. The isenthalpic-isobaric ensemble (NPH) is another statistical examples can be simulated in MD, where the enthalpy H is a conserved quantity as well pressure P and the number of atoms N while the volume of the domain scales as variable. This latter case is not directly relevant to this PhD work and further description is not included here.

1.2.3. Thermostats and barostats

In Classical MD, the application of the canonical ensemble or isothermal-isobaric ensemble to a system is done through specific algorithms called thermostats and barostats. Historically, several thermostats and barostats were developed to fulfil the NVT and NPT purposes. One of the most employed in materials simulation is the Nosé-Hoover thermostat and barostat [117, 118], because it limits the temperature and pressure fluctuations during the whole application. Thermostats and barostats formulation is built-in inside the integration algorithm (see paragraph 1.2) because both affects the dynamic at every integration step. The Nosé-Hoover dynamics applied to Velocity Verlet algorithm is expressed in equations 28, 29 and 30, where the concept of friction coefficient of the bath $\gamma(t)$ is introduced. Equation 31 and 32 reports the friction coefficient differential formulation, capital letter *T* is the target bath temperature, *Q* is a parameter that behave as the inertia associated to the motion and k_b, the Boltzmann constant. Here, when the kinetic term $m_i v_i^2(t)$ is greater than the Boltzmann factor gk_bT, the friction coefficient $\gamma(t)$ is positive, and then decreases the atom velocity until the target temperature is reached. At the opposite, a negative value of the friction coefficient $\gamma(t)$ will increase the atom motion, determining a rise in temperature up to the target temperature *T* is fetched.

$$\vec{r_i}(t+dt) = \vec{r_i}(t) + \vec{v_i}(t)dt + \frac{dt^2}{2}\left[\frac{\vec{F_i}(t)}{m_i} - \gamma(t)\vec{v_i}(t)\right] \qquad 28$$

$$\vec{v_i}\left(t+\frac{dt}{2}\right) = \vec{v}_i(t) + \frac{dt}{2}\left[\frac{\vec{F_i}(t)}{m_i} - \gamma(t)\vec{v_i}(t)\right] \qquad 29$$

$$\vec{v_i}(t+dt) = \frac{2}{2+\ \gamma(t+dt)dt}\left[\vec{v_i}\left(t+\frac{dt}{2}\right) + \frac{\vec{F_i}(t+dt)}{2m_i}dt\right] \qquad 30$$

$$\gamma\left(t+\frac{dt}{2}\right) = \gamma(t) + \frac{dt}{2Q}\left[\sum_i^n m_i v_i^2(t) - gk_bT\right] \qquad 31$$

$$\gamma(t+dt) = \gamma\left(t+\frac{dt}{2}\right) + \frac{dt}{2Q}\left[\sum_i^n m_i v_i^2\left(t+\frac{dt}{2}\right) - gk_bT\right] \qquad 32$$

The parameter Q expression is reported in Equation 33, where τ is the relaxation time of the bath. It controls how fast the temperature fluctuation attenuates, in MD simulations corresponds to the dumping parameter.

$$Q = 3(N-1)k_b T\tau^2 \qquad 33$$

1.2.4. Simulation setup: EMD, NEMD and beyond

Molecular Dynamics a technique that in principle can be used to simulate several chemical systems, from crystals to condensed matter such as polymer, gases and liquids and in principle every chemical system at the nanoscale. Nevertheless, MD applications originates to simulate proteins and biological systems, thus we can call Molecular Dynamics a multi-purpose technique, where, basing on the needs, the scientific community pushed the improvements and the application for each field. The development of specialized force fields is a typical example.

In heat transfer modelling three different techniques coexists, the Equilibrium Molecular Dynamics (EMD), the non-equilibrium Molecular Dynamics (NEMD) [119]and a novel method, the approach to equilibrium Molecular Dynamics (AEMD).

In **EMD**, the thermal transport is evaluated through the application of the Kubo's fluctuation-dissipation theorem [120], combined to Green's Functions. This powerful combination, usually referred as Green-Kubo, represents a popular method to evaluate the thermal conductivity of solid matter via MD simulations.

Within the Kubo's fluctuation-dissipation theorem, the transport coefficient η in steady state response regime after a perturbation is reported in (34).

$$\eta \sim \lim_{t\to\infty} \int_0^t \langle \xi(t')\xi(0)\rangle \, dt' \qquad 34$$

Where ξ represents a physical quantity, $\langle\ \rangle$ indicates the average over the statistical ensemble. If the perturbation is a thermal gradient, we can employ it within the SMA solution for BTE and thus obtain the Green-Kubo thermal conductivity (35)

$$k_{GKx} = \frac{1}{3\Omega_{GK} k_b T^2} \lim_{t\to\infty} \int_0^1 \langle J_{h,x}(t')J_{h,x}(0)\rangle_T \, dt' \qquad 35$$

Where, k_{GK} is the thermal conductivity in Green-Kubo formulation, Ω_{GK} is the system volume and $J(t)$ is the time dependent response.

NEMD method, sometimes called *direct method*, has the purpose to replicate the Conceptual scheme represented in Figure 6, where a perturbation (the temperature gradient $\vec{\nabla}$T) is applied a system systems and the response is a steady-state heat flux after an. Two strong hypothesis are assumed in this case:

- The validity of Fourier's law at the nanoscale

- Thermal conduction of the model in steady state regime

The NEMD method starts with the creation of the thermal gradient. The initial temperature of the whole system is thermalized at T_0 by conventional thermosetting operations, such as a run in NVT ensemble. The creation of the thermal gradient starts once concluded the thermosetting operation by the application of thermostats region at the two ends of the model with temperatures usually $T_{cold} < T_0 < T_{hot}$. Thermostats acts as cold and hot reservoirs meaning that their temperature will remain constant over the simulation time still injecting and removing energy as more conductive the system is. Within this stage, the model run in NVE, excluded the two thermostats, a condition that allows the creation of the thermal gradient.

To assess the creation of the steady state requirement, it is possible to calculate the temperature profile *T(x,t)* inside the model. This latter operation is a function of time and is done by averaging the collected kinetic temperatures, in finite slabs, over the heat flux coordinate x, such as x_1, x_2, … x_{n-1}, x_n. as depicted in Figure 26.

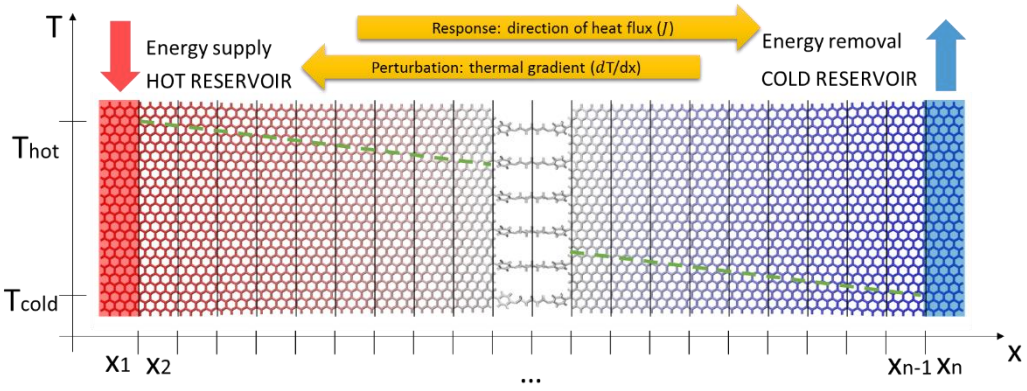

Figure 26. The temperature profile (dashed green line) in classical NEMD layout with the presence of an interface.

The thermal conductivity in NEMD is thus predicted by equation 36, where $\langle ... \rangle$ indicates the time averages take after a transient interval of time between the first thermosetting operation and the setup of the heat gradient.

$$k_{NEMD} = \frac{\langle J_{h,x}(T) \rangle}{\langle \frac{\Delta T}{L_x} \rangle} \qquad 36$$

Reverse NEMD [100] (RNEMD) or *inverse method*, can be considered an alternative to NEMD, it consists in imposing an energy flux by rescaling or swapping atom velocities and then evaluate the temperature profile. In this method the kinetic energy of any atom is rescaled by the same amount $\pm \Delta e_{kin}$ in time interval ΔT. The imposed flux becomes $J_{RNEMD} = \frac{\Delta e_{kin}}{2A\Delta T}$ where A is the cross section of the model and the thermal transport is evaluated similarly to what happens within direct method by equation 36.

The main drawback in calculating TC of materials via NEMD and RNEMD is represented from the dependency of the so-calculated thermal conductivity from the length of the model. This issue is due to the limitation that a small domain impose in the phonon mean free path [44]. The phonon mean free path of materials such as graphene was estimated of about 775nm at room temperature [35] and usually MD models are much shorter than this value. Simulating length close to the millimeter it is not common in MD, due to the computational weight that a similar long model would take. Despite this issue, it is possible to investigate such materials via NEMD or RNEMD considering this limitation of the method. In such case, a detailed investigation of thermal conductivity would include the extrapolation of TC values as a function of the model length and thus analyze the $\frac{1}{Lx} \rightarrow 0$ limit [12].

AEMD represents a novel method[121], it was developed in this decade to evaluate thermal transport during transients. The model is split in a cold region and a hot region by velocity rescaling creating thus a step-like function of the temperature along the heat transfer coordinate. The temperature gradient $\Delta T = \langle T_1 \rangle - \langle T_2 \rangle$ follows the equation 37.

$$\Delta T(t) = \sum_{n=1}^{\infty} C_n \, e^{-\alpha_n^2 \bar{k} t} \qquad 37$$

Where $\bar{k} = \frac{k}{\rho c_v}$ is the thermal diffusivity, ρ the density and c_v the specific heat. Cn a geometrical dependent parameter which contains the length of the model. Other details are available in literature [122]. AEMD can represent an innovative method to calculate thermal transport properties, the main advantage of AEMD if compared to NEMD and RNEMD is the reduced computational payload, a great advantage when dealing with very large systems (more than 10^5 atoms)[12].

1.3. Interatomic potentials in Molecular Dynamics

Equations 25, 26 and 27 illustrates how the interatomic forces affects position and velocity of the atoms, in few words, the whole dynamic. In classical MD, the interacting forces between the atoms of a system are calculated by the application of external force fields. A force field is a cumulative set of parameters that fits chemical species in predefined interactions equations; it can compute bonded or non-bonded interactions, depending on the inner formulation. Some force fields are even designed to manage chemical reactions thanks also to the integration of bonding and non-bonding contribution.

To describe the chemistry of gases, liquids, solids and soft matter as polymers, bond interactions non-bond interactions are taken account. The most important non-bonding force is the van der Waals one, represented by the Lennard-Jones (LJ) potential. This is a pairwise force, where the empirical parameter ε corresponding to the energy well is a function of the equilibrium distance σ. The electrostatic force is computed through Coulomb potential from the partial charges method of atom pairs.

However, this latter force contributes less in internal energy and it is often neglected. A detailed description of LJ and Coulomb potentials follows in next section.

The bonded interactions are more complex to represent than non-bonded one, due to the representation of the rigid constraints of chemical bond. Figure 27 reports the bonding terms commonly reproduced in force fields. As shown Figure 27, the only pairwise term in bonding interactions is the simple *bond* (Figure 27a), which is featured by typical values of length and energy. To represent more complex chemical species than monoatomic gases, many-body terms are adopted. The *angle* (Figure 27b) is a three body term which is the angle created by the atoms *i* and *k* atom across the atom *j* A *dihedral* (Figure 27c) is a four body term which describes the bond rotation between the *j* and *k* atoms across the planes created by *i-j* atoms and *k-l* atoms. The *improper* (Figure 27d) represents the angle formed by the plane that the *i,j,k* atoms belongs and the *l* atom.

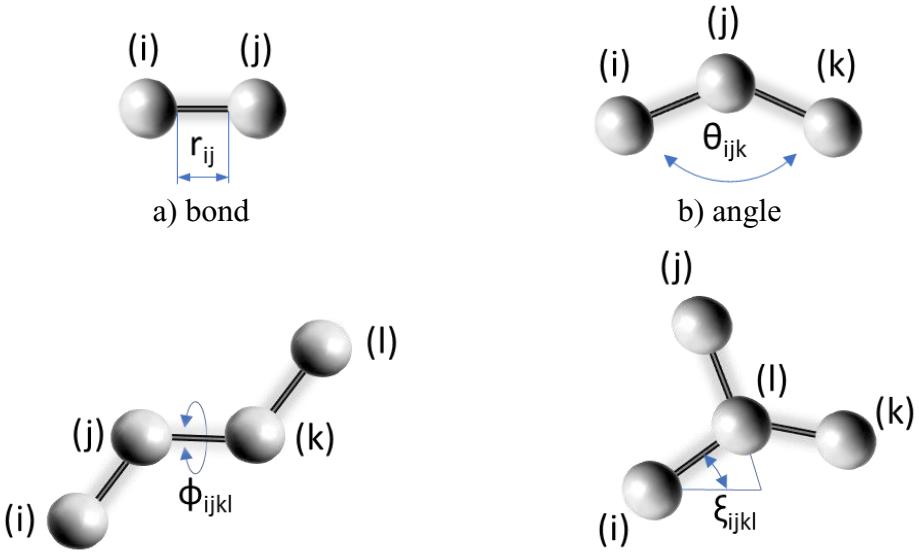

Figure 27. Bonding energy terms commonly described in interatomic potentials (a) Bond stretching, (b) Angle bending, (c) Dihedral rotation, and (d) improper angle bending.

The management of bond interactions is strictly dependent to the specific force field chosen. A former generation of force field, which includes REBO [123, 124], Tersoff [125, 126] and ReaxFF [127, 128], adopts a many-body approach to determine the chemistry of the system from model topology. In these force fields, designed to model crystals structures, a series of built-in switching functions manage the different allotropic forms based on the analysis of the bond length angles and torsions from of neighbor atoms. The above-cited force fields, sometimes referred as "Class 0", are widely adopted and validated and still represent a landmark in computational materials science community.

To provide a more detailed description of chemical species, especially in polymers, newer generations of force field were developed. Class I force fields (as

CVFF [129]) are often parameterized for biological systems, which functional form includes some cross coupled terms, and class II (as CFF93 [130] and COMPASS [131]) force fields, which adopt several cross-coupled terms, are designed for condensed matter as polymers and organic molecules. Class I and Class II force fields explicitly define the bonds, angles, impropers and dihedrals bonding terms and different atom types are parameterized for the same chemical element, depending on the atom surroundings and conjugation. Class II force fields includes also a large set of cross coupling terms, to represent vibrational anharmonicity [132, 133], as reported in Figure 28.

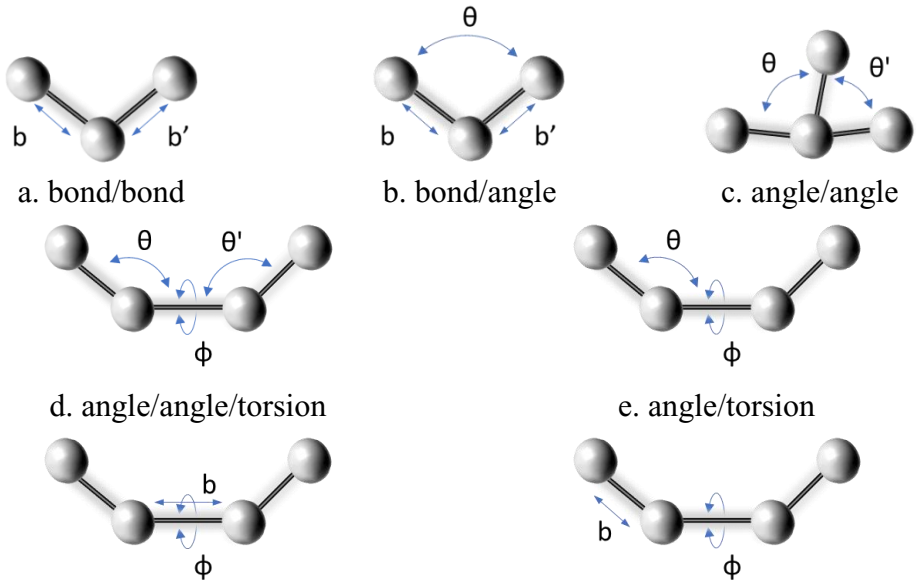

Figure 28. Anharmonic cross terms interactions in a class II force field.

At the beginning of classical MD simulations, force field parameters were usually calculated empirically through experimental analysis of small organic molecules [133]. Those small organic molecules were chosen because are viable to in-depth analysis. The validation in such systems was based on comparison of density, conformational energy, vibrational frequencies and more properties. From the early 90s, ab initio calculations [130] as quantum mechanics [134] were able to produce the large amount of data required to feed the development of newer generation of force field (Class I and Class II) with quantum-based parameters [131].

1.3.1. Non-bonded interactions

When the interaction between species is not mediated by a chemical bond, the term non-bonded is often adopted to group such interaction. The cumulative formulation for non-bonded potential energy is expressed from Equation 38; it is composed by contributions from single body, 2-body, 3-body and more terms. The single body interaction is related to external fields or container walls such as gravity force and usually is neglected for atomistic bulk system. The 2-body interaction corresponds to the interatomic pair potential, which is the commonest interaction for non-bonded

matter. Higher order terms, such as 3-body interactions and more are usually neglected, mainly due to high computational cost related to the benefit in terms of accuracy.

$$U_{nb}(r) = \sum_i v_1(r_i) + \sum_{i,j>i} v_2(r_i, r_j) + \sum_{i,j,k} v_3(r_i, r_j, r_k) + \dots \qquad 38$$

In MD simulations for materials science, most of non-bonded interactions are pairwise forces, calculated by differentiating the potential. The Lennard-Jones (LJ) potential was initially developed to study inert gases, nevertheless it become the most common potential to model pair interactions. The empirical potential form is expressed in Equation 39, where the parameter ε corresponds to the energy well as a function of the distance *r* and *σ* is the distance at which the potential is zero. The 12th power term in brackets corresponds to the repulsion between atoms while the 6th power one to the attraction. The plot of such Lennard Jones potential is shown in Figure 29 where the repulsive and attractive term are plotted distinctly. Equation 40 contains the force calculation from differentiation of the LJ12-6 potential. This potential is often tuned when dealing with condensed matter, to obtain a "softer" interaction [132] by lowering the exponent of the repulsive component, for example in LJ-9-6 built-in in MM3 (a force field parameterized for hydrocarbons, biological systems [135] and more) and COMPASS (a polymer-wise force field) formulations. In MD simulations, to save computational resources, a truncation parameter is used in LJ potential for long-range interaction called cut-off (described in paragraph 1.2.1). For these 6th power attractive Lennard Jones potential, the cut-off is usually set between 2.5σ and 3σ. Another variant of the Lennard Jones is the 9-3 exponential, which is used only for uncommon purposes, due to the longer distance and the longer 7σ cut-off. A comparison between 12-6, 9-6 and 9-3 variants in Lennard Jones is proposed in Figure 30.

$$v_{LJ}(r) = 4\varepsilon\left[\left(\frac{\sigma}{r}\right)^{12} - \left(\frac{\sigma}{r}\right)^{6}\right] \qquad 39$$

$$\vec{f}_{LJ}(r) = -\frac{\vec{r}}{r}\frac{dv_{LJ}(r)}{dr} = \frac{4\varepsilon}{r^2}\left[12\left(\frac{\sigma}{r}\right)^{12} - 6\left(\frac{\sigma}{r}\right)^{6}\right]\vec{r} \qquad 40$$

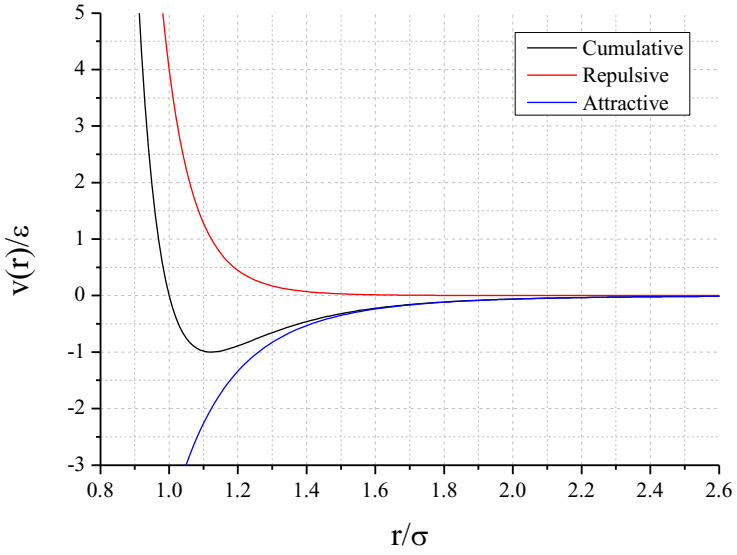

Figure 29. Standard Lennard-Jones potential in 12-6 formulation as a function of distance: attractive energy in blue, repulsive energy in red and cumulative energy in black lines.

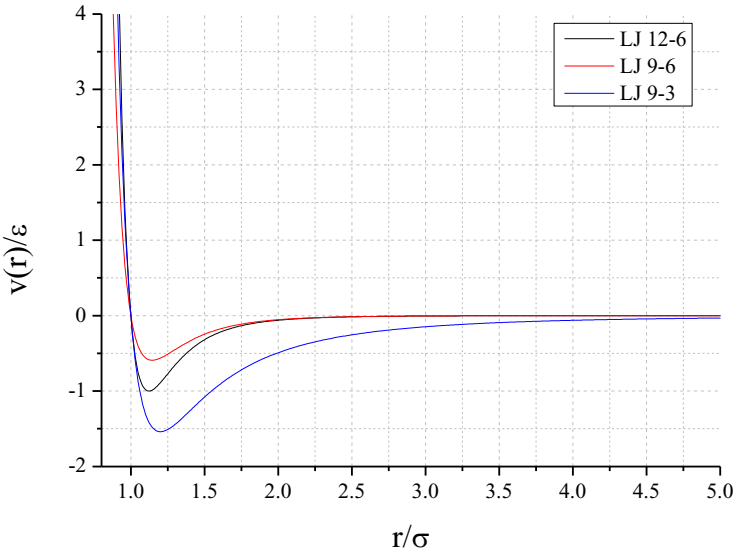

Figure 30. Lennard Jones 12-6 (in black) potential variants, the "softer" LJ 9-6 (in red) and the LJ 9-3. Note in this latter case the longer cut-off region.

When dealing with different materials, as in the case of nanocomposites, a possible MD approach is to apply different force fields to the same model. In such case, each interaction depends from the proper atom type and consequently refers to the right force field. Nevertheless, when atom types belonging to different force fields interacts, VdW interaction at the interface adopts mixing rules from Lorentz for the energy well (Equation 41) and Berthelot for the interatomic distance (Equation 42). Despite the adoption of mixing rules method is obsolete [136] and

cannot be accurate for every system [137], it is still employed in several composite works [73, 105].

$$\varepsilon_{ij} = \sqrt{\varepsilon_i \varepsilon_j} \qquad 41$$

$$\sigma_{ij} = \frac{\sigma_i + \sigma_j}{2} \qquad 42$$

More accurate methods were also developed for particular systems, as the one proposed by Waldman and coworkers for gases [138], but never imposed.

The electrostatic interaction arises from differences in charge distribution within a molecule. In MD and other computational methods, this is modeled by distributing point charges (partial charges) to every atom. Actually, electrons are delocalized in a molecule and similarly the total charge, so the partial charge is actually a primitive approximation that also ignores any quantum effect. Some force fields integrates the electrostatic force calculation by partial charges in their formulation. Some examples are COMPASS and ReaxFF, which own built-in versions the Coulomb potential. The standard coulomb potential is reported in Equation 43.

$$U_{coul} = \frac{1}{4\pi\varepsilon_0} \frac{q_1 q_2}{r_{ij}} \qquad 43$$

Where U_{coul} is the Coulomb potential, q_1 and q_2 are the partial charges of the atoms *i* and *j*, r_{ij} is the distance between *i* and *j*, $(4\pi\varepsilon_0)^{-1}$ is the Coulomb's constant which comprehends ε_0, the vacuum permittivity, and the 4π term from sphere integration from the Gauss' law.

The proper distribution of partial charges to the atoms can be faced in different ways. An advanced method has been developed in 1991 by Rappé *et al.* [139] and it is called QEq equilibration. QEq-calculated partial charges are determined by several parameters from literature values, atomic electronegativity, ionization potential, atom diameter and electron affinity. Moreover, the final value of the single atomic partial charge in QEq depends from the surrounding atoms. This method allows generating complex structures with a neutral overall charge. A simpler approximation is to attribute standard values to each atom type; this solution introduces higher levels of uncertainly, but it is still common where QEq equilibration is too much heavy to compute.

1.3.2. Intramolecular bonding potentials

The number of chemical species that a force field manages are usually limited, with some exceptions in general purpose force field as Universal [140], which however pays a limited accuracy as drawback. In this section, some of the most popular force fields adopted in material science simulations for nanocomposites are briefly presented.

Tersoff [125, 126, 141] is a three-body force field, initially developed for modelling crystalline silicon and later for carbon. The potential for carbon atoms was tested by calculating the cohesive energy and the structure of various carbon structures, the elastic constants, phonon frequencies and defect energies in graphite and diamond lattices. The results demonstrated good agreement with experiment, for elastic constants and phonon dispersion and with *ab initio* calculations for defect energies. Nowadays, Tersoff is a highly validated force field for carbon structures, as graphene and nanotubes due to an acknowledged agreement with experimental data for mechanical and thermal properties. In 2010, Tersoff potential was optimized [141] to fit better graphene vibrational properties: a large discrepancy with experimental in phonon modes was reported [142], also the typical G-peak in Raman spectroscopy was missing. The new optimized Tersoff force field matches with high accuracy the experimental values of in-plane phonon velocities for graphite and diamond, while lattice constants and cohesive energy become of secondary importance as closer matching in the original Tersoff and REBO [141]. With optimized Tersoff, Lindsay and coworkers [143] calculated a thermal conductivity of about 3000 $Wm^{-1}K^{-1}$ for a 10 μm flake, which is consistent with experimental results[144]. By the time, Tersoff force field was expanded for model various chemical species as germanium, oxygen, boron and nitrogen. The explicit potential form is expressed in Equation 44,

$$U_T(r_{ij}) = f_c(r_{ij})(A_{ij}e^{-\lambda_{ij}r_{ij}} - B_{ij}e^{-\mu_{ij}r_{ij}}) \qquad 44$$

Where $f_c(r_{ij})$ is a switching cut-off function (Equation 45), the term $A_{ij}e^{-\lambda_{ij}r_{ij}}$ is the attractive pair potential associated with bonding, $B_{ij}e^{-\mu_{ij}r_{ij}}$ the repulsive pair potential (Equation 46), similarly to a generic Morse potential.

$$f_c(r_{ij}) = \begin{cases} 1, & r_{ij} < R_{ij} \\ \frac{1}{2} + \frac{1}{2}\cos\left[\frac{r_{ij} - R_{ij}}{S_{ij} - R_{ij}}\right], & R_{ij} < r_{ij} < S_{ij} \\ 0, & r_{ij} > S_{ij} \end{cases} \qquad 45$$

$$B_{ij} = (1 + \beta^n \zeta^n)^{-\frac{1}{2n}} \qquad 46$$

Where *S*, *R*, *n* are atomic constants, which depend on atom type (carbon, silicon, germanium). Equation 47 reports the ζ function, which determines the atom coordination inside the cut-off and Equation 48 determines the angle coefficient $g(\theta_{ijk})$.

$$\zeta = \sum_{k \neq i,j} f_c\,(r_{ik})\omega_{ij} g(\theta_{ijk}) \qquad 47$$

$$g(\theta_{ijk}) = 1 + \frac{c^2}{d^2} - \frac{c^2}{d^2 + \left(h - \cos(\theta_{ijk})^2\right)} \qquad 48$$

$g(\theta_{ijk})$ is calculated from θ_{ijk} which is the bond angle between *ij* and *ik* bonds and *c*, *d*, *h* atomic constants. Equation 49 reports the mixing rules for pairwise bonding, where $\lambda, \mu,$ are atomic distances and *A*, *B*, are the attractive and repulsive energies coefficients.

$$\lambda_{ij} = \frac{\lambda_i + \lambda_j}{2};\ \mu_{ij} = \frac{\mu_i + \mu_j}{2};\ A_{ij} = \sqrt{(A_i A_j)}\ ;\ B_{ij} = \sqrt{(B_i B_j)}\ ;\ R_{ij} = \sqrt{(R_i R_j)} \quad (49)$$

The condensed-phase optimized molecular potential for atomistic simulation studies (COMPASS) [131] force field is a commercial Class II force field developed for both molecular systems and condensed organic structures as polymers. It is based on the CFF93 [130, 133] force field formulation from the early 90s and improved to manage alkanes [132], benzene compounds [131], siloxanes [145], aromatic polyesters [146], polysilanes [147] and more. The advantages of this class II force field comes from the weighting of the anharmonic terms and coupling interactions [132], already depicted in Figure 28, which contribute to a more accurate representation of vibrational energy in condensed organic materials. For the same purpose, COMPASS has a built-in "soft" Lennard-Jones potential 9-6 for van der Waals forces calculation optimized for condensed matter (polymer). This "soft" potential allows to fit rotations in molecular chains and also represent in crystals, both intramolecular and intermolecular energy barriers [132]. The COMPASS formulation is described from a single equation reported in Equation 50, which groups all terms. This formulation includes valence terms already depicted in Figure 27 for bonds, (b), angles (θ) torsion angles (ϕ) and out-of-plane (OOP) dihedrals angles (χ), the series of cross-coupling terms as combination of couples or triplets of terms (shown in Figure 28) from which anharmonicity is weighted. This formulation also includes non-bonding parameters: on bottom line of the Equation 50: the above-cited Lennard Jones 9-6 potential and a coulomb energy function $f(q_i q_j)$.

$$
\begin{aligned}
E_c = & \sum_b [k_2(b-b_0)^2 + k_3(b-b_0)^3 + k_4(b-b_0)^4] \\
& + \sum_\theta [k_2(\theta-\theta_0)^2 + k_3(\theta-\theta_0)^3 + k_4(\theta-\theta_0)^4] \\
& + \sum_\phi [k_1(1-\cos\phi) + k_2(1-\cos 2\phi) \\
& + k_3(1-\cos 3\phi)] \\
& + \sum_\chi k_2\chi^2 + \sum_{b,b'} k(b-b_0)(b'-b_0') \\
& + \sum_{b,\theta} k(b-b_0)(\theta-\theta_0) \\
& + \sum_{b,\phi} (b-b_0)[k_1\cos\phi + k_2\cos 2\phi + k_3\cos 3\phi] \\
& + \sum_{\theta,\phi} (\theta-\theta_0)[k_1\cos\phi + k_2\cos 2\phi + k_3\cos 3\phi] \\
& + \sum_{\theta',\theta} k(\theta'-\theta_0')(\theta-\theta_0) + \sum_{\theta',\theta,\phi} k(\theta-\theta_0)(\theta' \\
& - \theta_0')\cos\phi + \sum_{i,j} \frac{q_i q_j}{r_{ij}} \\
& + \sum_{i,j} \epsilon_{ij} \left[2\left(\frac{r_{ij}^0}{r_{ij}}\right)^9 - 3\left(\frac{r_{ij}^0}{r_{ij}}\right)^6 \right]
\end{aligned}
\qquad 50
$$

COMPASS is a widely used force field in the molecular dynamics simulation of organic materials, including GRM polymer nanocomposites [65, 148]; it allows a detailed representation of bond and non-bond interactions in the condensed phase. COMPASS also contains anharmonic bonding terms, providing a more accurate representation of thermal transport processes [149], which appear relevant in molecular junctions [150]. Despite COMPASS is not popular for the modelling of GRM, Zhang *et al.* [151] calculated a thermal conductivity in graphene finite slab value of 550 W m^{-1} K^{-1}.

The adaptive intermolecular reactive bond order (AIREBO) is a many-body force field, it was developed by Brenner [124] for modelling solid carbon and hydrocarbon molecules. Its second formulation [123] implemented from Stuart *et al.* [152], thanks also to a built-in Lennard-Jones term, can manage covalent bond forming and breaking associated to atomic rehybridization of carbon, thus it can be considered a reactive force field. The total energy of the hydrocarbon system comes out as sum of three different parameters as reported in Equation 51. The first term E_{ij}^{REBO} (Equation 52) is similar to the Tersoff one: the binding energy is written as difference over nearest neighbors for carbon pair interaction of the repulsive component V^R and the attractive component V^A as a function of the distance between *i* and *j* atoms (r_{ij}). Equations 53 and 54 are the repulsive and attractive components;

the function $f^c(r)$ limits the covalent bond range. A, B, Q, α, β are parameters evaluated from literature.

$$E = \frac{1}{2}\sum_i \sum_{j \neq i} \left[E_{ij}^{REBO} + E_{ij}^{LJ} + \sum_{k \neq i,j} \sum_{l \neq i,j,k} E_{kijl}^{tors} \right] \quad 51$$

$$E_{ij}^{REBO} = V^R(r_{ij}) - b_{ij} V^A(r_{ij}) \quad 52$$

$$V^R(r) = f^c(r)\left(1 + \frac{Q}{r}\right) A e^{-\alpha r} \quad 53$$

$$V^A(r) = f^c(r) \sum_{n=1,3} B_n e^{-\beta r} \quad 54$$

The bond order function is shown in Equation 55, where the strength of the covalent bonding interaction are grouped in this term. Coordination numbers, bond angles, and conjugation contribution to the strength of covalent bond contributes in AIREBO. This is used in different carbon hybrids where the c-c b_{ij} parameter is bigger in sp2 carbon atoms than sp3 carbons. This allows to weight more the attractive term for sp2 carbons, determining stronger double bonds. In AIREBO, all conjugations and hybridization states are derived from the system geometry.

$$b_{ij}^{\sigma-\pi} = \left[1 + \sum_{k \neq i,j} f_{ik}^C(r_{ik}) g_c\left(\cos(\theta_{ijk})\right) e^{\lambda_{ijk}} + P_{ij}(N_i^C, N_i^H) \right]^{-1/2} \quad 55$$

Where the g_c function (Equation 29) tunes the contribution of nearest neighbors to the bond order according to the angle cosine of the bonds between atoms i-k and i-j. The P function represents a 4th order spline, N_i^C (Equation 56) the carbon atoms that are neighbors of atom I, N_i^H (Equation 57) the hydrogen neighbors of the same atom.

$$N_i^C = \sum_{k \neq i,j}^{carbon\ atoms} f_{ik}^C(r_{ik}) \quad 56$$

$$N_i^H = \sum_{l \neq i,j}^{hydrogen\ atoms} f_{il}^H(r_{il}) \quad 57$$

Equation 55 uses the g_c parameter, defined in equation 58, which is determined through a switching function reported in equation 59 to determine atomic angles when atomic positions determines wrong coordination. The total coordination is calculated in Equation 60, where N_i^C and N_i^H formulations were proposed previously in Equations 56 and 57.

$$g_C = G_C(\cos(\theta)) + Q_i(N_i^t)[\gamma_C(\cos(\theta)) - G_C(\cos(\theta))] \quad 58$$

$$Q_i(N_i^t) = \begin{cases} 1\,, N_i^t < 3.2 \\ \dfrac{\left[1+\cos\left(2\pi(N_i^t-3.2)\right)\right]}{2}, & 3.2 < N_i^t < 3.7 \\ 0\,, N_i^t > 3.7 \end{cases} \qquad 59$$

$$N_i^t = N_i^C + N_i^H \qquad 60$$

The non-bond interaction in AIREBO is treated through a classic LJ-12-6 potential (similar to the expression of equation 39) and a series of switching functions at the region boundaries. The torsional component of the potential E_{kijl}^{tors} is described in Equation 61, where w is a bond weighting function, ω_{kijl} is the torsion angle between the plane defined by the vectors r_{ik}, r_{il} and r_{ij} and r_{jl}; and V^{tors} is the potential function reported in Equation 62.

$$E_{kijl}^{tors} = w_{ki}(r_{ki}) w_{ij}(r_{ij}) w_{jl}(r_{jl}) V^{tors}(\omega_{kijl}) \qquad 61$$

$$V^{tors}(\omega_{kijl}) = \frac{256}{405}\epsilon_{kijl}\cos^{10}\left(\frac{\omega_{kijl}}{2}\right) - \frac{1}{10}\epsilon_{kijl} \qquad 62$$

Minor functions and coefficient tables have been omitted but are available in refs [123, 152]. The constant improvement of the AIREBO force field made of it a landmark in carbon materials simulations, as demonstrated by the wide literature on carbon based materials as graphene family structures [153-155] and as well hydrocarbons [29].

ReaxFF [128] is a reactive force field, that means that it is able to simulate some chemical reactions. Initially, it was developed to simulate the oxidation of hydrocarbons [128] but by the time, many different version of ReaxFF have been developed and each variant can now manage about five or six different chemical elements. The main drawback of this reactive force field is represented by the higher computational demand if compared to a classical one. The general formulation of contribution energies of the potential is reported in Equation 63.

$$E_{system} = E_{bond} + E_{over} + E_{under} + E_{val} + E_{pen} + E_{tors} + E_{conj} + E_{VdWaals} + E_{coulomb} \qquad 63$$

Where E_{bond} is the bonding energy, E_{over} and E_{under} the energy penalty and contribution for over-coordination and under coordination, respectively. E_{val} is the valence angle term, E_{pen} is an energy penalty for double bonds E_{tors} is the energy for torsion angles, E_{conj} is the conjugation contribute of aromatics. The non-bonding parameters are the $E_{VdWaals}$ term, which is actually a distance-corrected Morse potential, and $E_{coulomb}$, a shielded Coulomb potential (see Equation 43 for Coulomb potential).

All the bonding energy are strictly related to the "bond order" function reported in Equation 64. Where the first term is the σ bond which takes place below 1.5 Å and negligible for more than 2.5 Å. The second term is the π bond that is unity below 1.2 Å and not occurs above 1.75 Å. The third term is another π bond that operates below 1 Å and negligible over 1.4 Å. More details are available in the original work from van Duin *et al*. [128].

$$BO'_{ij} = exp\left[p_{bo,1} \cdot \left(\frac{r_{ij}}{r_0}\right)^{p_{bo,2}}\right] + exp\left[p_{bo,3} \cdot \left(\frac{r_{ij}^{\pi}}{r_0}\right)^{p_{bo,4}}\right] + exp\left[p_{bo,5} \cdot \left(\frac{r_{ij}^{\pi\pi}}{r_0}\right)^{p_{bo,6}}\right] \quad 64$$

1.4. Fundamentals of finite element method for heat transfer

1.4.1. Introduction to the finite element method

An introduction to the finite element method (FEM) is presented in this section by the linear analysis of solids and structures, which is widely used in mechanical, biomechanical, nuclear, mining, ocean, civil, and more engineering problems.
The finite element method (FEM) is a numerical method to calculate approximate solutions to the partial differential equations where typical problem areas of application include thermal and mass transport, mechanical analysis and electromagnetic fields. In fact it can be said, FEM is a way that engineers invented to solve structural equations and to solve differential equations related to nature. The history of FEM actually begins in Russia with Galerkin who created a method to take the differential equation, which is a continuous problem. He used some trail functions, functions that he hoped whose combinations could be close to the right answer. Galerkin worked with few trail functions, so he had to make a very close guess of the solution. Nevertheless, decades later, when computing machines were developed with enough computational capabilities; it was possible to work with a hundred thousand functions. The sum of these hundred thousand simple functions makes that that their combinations can produce results close to the analytical answer. FEM has applications in linear, non-linear, static and dynamic analysis and it is used in various computer programs such as ANSYS, SAP, ADINA, ABAQUS and more.

The FEM employs a variational problem that includes an integral of the differential equation over the problem domain. The domain is split into a number of subdomains called finite elements. The solution of the partial differential equation (PDE) is approximated by a simpler polynomial function on each element. All these polynomials have to be joined together so that the approximate solution is uniform over the entire domain. After this step, the variational integral is calculated as the sum of the contributions from each finite element. The result is an algebraic system

in which the approximate solution have a finite size rather than the initial infinite-dimensional PDEs [156].

Within this section, only the linear analysis is considered and the linear analysis. The finite element solution process can be described by the scheme reported in Figure 31. In the analysis of an actual physical problem, first a suitable finite element model of the physical system should be established. Then the model will be solved and the results should be interpreted to revise or refine the model if necessary. The interpretation of the results depends very much on how the finite element model is established, what kind of model is used and so on.

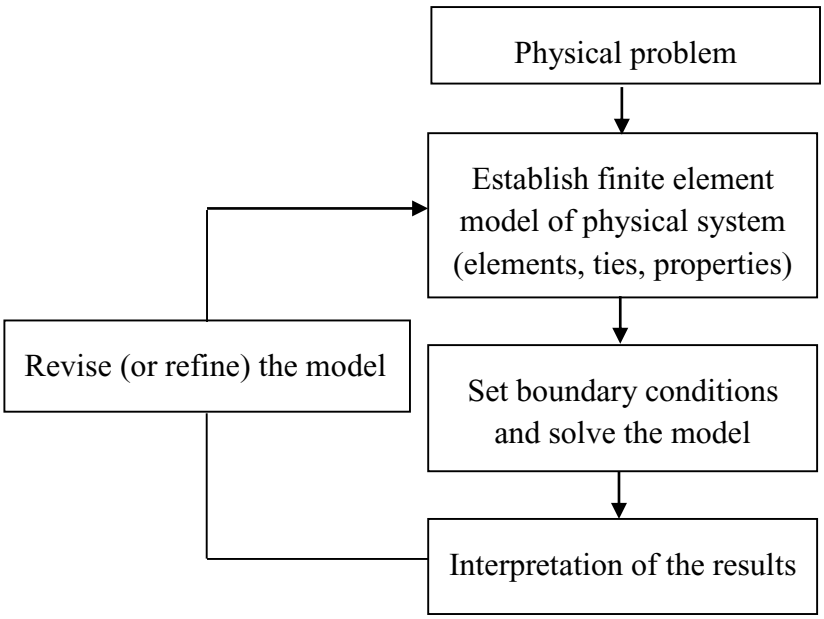

Figure 31. The finite element solution process

To illustrate what means establishing a finite element model, consider the area of the given complex geometry as shown in Figure 32.

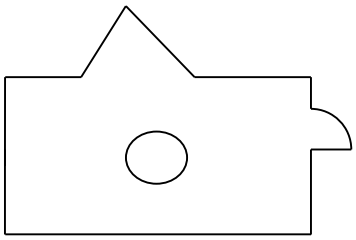

Figure 32. Example of 2D system geometry

From the mathematic, it is simply possible to compute the area of such complex geometry if we discretize it as reported by Figure 33. The key point is that other discretization may make the problem more complicated or impossible to solve. In finite element analysis process, also, an actual physical system will be discretized to finite elements such as beam elements, truss elements, plate and shell elements and so on which they are called mesh. Therefore, to identify a suitable mesh to discretize the actual physical system is very important.

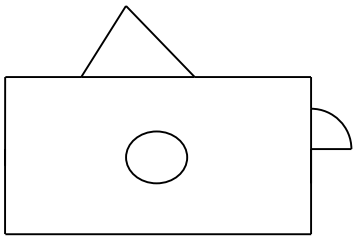

Figure 33. Example of discretization of the domain into its constituent shapes.

When we are talking about a system continuous and discrete system, actually all the systems are continuous systems. Despite this assumption, when system consists of springs, dashpots, beam elements, then we might refer to this continuum system to as discrete system. In this latter case, the response is described by variables at a finite number of points and we come up to a set of algebraic equations. However, in the continuous system, response is described by infinite number of points and we have to solve set of differential equations.

Nevertheless, the solution of complex differential equations could not happen analytically and it requires using numerical procedures, and FEM is one of the powerful methods that can be used. Steps to analyze discrete systems are similar to continuous systems. These steps involved:

- Idealization of the system in to elements
- Equilibrium requirements of each elements should be evaluated
- Element assemblage
- Solution of the response

It should be mention that dealing with discrete system, the system is discretized into elements, so the first step is automatically implemented. Moreover, in case of continuous systems the idealization of the system is not trivial.

When we want to analyze a continuous system we come up with two different approaches, one the differential formulation and the second variational formulation. In both approach we obtain continuous variables that means we have infinite state variables and we have to solve these continuous variables. However, it should be notice that for a complex system, it is not easy to solve the differential equation and we have to use numerical methods like weighted residual method in differential formulation or Ritz method in variational formulation. The FEM is an extension of

these methods and we will show that how FEM is related to these classical technics. In this dissertation, only the differential formulation is proposed with the Dirichlet-type boundary condition. If the highest order of derivative in the differential equation is $2m$, the highest order of derivatives in essential boundary conditions is $m-1$ and the highest order of derivatives in natural boundary conditions is $2m-1$. In addition, we call this kind of problem a c^{m-1} variational problem that c^{m-1} means continuity of order $m-1$.

1.4.2. Derivation of the Fourier's partial differential equation

The following part constitutes the derivation of the PDEs inside the domain by few mathematical steps [157]. In thermal conduction problems, by the application of the Fourier's law (Equation 65), it is possible to find the temperature distribution in every point the knowledge of the heat flux, and *vice versa*.

$$\vec{q} = -k\vec{\nabla}T \qquad 65$$

However, the only information about surface values is known, meaning that it is needed to solve partial differential equations (PDEs) to obtain the internal temperature profile. To this purpose the volume element $dV=dx\ dy\ dz$, reported in Figure 34, as a part of a three dimensional body, heat fluxes $\dot{q}_k$ and $\dot{q}_{k+dk}$ occur under the influence of a temperature gradient inside the body, where j is x,y or z coordinate.

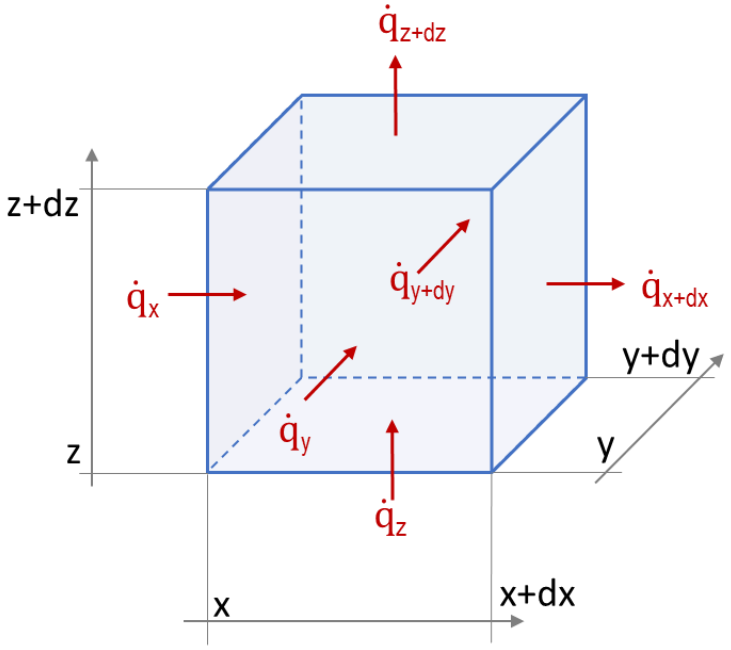

Figure 34. Volume element dV (in light blue) and correspondingly heat fluxes (red arrows) passing through its surfaces.

By a Taylor series approximation of first order (equation 66), the net heat transfer rates of the element rates in x,y,z axis are found in Equations 67, 68 and 69, respectively.

$$\dot{q}_{j+dj} = \dot{q}_j + \frac{\partial \dot{q}_j}{\partial j} dj \qquad 66$$

$$(\dot{q}_x - \dot{q}_{\mathrm{x}+dx}) dydz = -\frac{\partial \dot{q}_x}{\partial x} dxdydz = -\left(\frac{\partial \dot{q}_x}{\partial \mathrm{x}}\right) dV \qquad 67$$

$$\left(\dot{q}_y - \dot{q}_{\mathrm{y}+dy}\right) dxdz = -\frac{\partial \dot{q}_y}{\partial y} dydxdz = -\left(\frac{\partial \dot{q}_y}{\partial \mathrm{y}}\right) dV \qquad 68$$

$$(\dot{q}_z - \dot{q}_{\mathrm{z}+dz}) dxdy = -\frac{\partial \dot{q}_z}{\partial z} dzdxdy = -\left(\frac{\partial \dot{q}_z}{\partial \mathrm{z}}\right) dV \qquad 69$$

By adding and removal of the term $-k\left(\frac{\partial T}{\partial k}\right)$ from Fourier's equation in one-dimension for $\dot{q}_k$, yields to the neat heat balance of the volume dV reported in equation 70.

$$\dot{Q} = \left(\frac{\partial}{\partial \mathrm{x}}\right) k \left(\frac{\partial T}{\partial x}\right) dV + \left(\frac{\partial}{\partial \mathrm{y}}\right) k \left(\frac{\partial T}{\partial y}\right) dV + \\ + \left(\frac{\partial}{\partial z}\right) k \left(\frac{\partial T}{\partial z}\right) dV = \mathrm{div}(k \nabla T) dV \qquad 70$$

If we exclude internal heat generation and losses inside the element, $\dot{Q}$ is equal to the rate of thermal energy storage $\dot{H}$ from equation 71,

$$\dot{H} = c_p dm \frac{\partial T}{\partial t} = \rho c_p \frac{\partial T}{\partial t} dV \qquad 71$$

where c_p is the specific heat capacity ($Jg^{-1} K^{-1}$), dm is the infinitesimal mass of the volume dV, ρ is the density of the material and $\frac{\partial T}{\partial t}$ the time dependant partial derivative of the temperature respect to time.
From the sum of the equations 70 and 71, the PDE of Fourier, reported in equation 72 is:

$$\rho c_p \frac{\partial T}{\partial t} = \mathrm{div}(k \nabla T) \qquad 72$$

The Fourier's PDE be satisfied needs boundary conditions. Equation 73 reports a simple first type boundary condition

$$T(\mathbf{x}, \mathrm{t}) = \mathrm{T}_{\mathrm{known}}(\mathbf{x}, \mathrm{t}) \qquad 73$$

where $\mathbf{x} = (\mathrm{x}, \mathrm{y}, \mathrm{x})$ is a point inside the element, and $\mathrm{T}_{\mathrm{known}}$ a known function, usually a constant value (Dirichlet boundary condition).

1.4.3. Problem formulation

An example of the system domain is proposed in Figure 35 where the Representative Volume Element (RVE) is depicted. The RVE consists in an ideal composite volume, where the discs are the filler particles and the rest of the volume is occupied by polymer. The edges of the RVE are identified by eight triples by a Cartesian coordinate system as follows:

$$(x_1, y_1, z_1), \quad (x_2, y_1, z_1), \quad (x_1, y_2, z_1), \quad (x_2, y_2, z_1),$$
$$(x_1, y_1, z_2), \quad (x_2, y_1, z_2), \quad (x_1, y_2, z_2), \quad (x_2, y_2, z_2).$$

Thus, the domain of the RVE will denoted by Ω as Cartesian product of the coordinates:

$$\Omega = (x_1, x_2) \times (y_1, y_2) \times (z_1, z_2)$$

Where Ω is made of polymer $\Omega_{polymer}$ and filler flakes Ω_{filler}

$$\Omega = \Omega_{polymer} \cup \Omega_{filler} \wedge \Omega_{polymer} \cap \Omega_{filler} = \emptyset$$

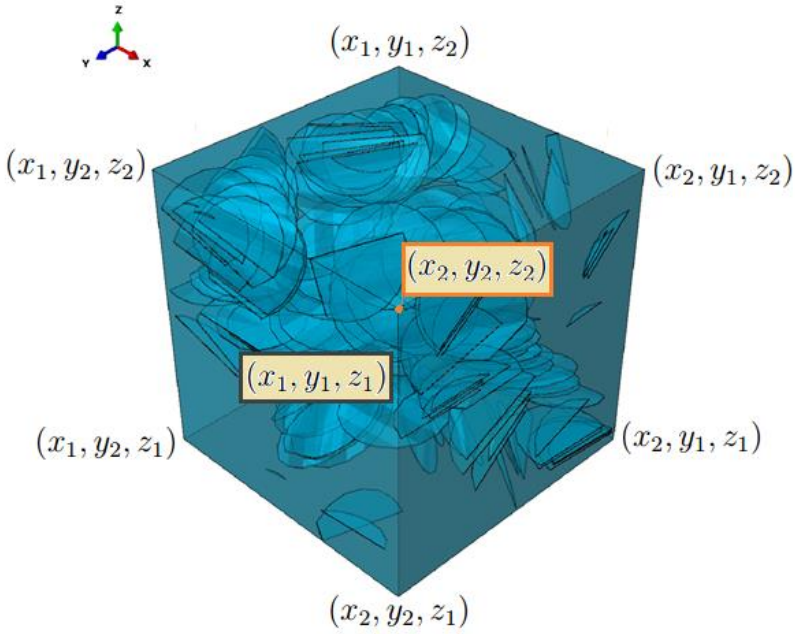

Figure 35. Representative Volume Element (RVE) for polymer based composite in FEM analysis. (x_1, y_1, z_1) edge corresponds to the origin of the axis and it is actually hidden.

Since all the present work is restricted to steady-state temperatures, where $\frac{\partial T}{\partial t} = 0$, the equation 72 becomes

$$\mathrm{div}\big(k(\mathbf{x})\nabla T(\mathbf{x})\big) = 0 \;\forall\, \mathbf{x} \in \Omega \qquad 74$$

With: $k(\mathbf{x}) = \begin{Bmatrix} k_{polymer} \ \forall \ \mathbf{x} \in \Omega_{polymer} \\ k_{filler} \ \forall \ \mathbf{x} \in \Omega_{filler} \end{Bmatrix}$

And Dirichlet boundary conditions specified on

$$\{\mathbf{x} \in \partial\Omega : \mathrm{y} = y_1 \ \vee \ \mathrm{y} = y_2\}$$

Symbolizing the initial temperature on opposite y faces of the RVE, while on the other surfaces

$$\{\mathbf{x} \in \partial\Omega : \mathrm{x} = x_1 \ \vee \ \mathrm{x} = x_2 \ \vee \ \mathrm{z} = z_1 \vee \ \mathrm{z} = z_2 \ \}$$

Where homogeneous Neumann boundary conditions are set to impose the heat flux and thus to calculate the effective thermal conductivity of the composite.

1.4.4. FEM Applications in polymer matrix composites

The first application of FEM analysis to thermal properties of composite materials starts from the mid 90's, when Ramani and Vaidyanathan [158] developed a representative volume element (RVE) for simulate a short fibers composite and applied Fourier's law on it. In such model, the volume fraction and the aspect ratio of the filler were tunable, a feature that is still in use. Moreover, the thermal conductance at the interface was modelled as a thin layer with low conductivity surrounding the fibers, similar to the representation proposed in Figure 36.

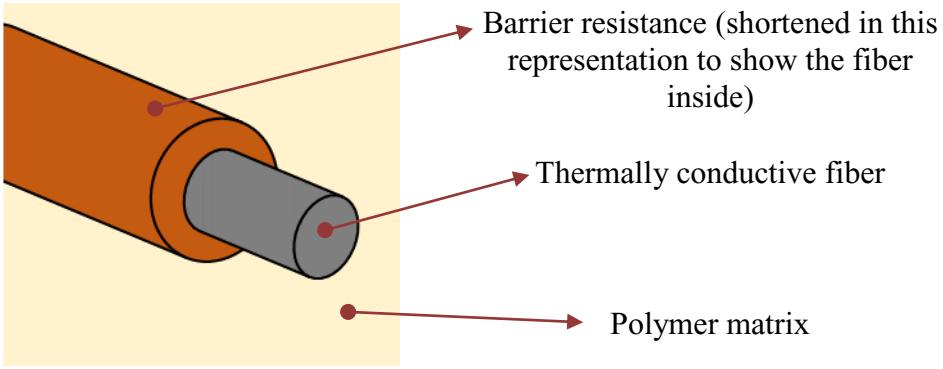

Figure 36. Schematic representation of a low conductivity layer in fiber-reinforced composite, similar to the one adopted by Ramani and Vaidyanathan [158].

The results were compared to experimental works and several predictive models, with a better agreement with experiments than predictive models. In 1999 the cross section of long fibers was used as RVE and tuned by Islam and Pramila [159] in round and square geometries, finding excellent agreement with literature values. Years later, FEM became a popular alternative to predictive models, especially combined to other simulation methods as MD, in Multi-scale approach.

In 2008 a combined Monte Carlo-FEM multi-scale approach was used by Sanada and coworkers [160] to investigate thermal properties of fillers at micro and nano scales as carbon nanotubes finding fair agreement with experiments. They developed three different RVEs to model spheres and nanotubes, as reported by figure

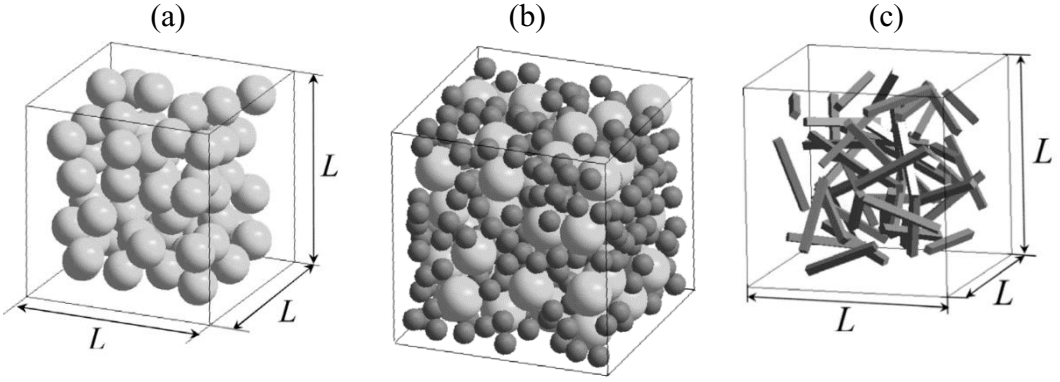

Figure 37. Three different RVE's developed from Sanada and coworkers with different particles. (a) with one type of sphere and (b) two types of spheres acting as fillers.(c) Modelled nanotubes in RVE. Reprinted from [160], with permission from Elsevier.

In 2010 Nayak *et al*. [161] did a direct comparison of FEM simulation made of spheres-in-cube RVE predictive models, finding a better agreement with experimental values of FEM than the compared predictive models. Mortazavi and co-workers contribute to multi-scale NEMD-FEM development in materials science by design of well suitable RVE's, which comprehends the weight of interfacial conductances, often calculated by NEMD or MD. Within this latter approach, the reported values were employed to simulate thermal properties of composites with carbon-based [72, 162, 163] and non-carbon-based fillers [164-166]. The multi-scale modelling technique was also employed to investigate heat transfer in polycrystalline materials [53, 167] and graphene laminates [74]. The proposed works demonstrates that despite FEM analysis is a traditional engineering tool, by developing proper RVEs it can become a powerful tool to investigate thermal properties of composite materials. Such consideration is particularly true for rare cases as multiple types of filler or shape of it where predictive models lacks [158].

1.5. Scope and structure of this dissertation

As introduced previously, a tight and effective percolative network is necessary to obtain thermally efficient polymeric nanocomposites. Moreover, the proper design and manufacturing of the filler-filler interfaces represents an advanced strategy to build thermally conductive percolative networks.

This dissertation addresses a computational approach to screen possible chemical species as candidates to reduce thermal resistance at the platelet-platelet interface. Most of this work represent an attempt to screen molecules as thermal linker, finding the parameters that could bring to thermal conductance improvements in GRM for nanocomposite building. On the other hand, the findings about molecular linkers

should be close related to chemical viable systems from an experimental point of view, which also includes large atomistic models and polymer mass.

To investigate the key factors in thermal transport across the interfaces, at the beginning of this PhD work, alkyl based junctions were investigated. The reduced number of chemical moieties and the capability of the alkyl chains to be adapted to different scenario, allowed driving the following efforts, where more chemically viable systems were simulated. The initial simple layout, made of a couple of graphene platelets creating a flat edge interface, allowed comparing covalently bonded and non-bonded linkers. Non Equilibrium Molecular Dynamics was chosen as an effective method to investigate the thermal property at the interfaces between graphene flakes, especially for larger models, where the alternative lacks.

Chapter 2 reports a resume of the methods employed in this PhD dissertation. The first part is constituted by the methods to determine thermal conductance at the interface in molecular dynamics simulations. In this section, the non-equilibrium method and the transient pump-probe technique were presented. Moreover, additional methods are described, as the velocities autocorrelation function employed to find the vibrational density of states and MD calculation for the internal stress calculation. An entire section is dedicated to the modelling of PDMS polymer that was employed in thermal transport works of chapters 5 and 6. The last paragraph illustrates FEM modeling of composites, where FEM is employed to calculate the thermal conductivity.

Chapter 3 reports the results in terms of thermal conductance analysis between graphene platelets bonded with non-covalent molecular junctions. Through non-equilibrium molecular dynamics simulations, the thermal conductance was calculated for interdigitated alkyl junctions, which exploited van der Waals forces to carry heat. In a second study, a fine-tuning of the distance in edge-functionalized graphene platelet, bonded with pending phenols was performed. In this latter case, the thermal conductance was investigated weighting the different contributions from the charged O-H interactions and the aromatic stacking rings. Part of the results are published in "Molecular junctions for thermal transport between graphene nanoribbons: Covalent bonding vs. interdigitated chains" *Computational Materials Science* 142 (2018) 255-260 and "Edge-Grafted Molecular Junctions between Graphene Nanoplatelets: Applied Chemistry to Enhance Heat Transfer in Nanomaterials" *Advanced Functional Materials* 28 (2018) 1706954.

Chapter 4 is focused on the thermal conductance in covalent bonded junctions. In the first part, the role of chain length and the number of linkers has been evaluated. The encouraging thermal properties of covalently bound linkers, compared to non-covalent forces induced a second study that investigates also the role different chemical moieties. In this work, the phonon vibrational density of states and uniaxial pulling force were analyzed. Part of the results proposed in chapters 3 and 4 are published in the following papers:

- "Molecular junctions for thermal transport between graphene nanoribbons: Covalent bonding vs. interdigitated chains" *Computational Materials Science* 142 (2018) 255-260
- "Edge-Grafted Molecular Junctions between Graphene Nanoplatelets: Applied Chemistry to Enhance Heat Transfer in Nanomaterials" *Advanced Functional Materials* 28 (2018) 1706954
- "Aromatic molecular junctions between graphene sheets: a Molecular Dynamics screening for enhanced thermal conductance, currently submitted to RSC Advances.

Chapter 5 describes the endeavor to weight the thermal contribution of molecular junctions within a polymer matrix. This environment represents a condition closer to an actual nanocomposite material. The scope of this work is to evaluate how molecular junctions, selected from the molecules investigated in Chapter 4 could perform surrounded by a polymeric environment. In this work, a couple of graphene nanoplatelets, stacked above and below by a dense PDMS matrix, undergoes NEMD simulations exploiting the different thermal linkers. The results presented in this chapter will be part a paper currently in preparation.

Chapter 6 reports a multiscale modeling by coupling MD and FEM simulation to predict the thermal conductivity of a nanocomposite material via a completely computational approach. As first step, the thermal equilibration method (described in paragraph 2.3) is adopted in MD simulations to calculate the thermal conductance for PDMS and Graphene interface. Moreover, for the sake of comparison, the PDMS and Borophene interface was investigated too. The results from MD calculations were then employed in FEM analysis to evaluate the thermal conductivity the composite made of those components, by tuning the filler volume fraction, the platelets thickness, and the platelets aspect ratio. This chapter reports results that will be fitted in a paper currently under development.

Chapter 2

Methods

In this chapter, the methods and tools employed to calculate the thermal, mechanical and physical properties of the investigated matter are illustrated. In section 2.2, the non-equilibrium method to calculate BTC in cross-linked systems is presented. Paragraph 2.3 reports the transient pump-probe technique used in multi-scale modelling to evaluate ITC in large interfaces.

Moreover, side methods are described, as the autocorrelation function (2.4) of the atomistic velocities, employed to find the vibrational density of states and MD calculation for the internal stress calculation (2.5). Section 2.6 is dedicated to the modelling of PDMS polymer, which required the development of specific thermodynamic cycle to obtain a stable system. The last paragraph (2.7) explains the FEM modeling of composites employed to calculate the thermal conductivity of the overall composite.

2.1. Introduction to LAMMPS

The MD simulations presented in this dissertation were performed with the Large-scale Atomic/Molecular Massively Parallel Simulator (LAMMPS) [168, 169]. The LAMMPS package allows classical molecular dynamics with a focus on materials modeling. It works with all the potentials presented in paragraph 1.3 for solid matter (as metals and semiconductors) and soft matter (polymers and large molecules). LAMMPS is released under General Public License and is distributed by Sandia National Laboratories and Temple University from Albuquerque, NM. This form of licensing allowed LAMMPS to gain a continuous development and expansion of functionalities from a wide scientific community, making of LAMMPS a big player among the computational materials scholars. LAMMPS works in parallel using message-passing interface such as MPI/OpenMPI by spatial-decomposition of the simulation domain [168]. This parallelization solution makes LAMMPS a scalable code, capable of running from a cheap PC to the powerful cluster for high performance computing (HPC). Moreover, thanks to the contributions from the community, LAMMPS supports the edge technology in terms of accelerated computing performance from GPUs [170], and Intel Xeon Phis cards.

2.2. Non-Equilibrium Molecular Dynamics

To evaluate the thermal properties of condensed matter, Non-Equilibrium Molecular Dynamics (NEMD) approach is an established technique used to investigate the thermal property of materials [119]. In NEMD, the basic idea is to create a thermal gradient inside the material and measure the derived heat flux. The temperature gradient arises by the application of thermostats to limited regions of the domain (Figure 38). The regions excluded from the thermostats run inside NVE statistical ensemble, experiencing the temperature difference, according to the model design.

All the simulations that involved only alkyl chains between the graphene sheets adopted the AIREBO force field, while for the systems which required various chemical species, the COMPASS force field was employed.

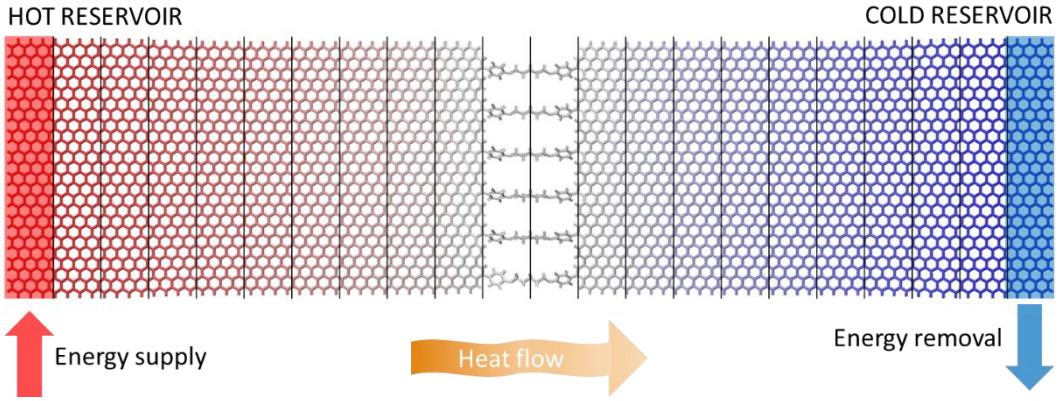

Figure 38. The typical layout adopted in NEMD simulations. The vertical lines (in black) highlights the thermal layers slicing.

Periodic Boundary Conditions (PBC) were set in x,y,z with padding space more than double of the cut-off distance in order to avoid PBC interaction. The thickness of the sheet (Z-axis) was considered 3.45 Å from the van der Waals (VdW) diameter of the carbon atom. Because the graphene size is several times shorter than the phonon mean free path, no phonon scattering is expected inside it [44]. The C-C bond length adopting AIREBO force field measured 1.41 Å as average value (Figure 39), very close to which reported from Diao *et al.* [155].

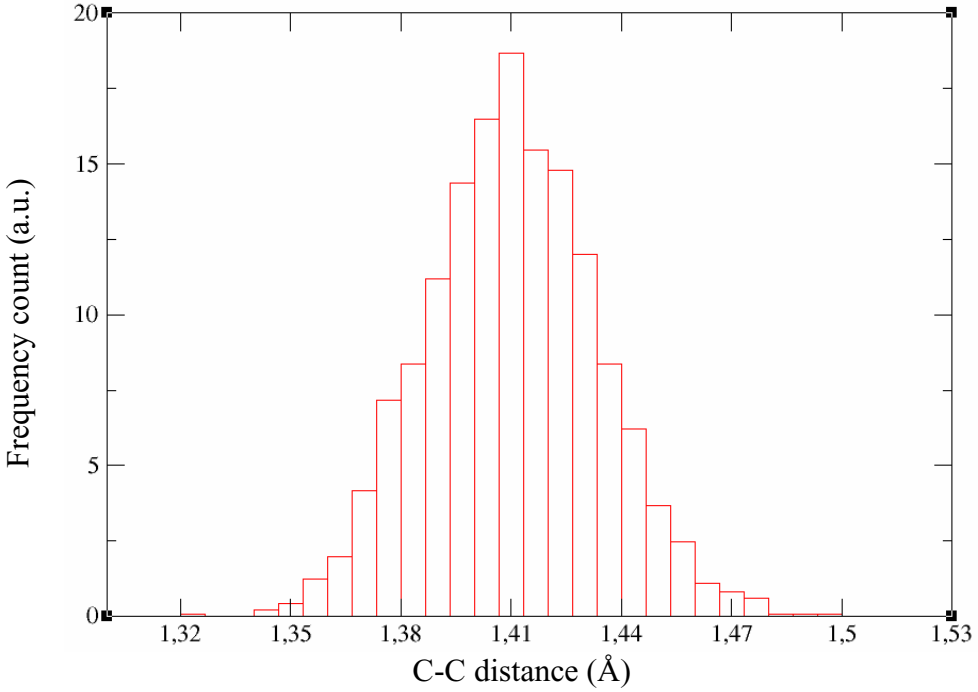

Figure 39. Calculated C-C distance in actual MD simulations employing AIREBO force Field.

The models were composed of about 4100 atoms, divided in two graphene nanoribbons (approximately 100 Å by 50 Å) grafted through the armchair edge by 4,6 or 12 covalently bound junctions, or in case of interdigitated systems, by six linkers with alternated partial grafting in each sheet. The molecular junction length refers to the distance "d" between platelets edges (Figure 40). All the aromatic molecules ends were bonded in para (p-) with the graphene nanoribbons (Figure 40) except for the fully aromatic acene-based thermal bridges, which exploited aromatic bonding (Figure 41).

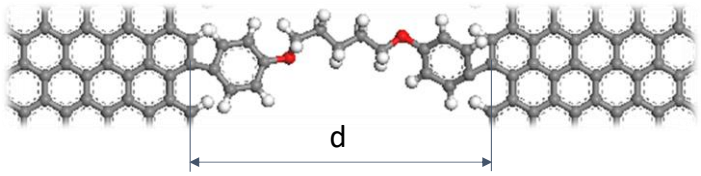

Figure 40. Example of aliphatic-aromatic junction detail of 1,5-bis(p-phenylenoxy) pentane with dimensioning ("d") for platelets distance measurements.

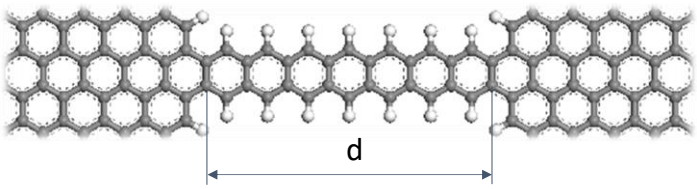

Figure 41. Heptacene, as example of aromatic bonding, with dimensioning ("d") to measure platelets distance.

The simulation procedure follows a stepwise scheme: at the beginning, the whole system was initially relaxed through an equilibration period of at least 125 ps in canonical ensemble at 300 K, a temperature in which the quantum effect is considered negligible [171]. Then, the ends of the model were fixed in a 8Å long region and the rest of the model is virtually split into 22 thermal layers along the x coordinate to avoid sliding and PBC interference. In this stage, two thermostats are applied to the first and last thermal layers [172] between the fixed atoms region. At the end of the thermal equilibration, followed a minimum 250 ps of thermo-stated preheating. In this stage, Nosé-Hoover thermostats were set to 310 K and 290 K and applied to the model ends. All the atoms in the system, except those in thermo-stated regions, run in microcanonical ensemble and a thermal gradient is gradually established inside the model. With the system in steady state, data collection [50, 74] of energy and temperature was performed for at least 4 ns. The thermal flow through thermostats was is calculated from the slope the energy versus time plot [172], while the group temperatures were computed from the averaging the instantaneous local kinetic temperature [50, 74] as reported in Equation 75.

$$T_i = \frac{2}{3N_i k_B} \sum_j \frac{p_j^2}{2m_j} \qquad 75$$

In Equation 75, T_i is the temperature of i^{th} group of atoms, N_i is the number of atoms in I^{th} group, k_B is the Boltzmann's constant, m_j and p_j are atomic mass and momentum of atom j, respectively. The temperature of each slab is computed by a time averaging operation along the simulation time.

Within this method, longer simulation time assures higher accuracy of the temperature calculation. From the plot of the averaged temperature of the slabs, as a function of the coordinate displacement, it is possible to evaluate the thermal jump across the junction. The thermal conductance is then computed through equations 18 or 19 as appropriate for the addressed system. Dealing with molecules, the single chain thermal conductance, G_{chain}, is proposed as a parameter to compare different junctions. In this case, the TBC is expressed in pW K^{-1} and calculated through the Equation 76 as the per molecule formulation of interfacial thermal conductance (Equation 19).

$$G_{chain} = \frac{\dot{q}_x}{n \cdot \Delta T} \qquad 76$$

Here, n is the number of molecules bridging the two adjacent graphene nanoribbons, q_x is the thermal flow derived from the energy versus time plot slope and ΔT is the thermal difference across the jump, as projection of the two linear fit of the temperature-length plot in the junction middle point.

2.3. Thermal equilibration method

Another method to calculate the thermal conductance through MD calculation is the thermal equilibration method, sometimes called pump-probe method [71, 73, 166, 173]. This method works on the reach of thermal equilibrium of two phases across an interface, where an initial temperature difference was set. At the beginning of the simulation, new velocities were attributed in canonical ensemble and an initial equilibration step is performed: the purpose of this equilibration is to relax the designed structure coherently with the force field parameters and attenuate the initial velocities fluctuations. In this stage, the polymer volume run at 300 K and the stacked filler was set at 350 K for 25 ps. The second step is where the heat transfer takes place; with the polymer and the filler running at different temperatures, all the system is set in microcanonical ensemble. In this stage, heat transfer occurs at the interface without energy loss and the temperature of polymer and filler are recorded for 500 ps, when complete convergence is reached. In this transient stage, the temperature variation of each phase is recorded, allowing to measure the magnitude of the exponential decay time (τ) of the temperature difference (ΔT) as reported by Equation 77.

$$\Delta T(t) = \Delta T(0) e^{-\frac{t}{\tau}} \qquad 77$$

By knowing the mass (M_{poly}) and heat capacity of polymer (Cp_{poly}), filler (M_{fill}, Cp_{fill}) respectively, and the interfacial area (A), it is possible to estimate the thermal conductance across the interface (λ), as Equation 78 reports.

$$\Delta T(t) = \Delta T(0) e^{\left[-\left(\frac{1}{M_{poly} Cp_{poly}} + \frac{1}{M_{fill} Cp_{fill}}\right)\right] \lambda A_t} \qquad 78$$

By the thermal equilibration method, the temperatures are still computed through equation 75. Here, however, the sampling interval is dependent from the decay time (τ), a condition that increases the uncertainty if compared to NEMD where it is arbitrary long. For the same reason, the uncertainly rises even when the atoms inside the group is scarce. These conditions combined to the need of external parameters as heat capacity and interfacial area, increases the uncertainly, making this method suitable for few applications niches.

The temperature of the components has been evaluated by averaging six different simulations to reduce the effect of velocity fluctuations during heat transfer, a phenomenon that affects particularly small systems. The normalized difference in decaying temperature (NDT) was calculated from the difference of the averaged temperature across the interface by the equation 79 .

$$NDT = \frac{T_{fill} - T_{poly}}{\Delta T} \qquad 79$$

Where T_{fill} and T_{poly} are the temperatures of the filler and the temperature of the polymer, respectively, and ΔT is the initial temperature difference between T_{fill} and T_{poly}, 50 K in this work.

The heat capacities values adopted in this work are 1.46 J g^{-1} K^{-1} for PDMS [174], 0.71 J g^{-1} K^{-1} for graphene [175] and 1.02 J g^{-1} K^{-1} for borophene [176].

2.4. Calculation of vibrational density of states

Within the acoustical mismatch model is assumed that the presence of boundaries, as interfaces, induces the rise of interfacial thermal resistance. The analysis of the vibrational density of states (VDOS) reports the phonon spectra as a function of the phonon frequency. In this work, the VDOS was performed on interface components, as graphene sheets or molecules selected as thermal linkers.

The VDOS was calculated from the analysis of the atoms velocities in x, y and z coordinates through the discrete Fourier transform of the autocorrelation function as reported in equation 80:

$$D(\omega) = \int_0^{\tau} \langle v(0) \cdot v(t) \rangle e^{-i\omega t} dt \qquad 80$$

where $D(\omega)$ is the VDOS at the frequency ω, $\langle v(0) \cdot v(t) \rangle$ is the correlation function of atoms velocities. The autocorrelation function was computed by Phyton code exploiting Numpy and Scipy libraries.

The information about atom velocities was obtained by a specific MD run with suppressed periodicity and fixed size of the simulation box with about 50Å of padding room. In this calculation, an initial step in canonical ensemble at 300 K for 250 ps allowed structure relaxation coherently with force field parameters and a second step, where velocities data collection was performed, occurred in microcanonical ensemble, by damping the velocities every timestep for 12.5 ps, determining a collection of 50000 states.

2.5. Internal stress calculation

The internal stress calculation in tensile testing was performed trough LAMMPS via compute stress/atom command. This command computes the symmetric per-atom stress tensor for each atom inside an atom group. For each atom, the tensor has six components, stored as a six-element vector as described: xx, yy, zz and the shear xy, xz, yz. The stress tensor S_{ab} for atom *i* is given by the Equation 81,

$$
\begin{aligned}
S_{ab} = -\Bigg[& mv_a v_b \\
& + \frac{1}{2}\sum_{n=1}^{N_p}(r_{1a}F_{1b} + r_{2a}F_{2b}) \\
& + \frac{1}{2}\sum_{n=1}^{N_b}(r_{1a}F_{1b} + r_{2a}F_{2b}) \\
& + \frac{1}{3}\sum_{n=1}^{N_a}(r_{1a}F_{1b} + r_{2a}F_{2b} + r_{3a}F_{3b}) + \frac{1}{4}\sum_{n=1}^{N_d}(r_{1a}F_{1b} \\
& + r_{2a}F_{2b} + r_{3a}F_{3b} + r_{4a}F_{4b}) \\
& + \frac{1}{4}\sum_{n=1}^{N_i}(r_{1a}F_{1b} + r_{2a}F_{2b} + r_{3a}F_{3b} + r_{4a}F_{4b}) \\
& + Kspace(r_{ia}F_{ib})\Bigg]
\end{aligned}
\tag{81}
$$

where a and b assume the coordinates values to generate the six components of the symmetric tensor: the first term is a kinetic energy for atom *i*. The second term is a pairwise energy, where *n* loops over the N_p neighbors of atom *I*, r_1 and r_2 are the positions of the two atoms in the pairwise interaction. F_1 and F_2 are the pairwise forces on the two atoms. The third term is a bond contribution which form is similar to the N_b bonds where *I* belongs. Other similar terms are N_a for the angle, N_d for dihedral, and N_i for improper interactions where atom *I* is involved. There is also a term for the KSpace contribution from long-range Coulombic interactions. The per-atom array values will be in pressure*volume units [177, 178], the molecular volume considered for the calculation of the tensile modulus was approximated as half of the volume among the edges interface of the specimen (in x,y,z of about d*5*3.4 $Å^3$), where *d* is the platelets distance. Due to this approximation, the results presented herein should be considered more in relative terms between the molecules than as absolute values.

The Elastic modulus was calculated through linear fitting from 0 to 10% of deformation in elastic regime. Uniaxial strain simulations were conducted for six replicas along z at 0.1K, similarly to the method previously applied to metal nanowires [179, 180], to minimize the velocity fluctuation noise in stress tensors calculation. A specific model was made out of two small graphene ribbons (about

80x10 $Å^2$) with a single junction has been designed for every molecule (as example, C5OP in shown in Figure 42). The simulation box PBC were set as fixed in x and periodic in y and z, adopting a 50 Å padding room as already adopted in VDOS calculation. An initial relaxation step in NVT was set bringing the temperature from 5 K to 0.1K inside a 5 ps interval. Then, the left slab of the specimen was fixed and a longitudinal uniaxial velocity of 0.5 Å ps^{-1} was applied to the right-end graphene ribbon generating a constant pulling force overall the system. The simulation run in NVE for 20ps or until the molecule broke, whichever occurred first. The accuracy of this method was proven by changing the velocity seed, where the tensile modulus exhibited a variation smaller than one percent.

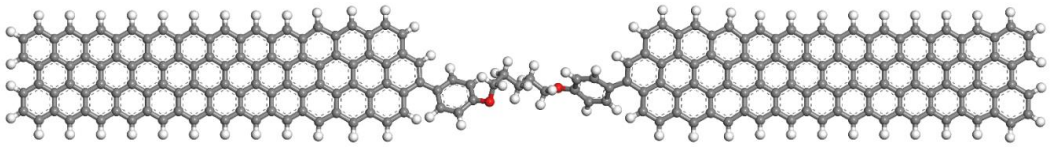

Figure 42. Model for tensile simulation with C5OP molecule in between.

2.6. Polymer modelling and relaxation

PDMS modelling started by the design of a 49 monomer single chain, Si-methyl terminated, for a sum of 507 atoms and a mass of about 3722u (Figure 43). All bonds were described using COMPASS force field.

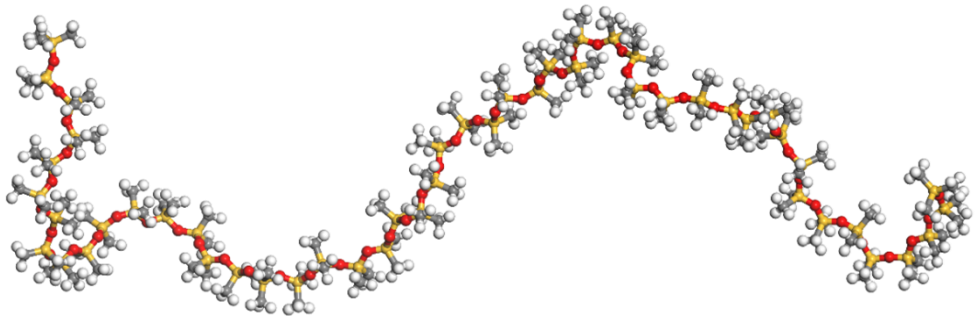

Figure 43. Representation of a PDMS single chain. Color codes: carbon in grey, hydrogen in white, oxygen in red and silicon in yellow.

To define a significant polymer mass to interact with molecular junctions joint platelets, PDMS molecules were packed in larger simulation box (Figure 44), with PBC set in all coordinates. This system was made of 15 PDMS chains (7605 atoms) made by a modified Markov process[4] inside a cubic volume of about 46Å by side. The final density of the polymer volume was set to 0.97 (±0.05) g cm^{-3}, to fit the typical values reported in the previous literature[174].

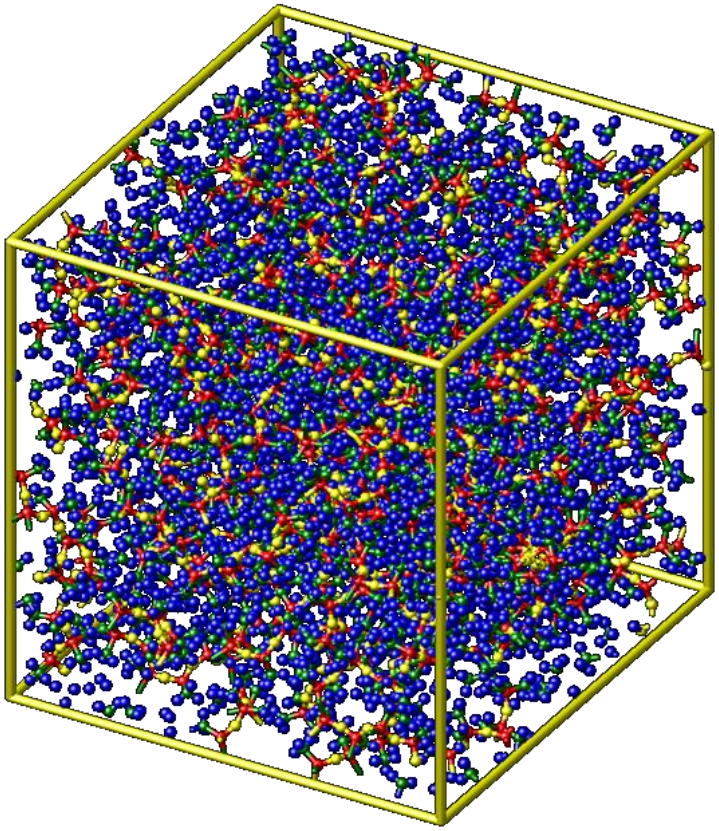

Figure 44. PDMS model from the actual LAMMPS *dump image* command. Color codes: yellow for oxygen, green for carbon, blue for hydrogen and red for silicon. The yellow cage represents the simulation box with periodicity in all coordinates.

Thermodynamic stability revealed to be a major issue in large polymer domains because the system "as designed" exhibited a continuous rise in the internal energy, reflecting a continuous temperature rise in microcanonical ensemble. This phenomenon was due to the rise of contributions from pairs, bond and angles bringing the simulation to unphysical results. To overcome this issue, several thermodynamic cycles were attempted to get stability. A typical thermodynamic cycle is reported in Figure 45.

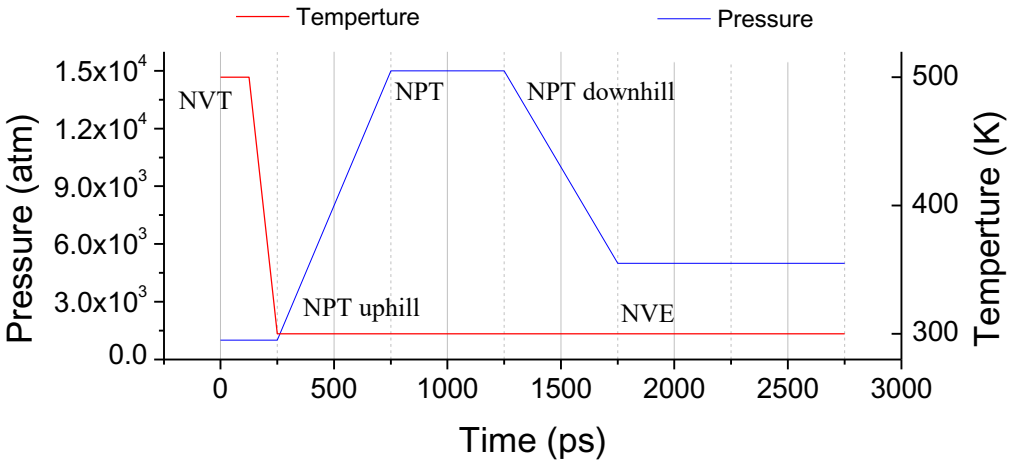

Figure 45. PDMS relaxation cycle, temperature and pressure evolution across different statistical ensembles.

The cycle started at 500 K in canonical ensemble for 125 ps with the purpose to make the velocities of the atoms stable and to reduce the polymer entanglements, thanks to the relatively higher temperature that increased polymer mobility and allowed conformational rearrangement. In a second 125 ps step, the temperature was progressively reduced to 300 K and followed a pressure ramp in NPT up to 15 K atmospheres for 500 ps. Such pressure was then maintained constant for 500 ps. After this stage, the pressure was reduced to about 5 K atmospheres to reach final density of the polymer of 0.97 (±0.05) g cm^{-3}. The last step was the evaluation of energies in microcanonical ensemble, where the energy contributions from pairs, bond and angles was expected to remain stable for at least 1 ns. Within this cycle, the Lennard-Jones cut-off was set to 10 Å, while Coulomb interaction was neglected.

2.7. FEM composite modelling for heat transport

The finite element analysis has been performed on Abaqus Standard 6.14. To model the composite material, a representative volume element (RVE) was chosen. All the RVE of the composite materials were generated through combined C++ and Python scripts, written by the co-supervisor of this Ph.D. thesis, Dr. Bohayra Mortazavi [162]. In this RVE model, which sample is depicted in Figure 46, the filler was modelled as flat disks dispersed randomly inside a polymer matrix. The aim of the random orientation of the disks in the RVE is to reproduce a status closer to those in experimentally made composites. In this model, the geometry of the filler is taken into account by the use of the aspect ratio of the disks, defined as the diameter to thickness ratio of the plate. Within this RVE, no particle-particle contact is allowed and neither disk bending. Moreover, the filler concentration and the number of perfect disks can be tuned inside the RVE, satisfying periodicity criterions to render as best the bulk composite. The periodicity of the RVE is however a virtual property which resemble the PBC in MD simulations (paragraph 1.2.1). In this hypothesis, by placing the RVE and a neighbor RVE together, no discontinuity in filler and particles can be observed, despite no actual PBC is applied in FEM simulations.

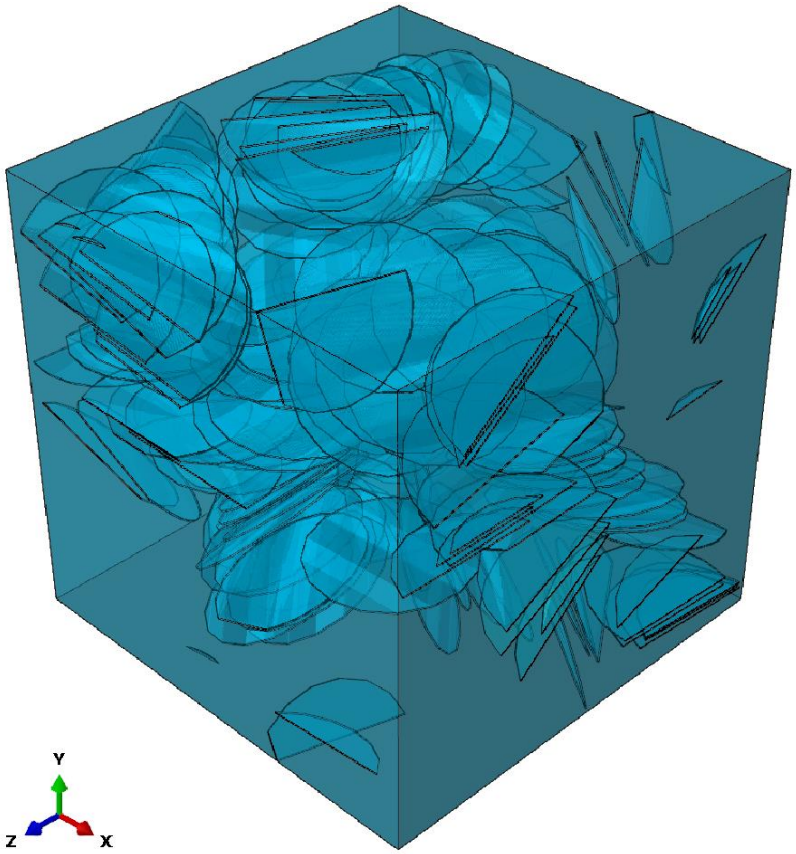

Figure 46. Example of composite RVE for FEM analysis: in this RVE the filler is represented by 150 flat disks of aspect ratio 1:100 in a 4% of volume concentration.

In this FEM analysis, the thermal conductivity of matrix and filler adopted literature values while the interfacial thermal conductance was found through MD calculations by thermal equilibration method (paragraph 2.3). The length of the RVE cubic side varied from about 200 to 500 nm and despite the differences, the same size mesh (3 nm) was adopted for all RVE. The mesh elements were heat transfer elements (DC3D4) with 4-node linear tetrahedron shape (Figure 47).

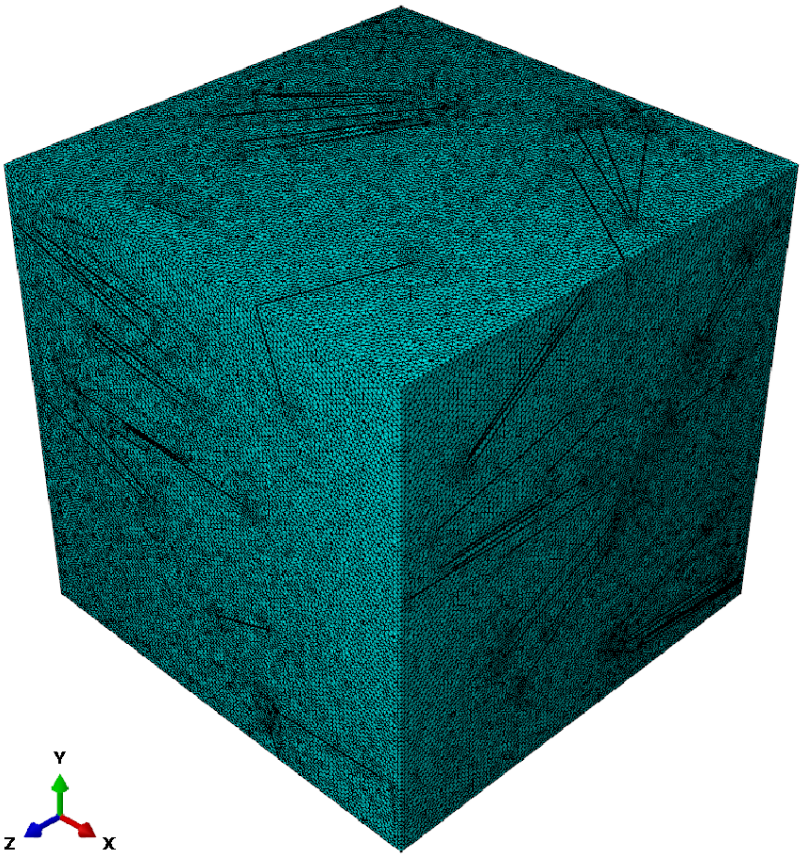

Figure 47. The 4-nodes linear tetrahedron shape mesh for the RVE depicted in Figure 46.

For the evaluation of the thermal conductivity, steady heat flux was imposed to the opposite surfaces. Within this layout, the heat flux passes through the meshed RVE, determining the rise of a temperature gradient (dT/dx) inside the volume. The effective thermal conductivity was then calculated by the application of the one-dimensional Fourier's law (Equation 4)

Chapter 3

Non-covalent molecular junctions

Computational modelling suggested covalent bonding to be more effective than secondary interactions to drive phonons at the interfaces [99], however, covalent crosslinking of graphene remains experimentally hard to achieve. It is therefore appropriate to consider non-covalent functionalization as a possible way to modify the thermal boundary resistance in graphene networks. Non-covalent crosslinking of graphene flakes may be obtained in different ways. As a first option, bi-functional molecules able to bridge two adjacent graphene sheets by non-covalent interaction of its terminal groups with graphene surfaces may be exploited. This could be in principle obtained via π-stacking with polyaromatic molecules as bis-pyrene, bis-perylene or bis-anthracene, as previously explored by Li and coworkers [99].

Alternatively, covalently grafted organic chains may be used to drive self-assembly of graphene flakes, based on the supramolecular interaction of the grafted molecules. While both approaches currently remain experimentally challenging, the second route has the advantage of being (at least theoretically) controllable in terms of location of organic function on graphene. Indeed, a higher reactivity of graphene edges has been reported [89], allowing in principle to preferentially locate chemical functionalization on the graphene edges, rather than on graphene surface. This approach also fulfils the need to preserve the sp^2 graphene structure, avoiding damaging the graphene lattice and thus preventing a fall in its thermal conductivity. The following chapter describes the attempts to exploit enhancements of thermal boundary conductance in graphene flakes edges by functionalization of pending molecules.

3.1. van der Waals Forces

The first case study is limited to the analysis of the thermal transport across van der Waals interdigitated junctions. To investigate the VdW interactions contribution in thermal transport, the 2nd generation of the AIREBO force field (paragraph 1.3) was employed in NEMD layout, as described in paragraph 2.2.

In the study of VdW interactions, a pending pentyl molecule was chosen. The equilibrium distances between the nanoflakes was stepwise increased at 9.8, 10.6, 11.5, 12.4 and 13.0 Å, directly reflecting a decrease in the interdigitation depth between chains as Figure 48, from A to E depicts.

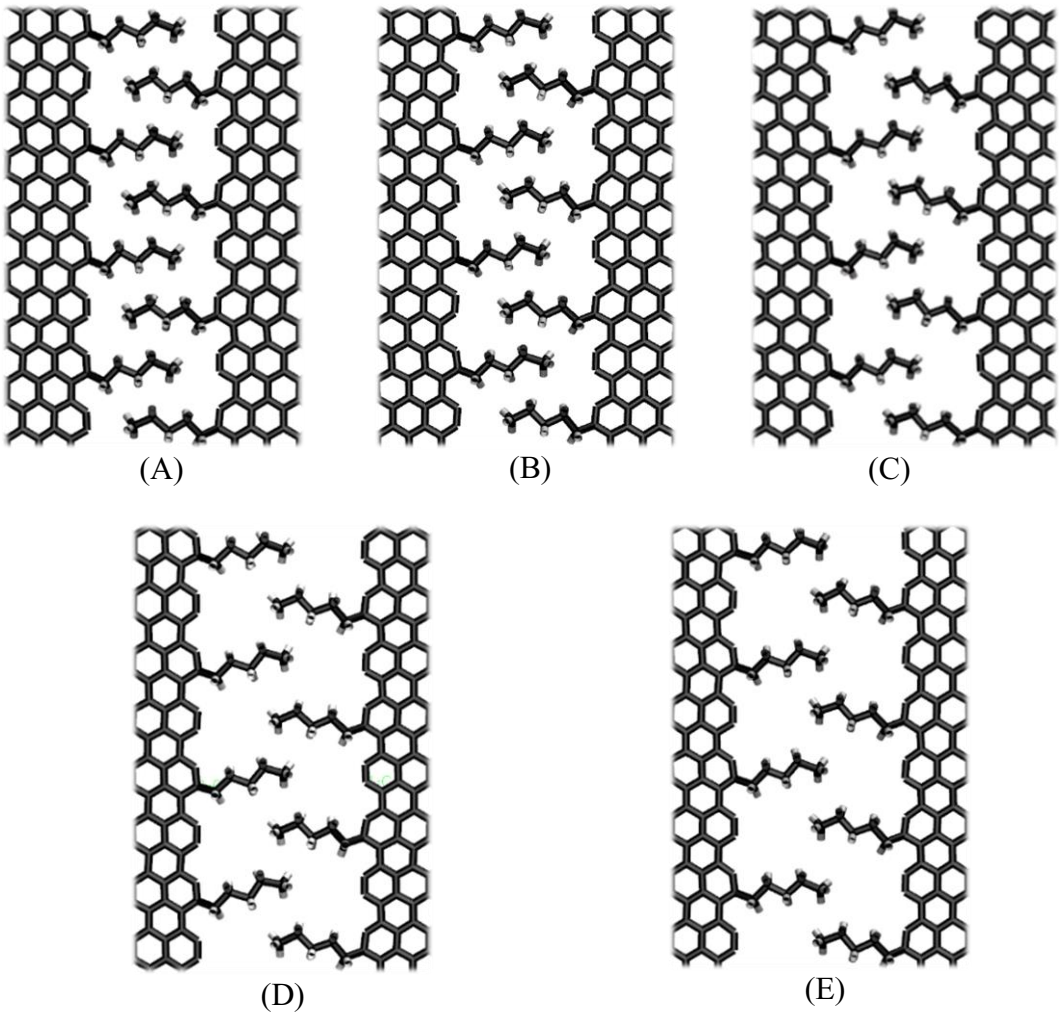

Figure 48. Interface detail of interdigitated models (A) 9.8 Å, (B) 10.6 Å, (C) 11.5 Å, (D) 12.4 Å and (E) 13.0 Å.

NEMD calculations were performed by the application of Nosé-Hoover thermostats at the two ends of the simulation box, which coincides with the graphene sheets ends. The thermostats regions were set to 290 K for the cold bath and 310 K for the hot one. All the simulations were carried out for 5 ns after an initial 500ps of equilibrium heating at 300 K and a second 500 ps stage of transient non-equilibrium heating with the purpose to reach a constant heat flux (as described NEMD method described in paragraph 2.2). A relatively small 0.25 fs timestep was set to manage the high frequency of hydrogen vibrational modes.
The thermal flow inside NVE regions is derived from the slope of energy versus time plots [50]. All the slabs temperatures were then time-averaged, with the exclusion of the non-linear regions at the nanoribbon boundaries, i.e. the ones close to the thermostats and the ones coupled to the junction. Finally, the thermal conductance was evaluated trough Equation 76, as described in methods.

Table 3 summarize the obtained results for the averaged platelets distances during the simulation. The same data were employed in Figure 49, which depicts the single chain conductance as a function of the platelets distance, where the linear fitting curve highlights a linear decay of the thermal conductance. Such decaying

trend clearly reflects on the extent of interaction volume between interdigitated molecules of the two platelets.

Table 3. Platelets distance and molecular thermal conductance for interdigitated pending pentyl chain.

Platelets distance (Å)	**Molecular thermal conductance (pW K^{-1})**
9.80	131 ± 13
10.60	93 ± 9
11.52	70 ± 7
12.40	36 ± 4
13.00	25 ± 3

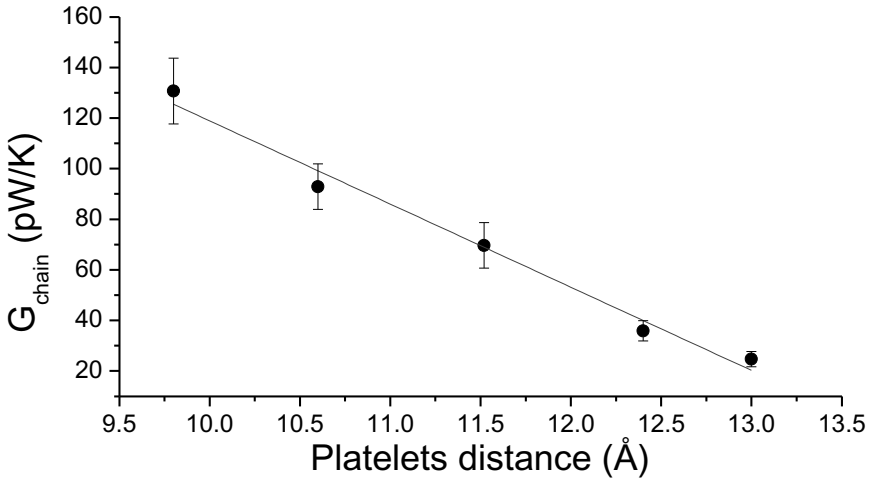

Figure 49. Single chain thermal conductance of interdigitate models as a function of platelets distance.

For the sake of comparison, from the values of molecular thermal conductance obtained above, the equivalent overlapped surface of graphene was calculated. To investigate this relation, a set of partially overlapped graphene nanoribbons were simulated (with same dimensions to previous ones, about 100 Å in length x 50 Å in width, Figure 50). In this model, the overlapped graphene exploited the same distance (3.40 Å) and offset to the actual graphite in crystal lattice stacking. The overlapped area was tuned from one-half, to one-third and one-quarter of the nanoribbons surface, corresponding to 4395 $Å^2$, 2973 $Å^2$ and 2198 $Å^2$, respectively. The thermal boundary conductance for these overlapped areas, calculated from equation 19, was found 1681, 1024 and 907 pW K^{-1}, respectively, and yield to an average thermal boundary conductivity G_c, calculated from equation 18, of about 0.38 ± 0.04 pW Å^{-}

^{2} K^{-1}. From this evaluation, the same value of thermal conductance was calculated for the of the closest chain, lying at 9.8 Å with a 131 pW K^{-1} of TBC and a corresponding contact area of 345 ± 34 $Å^2$, from the overlap of 131±13 atoms per layer, (assuming the atomic density value of 0.38 atoms $Å^{-2}$ [181]). Such comparison provides a brief estimation of correspondence between TBC through simple graphene overlapping and trough covalent crosslinking.

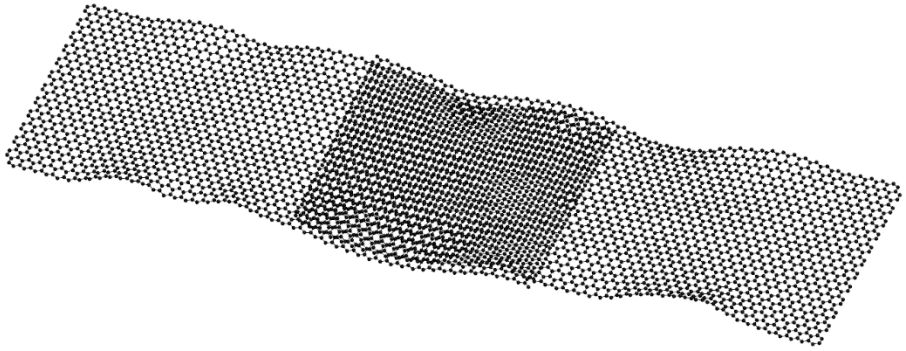

Figure 50. A one third partial overlapped nanoribbons, corresponding to a contact area of 2973 $Å^2$ in VMD[182] orthographic view.

This first study illustrated how interdigitated molecules, as can be produced by incomplete functionalization, are effective to enhance thermal transport in edge functionalized graphene platelets. However, as the edge grafting of alkyl chains currently appears experimentally unviable, more realistic rafted functionalization will be addressed in the following section.

3.2. Hydroxyl – hydroxyl interaction

To investigate the thermal transport of chemically feasible linkers that exploits non covalent bonding, pending phenols were modeled analogously to the edge functionalization with substituted aromatic molecules via aryl diazonium chemistry reported from Sun and coworkers [89].

The reaction of 4-aminophenol on graphene was investigated as a possible candidate to deliver edge functions able to self-assembly and build non-covalent molecular junctions for enhanced heat transport. Figure 51 depicts the edge functionalization of 4-aminophenol by initial solution of the constituents in N,N-dimethylformamide (DMF) and further processing steps, as described in Bernal *et al.*[183].

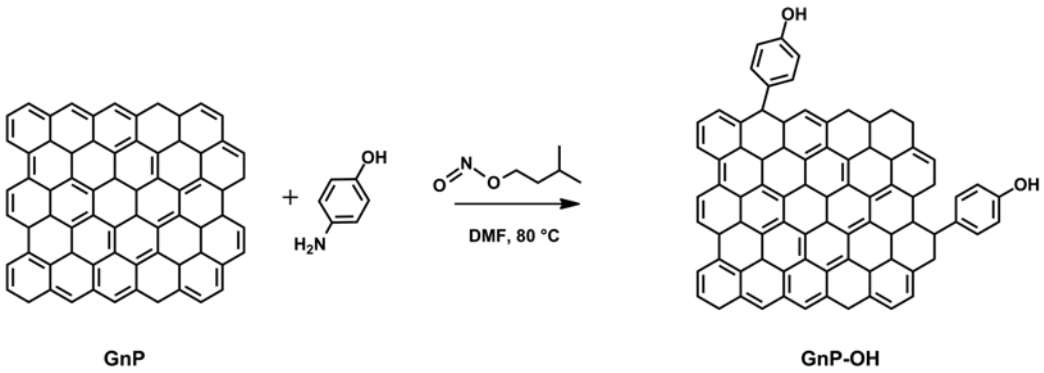

Figure 51. Edge selective functionalization with 4-aminophenol, from Bernal *et al.*[183].

The NEMD modeling followed the scheme depicted in Figure 38 where the model topology was similar to the one adopted for alkyl chains, composed by two ≈100Å graphene nanoribbons in zigzag configuration. The width (Y-axis) was set to ≈50 Å, while the total length of simulation box (X-axis) was about 200 Å. This simulation employed the COMPASS force field (paragraph 1.3) with 10 Å cutoff in Lennard-Jones and Coulomb interactions. Partial charges were set by QEq equilibration. The pending phenols were free to align with the platelets distance as the only constraint (Figure 52).

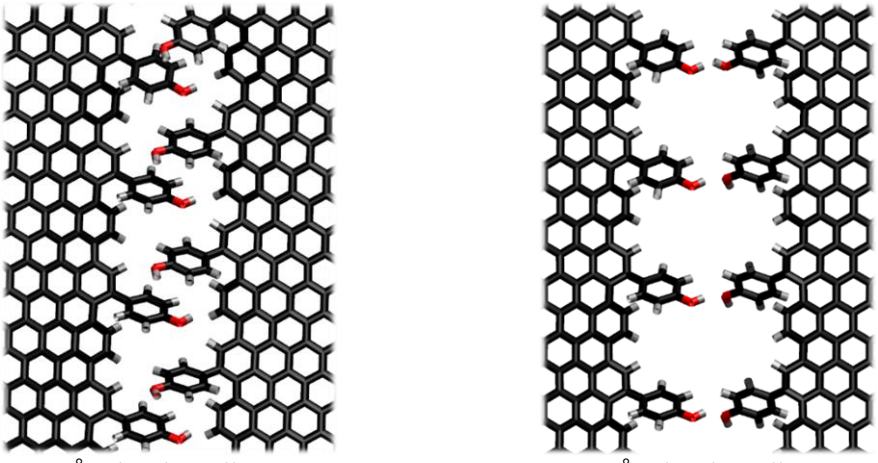

9.8 Å platelets distance 12.8 Å platelets distance

Figure 52. VMD graphical representation of phenol models. (A) Slight overlapping of the pendant phenols as observed usually up to about 10.5 Å of platelets distance and (B) OH alignment observed above 10.5 Å.

The interaction of phenol groups is obviously expected to be a function of the relative distance. In fact, the distance between two functional groups was fine-tuned to pursue the effect on the thermal conductance of the junction. For all the spatial measurements, VMD software was adopted. For clearness, the term *single direct measure* (SDM) indicates the time averaged measure of the atomic distance along all the simulation states at the equilibrium value. To evaluate the platelets distance

(Figure 53), six SDM were done in different locations, discarding the maximum and the minimum values to reduce the error from planarity and parallax.

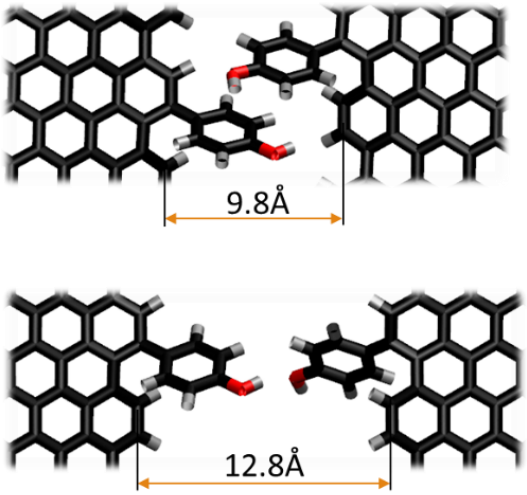

Figure 53. Detail of graphene functionalized by pending phenol. The quote reports platelets distance.

A deeper investigation was performed on the hydroxyl moiety of the phenols. In this case, for all the six couples of the atoms in OH group were measured and averaged to collect data. The measurements of the OH distance involved all the six phenols couples of OH groups (O left - H right; H left - O right; O-O; H-H), as reported in Figure 54, determining 24 SDM for every simulation.

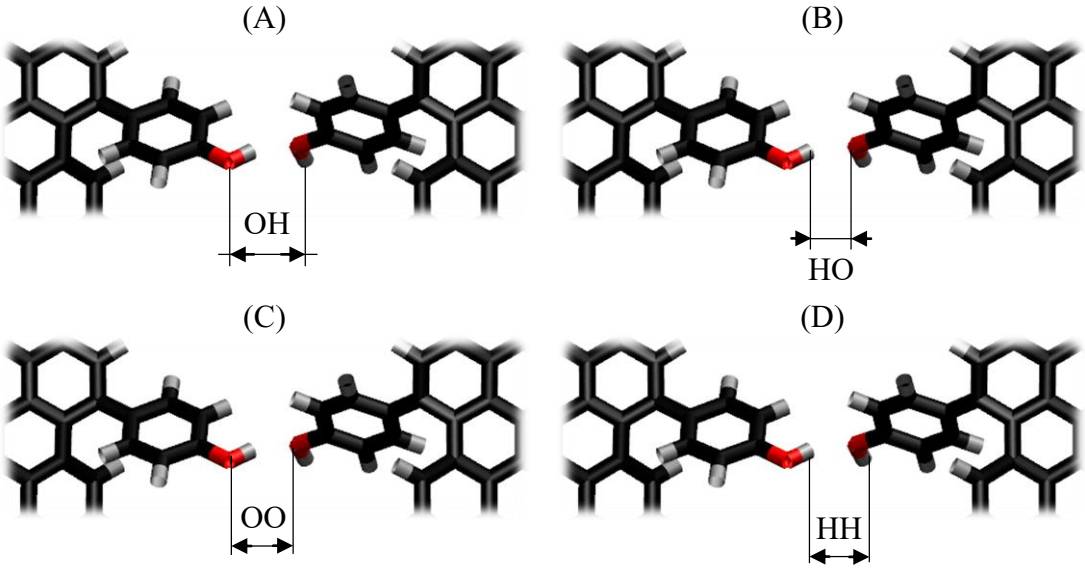

Figure 54. OH, HO, OO and HH distances evaluated in pending phenols analysis.

The thermal conductance as a function of the platelets distance was reported in Figure 55A. Below 9 Å, the thermal conductance exhibits relatively high values (about 18 pW K^{-1}). This phenomenon was attributed to partial $\pi - \pi$ stacking of phenol ring as depicted in Figure 52(A) whilst, increasing the platelets distance up to

the 10.5 Å plateau, the thermal conductance almost halves. Above this plateau region, thermal conductance slightly increases up to a broad peak region close to 12.5 Å. This relatively high thermal conductance region (about 20 pW K^{-1}) was attributed to the O-H interaction of the pending phenol groups at the interface as shown in Figure 52B. A further increase of the platelets distance determines a rapid decay in thermal conductance bringing thermal conductance to about 1 pW K^{-1}.

Figure 55B represents the OH distance as a function of the platelets boundary. Initial outlier values, below 9 Å, can be attributed to misalignment due to partial π – π overlap ad described previously. Above 9 Å the OH distance exhibits a minima in the 12 -13 Å range whereas a steep growth was found above 13 Å due to the system geometry that forces remotely the OH phenols. From the values calculated in this work, the thermal conductance as a function of the platelets distance (Figure 56) is not a linear phenomenon, however, as expected, the conductance exhibited a general declining trend while increasing the OH distance.

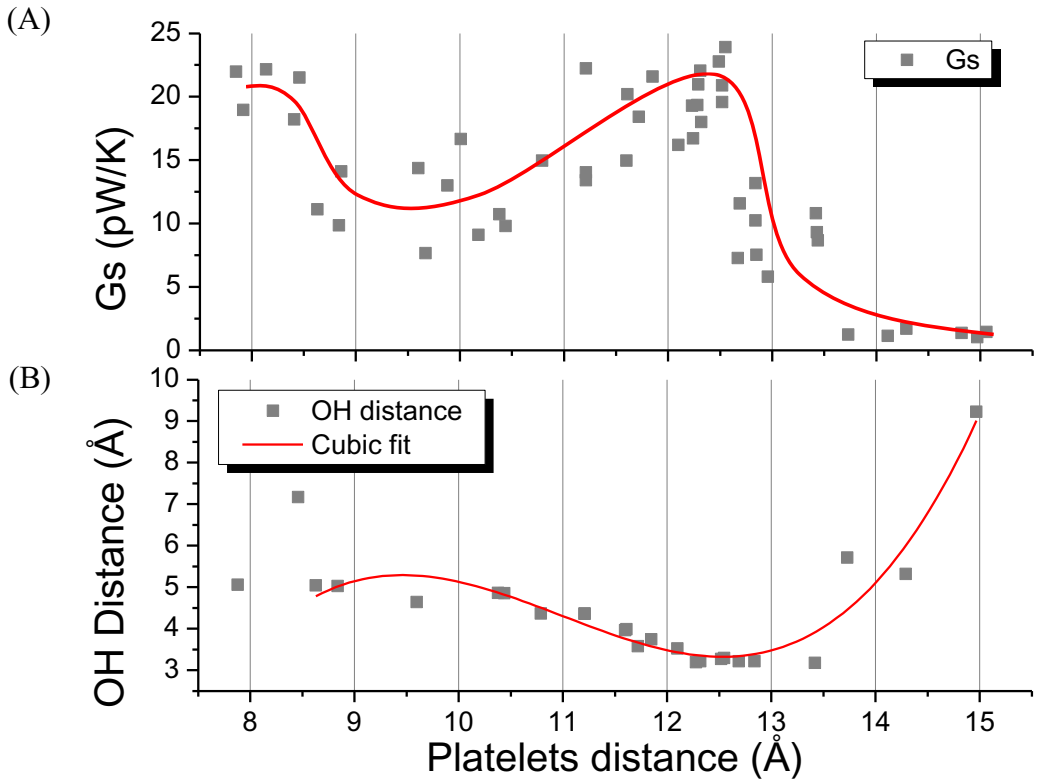

Figure 55. (A) Thermal conductance (Gs) as a function of the platelets distance in the range from 7.8 to 15.3 Å. A hand-drawn red line drives the eye through data. (B) OH distance as a function of the distance between nanoribbons, red line represent the cubic fit of data.

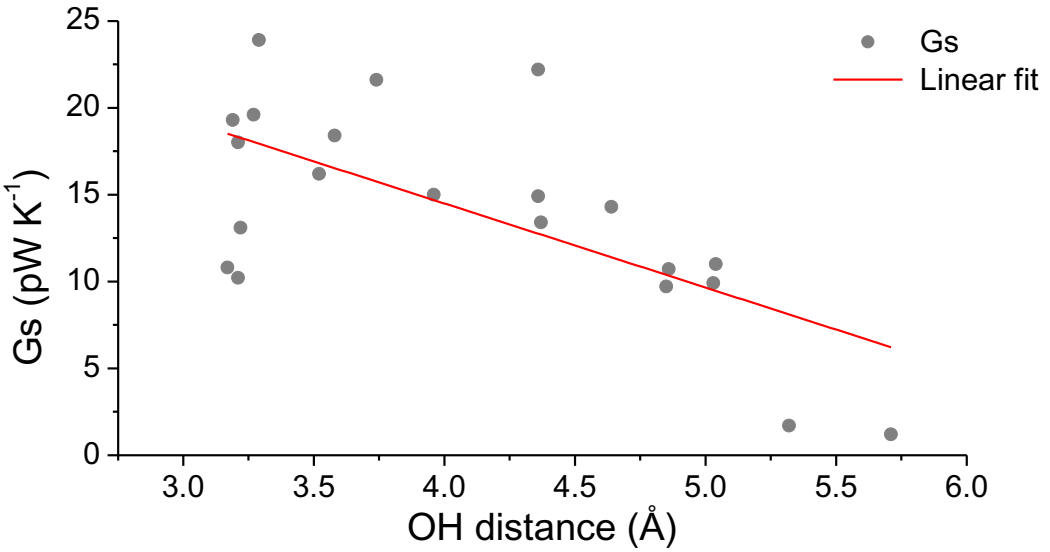

Figure 56. Thermal conductance (Gs) as a function of the measured OH distance among phenol groups. Red line represents a linear fit of data.

Figure 57 reports the distance of flakes, OH, OO, and HH groups (depicted in Figure 54) grouped for simulations within shortest platelets distances (below 10.5 Å). Such data displacement was find helpful to highlight the distance between the OH, OO and HH atomic couples. The observation of the coupled atom distances evidenced an unclear orientation when platelets distance is below 10 Å. In this case, below 8.5 Å, the attraction among oxygen groups, which reports a lower distance, seems to be the stronger force while an almost parallel overlap is reported for simulation with distances ranging from 8.5 to 10 Å. Above 10 Å the hydrogen atoms seems to drive the interaction between the pending phenols, as widely reported in Figure 58.

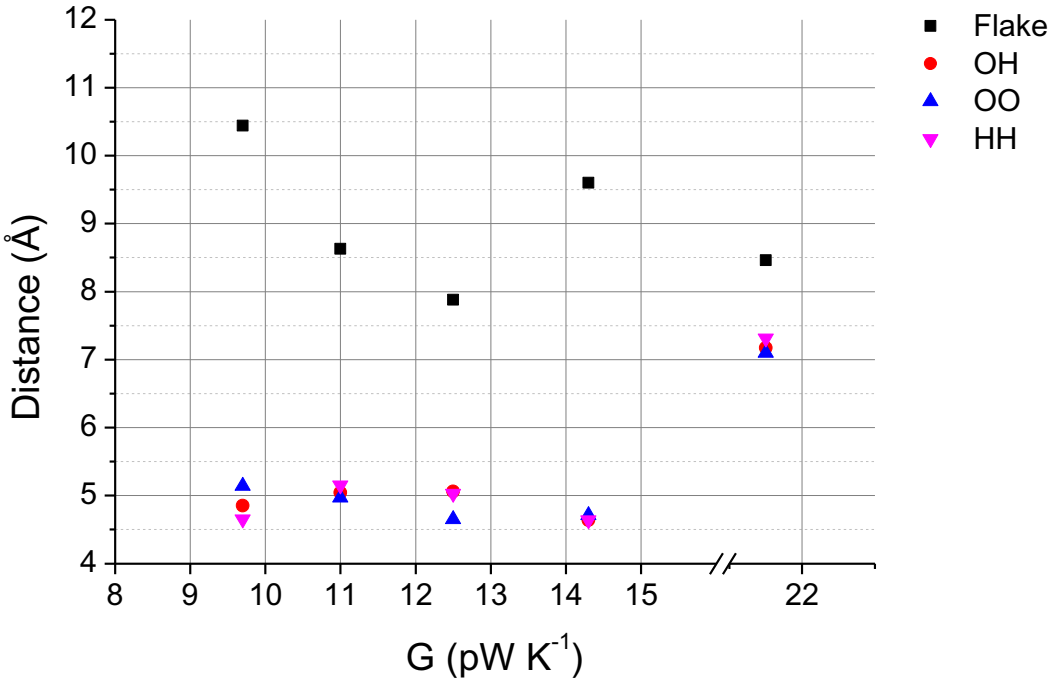

Figure 57. Distance of the flakes, OH, OO and HH for simulations with flake distance below 10.5 Å. The distances in OH, OO and HH groups does not follow any order, indicating a random displacement of hydroxyl groups in the junction.

When the distance between the platelets is increased above 10.5 Å, the measurements, plotted in Figure 58, always report a lower distance than OH/HO end even less than OO ones. This trend evidences the attraction between the hydrogen atoms of hydroxyl moiety. Such finding can prove that thermal transport is driven by a different interaction (O-H interaction) than in overlapped moieties where $\pi - \pi$ stacking occurs. Despite this finding, no further relation was evidenced between each thermal conductance value and the amplitude of the distance between the OH, OO and HH atomic couples.

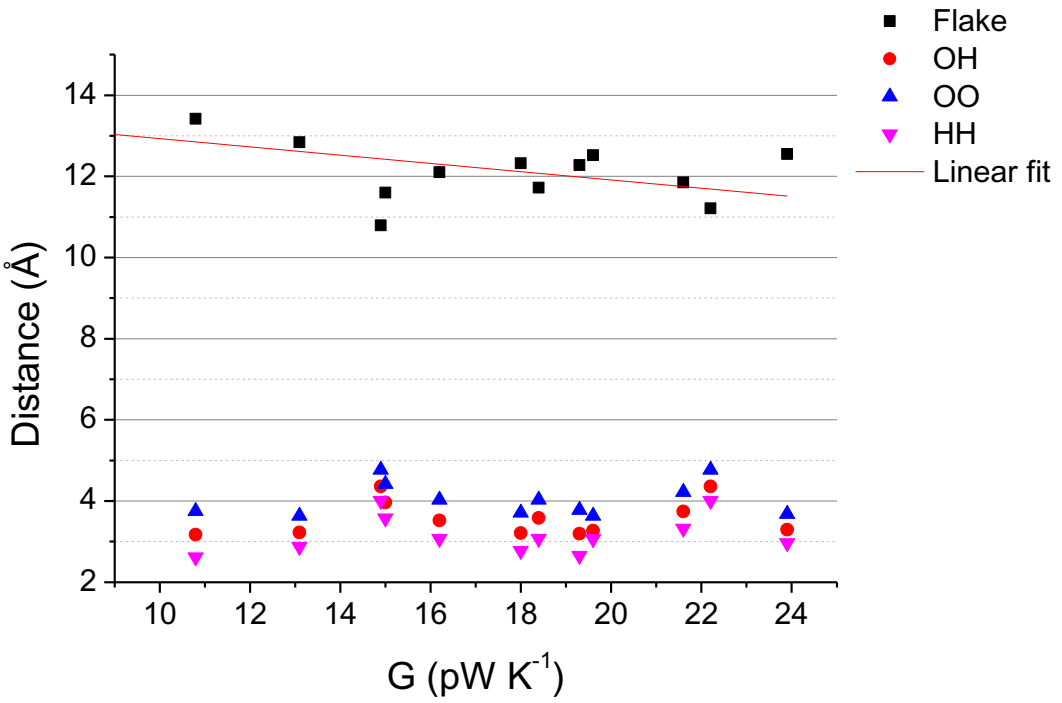

Figure 58. Distance of the flakes, OH; OO and HH for simulation with flake distance above 10 Å. HH atoms closer than OH and even OO indicates that hydroxyl groups orientation is constant, with phenol tips protruding to the junction center.

3.3. Conclusions

The thermal conductance of pending moieties as candidates for graphene functionalization in thermal transport was investigated trough NEMD simulations. The interdigitation depth in pending pentyl chains, which is strictly related to the contact tightness among them, drove thermal transport with a linear proportionality in TBC. The interdigitated functionalization demonstrated as a possible way to improve thermal conductance among nanoplatelets. Such observation was confirmed by the comparison of such values (up to 131 pW K^{-1}) with the corresponding overlapped area in graphene platelets, where the deeper penetration of a couple of the chains corresponded to about 344 $Å^2$ in the same scenario. Despite the encouraging values reported, the possibility to exploit alkyl chains as linkers is experimentally challenging and far from an actual application. A deeper investigation was performed on phenols, based on the experimental evidences of possible edge grafting onto graphene nanoplatelets [89]. The use of pending phenols as thermal bridges suggested overall lower thermal conductances (limited to a maximum of about 24 pW K^{-1}) than for alkyl chains. The difference is mainly attributed to the lower contact area between phenols, compared to interdigitated alkyl chains, despite a direct comparison of conductance values obtained with different force field is not obvious and differences may also be partly related to force fields artifacts. A deeper insight of the interaction between phenols evidenced two different interactions, the first occurring when platelets were closer and a partial overlap of the molecules occurred. In this case, thermal transport was attributed to the aromatic ring

interaction. A second interaction occurred for longer distances of the platelets, related to the coupled hydroxyl moiety interaction in head-head configuration. The sum of these contributions determined a non-linear behavior for thermal conductance as a function of the imposed distance, where two peaks were found.

Chapter 4

Covalent molecular junctions

Molecular junctions joint by covalent bonding are expected to be a more efficient media to drive phonons than pending molecules. In this chapter, several molecular structures are evaluated as possible thermal junction between graphene sheets. The first study presented herein, represent a preliminary work with the purpose to identify the parameters that contributes more in thermal transport. For this purpose, different molecules based on aliphatic chains were analyzed. A second work followed with the aim to identify the best chemical species suitable to act as a molecular linker. In this second case, the focus was kept on the chemical feasibility of the functionalization.

4.1. Aliphatic molecular junctions

As a first case, NEMD simulation for the calculation of thermal conductance were carried for alkyl molecular junctions, as function of the chain length as well as the grafting density onto the graphene edges. The same layout and parameters adopted for pending pentyl (described in paragraph 3.1) however, covalent bonding on both nanoribbons was exploited. The first parameter evaluated was the length of the alkyl chains between the two graphene sheets, as depicted in Figure 59 from A to B.

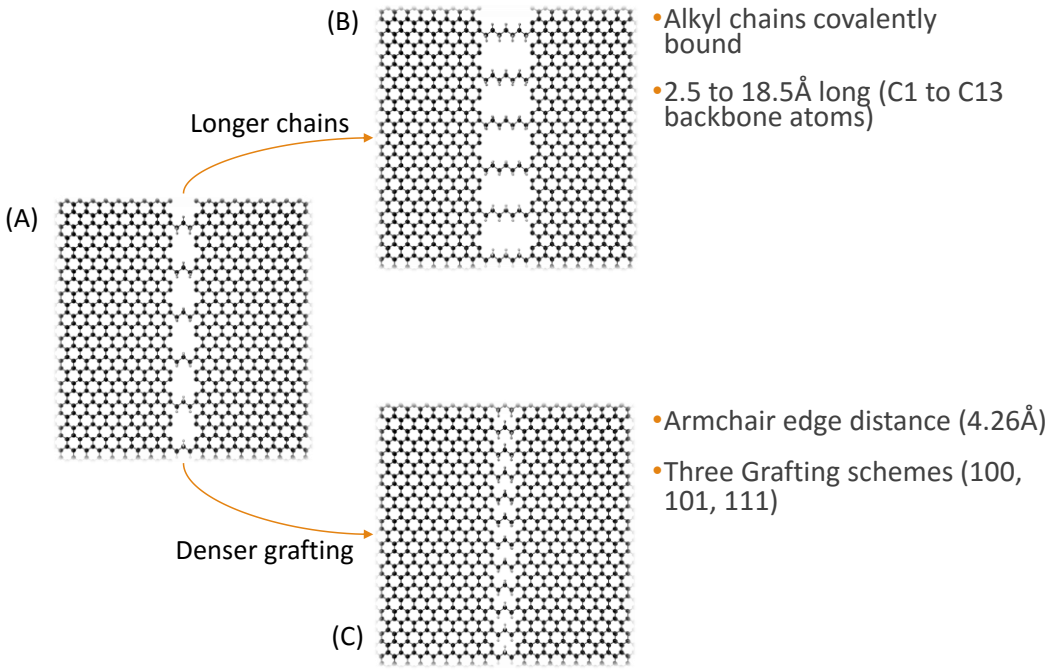

Figure 59. Molecular junction details across graphene platelets. (A) The top view of 101 C3 model shows the C3 chain length in alternate configuration between chains and empty sites. (B) The same grafting scheme for the longer C5 chain length and (C) shows denser grafting scheme 111 is for the C3 chain length. VMD [182] software is used for all graphical representations.

Five different backbones chain length were tested (in brackets the short name and the molecule length): methyl (C1; 2.46 Å), propyl (C3; 4.97 Å), pentyl (C5; 7.49 Å), eptyl (C7; 10.00 Å) and tridecyl (C13, 18.53 Å), with a constant grafting density, defined as the number of chains per unit length of graphene armchair edges. The grafting density is the second parameter considered, while keeping constant the length of the covalently bound chains. The maximum grafting density in this work was defined as one chain per aromatic ring along the armchair graphene edge (4.26 Å vertical spacing distance), referred to as 111. Lower grafting densities were defined as one chain every two aromatic rings (referred to as 101) and one chain every three aromatic ring, referred to as 100, as were defined as depicted in Figure 59.

The Energy added to hot reservoir and removed from the cold reservoir versus time was found linear and symmetric, with slopes dependent on chain length (Figure 60) and grafting density (Figure 61). These observations evidence that the total energy inside the ensemble is kept constant and a constant heat flux passes through the model. Figure 60 reports all the plots obtained with the maximum grafting density. Quantitatively, the slopes varied from 0.19 eV ps^{-1} for the longer C13 chain to 0.40 eV ps^{-1} for the shortest C1 chain. However, dependency of the slope with the chain length is not linear, as the slope is almost constant for C5 chains and longer ones. The energy flux flowing through reservoirs was found proportional to the grafting density, where denser grafting reflected higher slopes as depicted in Figure 61. The heat flux, q_x, defined as the energy transferred from the atoms inside the hot reservoir to those inside the cold reservoir at each timestep, was calculated from these curves. All the slopes are reported in Figure 62.

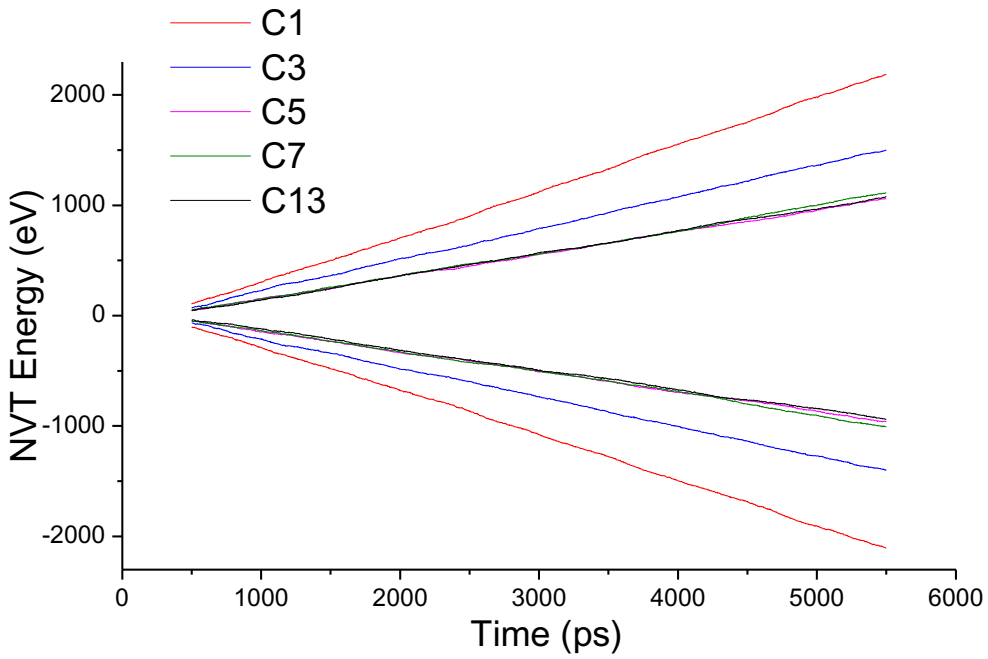

Figure 60. Energy added to hot reservoir (positive slope) and removed from the cold reservoir (negative slope) for all the chains in 111 grafting scheme.

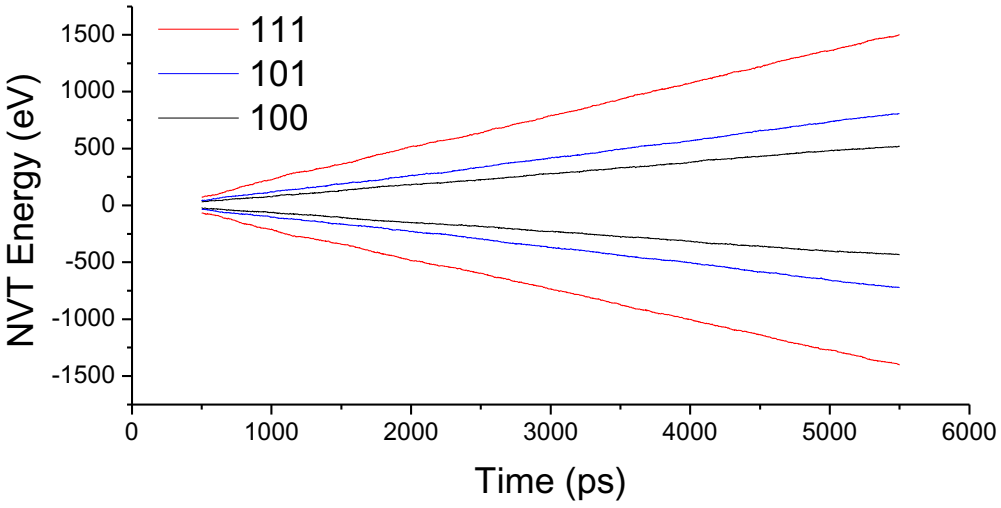

Figure 61. Energy added to hot reservoir (positive slope) and removed from the cold reservoir (negative slope) for a C3 junction in 100, 101 and 111 grafting schemes.

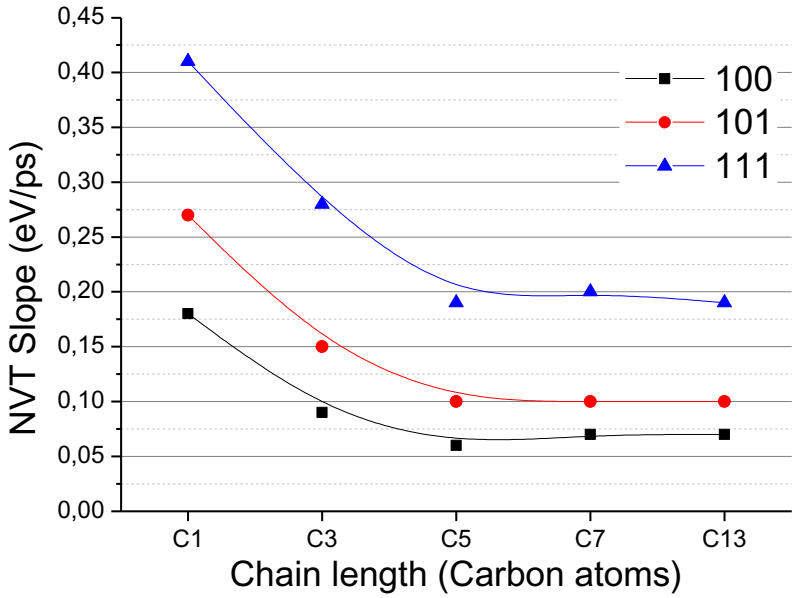

Figure 62. Energy versus time plot slopes for 300 K simulation set. All the three grafting schemes are represented. Lines drives the eye over values.

The temperature profile along the graphene nanoribbons is reported in Figure 63 for all the molecular linkers in 111 grafting schemes.

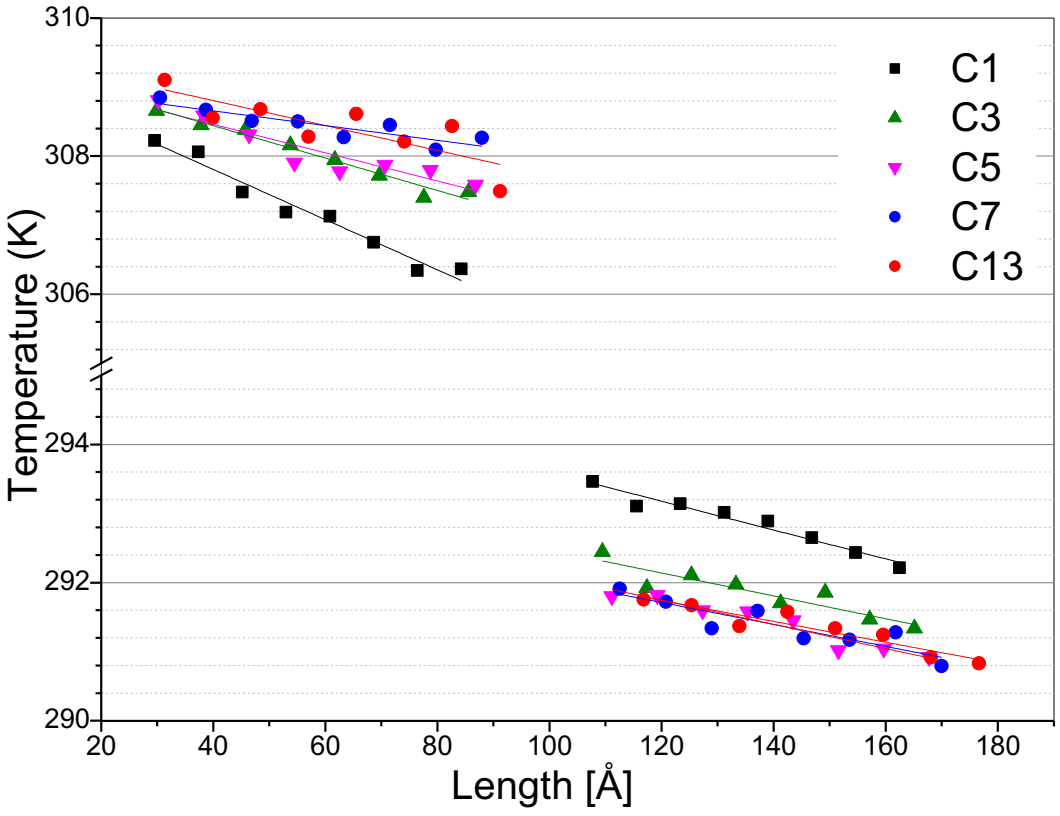

Figure 63. Temperature profile for all the molecular junctions in 111 grafting scheme.

Despite a non-perfect convergence to the thermostats value due to the exclusion of the boundary regions which classically shows non-linearity close to the thermostats [74], linear fitting of the temperatures along the graphene sheets allow to extrapolate the temperature jump across the interface, which is a function of the length of the bridging chain. As expected, shorter chain bonding exhibits a lower thermal jump between the graphene sheets compared to the longer ones (Figure 64) reflecting a better thermal exchange through the junction, *i.e.* a higher TBC, accordingly with equation 19. Similar temperature plots are obtained for all of the chain length explored and the three different grafting schemes. Temperature jump dependency on grafting density is in qualitative agreement with previous report form Liu *et al.* [75] for partially overlapped nanoribbons.

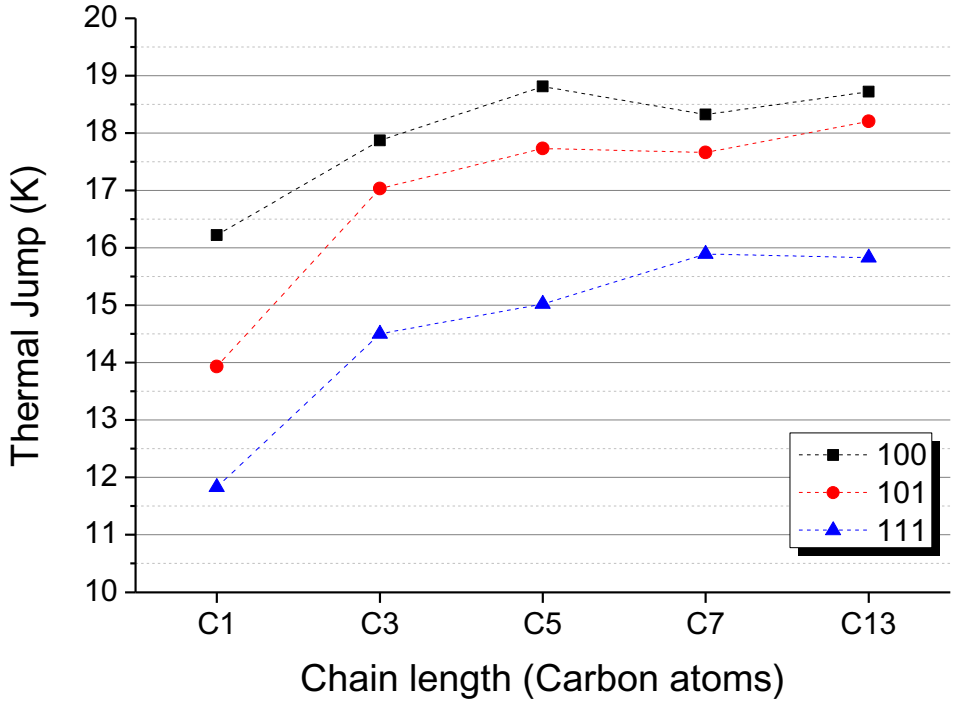

Figure 64. Thermal jumps as a function of chain length for 300 K simulation set. All the three grafting schemes are represented. Lines drives the eye over values.

The thermal boundary conductance was calculated from equation 19 and the plot of the values is reported in Figure 65. The TBC rapidly decreased with increasing length up to C5 chain, whereas TBC for longer chains appears to level off reaching a plateau region.

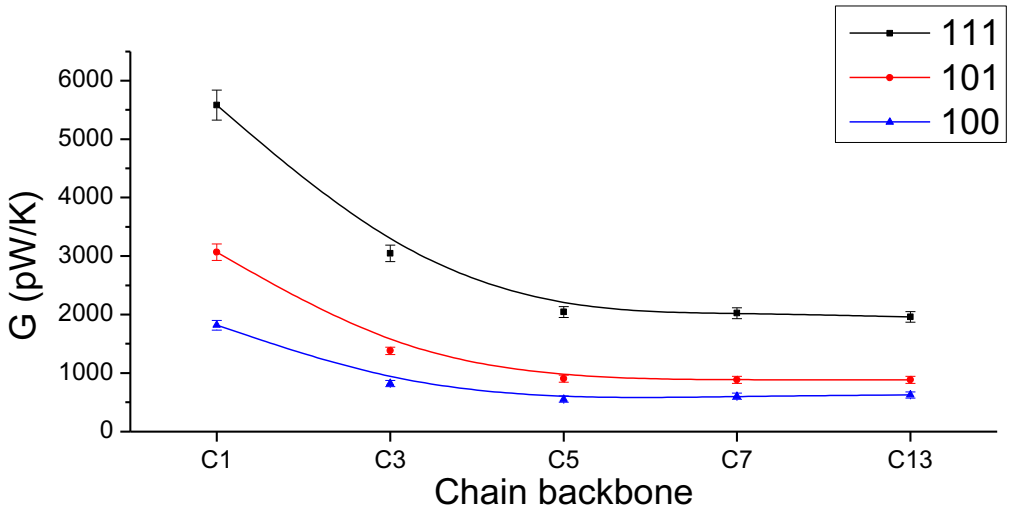

Figure 65. Thermal boundary conductance as a function of the backbone chain length, each series represent a different grafting scheme. The lines guide the eye among the values. Alternatively, a vertical reading direction highlights the thermal conductance as a function of grafting density. The TBC uncertainty is estimated from variations obtained between simulations made using three different seeds per run in velocities assignments, on selected chain length grafting configurations (the values from seed change for C3 chain is detailed in Table 5).

In the case of an ideal material observing Fourier's law in the diffusive regime, a decrease in the thermal conductance is expected with increasing chain length. However, it was previously reported that conductivity of linear (1D) chains diverges with chain length [77]. Examples of asymptotic decrease of conductance with increasing alkyl chain length were reported by several authors, both form experimental measurements [77] and computational work [184, 185]. For such observation, different explanations have been proposed, including quasi-ballistic transport, effect of direct mechanical coupling or the variation of phonon modes as a function of chain length [77]. Figure 65 also reports the effect of the different grafting schemes: as expected, the reduction in the number of bridging chains per unit length leads to a rapid decay of the interfacial thermal conductance. Table 4 reports G_{chain} values calculated from Equation 76 for all the cross-linkers schemes and chain lengths.

Table 4. Average single chain conductance (G_{chain}) for covalently bound chains.

Chain Backbone	**111 G_{chain}**	**101 G_{chain}**	**100 G_{chain}**	**Average G_{chain}**
		(pW K^{-1})		
C1	455	504	442	467 ± 31
C3	252	230	215	232 ± 19
C5	169	149	137	152 ± 16
C7	169	147	151	156 ± 11

C13	163	147	156	156 ± 8

The values of G_{chain} are found independent on the grafting scheme and therefore reflect the contribution of single chains to the interface between two nanoribbons, confirming the additive effect of the single linker reported in previous works [75, 78]. Quantitatively, conductance values are aligned with results previously reported from literature. Indeed, Li *et al.*[111] reported a G_{chain} of about 160 pW K^{-1} at 300 K for edge-grafted C11 alkane chain bridging two graphene nanoribbons, while G_{chain} of about 330 pW K^{-1} was calculated for CH_2-CH_2- linkers intercalated between graphene planes [75]. Conductances of the same order of magnitude (about 250 pW K^{-1}) were also reported for methylene linkers between carbon nanotubes [107]. Figure 66 reports the TBC as a function of the equilibrium temperature in the range between 200 and 500 K. Limited variations (± 10% on the average values) were obtained and no clear trend was observed for thermal conductance values with increasing temperature. We therefore assume thermal conductance approximately constant in the explored temperature range.

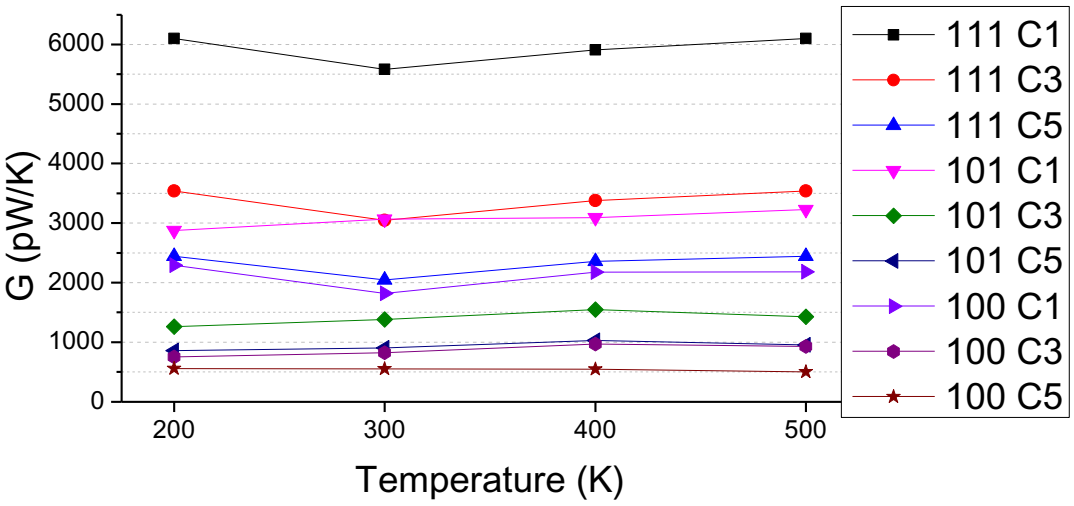

Figure 66. Dependency of thermal conductance for C1, C3 and C5 chain lengths in all grafting schemes at 200 K, 300 K, 400 K and 500 K.

Table 5. Thermal Boundary Conductances and single chains thermal conductances, energy versus time slopes and thermal jumps in C3 joint sheets for three different velocities seeds at 300 K: average values and average error.

Grafting density	**TBC [pW K^{-1}]**				
	Seed 0	**Seed 1**	**Seed 2**	**Average**	**Deviation**
111	3045	3150	3200	3132	77
101	1379	1366	1431	1392	33
100	820	757	885	821	64
	G_{chain} [pW K^{-1}]				

	Seed 0	Seed 1	Seed 2	Average	Deviation
111	254	263	267	261	7
101	230	228	238	232	6
100	205	215	221	214	9
	NVT slope [eV ps^{-1}]				
	Seed 0	**Seed 1**	**Seed 2**	**Average**	**Deviation**
111	0.280	0.270	0.270	0.273	0.005
101	0.150	0.140	0.150	0.147	0.005
100	0.090	0.100	0.100	0.097	0.005
	Thermal Jump [K]				
	Seed 0	**Seed 1**	**Seed 2**	**Average**	**Deviation**
111	14.50	13.59	13.64	13.91	0.46
101	17.03	16.98	16.79	16.93	0.12
100	17.87	18.05	18.09	18.00	0.11

The results reported in this section evidence a strong dependence of thermal conductance between edge-bounded graphene platelets as function of short chain length, suggesting transport trough alkyl molecules is driven by diffusive modes. Such hypothesis is confirmed by the dependency of thermal conductance with length, where shorter molecules were found more capable to drive heat than longer ones, before a plateau in TBC was reached. Moreover, from literature it is known that chemical grafting in graphene determines the rise of defects, which limits the thermal transport in plane. By exploiting the chemical grafting at the edges of the platelets, such detrimental effect, due to the inner defective behavior of the interface it is virtually suppressed. Because of this phenomenon, the thermal transport between graphene platelets was found as more effective as much linker were employed. These findings drove further efforts to research more chemical viable systems to act as molecular linkers, as reported in the following section.

4.2. Aliphatic/aromatic hybrid molecular junctions

The thermal transport of chemically feasible linkers exploiting edge functionalization via aryl diazonium chemistry, as reported from Sun and coworkers [89] was simulated in the present work. Based on the previous study results, ten molecular junctions were considered, as summarized in Table 6. Those molecules represents a variety of diphenyloxyalkanes: diphenoxymethane (C1OP); 1,2-diphenoxyethane (C2OP); 1,3-diphenoxypropane (C3OP); 1,4-diphenoxybutane (C4OP); 1,5-diphenoxypentane (C5OP); 1,6-diphenoxyhexane (C6OP); 1,7-diphenoxyheptane (C7OP). 1,3 dibenzylbenzene (PCP) a 1,7 diphenylheptane (C7P) were also addressed as ether-free counterparts. Diphenoxybenzene (POP) exploited a central

aromatic moiety instead of the aliphatic one. It is worth mentioning that all of these junctions may be obtained between graphene sheets via aryldiazonium chemistry, as demonstrated experimentally for C5OP [183].

Table 6. The hybrid aliphatic/aromatic molecular junctions addressed in this work: Chemical structures, molecular thermal conductance (G_m), elastic modulus (E) and application distance (d). All molecules are bonded in para (p-).

Short name	**Long name**	**G_m [pW/K]**	**E [GPa]**	**d [Å]**	**Structure**
C1OP	diphenoxymethane	208±53	145	12.5	
C2OP	1,2-diphenoxyethane	182±5	80	13.8	
C3OP	1,3-diphenoxypropane	161±20	94	14.9	1,n-diphenoxy alkane (CnOP)
C4OP	1,4-diphenoxybutane	148±23	72	16.3	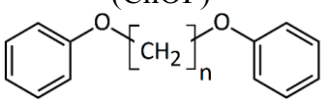
C5OP	1,5-diphenoxypentane	139±7	93	17.2	
C6OP	1,6-diphenoxyhexane	130±9	53	18.8	
C7OP	1,7-diphenoxyheptane	123±6	70	20.0	
POP	1,3-diphenoxybenzene	260±16	152	16.6	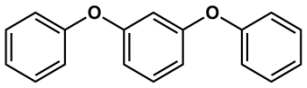
PCP	1,3-dibenzylbenzene	221±14	85	16.3	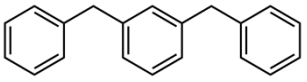
C7P	1,7-diphenylheptane	139±33	65	17.5	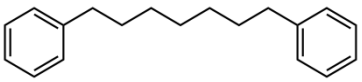

By the energy flux analysis, it was observed that the heat injected into the heat source and removed from the heat sink evolved linearly with the time, with equivalent slopes, as reported by Figure 67. Figure 67 groups for all the aliphatic/aromatic hybrid molecules, the energy flowing from and to the thermostats.

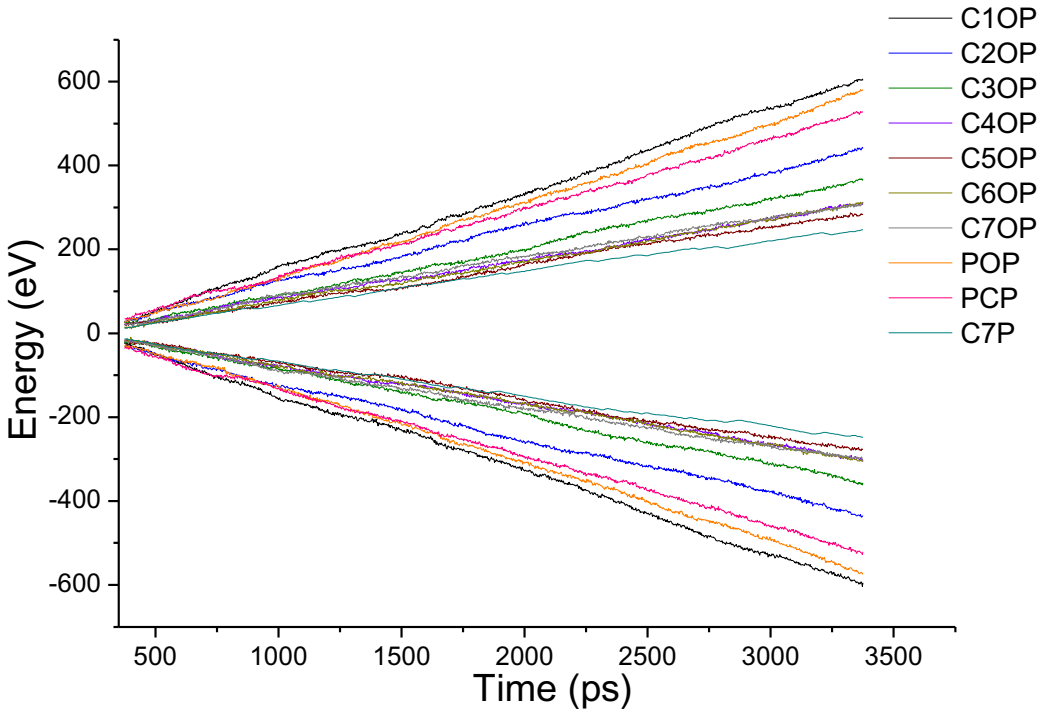

Figure 67. Energy vs time plot in aliphatic/aromatic molecules. The energy evolution with the time highlights a constant heat flux in thermostats.

Figure 68 shows the calculated temperature profiles along the graphene nanoribbons for a set of simulations with diphenyloxyalkanes family molecules as thermal linkers. In this plot, the temperature scale is magnified to limit the overlap and highlight data points with relative linear fit. Overall, the thermal jump is not particularly affected by the linker length in this type of junction where the large difference in plot is mostly caused by the temperature axis magnification.

A similar scattering was found also with the variants of the diphenyloxyalkanes molecules represented by C7P, POP and PCP reported in Figure 69. Due to the presence of velocity noise between groups, the thermal conductivity values proposed in this section were calculated from several simulations obtained by changing the velocities seed. Each value proposed was obtained by averaging from up to 6 replicas, to obtain a representative average result, along with uncertainty bands.

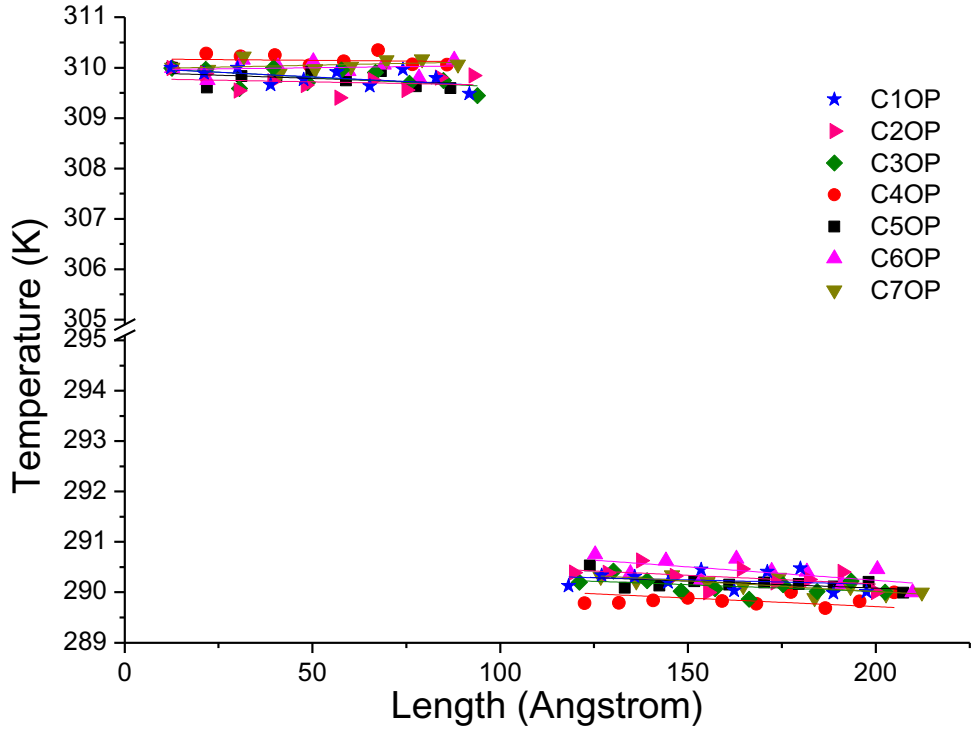

Figure 68. Thermal profile of graphene sheets bonded by diphenyloxyalkanes family molecules. The temperature scale includes 10 K break to highlight data points and linear fitting of data.

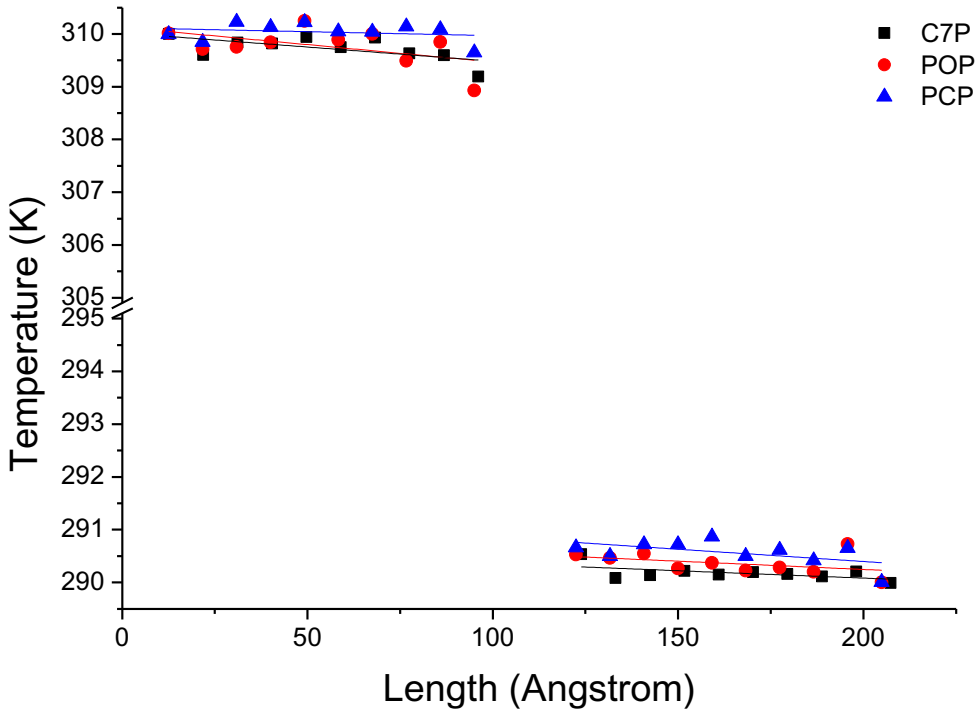

Figure 69. Thermal profile of graphene sheets bonded by C7P, POP and PCP. The temperature scale includes 10 K break to highlight data points and linear fitting of data.

As a first case study, C5OP was analyzed in a range of parameters, including Thermostat Temperature Difference (TTD), molecular conformation and junction topology. The TTD effect was evaluated keeping the simulation equilibrium temperature centered at 300K and increasing the TTD from 20 K to 25 K and 30 K, leading to G_m values of 139 ± 7, 131 ± 6 and 135 ± 4 pW K^{-1}, respectively, which are considered constant within the experimental uncertainty. When shortening the alkyl chain in aliphatic/aromatic (CnOP) junctions to C4OP and C3OP, an enhancement of G_m to 148 ± 23 and 161 ± 20 pW K^{-1} was obtained, respectively. Further shortening to C2OP and C1OP exhibited further increased values up to 182 ± 5 and 208 ± 53 pW K^{-1}, thus confirming the increasing conductance with shortening junction length. On the other hand, as expected, longer component of the alkyl portion reported lower G_m: 130 ± 9 pW K^{-1} in C6OP and 123 ± 6 pW K^{-1} in C7OP. It is also worth noting that the calculated thermal conductances of those molecules were in the same order of magnitude of similar length alkyl ones [111, 186].

To investigate the CnOP family molecular junction stiffness as a function of the chain length, a set of tensile simulations have been performed. The Elastic modulus was calculated through linear fitting up to 10% of deformation in elastic regime. Stress-strain plots are reported in Figure 70. The resulting elastic moduli (E) were found in the range between 145 and 53 GPa for C1OP and C6OP, respectively, with an overall decreasing trend over values with increasing alkyl chain length (Figure 71). As matter of comparison, elastic modulus of 487 GPa was calculated for pristine graphene slab. Despite this value is significantly lower, compared to 980 GPa previously reported [50], (which may be related to the different force field as well as to the small model size), a comparison of the obtained modulus remains possible within this set of results. Interestingly, the tensile modulus trend vs. CnOP junction length was found to be consistent with the decrease in thermal conductance (Figure 71), despite an odd-even effect is observed in calculated elastic modulus.

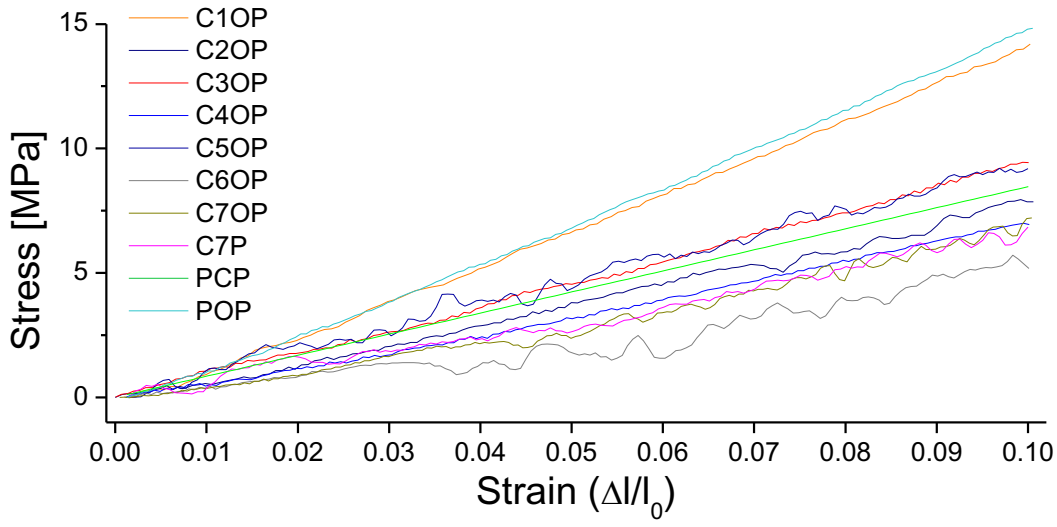

Figure 70. Stress-strain curves for diphenyloxyalkanes and C7P, PCP and POP molecules in the range up to 10% of elongation.

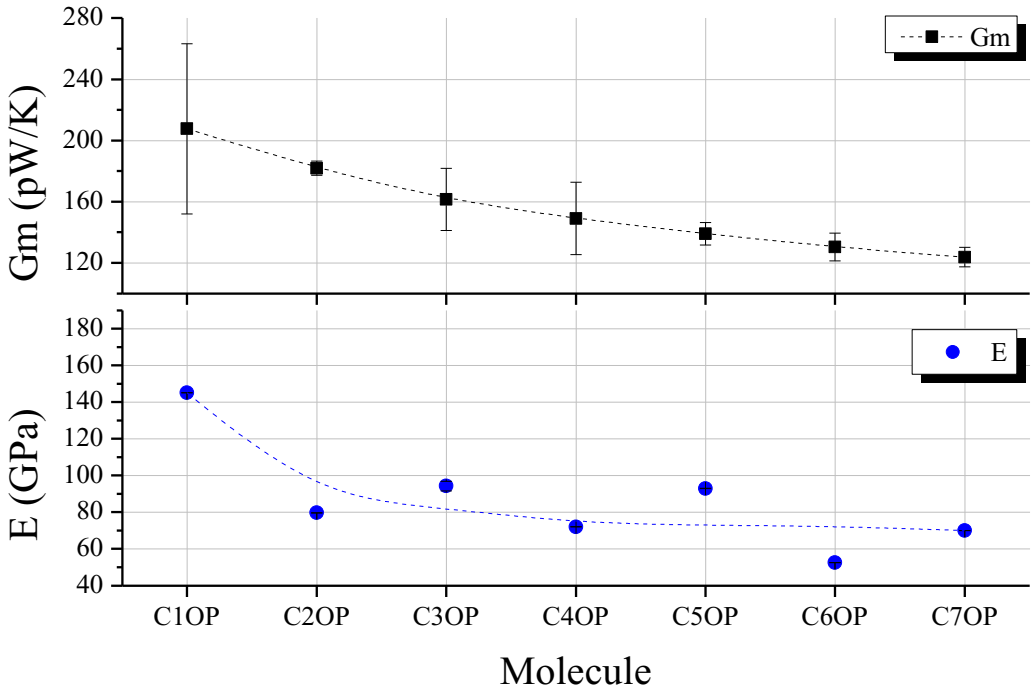

Figure 71. G_m and elastic modulus E for aliphatic-aromatic molecular junctions, the dashed lines guides the eye through values reported in Table 6. Error bars in E are below 1% and barely visible.

To investigate the phonon match between molecules and graphene [42], vibrational spectra has been calculated for the isolated molecules as well as for a hydrogen-terminated graphene nanoribbon (Figure 72). Graphene exhibited a broad region of vibrational states up to 5 THz, a sharp peak at 45.2 THz (called G peak from Raman analysis, usually at 47THz [43]) and broad peak around 17 THz. For molecular junctions, several additional bands are observable in the regions 0 to 25 THz and 42 to 46 THz. However, very limited match is observed between VDOS spectra for pristine graphene and in the presence of CnOP molecular junctions. The almost linear decay in thermal conductance reported in Figure 71, combined with the phonon spectra mismatch, it is indicative of a diffusive regime with scattering at the interface strongly limiting heat transfer.

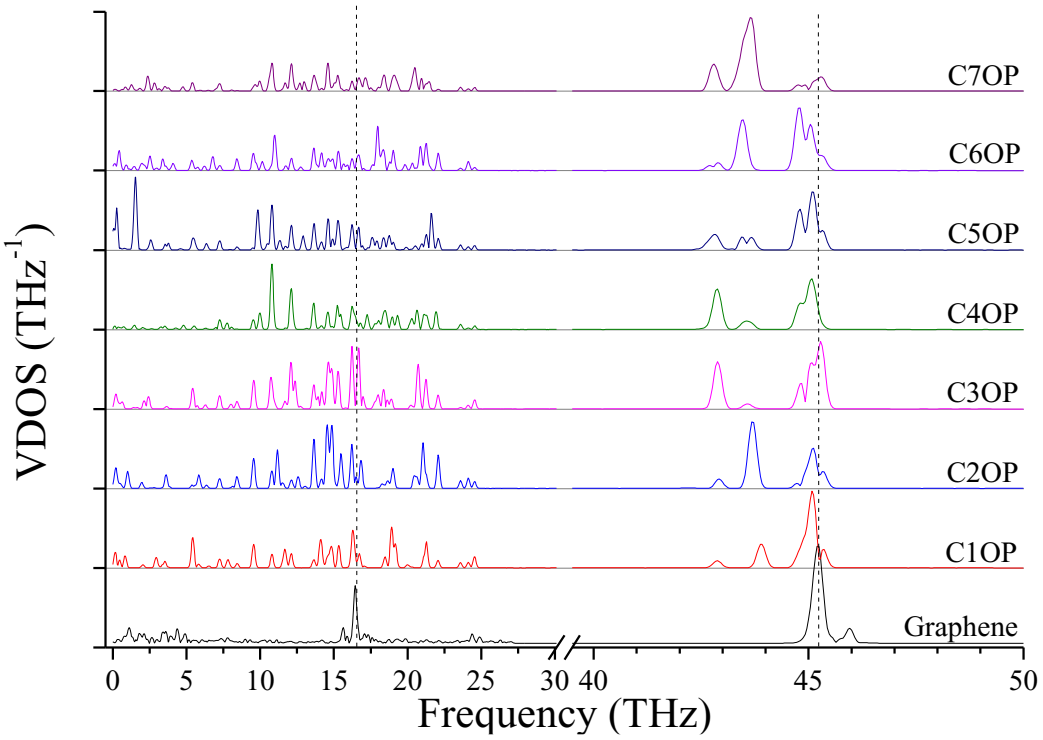

Figure 72. VDOS for the aliphatic-aromatic molecular junctions, scale in 40-50 THz is magnified by a factor of three. The dashed lines highlights the most intense graphene peaks at 16.5 THz and 45.2 THz (G-peak).

The role of ether bond was studied comparing junctions with similar length, namely C5OP and C7P. Despite the stiffness of C7P (65 GPa) was found approx. 30% lower than C5OP, the 139±33 pW K^{-1} conductance for C7P is equivalent to the value for C5OP. This finding suggests that the presence of the soft alkyl component in the center of the molecular junction limits the overall heat transfer and ether substitution in a relatively long alkyl chain has a negligible effect. The VDOS for C7P is reported in Figure 73, which shows the main contribution from alkyl moieties as broad peaks in the 42-44 THz region, in fair agreement with the spectrum for C5OP. The role of flexible groups (ether vs. methylene bridges) was further investigated in stiffer aromatic structure. Junctions based on diphenoxybenzene (POP, d=16.6 Å, H in Table 6) and dibenzylbenzene (PCP, d=16.3 Å, I in Table 6) were compared in both thermal conductance and stiffness. The thermal conductances for these systems were found about 260 ± 16 pW K^{-1} for POP and 221 ± 14 for PCP, suggesting ether bridges are more effective that methylene in phonon transfer. Furthermore, these values were compared to a junction of comparable length, C4OP, (148 ± 23 pW K^{-1}, d = 16.3 Å, D in Table 6) which clearly evidenced the advantage of aromatic structures in terms of thermal conductance. The analysis of VDOS spectra, depicted in Figure 73, provided further support for the differences in heat transfer. Indeed, signal in VDOS spectra between 43 and 44 THz progressively reduced from C7P to PCP, while no significant counts in this band remains for POP. Furthermore, a stronger peak rises around 16.5 THz in PCP and POP, while the G

peak for POP junctions appears to best overlap with the main vibration of pristine graphene.

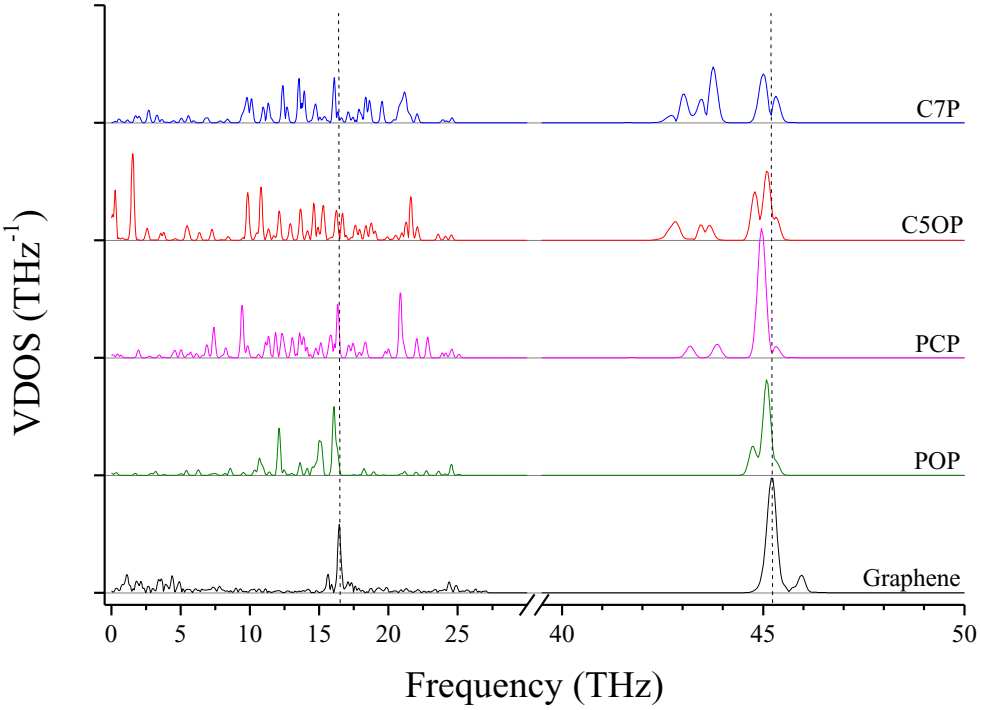

Figure 73. VDOS for molecular junctions with/without ether bridge, the scale in 40-50 THz is magnified by a factor of three for clarity. Dashed lines highlights the most intense graphene peaks at 16.5 THz and 45.2 THz (G-peak).

Tensile simulations highlighted a wide gap between elastic moduli for POP (152 GPa) and PCP (85 GPa). This difference suggested that the deformability of flexible moieties is indeed crucial in controlling the overall junction stiffness, also when rigid aromatic rings are present in the molecular structure. Moreover, by looking at carbon type and oxygen type bond parameters in COMPASS, reported in Table 7 and fitting the equation 82, an higher bond energy was found for c4o-o2e compared to carbon-carbon one. Here, the 2nd 3rd and 4th power coefficients are remarkably higher than c4-c4 [131]. The placement of such atom types in molecular junctions is reported in Figure 74.

$$E_{bond} = K_2(r - r_0)^2 + K_3(r - r_0)^3 + K_4(r - r_0)^4 \qquad 82$$

Table 7: Bond coefficients for ether oxygen (o2e), aromatic (c3a) and alkyl carbon (c4) adopted in COMPASS force field.

E_{bond}	r_0	K_2	K_3	K_4
o2e-c3a	1.37	428.88	-738.23	1114.96
o2e-c4o	1.42	400.39	-835.19	1313.01
c4o-c4	1.53	299.67	-501.77	679.81
c4-c4	1.53	299.67	-501.77	679.81

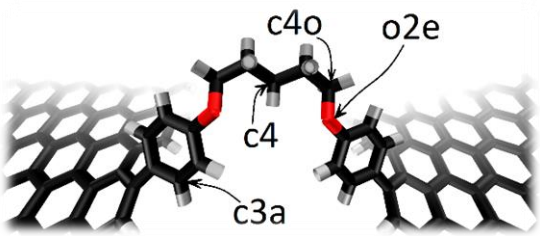

Figure 74: COMPASS© Atom types for oxygen and carbon adopted in C5OP molecular junction taken as example.

The hybrid aromatic-aliphatic chains demonstrated to provide an appreciable contribution in thermal transport in suspended graphene. The comparison between thermal conductance and the bond strength suggested a correlation between bond strength and thermal conductance. Despite these considerations, the overall phonon match in VDOS comparison was found poor between graphene and aliphatic species.

4.2.1. Multilayered structures

The thermal contribution of molecular junction was evaluated in three different multi-layered structures. The purpose of the investigation was to model a system slightly closer to a hypothetical experimental layout, where the single flake of graphene is challenging to isolate. The previously adopted C5OP molecule was employed as testing linker while two trilayers and a pentalayer were designed to fit molecules in different grafting schemes. One of the trilayers was designed to accommodate three molecules on the central flake (a in Figure 75), the other trilayer had five grafted molecules laying across all the flakes (b in Figure 75) and the pentalyayer had 8 molecule between the platelets as depicted by c in Figure 75. Such grafting schemes were designed to accommodate molecules without any interference among layers. Those models adopted slightly thinner flakes than the ones employed above (which are about 50x100 Å). In this case, the width was reduced to about 35x100 Å. The reason of this choice was to reduce the computational request of NEMD calculations. With the thinner flakes, the models were made of about 8300 atoms for trilayers and about 13000 atoms for the pentalayer. The results that follows comes from three replicas with different velocities seeds.

(a) • • •

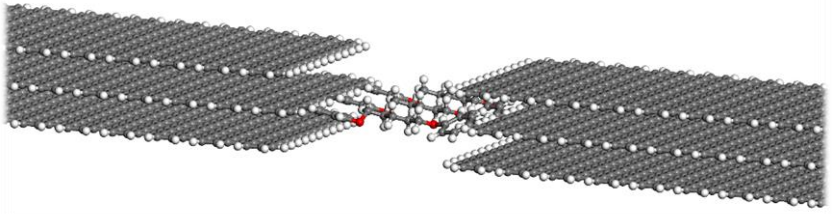

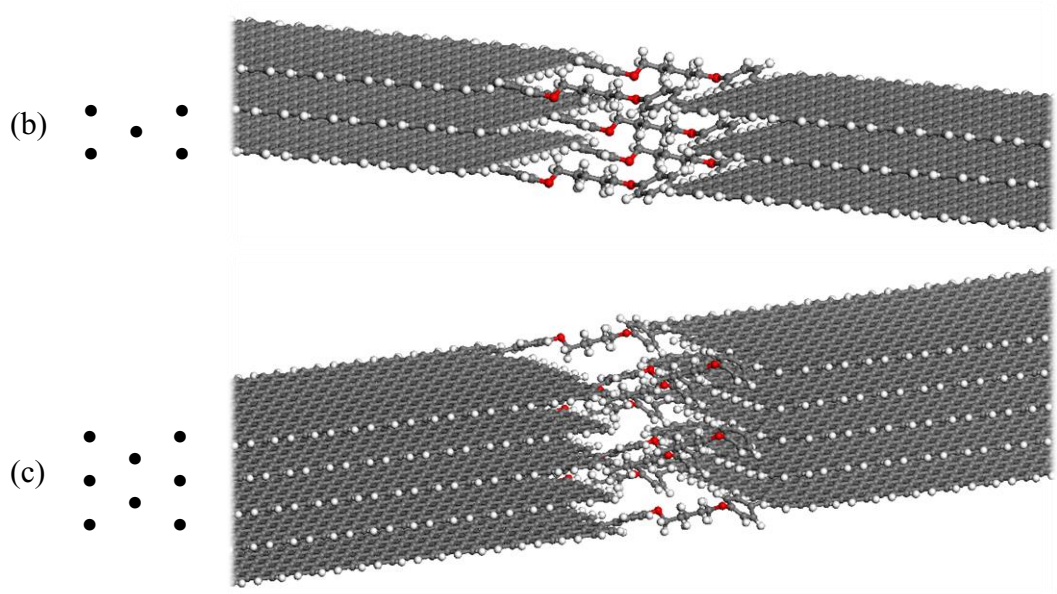

Figure 75. Multilayered structures. (a) Trilayer with three inline grafted molecules. (b) Trilayer with five molecules grafted forming a cross. (c) Pentalayer with eight molecules grafted forming a double overlapped cross. The cross-section grafting schemes are reported with black dots on the left.

The energy flux plots in terms of positive and negative slopes reported by Figure 76 were found linear and symmetric meaning that a constant heat flux was established without energy loss or gain. The amount of transferred energy evidenced that the energy flowing through the models was proportional to the number of grafted molecules. This finding is coherent with the previous work on alkyl chains, where the single layer graphene was grafted with different density of linkers.

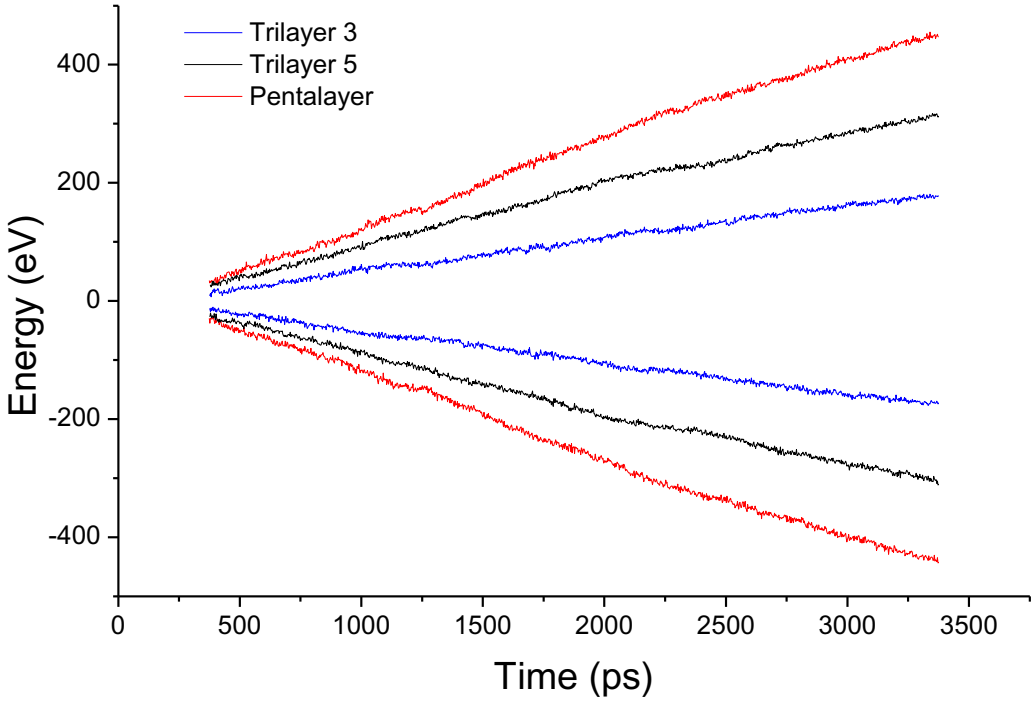

Figure 76. Energy flux in multilayered structures, the trilayer with three grafted molecules (blue line), trilayer with five grafting molecules (black line) and the Pentalayer (red line).

The temperature profile reported in Figure 77 shows the reduction of temperature jump for all the multilayers. Despite the thermal noise is lower than in single layer analyzed above, probably due to larger amount of atoms composing the thermal layers, the thermal profile is not strictly proportional to the number of grafting molecules.

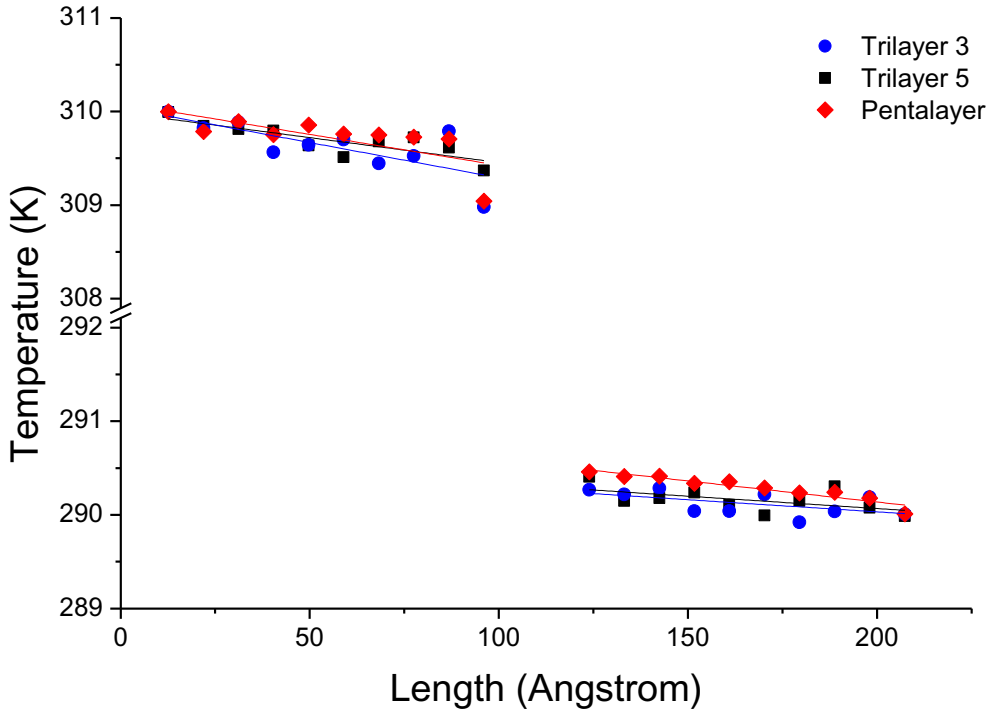

Figure 77. Thermal profile of multilayered structures bonded by C5OP linker. The temperature scale includes a 16 K break to highlight data points and linear fitting of data.

The thermal conductance values reported in Table 8 are based on three different simulations replicated by changing the velocities seed. The linker thermal conductance for the trilayers is almost the same, about 159 pW K^{-1}, where the pentalayer exhibited a slightly lower value (151 pW K^{-1}). Nevertheless, all those value are generally higher than calculated in SLG models (139 pW K^{-1}) by 9% for pentalayer and 14% for trilayers. This slight dependency of G_c with the topology drove further efforts to focus only to the SLG models, with the aim of analyze coherent sets of data.

Table 8. Thermal conductance (G_c) of C5OP linker in multilayered structures.

Structure	Number of linkers	G_c	Error
Trilayer 3	3	159.43	16.83
Trilayer 5	5	159.51	10.52
Pentalayer	8	151.87	13.16

4.3. Aromatic molecular junctions

Based on this landmark, polyaromatic hydrocarbons were also studied as potentially effective molecular junctions. In fact, polyaromatic molecules exhibits highly delocalized electronic structures, and limited conformational freedom of the

molecule, becoming progressively more similar to graphene itself when increasing the number of condensed aromatic rings. Fully aromatic junctions included, biphenyl (BP), phenanthrene (PH) and pyrene (PY), reported in Table 9.

Table 9. The aromatic molecular junctions addressed in this work: Chemical structure, molecular thermal conductance (G_m), elastic modulus (E) and application distance (d). All molecules are bonded in para (p-).

Short name	Long name	Gm [pW/K]	E [GPa]	d [Å]	Structure
BP	Biphenyl	472±26	141	9.7	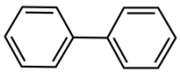
PH	Phenanthrene	608±25	165	9.8	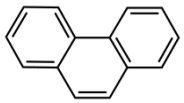
PY	Pyrene	648±14	179	9.7	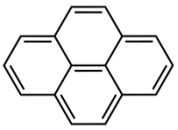

NEMD post-processing analysis confirmed a linear behavior in energy flowing from the heat-source to the heat sink (Figure 78). The higher slopes when compared to the hybrid aromatic/aliphatic molecules seen before, indicates higher power transmitted through the junction. Moreover, the thermal profile along the model, reported in Figure 79, exhibited the steepest slope seen before, indicating a reduction of the thermal jump and thus the thermal resistance.

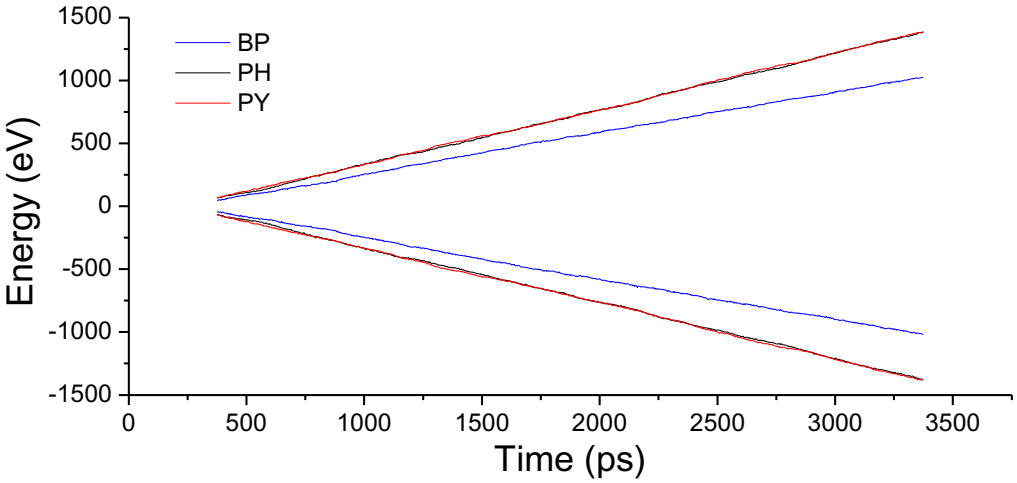

Figure 78. Energy versus time plot for aromatic junctions BP, PH, and PY.

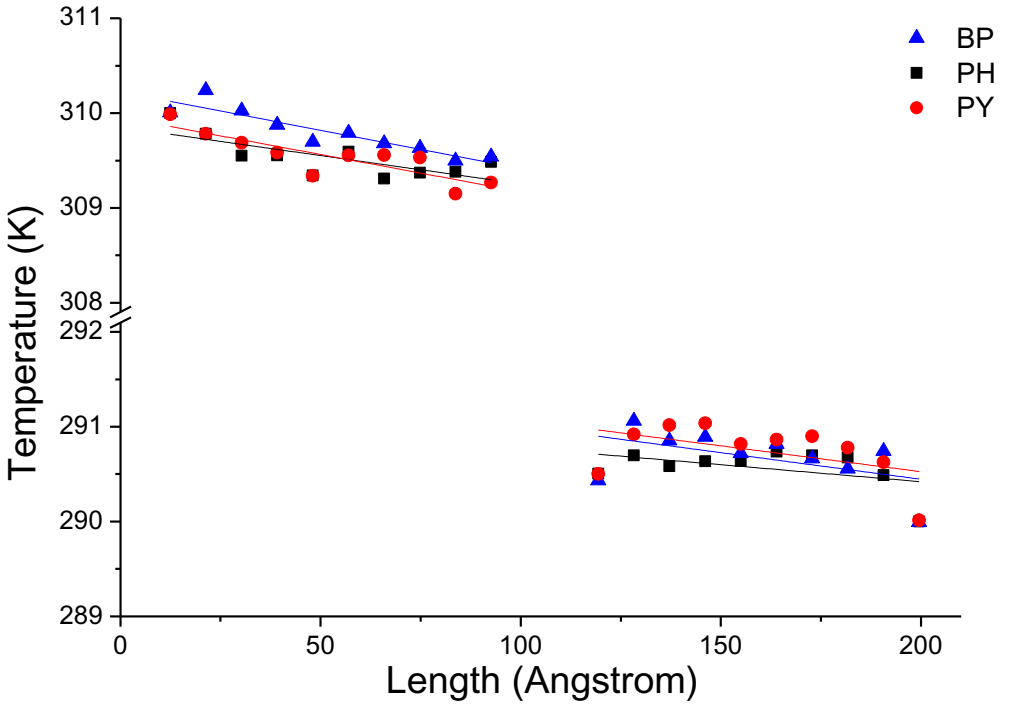

Figure 79. Thermal profile of graphene sheets bonded by aromatic molecular junctions. The temperature scale includes 16 K break to highlight data points and linear fitting of data.

A thermal conductance of 472±26 pW K^{-1} was calculated for biphenyl junction (BP in Table 9) and further enhancement was obtained for higher aromatic condensation, as 608±25 pW K^{-1} was calculated for phenanthrene (PH in Table 9) and 648±14 pW K^{-1} for pyrene (PY in Table 9). The tensile deformation of aromatic junctions (Figure 80) reflects a higher stiffness than the alkyl based ones, with calculated elastic moduli of 141 GPa for biphenyl, 165 GPa for phenanthrene and 179 GPa for pyrene.

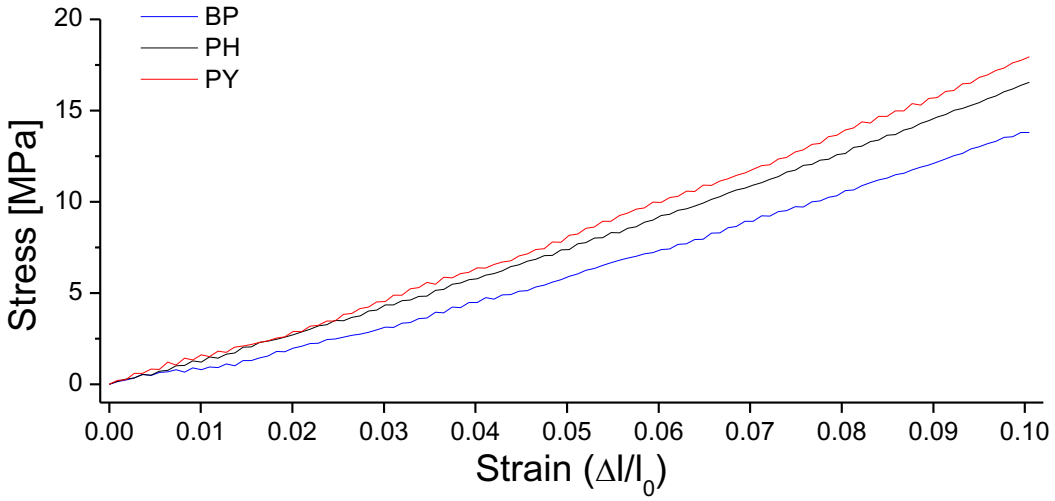

Figure 80. Stress versus strain curves for aromatic molecules BP, PH and PY in range 0-10%.

Indeed, VDOS analysis of selected polyaromatic junctions (Figure 81) confirmed the general excellent overlapping of the two most intense signal for polyaromatic junction with the 16.5 THz and 45.2 THz peaks for graphene. Some differences are clearly observable between the aromatic junctions and graphene. The aromatic molecular junctions owns more vibrational modes from 5 to 20 THz.

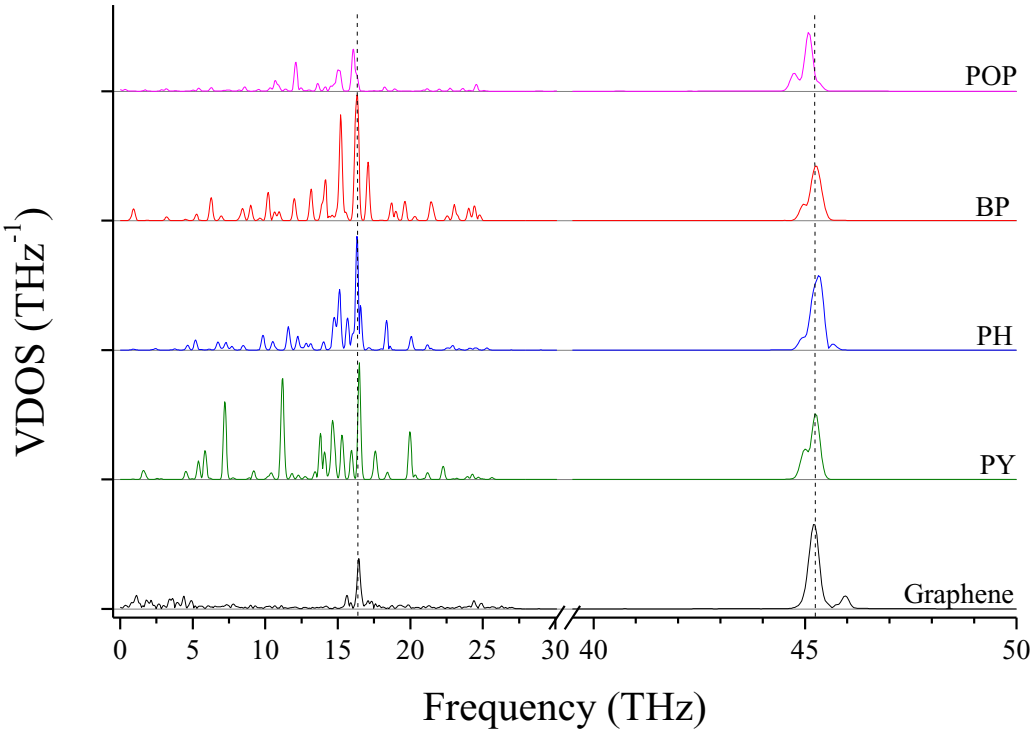

Figure 81. VDOS for aromatic molecules, scale in 40-50 THz is magnified by a factor of three. Dashed lines highlights the most intense graphene peaks at 16.5 THz and 45.2 THz (G-peak).

Based on the results obtained for aliphatic and aromatic junctions described so far, the combination of length and stiffness of the bridging chain appear to control the overall efficiency of the thermal transport through the interface. In fact, short and stiff junctions lead to the highest values of thermal conductance.

4.4. Acenes: the upper-bound in molecular thermal conductance

Finally, acene-based junctions, which preserve the conjugation of sp^2 carbon across the bond of two graphene sheets, were included in this study for sake of comparison. Three different acene-based junctions made of 3, 5 and 7 aromatic rings were addressed: anthracene (ACN), pentacene (PCN) and heptacene (HCN) as reported in Table 10.

Table 10. Acene as molecular linkers: detail on acene length (d), molecular thermal conductance (G_m), elastic modulus (E), and molecular structure.

Short name	Long name	G_m [pW K^{-1}]	E [GPa]	d [Å]	Structure
ACN	Anthracene	1121±35	279	7.4	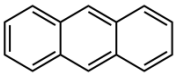
PCN	Pentacene	1076±44	285	12.3	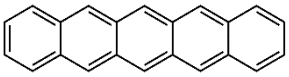
HCN	Heptacene	1007±40	268	17.1	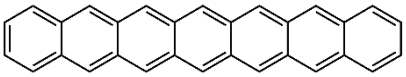

Despite the exploitation of acenes in molecular junctions is extremely challenging, these junctions were addressed here as a kind of theoretical "upper bound" for the thermal conductance for thermal bridges between graphene sheets, as it preserves the conjugation of sp^2 carbon across the contact of the two graphene sheets.

For those junctions, the energy flowing through the domain (Figure 82) reported the highest slopes and consequently power, among all the molecules seen before. Nevertheless, the thermal profile along the model, reported in Figure 83 exhibited a steepest slope compared to previous junctions, reflecting the lowest thermal resistance. The G_m values of 1121±35, 1076±44 and 1007±40 pW K^{-1} obtained for ACN, PCN and HCN, confirmed the enhancement in thermal transport that such junction gives. Moreover, the tensile testing revealed almost constant elastic modulus values, namely 279 GPa for ACN, 285 GPa for PCN and 268 GPa for HCN. The stress-strain curves for acenes are reported in Figure 84.

The thermal conductance values appear to be only slightly affected by the acene length, which more than doubles, rising from 7.4 Å for ACN to 17.1 Å for HCN. These results suggest the phonon transfer on these junctions to be ballistic, in contrast with the diffusive regime observed in alkyl junctions. As expected, the VDOS (Figure 85) for polyaromatic junctions closely matches the main bands for pristine graphene, similarly to other aromatic junctions (already reported in Figure 81).

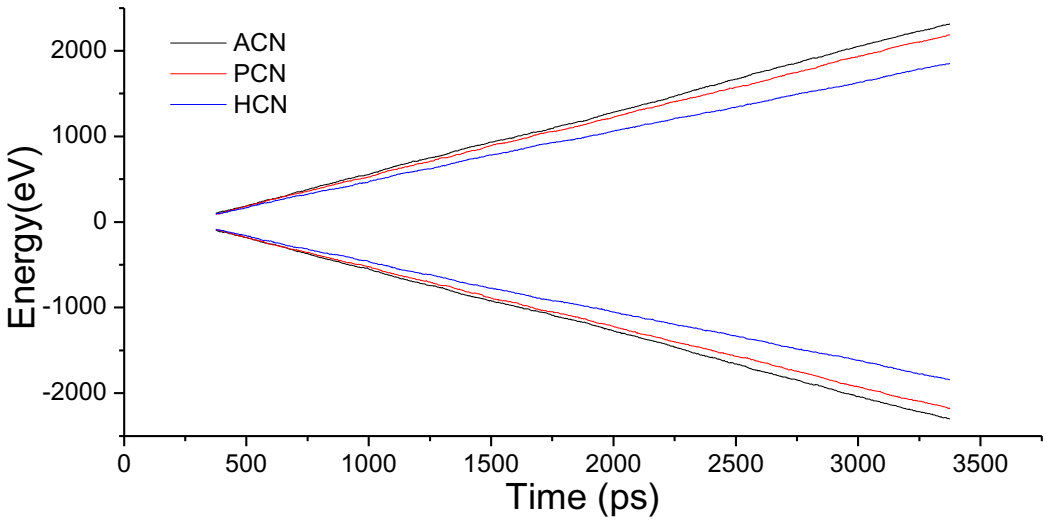

Figure 82. Evolving energy during simulation time in acene junctions.

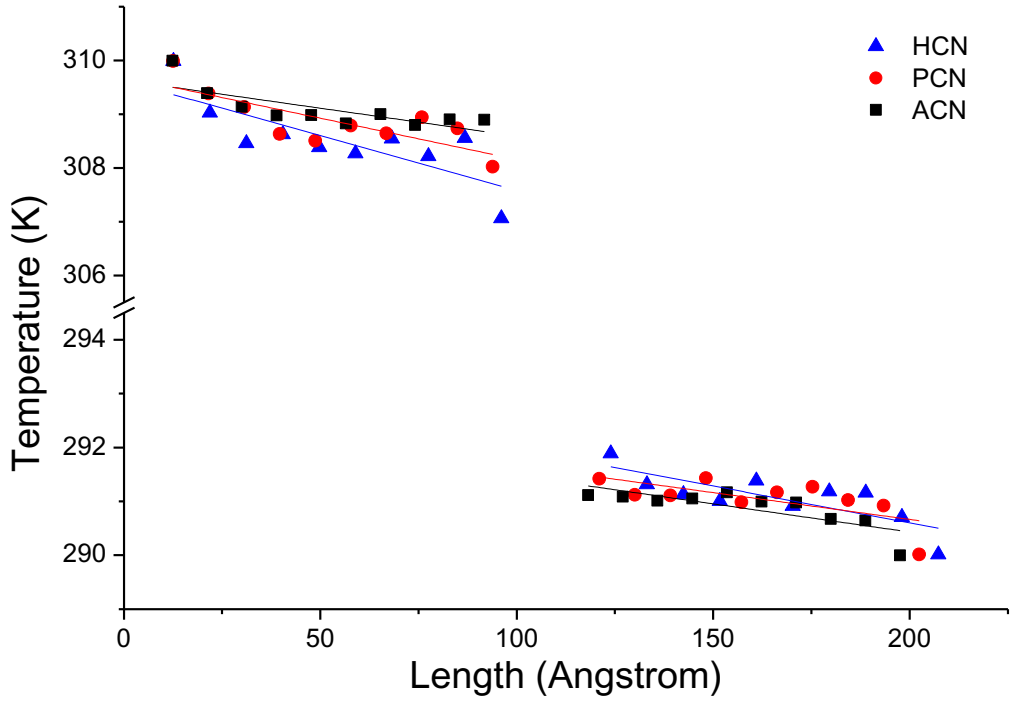

Figure 83. Thermal Profile of acene-joint graphene sheets. The temperature scale includes a 12 K break to highlight data points and linear fitting of data.

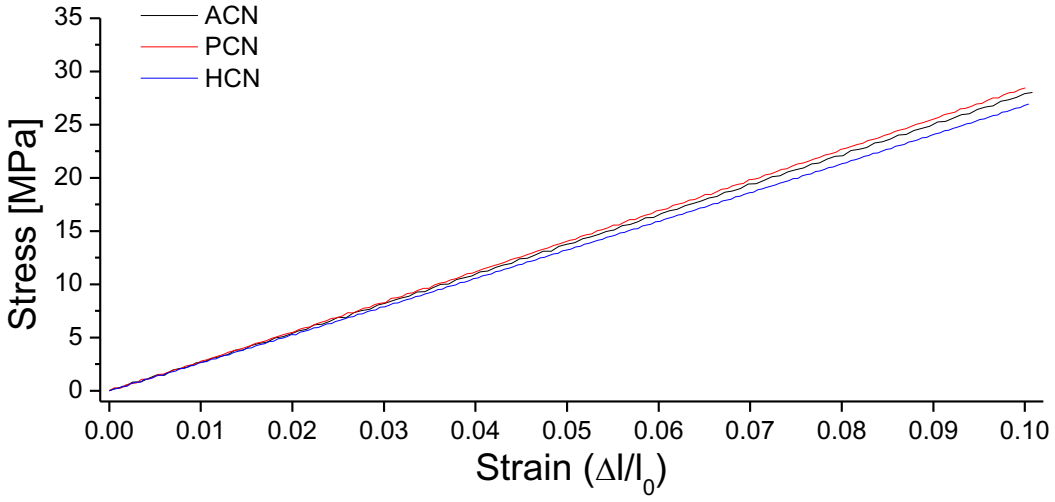

Figure 84. Stress-strain curve for Acenes (ACN, PCN and HCN).

The vibrational density of state for acenes was found comparable to the graphene one, resulting in values of thermal conductance that exceed 1000 pW K^{-1} We found that thermal conductance varies little with acene length, suggesting ballistic phonon transfer through the interface.

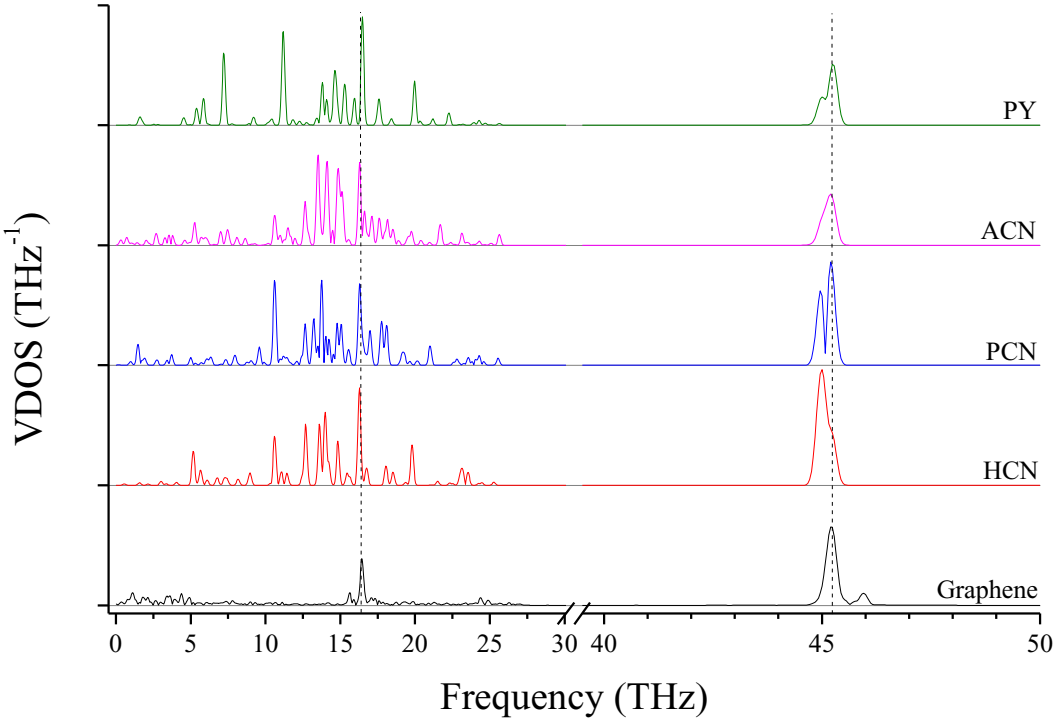

Figure 85. VDOS in acenes, scale in 40-50 THz is magnified by a factor of three. Dashed lines highlights the most intense graphene peaks at 16.5 THz and 45.2 THz (G-peak). PY is added for the sake of comparison.

While acene junction-type synthesis is currently very challenging, the simulated conductance values obtained here should be considered as a theoretical upper limit to the thermal performance of any experimentally viable junction.

4.5. Conclusions

The thermal conductance of interfaces made of molecular junctions between graphene nanoribbons was investigated by means of non-equilibrium molecular dynamics simulations. Molecular junctions joint by covalent bonding represent a more efficient media to drive heat compared to pending molecules. In particular, selective edge functionalization was addressed, thus preserving the efficiency in phonon transfer over the sp^2 graphene neat structure.

Initially, alkyl molecular linkers were investigated as candidates to improve thermal transport between edge-bounded graphene platelets. The thermal transport driven through alkyl chains was found dependent with length. Overall, shorter species were found more capable to drive heat than longer ones due diffusive mismatch of phonons along the chains interface. Despite this phenomenon, a plateauing trend was found for longer alkyl chains, suggesting that phonon scattering neither occurs inside the chain above a threshold value of length. All those findings drove the efforts to find more chemical viable systems capable to act as molecular linkers. The focus was set on synthesizable junctions via aryldiazonium chemistry, as demonstrated from literature. The elastic modulus of the molecular junctions was found correlated with the TBC, where TBC was found to be lowest for aliphatic/aromatic junctions, characterized by the long and flexible alkyl chain and highest for the short and rigid polyaromatic bridging molecules (e.g. phenanthrene and pyrene). Moreover, the chemical structures that are able to change structural conformations, due to the presence of free rotating single bonds, appeared to limit more the thermal transport capability. Similar differences were also observed between junctions containing methylene and ether groups, related to the different features of their bonds to carbon. The relation found between TBC, molecular length and elastic modulus is summarized in Figure 86, where it is apparent that highest TBC are obtained for short and stiff molecular junctions.

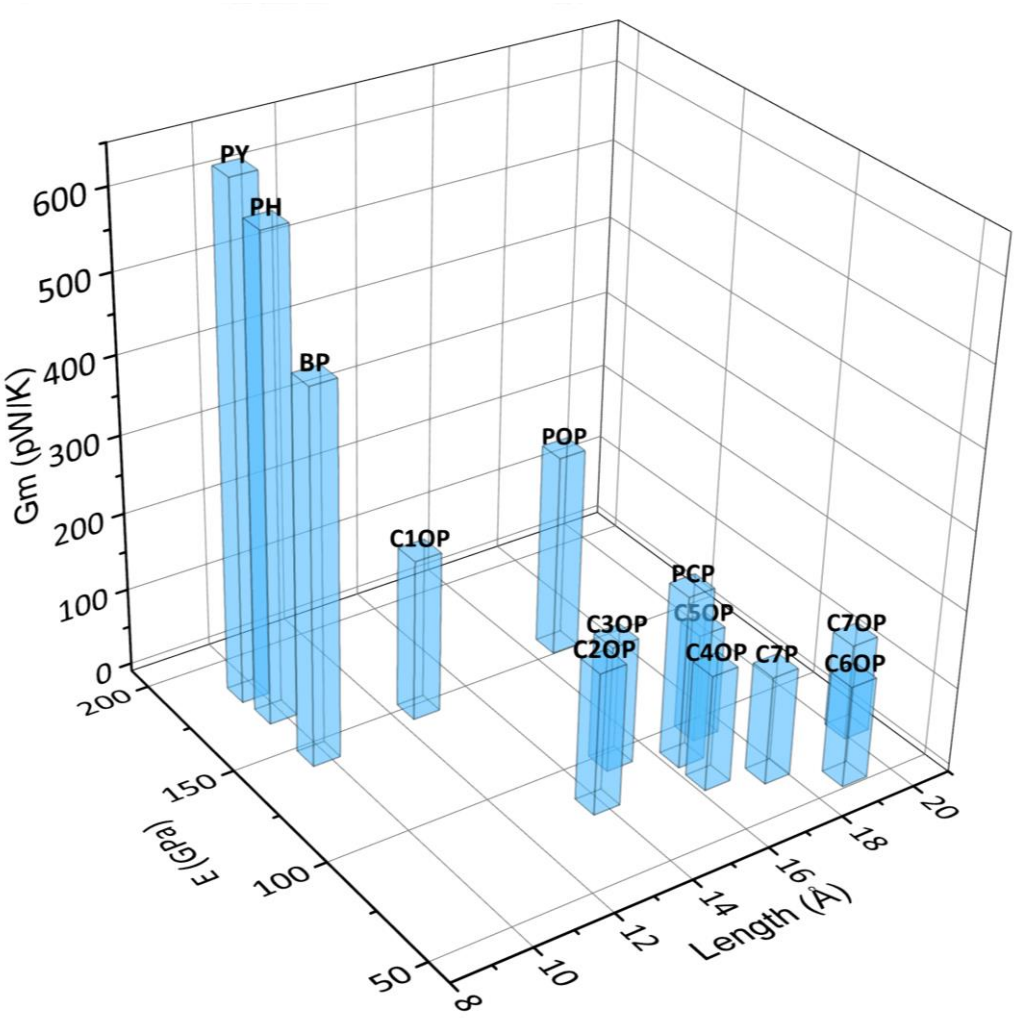

Figure 86. Calculated thermal conductance G_m of thermal junctions as a function of length and stiffness.

The overlapping of vibrational modes in density of states between molecular junctions and graphene was found useful to attribute vibrational frequency intervals with the thermal conductance of the junctions. While VDOS for aliphatic/aromatic junctions exhibited limited overlapping with the main vibration bands of graphene at both 16.5 THz and 45.2 THz, aromatic and polyaromatic structures displayed vibrational spectra more similar to the graphene one.

The screening of the different covalent junction structures addressed here provides a guideline for the development of thermally efficient interfaces to be exploited in graphene-based thermal management materials. Furthermore, the molecular thermal conductance values calculated in this section can be used in upper-scale continuum models to predict effective thermal conductivity in graphene-based laminates or polymer nanocomposites.

Chapter 5

Polymer-embedded molecular junctions

The previous chapters demonstrated how molecular junctions could improve thermal transport between suspended structures as single or multi-layered graphene flakes. All the simulations presented above, thus, considered only the graphene suspended junction without any external interaction. However, suspended junctions are poorly representative of nanostructured materials, in which the interactions between the graphene and the surrounding matrix is expected to have a significant role. As an example, in a polymer matrix, the interaction between the surface of graphene flakes and adsorbed macromolecules allows heat transfer between the conductive particles and the polymer, although the relatively high interfacial resistance [102]. Despite the enhancement of polymer/graphene contact was proposed to enhance the overall heat transfer in nanocomposites [68, 104], the very low mean free path for phonons in the polymer (a few angstroms) [11] compared to the mean free path on graphene (hundreds of nanometers) [35] is strongly limiting the efficiency of this approach. Indeed, a different approach is primarily addressed in this thesis, by the enhancing of thermal contacts between conductive nanoflakes forming a percolating network, within the polymer matrix. Nonetheless, the presence of polymer chains around the junction between two graphene sheets is expected to contribute to the local thermal transfer within the polymer matrix. The aim of this chapter is to quantify the contribution of molecular junctions when the graphene and the molecular junctions are surrounded by a model polymer, representing phenomena occurring inside a polymer nanocomposite.

Polydimethylsiloxane (PDMS) was chosen as polymer matrix, based on previous reports [187], demonstrating its strong interaction with graphene, as well as for its application-relevant set of properties, including chemical inertia, a low glass transition temperature and a wide range of physical states, from liquid to rubbery state. PDMS/graphene composites currently represent a promising and versatile class of materials, potentially suitable for applications in highly deformable and thermally conductive devices.

5.1. Molecular junctions in polymer matrix

In this section, the contribution in thermal transport of molecular junctions between graphene flakes, within a polymer matrix is studied. Three different linkers, from the previous studied ones, were selected and incorporated in PDMS. The modelling of

PDMS polymer is described in paragraph 2.6. As a first case study, an unjointed model made of two graphene sheets was designed to represent a classical "contact" between graphene flakes inside a polymer composite, referred as "No Linkers" and depicted in Figure 87A. The first molecular junction is the aliphatic/aromatic C5OP, Figure 87B. The second molecule is biphenyl (BP, Figure 87C), which represents a short aromatic junction, and third, the anthracene (ACN, Figure 87D), as theoretical upper bound junction.

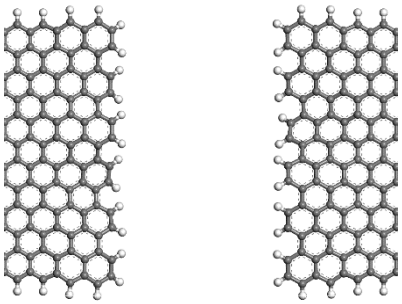

(A) No Linkers, platelets distance 17.2 Å

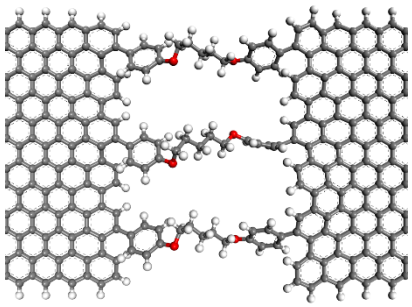

(B) C5OP molecular junctions, platelets distance 17.2 Å

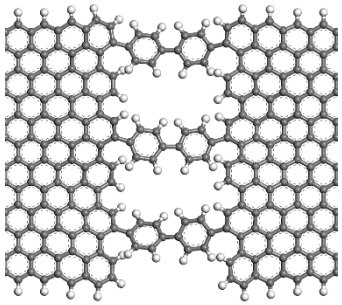

(C) BP molecular junctions, platelets distance 9.7 Å

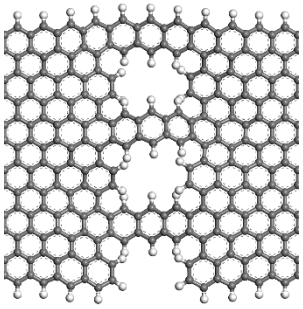

(D) ACN molecular junctions, platelets distance 7.4 Å

Figure 87. Junction details in polymer bound models. The platelets distance measurement is described in methods, paragraph 2.2. Color codes: carbon atoms in grey, oxygen in red, hydrogen in white.

Independently on the presence and type of molecular junctions, the system layout is based on a graphene sandwich between two blocks made of PDMS molecules (Figure 88).

The specifications of the model with embedded junction were:

- Two 95 x 25 $Å^2$ graphene platelets in armchair configuration
- Two 220 x 35 $Å^2$ polymer blocks above and below the graphene platelets and junction region.
- Three molecular junctions (for C5OP or BP or ACN models)

Overall, about 37000 atoms constitutes the assembly of polymer, graphene and thermal linkers. Figure 88 depicts the typical initial model layout, from which flakes, junctions and polymer are clearly distinguishable.

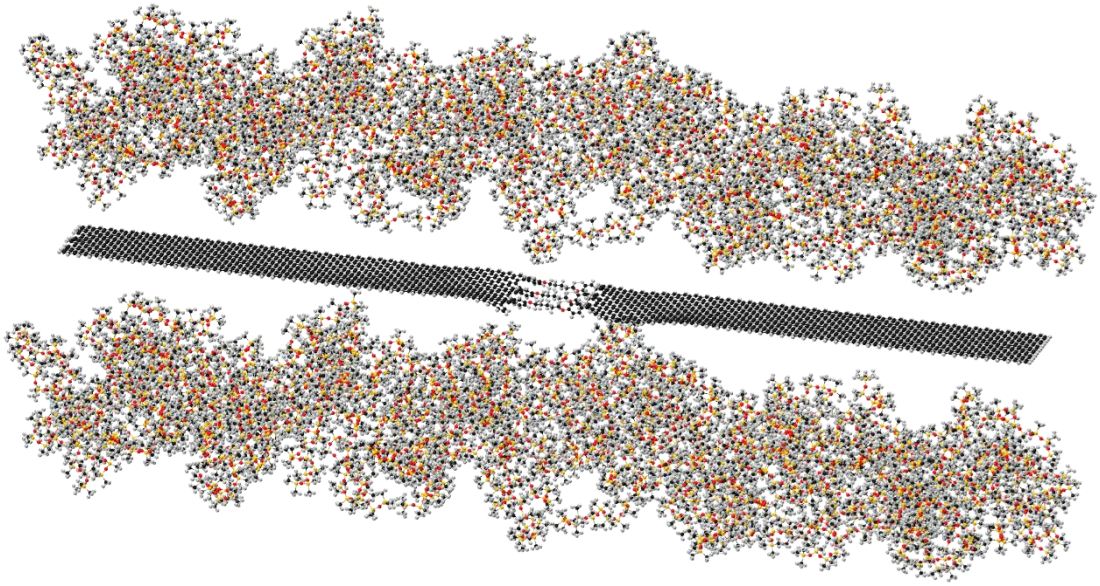

Figure 88. Initial design view of graphene flakes joint by three C5OP linkers with blocks of PDMS molecules above and below the junction. Color codes: carbon atoms in black, oxygen in red, hydrogen in light gray and silicon in yellow.

The thermal transport across graphene platelets and molecular junctions was determined through NEMD calculations. At the beginning of the simulation, a 500 ps NPT high-pressure stage was performed to relax the structure and bring the system close to the PDMS actual density, similarly to the polymer modelling described in paragraph 2.6. After this stage, the PDMS polymer and the graphene junction became a dense system, where the graphene junction is embedded in the surrounding polymer. The picture of Figure 89 represent how the polymer embeds the graphene junction. It is worth noting that the graphene sheets are not flat after the compression stage. This is due to the strong interaction of graphene with PDMS [187], where the larger mass of PDMS forces the thin graphene sheets (including junction) to fold and crease. This is fact realistic and well representative of actual flexible graphene sheets dispersed in a polymer matrix [188], as typically observed through transmission electron microscopy [189-191].

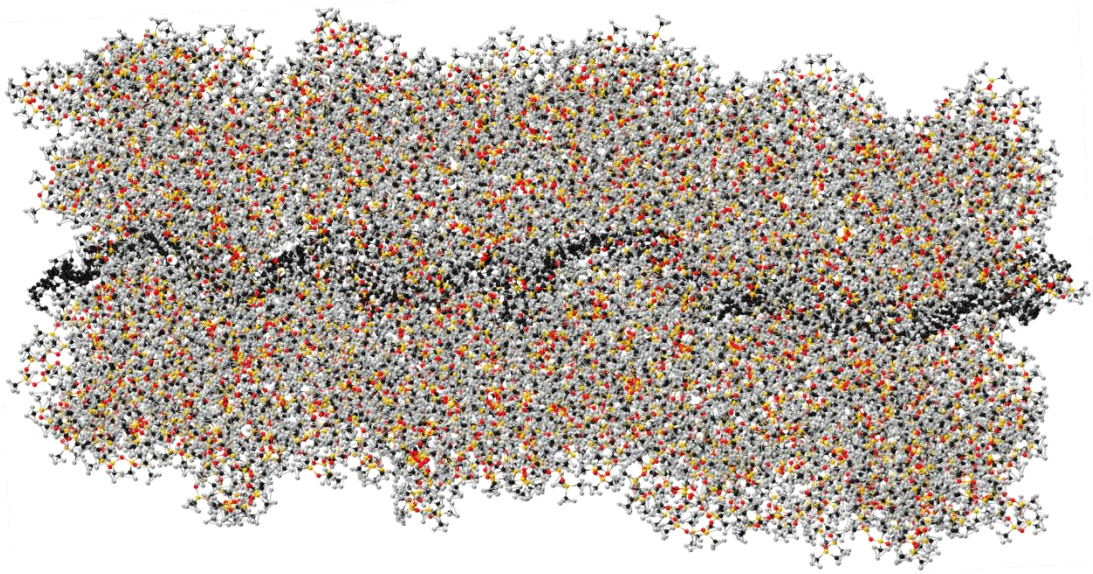

Figure 89. PDMS polymer surrounding graphene flakes jointed by three C5OP linkers (not clearly visible owing to the presence of polymer). Color codes: Carbon atoms in black, Oxygen in red, Hydrogen in light gray and silicon in yellow. The simulation box size is about 180x75 $Å^2$.

The application of NEMD method began with 1 ns of non-equilibrium pre-heating, as described in paragraph 2.2. in addition, followed 2.5 ns of simulation time, where energy and temperature information were collected. For this layout, two thermal layers, corresponding to the graphene sheets ends, acted as thermostats (Figure 90A) at 300 K and 330 K. The rest of the model, including the PDMS atoms, run in microcanonical ensemble with 300 K of initial temperature.

In suspended graphene junctions, the thermal linkers were the only possible paths from which thermal transport could occur between the hot and the cold ends of the system. The presence of polymer above and below the graphene platelets allows additional heat transfer modes, driven by VdW interaction. These include:

- Heat transfer between the graphene surface and the PDMS matrix (Figure 90A) parallel to graphene flakes. The large contact area made by graphene and polymer, from the upper and the lower surface of both flakes (corresponding to about 9500 $Å^2$) drains significant heat flux from the hot graphene flake to the matrix and from the matrix to the cold graphene. A detail is reported in Figure 90D where the heat is transferred through the surface in graphene ends.
- Transfer between molecular junctions and the surrounding polymer molecules (Figure 90B). This mode is proper of the presence of molecular junctions.
- Transfer by molecules trapped between the graphene tips in the center of the model. In this case, PDMS molecules acts in series with graphene tips (Figure 90C). This mode is relevant considering the creased shape that graphene assumes during simulation.

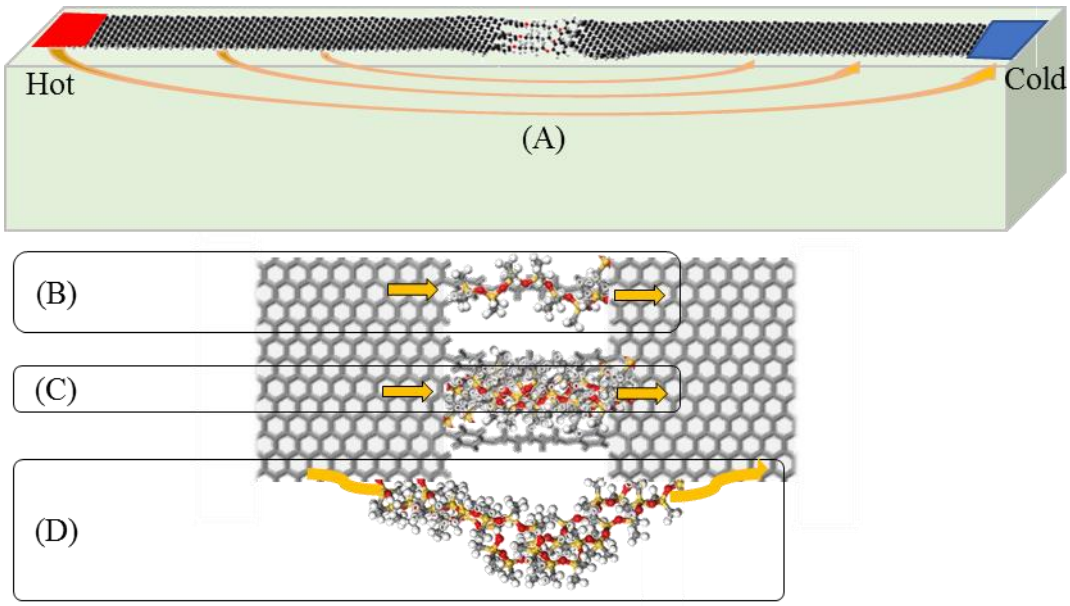

Figure 90. Heat transfer modes inside PDMS-embedded molecular junctions. (A) The green block represent the PDMS while yellow arrows the heat flux inside a thin PDMS contact layer. Red and blue region corresponds to hot and cold thermostats, respectively. (B) PDMS interacting with a C5OP covalent bound linker. (C) Trapped polymer driving heat flux between graphene ends. (D) Heat transferred by PDMS parallel to the graphene ends.

5.2. Results

For the four different systems described above, a representative simulation of the three replica was selected. Within this representative group of simulations, the energy transferred from the hot thermostat region to the cold thermostat region is reported in Figure 82. The plots for all the systems exhibits a linear behavior, however comparing those curves with the isolated junction, a larger noise features those curves, suggesting energy transfer to be affected by the variable conformation of PDMS chains around the junction. Moreover, the plots for the upper branch, corresponding to the injected heat from heat source, and the lower branch, which represents the drained energy from the heat sink, appear slightly asymmetrical, always below ± 10% from the average value, reported as thermostat error in Table 11. This phenomenon was attributed to the noise from the interaction of graphene with the polymer, because no clear trend emerges from replications where the upper branch and the lower branch exhibited alternately slightly higher slopes.

The energy flux slopes are reported in Table 11, the reported values herein are obtained for the entire set of replicas, each adopting a different velocities seed. Within the same table, the uncertainty from differences in slope between the upper and lower branches (thermostats error) and the uncertainty from replication (seed error) are reported. Moreover, the last column of Table 11 indicates the ratio between the heat flux enhancements from the linker adoption, over the linker-less condition.

The amount of the transferred heat reported in Table 11 indicates that the presence of molecular linkers induces an overall improvement in thermal transport between the graphene flakes. In fact, the aliphatic/aromatic C5OP molecular junction determines a moderate increase in heat flux, rising from 1.47 to 1.53 eV ps^{-1} with an average improvement of about 4 %. For the aromatic biphenyl, the heat flux rises up to 1.65 eV ps^{-1} and for the anthracene, a value of 1.78 eV ps^{-1} was calculated, with a gain of about 12 % and 21 % respectively.

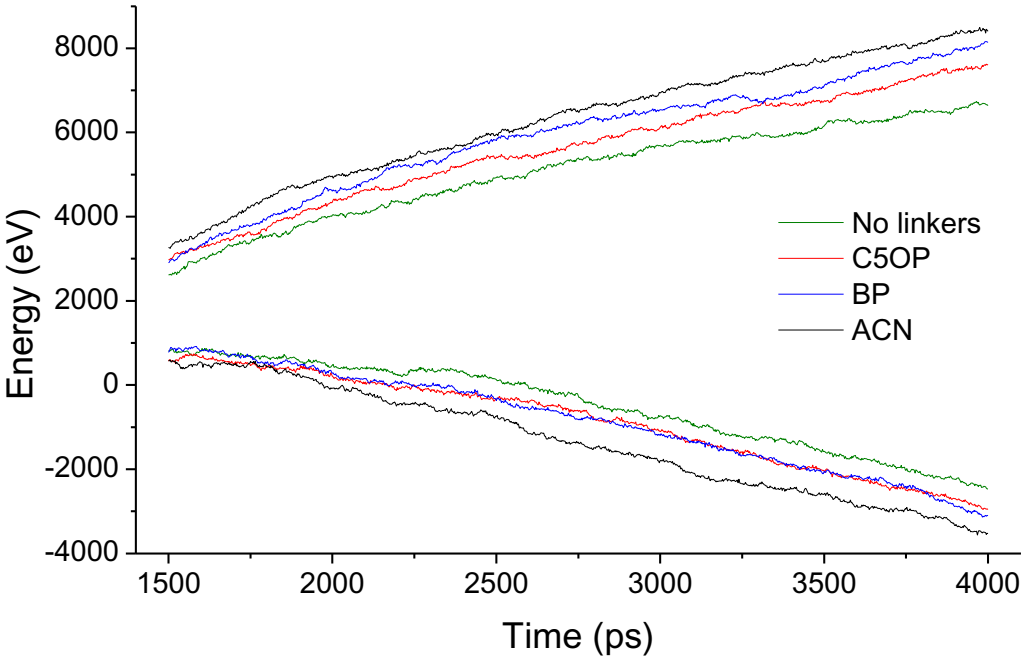

Figure 91. Energy flowing through thermostats as a function of the time for PDMS-surrounded graphene interfaces. Four simulations are taken as examples for three different linkers (C5OP, BP, and ACN) and a linker-less model (No linkers).

Table 11. Averaged Heat flux for different linkers in PDMS enclosed models. Average value, thermostat error, seed error from replicas and linker gain as the ratio of linker heat flux over linker-less heat flux value.

Model	**Energy flux [eV/ps]**			**Linker gain [%]**
	Average value	**Thermostat error** $\frac{\text{max} - \text{min}}{2}$	**Seed error** $\frac{\text{max} - \text{min}}{2}$	$\frac{\text{linkers} - \text{no linkers}}{\text{no linkers}}$
No linkers	1.47	± 0.07	± 0.02	-
C5OP	1.53	± 0.12	± 0.09	4.0
BP	1.65	± 0.14	± 0.08	12.2
ACN	1.78	± 0.11	± 0.06	21.1

For each junction type, the more representative simulation was selected and reported here. The temperatures of the graphene thermal layers, for set of junctions investigated it is reported in the following plots. Figure 92 reports the plot for the model without linkers, Figure 93 for C5OP bridged graphene sheets, Figure 94 for biphenyl linkers, Figure 95 and Figure 97 for Anthracene.
For all the following plots, empty dots indicated the points excluded from the fitting operation, as the one close to thermostats or across the junction. The model without any linker across the junction (Figure 92), reported an average temperature jump, evaluated from the projection of the slopes, as described in paragraph 2.2, of about 8.65 ± 0.57 K. By the heat flux calculation reported in Table 11 and the temperature difference across the junction (

Table 12), the thermal conductance reported a value of about 288 ± 21 MW m^{-2} K^{-1}.

Is noteworthy that all the conductance values reported herein are calculated as described in paragraph 1.1, considering the whole interface between graphene flakes and PDMS as contact area (9500 $Å^2$), thus representing the conductance of the whole system between the two thermostats as a contribution of ITC between graphene and PDMS and BTC trough edges.

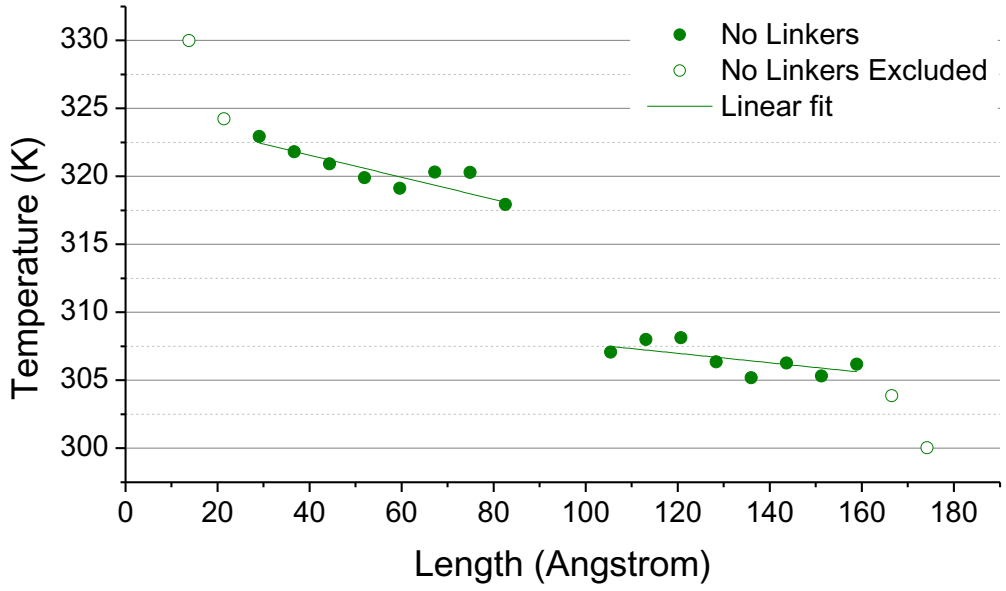

Figure 92. Thermal slabs temperature as a function of the spatial arrangement for polymer embedded graphene platelets without linkers.

Table 12. Thermal jump, seed error and thermal jump reduction in polymer surrounded junctions for all the investigated linkers.

Model	**Thermal jump [K]**		**ratio [%]**
	Average value	**Seed error** $\frac{\max - \min}{2}$	$\frac{\textbf{linker type}}{\textbf{no linkers}}$
No linkers	8.65	± 0.57	100
C5OP	7.46	± 0.31	86
BP	5.78	± 0.40	67
ACN	2.03	± 0.32	23

Adopting the same methodology for the other models where linkers were employed, the C5OP temperature jump (Figure 93 and

Table 12) was calculated of about 7.46 ± 0.31 K and consequently the thermal conductance increased to 346 ± 26 MW m^{-2} K^{-1}.

By the use of C5OP linkers, the temperature across the interface became the 86% of the initial value when no linkers were adopted. Thus, we can assume that the reduction in thermal jump is responsible for the overall increase in thermal conductance, quantified in about 20% for C5OP. This finding evidences a difference

if compared to the suspended molecular junctions where the heat flux drove the thermal conductance evaluation and the difference in heat flux was almost negligible.

It is also worth noting that temperature values across the junction were obtained much closer to the PDMS polymer than to the graphene platelets. This phenomenon may suggest that thermal exchange between molecular junctions and the surrounding polymer chains (Figure 90B) is particularly strong for this type of linker.

The temperature trend in biphenyl junction is reported in Figure 94. The temperature jump reported a reduction of about one third compared to the linker-less model, decreasing from 8.65 ± 0.57 K to 5.78 ± 0.40 K with biphenyl linker (as reported in

Table 12). The temperature plot indicated a strong coupling between the graphene flakes, where the calculated temperature of the junction progressively matches the linear fit of the temperature slabs in graphene.

Overall, for the three replicas, biphenyl jointed models reported a calculated thermal conductance of about 484 ± 55 MW m^{-2} K^{-1}, 68% more than the linker-less model, mainly from the contribution of thermal jump reduction (67%,

Table 12) than increased heat transferred, slightly over 12% (Table 11).

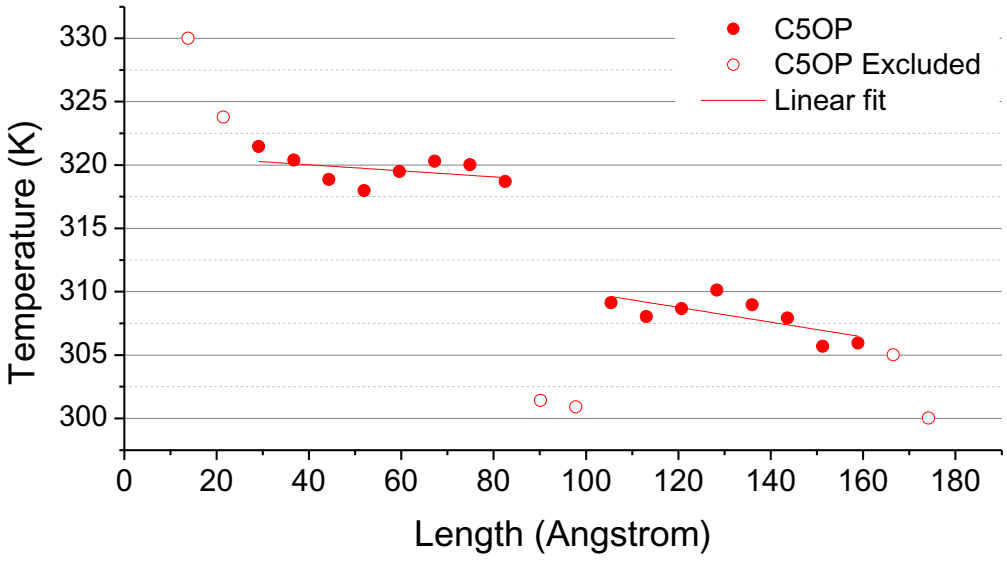

Figure 93. Temperature of thermal slabs as a function of the postion in C5OP grafted graphene platelets.

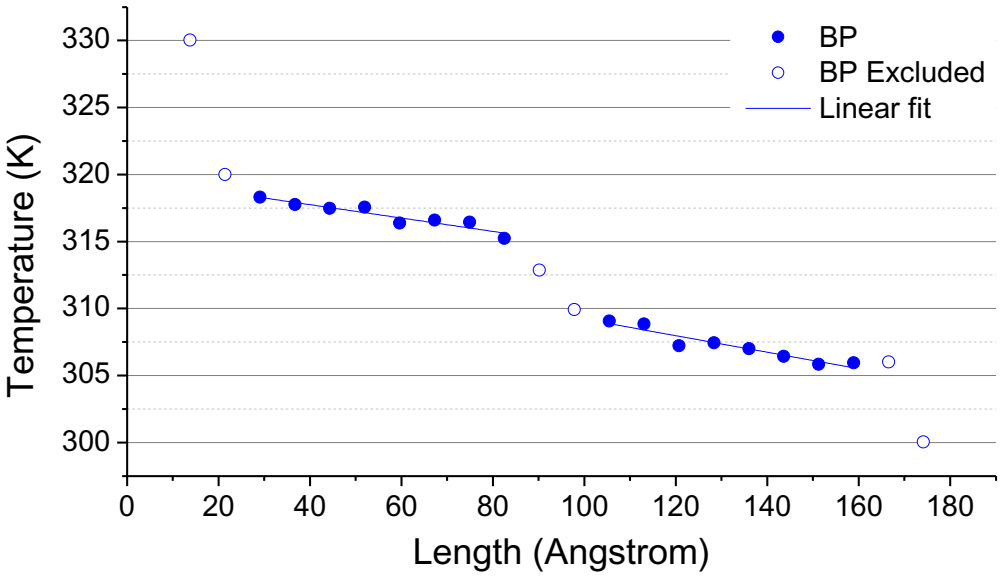

Figure 94. Temperature trend as a function of the slab position in polymer surrounded graphene junction joint by Biphenyl (BP) molecules.

Acene junction was also investigated with the purpose to find the upper-bound condition, as previously did in for suspended molecular junctions (paragraph 4.4). The temperature of the junction as a function of the slabs displacement is reported in Figure 95. In this case, a strongly reduced thermal jump (2.03 ± 0.32 K) is reflected into a superior thermal conductance (1363 ± 18 MW m^{-2} K^{-1}), corresponding to about 4.7 times the thermal conductance of the linker-less junction. All the thermal jumps and related details are reported in

Table 12.

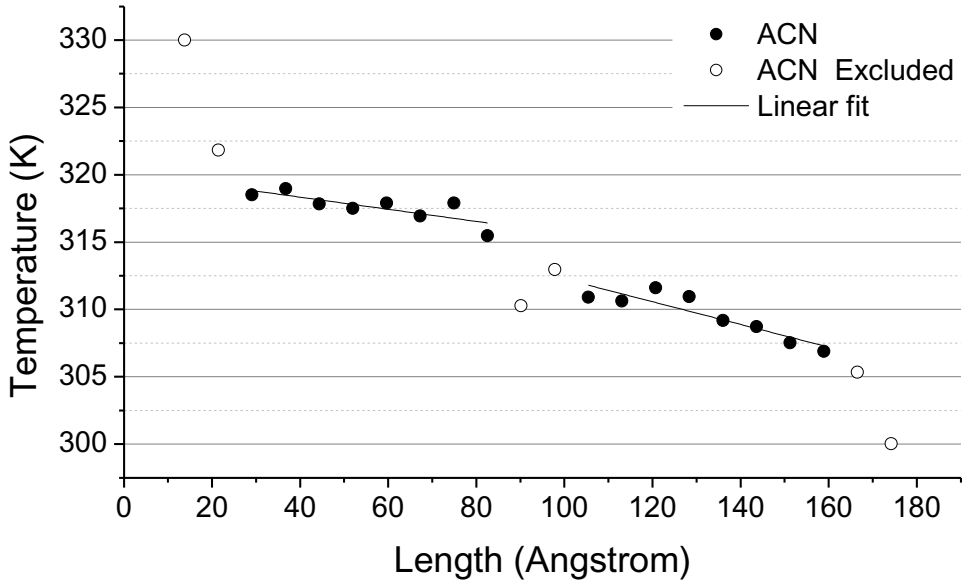

Figure 95. Temperature as a function of the position of thermal slabs for Anthracene (ACN) grafted graphene platelets in PDMS mass.

Figure 96 sums up the thermal conductances of the models for all the investigated linkers

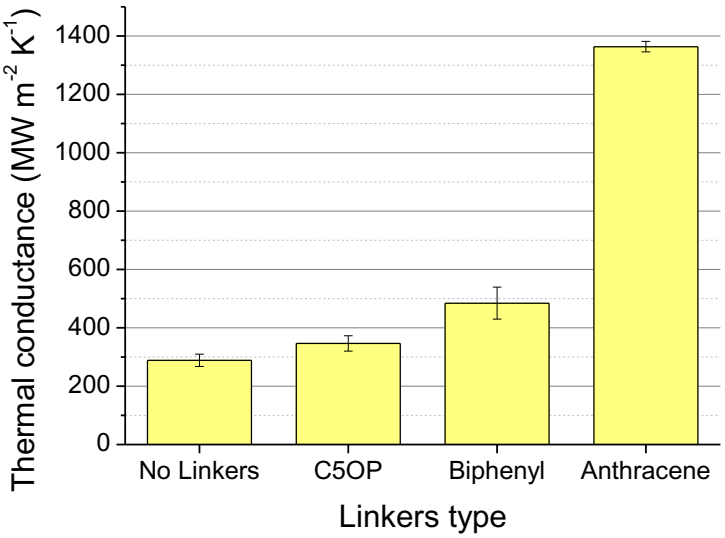

Figure 96. Thermal conductance between graphene platelets and PDMS polymer for graphene platelets without linkers (No Linkers), C5OP, Biphenyl and Anthracene.

Splitting the contribute in thermal transport from the PDMS mass and the molecular junctions represents a tricky issue, because the calculated thermal conductances are strongly dependent on the layout, in particular for the different heat transfer area, a parameter hard to quantify in molecules. A first example explains this issue: The thermal conductance of three Biphenyl molecules was calculated of about 1416 pW K^{-1} while the thermal conductance of the PDMS embedded junction without linkers, from the proposed value times the contact area, is about 31000 pW K^{-1}. The thermal parallel calculus from the equivalent thermal resistance (R =) ($R_{junction} * R_{PDMS}$) / ($R_{junction} + R_{PDMS}$) brings to the sum of the values, 32416 pW K^{-1}, less than half than the value calculated from the direct NEMD simulation of 66567 pW K^{-1}. The reason of this trend is due to the fact that, the thermal conductance at the interface in suspended molecules is mainly driven by the variation of the heat flux while in PDMS-embedded junctions the largest contribute comes from the reduction of the thermal jump. This is why; it is not enough consider such different systems each contribute as simply parallel objects.

Despite this premise, it is possible to consider the isolated heat flux contribution, neglecting the contribution of the thermal jump. In this case the heat flux from the suspended model of C5OP, BP and ACN, (with six molecules grafted, thus halved for this comparison), is about 0.05, 0.17 and 0.35 eV/ps, respectively. Table 13 reports the contribution from matrix (No Linkers) and the suspended molecules evaluated in chapter **Errore. L'origine riferimento non è stata trovata.** and embedded in PDMS in this chapter. From this analysis, the thermal contribution and matrix appears cumulative, with value very close to the direct method calculation, made of polymer and junction, and the case where these constituents were taken separately.

Table 13. Heat flux from direct method calculations (already reported in Table 11) and separate contribution from linkers and matrix

Model	**Energy flux [eV/ps]**			
(direct method)	**Direct method (average)**	**Thermostat error** $\frac{\max - \min}{2}$	**Three suspended linkers**	**No Linkers + Three suspended linkers**
No linkers	1.47	± 0.07	-	-
C5OP	1.53	± 0.12	+ 0.05 ± 0.01	1.52 (-0.6%)
BP	1.65	± 0.14	+ 0.17 ± 0.01	1.64 (-0.6%)
ACN	1.78	± 0.11	+ 0.35 ± 0.02	1.82 (+2.2%)

The very limited thermal jump across the acene-bound interface, induced to treat the junction as an equivalent continuous material, constituted by the two joined graphene sheets, thus neglecting the junction discontinuity. With this hypothesis, the temperature plot and linear fit depicted in Figure 97 was obtained.

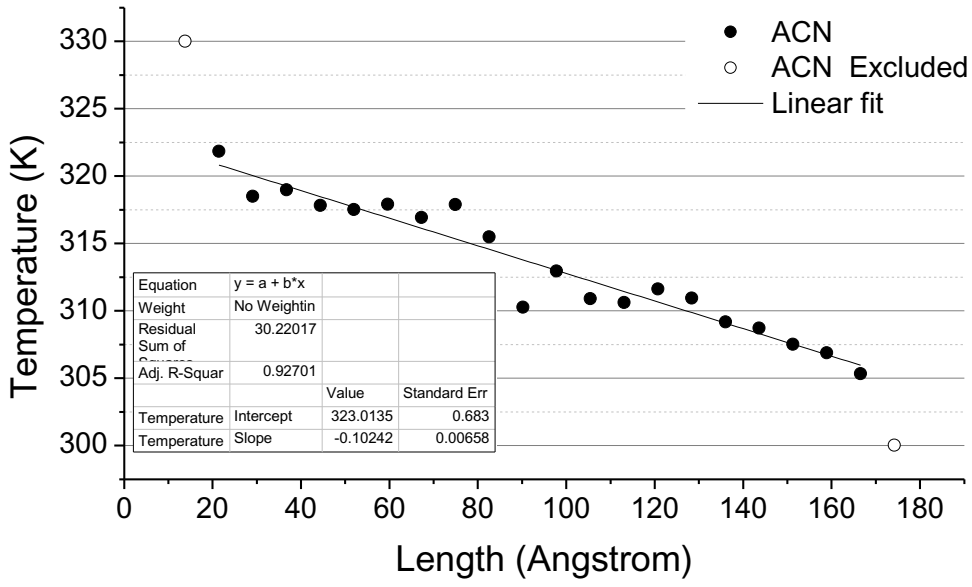

Figure 97. Temperature of thermal slabs as a function of the position. The linear fit among Anthracene (ACN) slabs temperature suggests the suppression of the thermal jump across the junction.

From the application of Fourier's law, the thermal conductivity of the joint graphene slabs was calculated at about 332 W m^{-1} K^{-1}. This value may be considered representative of a network of graphene flakes fully joined by acene junctions within

a PDMS matrix and represents a theoretical upper value for molecularly joined graphene nanocomposites.

5.3. Conclusions

The thermal conductance between graphene platelets embedded in PDMS polymer matrix has been evaluated trough NEMD simulations. As expected from the study of the suspended junctions, the linker type influenced the overall conductance value also within the PDMS matrix. The aliphatic/aromatic C5OP junction yields a thermal conductance improvement of about 20% compared to the unbound sheets, while aromatic structures provided better enhancements, in agreement with results reported in Chapter 4. In particular, Biphenyl junctions enhanced thermal conductance by about 68% while anthracene linkers, considered as a sort of upper bound case study, yielded an almost 5-fold increase in thermal conductance.

By the comparison of the results, it is noteworthy that that overall the transferred heat through the junction is increased only to about 22% in the most efficient junction, the anthracene case, and even less for biphenyl and C5OP. This finding indicates that most of the contribution in heat conductance improvement is a consequence of the reduction of the thermal jump across the junction, as shown in temperature trend plots. The thermal jump across the junction is the parameter that is mostly affected by the junction type; it progressively reduced to 86, 67 and 23 percent for C5OP, biphenyl and anthracene, driving the reduction of the thermal resistance. The strong dependence of the thermal conductance in PDMS/graphene model is related to both the length and the chemistry of the linker. On one hand, short linkers forces the flakes to keep a smaller distance between the platelets than longer ones and consequently the volume of interposed polymer is smaller. On the other hand, the length of the linker is not enough to justify the observations and it is therefore suggested that the chemistry of the linker strongly affects the efficiency of the junction, even within the polymer matrix. In fact, the thermal conductance in unbound platelets and the C5OP, which shares the same distance, it is increased by about 20% for the model that employs molecular linkers. Similarly, the comparison between the similar lengths for biphenyl and anthracene (difference of only 2.5Å), does not match with the large difference in thermal conductivities. Despite further studies would be required to clarify this issue, it appears likely that the differences are related to differences in phonon transfer across the interface. In particular, based on the phonon spectra results reported in Chapter 4 for suspended junctions, it is possible that the presence of fully aromatic junction decreases the phonon scattering across the junction also within the PDMS matrix. The contribution from the PDMS matrix and the suspended molecules evaluated in previous chapter and embedded in PDMS in this chapter indicated that the thermal contribution and matrix is almost cumulative. The values calculated by the direct method, made of polymer and junction, and the case where these constituents were taken separately, reported a difference with a maximum uncertainly of about 2.2%.

Therefore, the heat transfer from the graphene sheets to the matrix might be reduced, thus concentrating the heat flow through the graphene-graphene junctions, eventually leading to a thermally efficient percolation network.

Chapter 6

Multiscale modeling of thermal conductivity in nanocomposites

In this chapter, the thermal conductivity of composite materials made of PDMS and conductive nanoflakes are evaluated by a multiscale approach. Indeed, to evaluate the effective thermal conductivity at the macro-scale, the atomistic approach exploited for the molecular junctions in the previous chapters is not sufficient and should be complemented with higher scale methods.

The thermal conductance between PDMS and the conductive filler was calculated by MD calculations through the thermal equilibration method. The thermal conductance from MD calculation were then implemented in a Finite Element Model (FEM) analysis (paragraph 2.7) of the composites, where knowing the ITC value is crucial to estimate properly the thermal conductivity (TC) of the composite. The FEM model developed and described in this chapter enabled us to investigate the thermal conductivity of composite materials, with various fillers characteristics, such as the aspect ratio, volume fraction and thicknesses. Furthermore, the FEM model may easily be applied to other conductive nanoflakes: in this work a direct comparison between graphene (2000 W $m^{-1}K^{-1}$ [14, 15]) and borophene (75 W m^{-1} K^{-1} [192]) was carried out, to investigate the difference in the nanocomposites thermal conductivity.

6.1. Thermal conductance evaluation in platelets-polymer interface

To evaluate the ITC between polymer and filler, the thermal equilibration technique was employed, as described in paragraph 2.3. The composite modelling adopted a hybrid approach for the force fields, in which the PDMS modelling was based on the description presented in paragraph 2.6. The employed force field for PDMS was COMPASS while for the graphene we adopted optimized Tersoff [141] one and for borophene, a particular version of ReaxFF for Ammonium and Boron [127] was used. The coefficients for pair interactions were calculated by mixing rules, from Universal force field [140].

The ITC between PDMS and graphene nanoflakes was calculated as a function of the number of graphene layers, from one to seven layers. Literature works reported that in layered 2D materials, the ITC is affected by the thickness or number of layers [193]. Such phenomenon was predicted computationally [166], confirmed experimentally [194, 195]. A possible explanation of this finding was attributed to the progressively improvement in cross-plane phonon transmission among the low frequency modes, as the number of layers increases[193].To determine the ITC values for PDMS/borophene and PDMS/graphene interfaces, the asymptotic value of ITC convergence, occurring around six layers [166, 193] were considered.

The model layout, with the stacked layers of graphene over a block of PDMS polymer, it is depicted in Figure 98. Such systems adopt PBC in all directions meaning that actually both interfaces between nanoflakes and polymer engage in the thermal transport. Moreover, PBC creates a virtually continuous surface, without boundary issues, so the nanoflakes are designed to preserve the crystal periodicity even at boundaries. The specifications for a single layer graphene (SLG) model (1 in Figure 98) and all the derived family were a=99.64; b=47.48Å; featured by a contact area of about 4731 $Å^2$ computed twice in thermal conductance calculations due to the double interaction surfaces within the PBC assumption. The height c (1 in Figure 98) reported for 1-7 in Figure 98 varied from 84.6 to 105 Å, depending on layers stacking. Each layer of graphene, 3.4 Å thick, was made of 1760 carbon atoms, bringing the total amount of atoms, included PDMS, from 32180 of the SLG to 42740 atoms of the hepta-layer graphene.

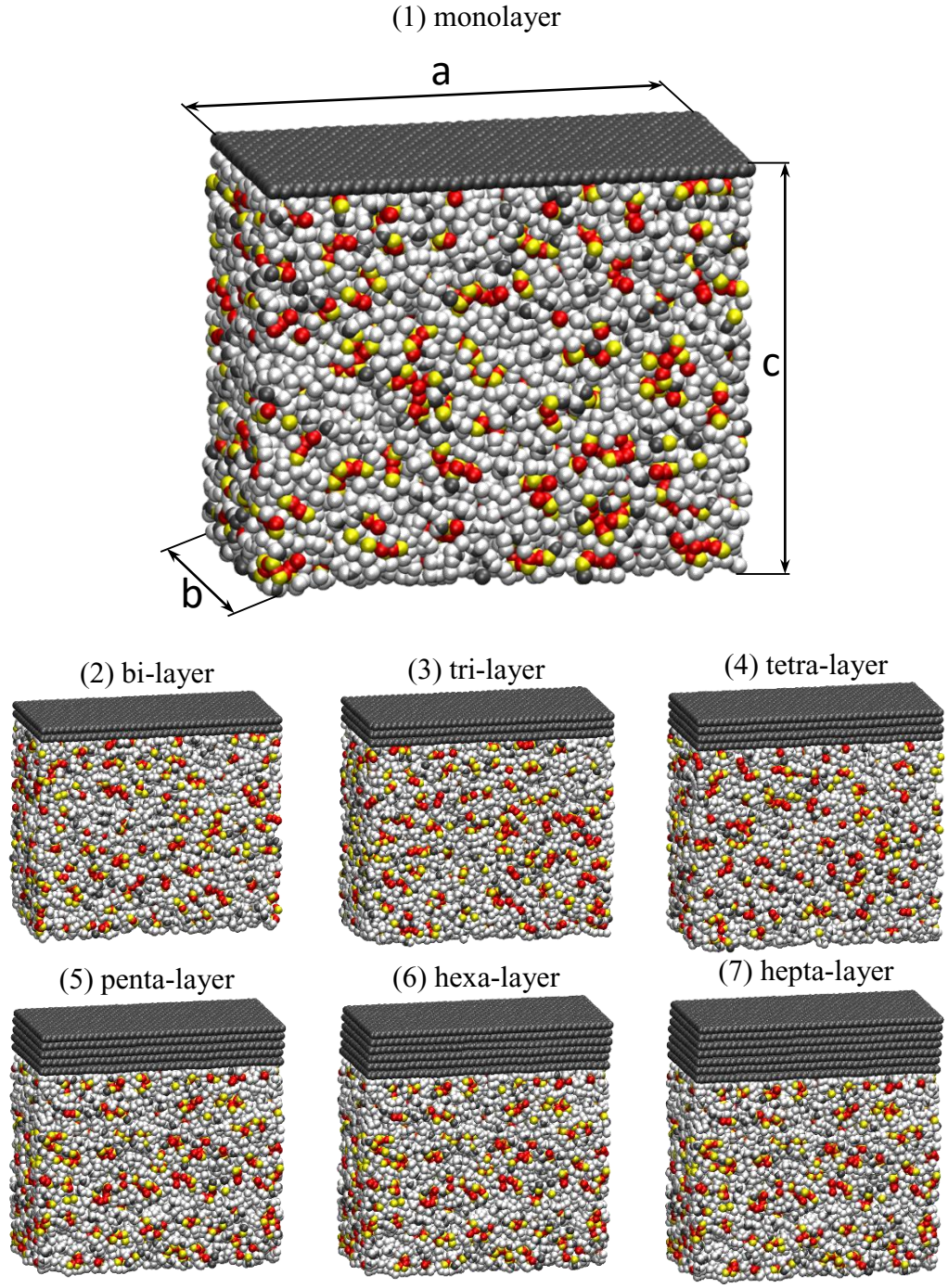

Figure 98. Model of 1 to 7 graphene layers stacked over PDMS polymer for ITC calculation. Parameters value a=99.64, b=47.48Å, c varied from, 84.6 Å for the monolayer (1), 88 Å for the bilayer (2), 91.4 Å for the tri-layer (3), 94.8 Å for the tetra-layer (4), 98.2 Å for the penta-layer (5), 101.6 Å for the hexa-layer and 105 Å for the hepta-layer. Wrapped view with VMD, color codes: carbon in grey, hydrogen in white, oxygen in red and silicon in yellow.

The temperature variations in the SLG and bi-layer graphene and PDMS polymer as a function of the time are illustrated in Figure 99. For the SLG the convergence of

temperatures occurs around 300 ps (a in Figure 99). We next calculated the normalized difference in decaying temperature (NDT), as plotted in the Figure 99 section b. NDT was calculated from the difference of the averaged temperature normalized on the initial value, as described in the method section (see equation 79). NDT plot table reports for each simulation the exponential fitting coefficient, used in equation 79, χ^2 and $R^{2\ are}$ statistical coefficients that indicate the accuracy of fit and the data variability, respectively.

For the case of bi-layer graphene, the temperature curves (section c in Figure 99) converge after around 400 ps of NVE simulations, with a reduced noise from velocity fluctuations with a better fitting of the NDT plot (section d in Figure 99) where χ^2 parameter is one order of magnitude lower than for SLG, indicating a better fitting operation.

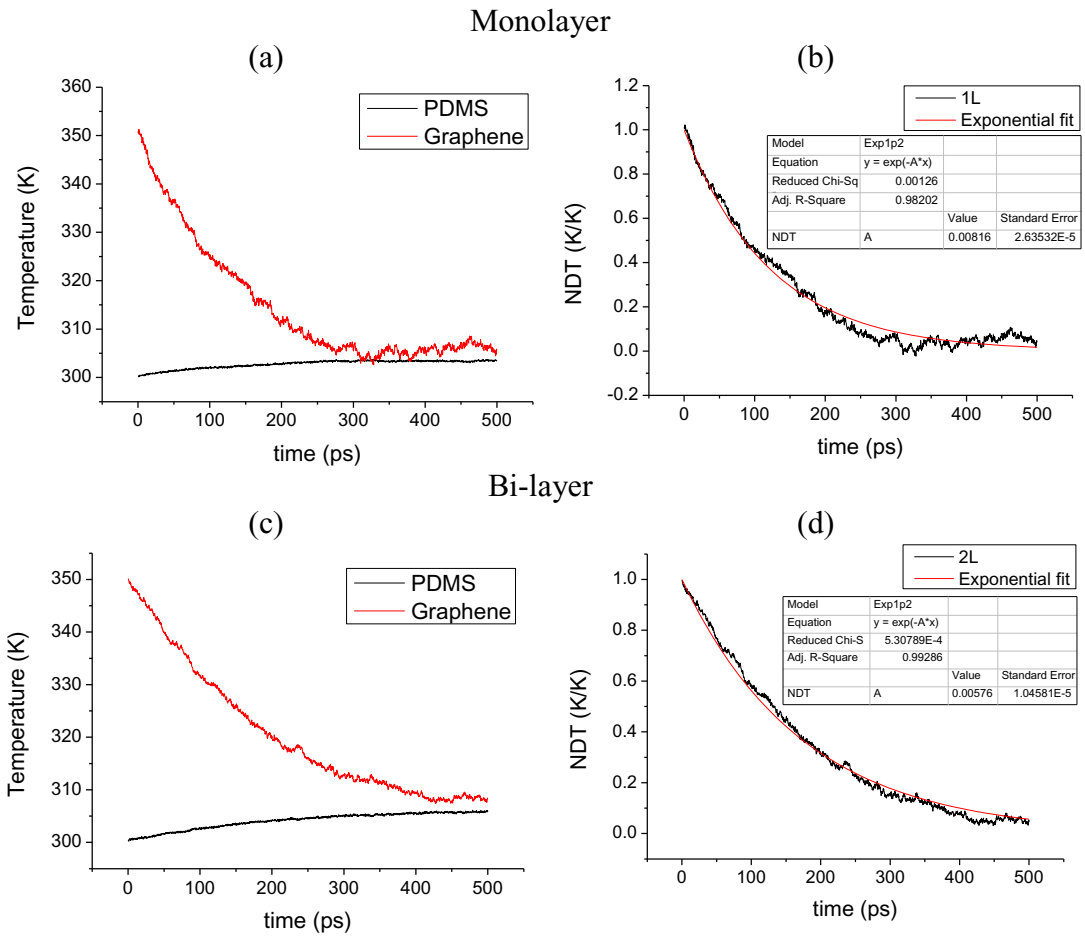

Figure 99. Actual temperatures (left) and normalized values (NDT, right) as a function of relaxation time for PDMS-graphene interface in the SLG and bi-layer graphene systems.

Figure 100 reports the temperature profiles as a function of the relaxation time for tri-layer (e,f) and tetra-layer (g,h) graphene/PDMS systems. From comparing these plots with the previous results, it can be seen that as the number of layers increases, the convergence in temperatures (e,h) occurs in longer times. At the same time, however, the polymer reaches temperatures up to 310 K indicating that heat

transfer occurs from the graphene to the polymer. The noise from temperature scattering observed in SLG and bi-layer, is slightly reduced thanks to larger amount of atoms. The exponential curves shown in Figure 100f,h report χ^2 values in the orders of $1e^{-4}$ and R^2 close to 1 indicating a closer fit of the exponential decay function with the simulations data, as compared with the previous results.

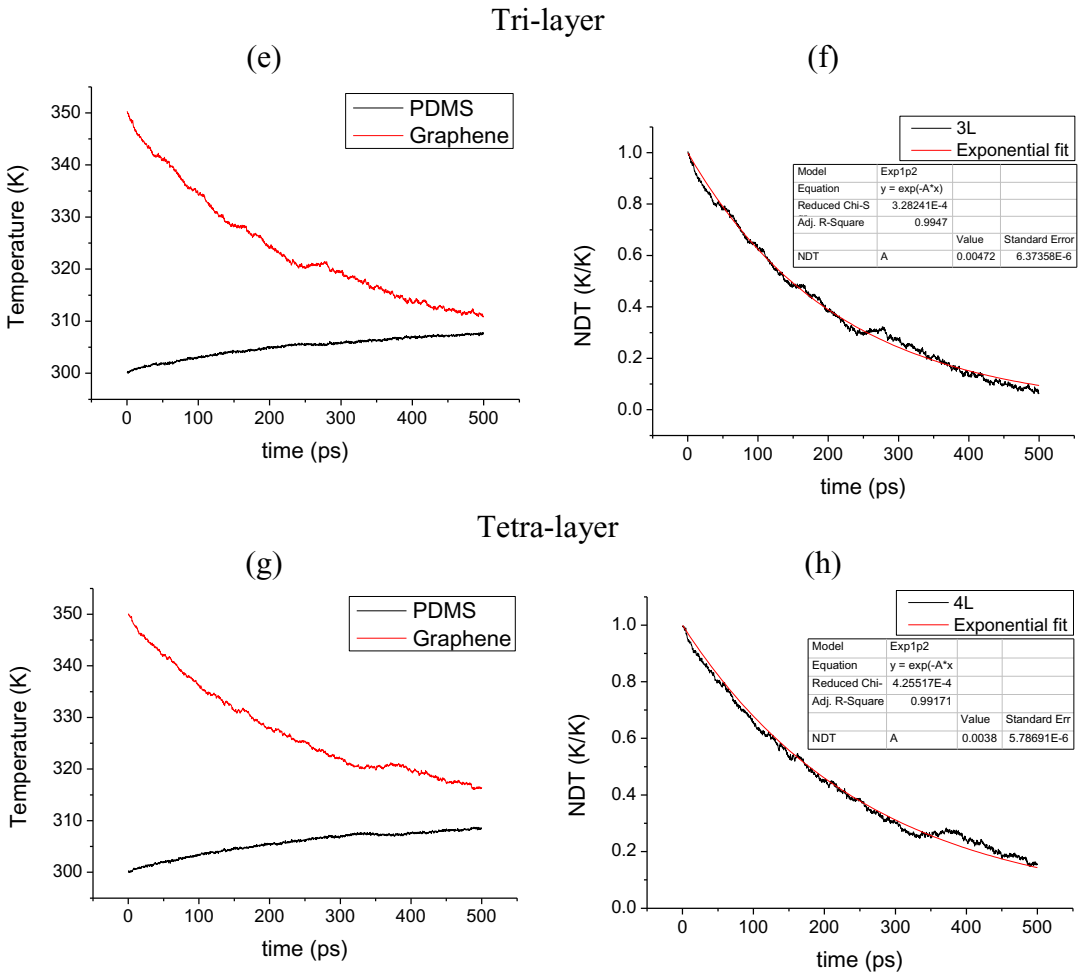

Figure 100. Temperature (left) and normalized values (NDT, right) with exponential fitting as a function of time for PDMS-graphene interface for tri-layer (e,f) and tetra-layer (g,h).

The plots for thicker layered systems as penta-layer, hexa-layer and hepta-layer, are reported in Figure 101. The convergence in temperatures between PDMS polymer and graphene occurs in longer time than the simulation end. Despite this observation, the PDMS temperature rises more than 10 K from the initial value (i,m,o in Figure 101), reflecting a larger amount of heat transferred through the interface. Thanks also to the large amount of atoms in graphene, the noise in plots is negligible and the fitting parameters within the exponential decay curve indicates a good match with simulations output (l,n,p) for χ^2 and R^2 values in the order of magnitude of $1e^{-4}$ and close to 1, respectively.

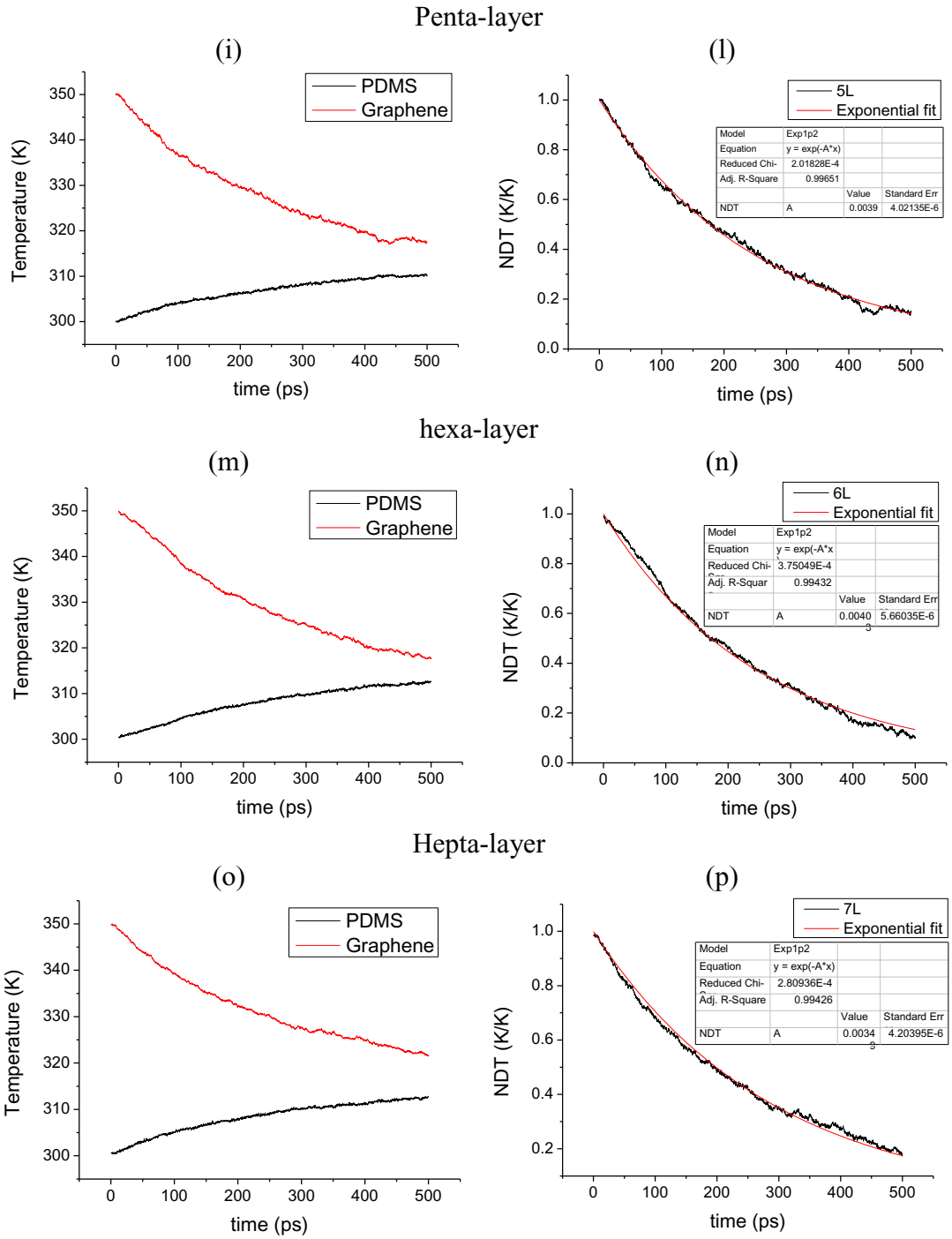

Figure 101. Actual temperature (left) and normalized values (NDT, right) with exponential fitting as a function of time for PDMS-graphene interface for penta-layer (i,l), hexa-layer (m,n) and hepta-layer (o,p).

From equation 78, as described in method, the ITC was calculated for the all systems. For every system, the calculations were conducted for 12 uncorrelated simulations and the temperatures were averaged. Figure 102 reports Table 14 data, which shows that the ITC increases from the SLG to multilayered structures, till it reaches a plateau and converges to a value of around 30 MW m^{-2} K^{-1} for the six and seven layered graphene/PDMS systems, in agreement with literature [166, 193]. The

converged value for the ITC was then employed in the FEM analysis to investigate the thermal properties of composite materials.

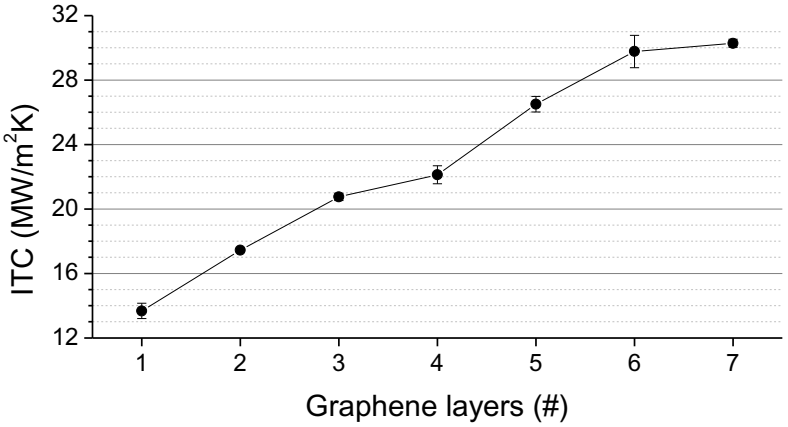

Figure 102. ITC as a function of layer stacking for graphene-PDMS interface, from Table 14 data.

Table 14. ITC in MD calculations as a function of graphene stacking for two different batch of six simulations.

Graphene layers	**ITC MW m^{-2} K^{-1}**			
#	**Batch 1**	**Batch 2**	**Average**	**Seed error** $\frac{\text{max} - \text{min}}{2}$
1	13.20	14.15	13.68	0.48
2	17.53	17.36	17.44	0.09
3	20.51	20.97	20.74	0.23
4	21.56	22.68	22.12	0.56
5	26.02	26.98	26.50	0.48
6	30.77	28.77	29.77	1.00
7	30.03	30.53	30.28	0.25

Analogously to graphene model, the heat transfer in the borophene/PDMS systems was also simulated. In this case, the number of borophene layers was limited to six because the convergence in the ITC as a function of number of layers happen earlier than the graphene/PDMS systems. The model layout, where the layers of filler are stacked onto PDMS polymer, it is depicted in Figure 103.

Similarly, for the borophene models reported in Figure 103, the parameters were, a=98.2 and b=43.68 Å, with a contact area of about 4289 Å^2. The height c varied with borophene layer thickness, around 4 Å/layer, from 92 Å for the monolayer to 112 Å for the hexa-layer. The differences in topology is due to the differences in lattice between graphene and borophene, where borophene atoms are packed over

two planes for each layer of borophene. 1260 atoms constitutes each layer of borophene, 500 atoms less than graphene, bringing the total amount of atoms from 31680 of the single layer borophene to 39780 atoms of the hexa-layer borophene.

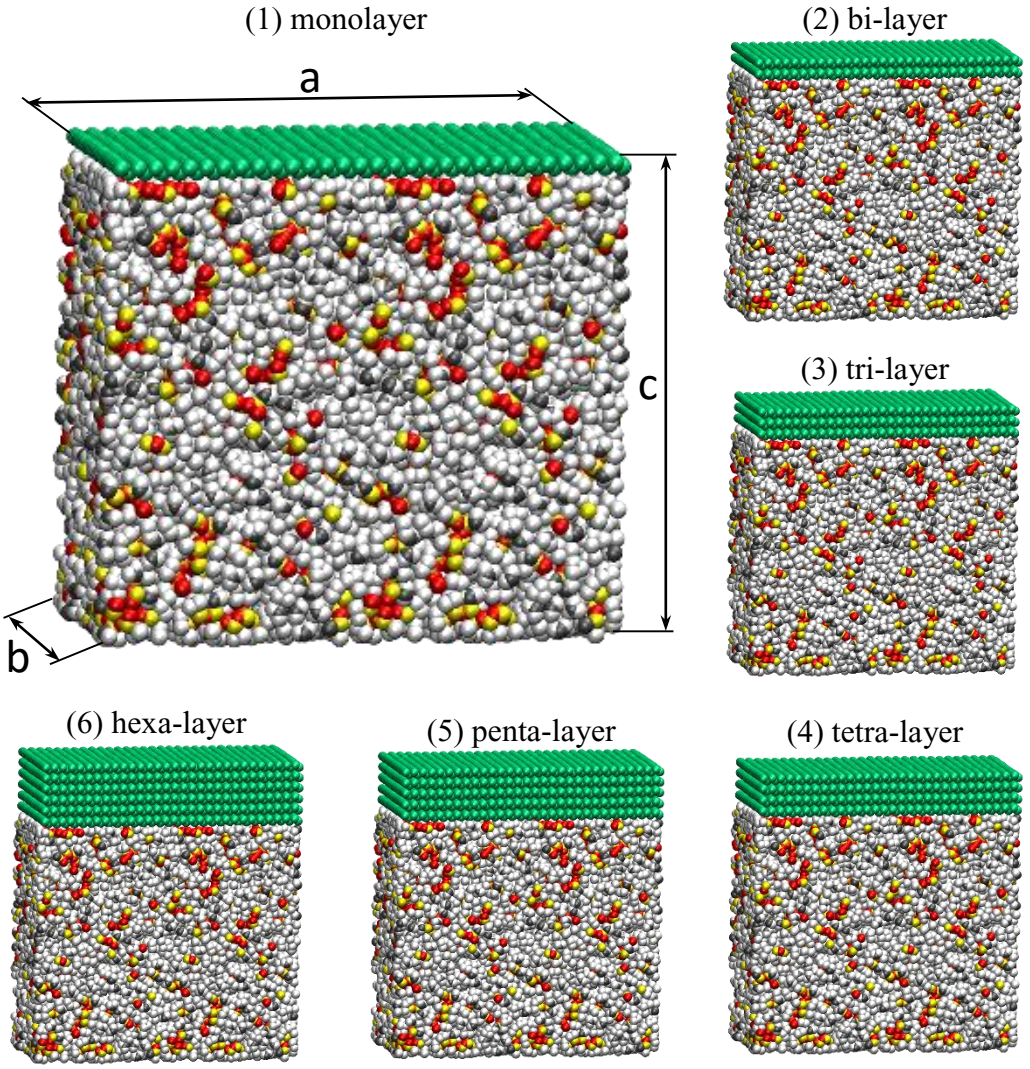

Figure 103. Models of 1 to 6 borophene layers stacked over PDMS polymer for ITC calculation. Parameters value a=98.2, b=43.68Å, c varied from, 92 Å for the monolayer (1), 96 Å for the bilayer (2), 100 Å for the tri-layer (3), 104 Å for the tetra-layer (4), 108 Å for the penta-layer (5) and 112 Å for the hexa-layer. Wrapped view with VMD, color codes: boron in green, carbon in grey, hydrogen in white, oxygen in red and silicon in yellow.

The temperature relaxation between borophene and PDMS was simulated for each model. The results for borophene/PDMS are grouped for the monolayers up to the tri-layer in Figure 104 and for more layered structures in Figure 105. From single-layer to three-layered borophene, the convergence of temperature was reached at about 150 ps (a,c,e in Figure 104). Despite the averaging of 12 independent simulations, these systems suffer from a quite large scattering of velocities, very

noticeable above 150 ps, where a steady temperature is expected. The reason of this finding can be attributed to the relatively small amount of atoms forming each layer (1260). In fact, such phenomenon is almost absent in PDMS, where 15210 atoms constitutes the polymer mass. The relatively noisy plot for borophene temperature drives the exponential fitting of NDT, which reflects relatively high values in χ^2 compared to other ones. Despite this consideration, the decay time can be evaluated from b, d and f in Figure 104.

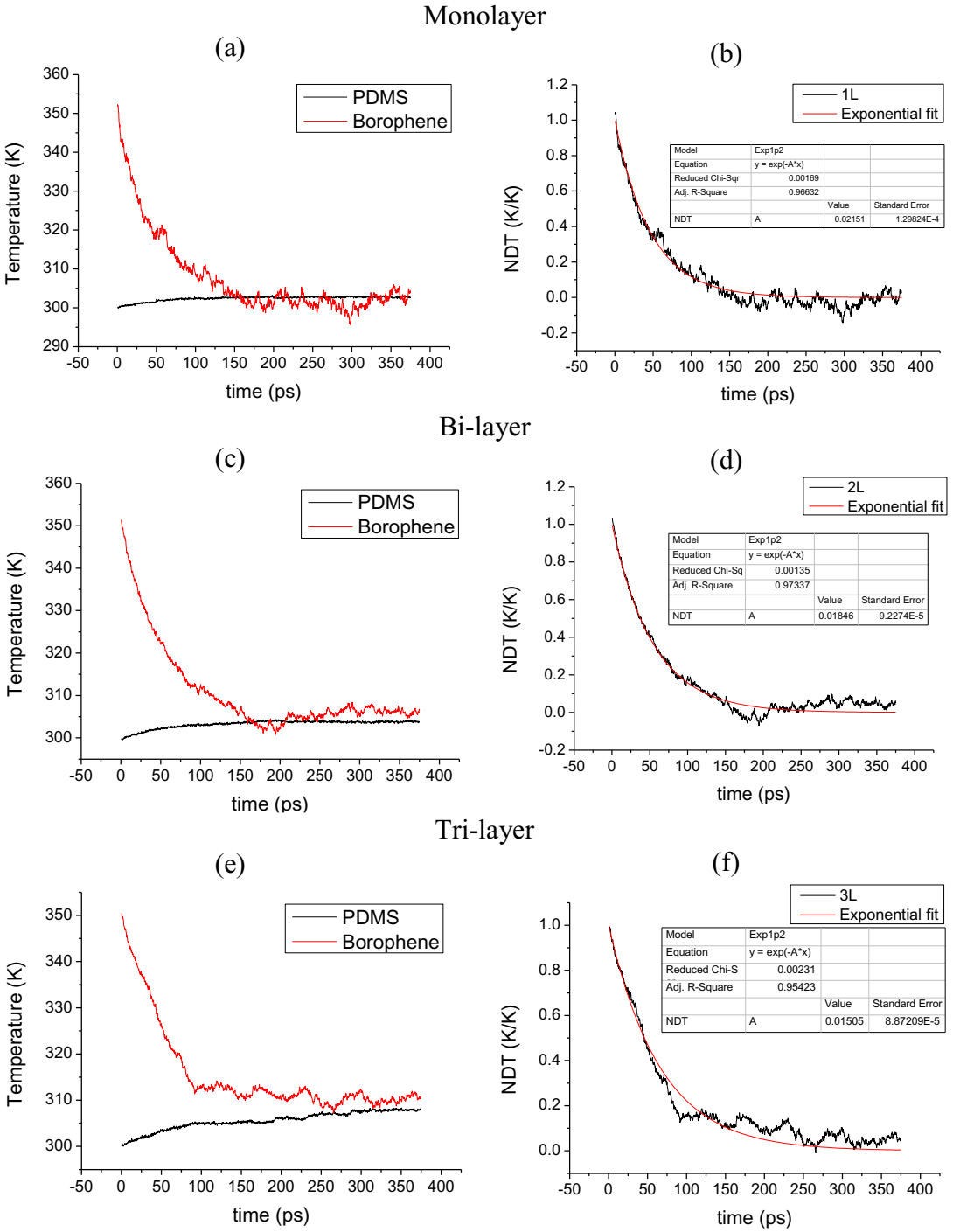

Figure 104. Temperature (left) and normalized values (NDT, right) as a function of time for PDMS-borophene interface in models made of up to three borophene layers.

For thicker stacked structures the convergence of the temperatures between PDMS and borophene occurs during simulation time (a,c,e in Figure 105), as the opposite of graphene where convergence occurred in longer time. Despite this observation, a clear dependency with layer staking can be observed. Finally, thanks to the larger number of atom, for the thicker borophene layers, smaller temperature fluctuations were recorded. The exponential fits of NDT are reported in Figure 105 b,d and f, reflecting better fits than the models with less stacked borophene layers.

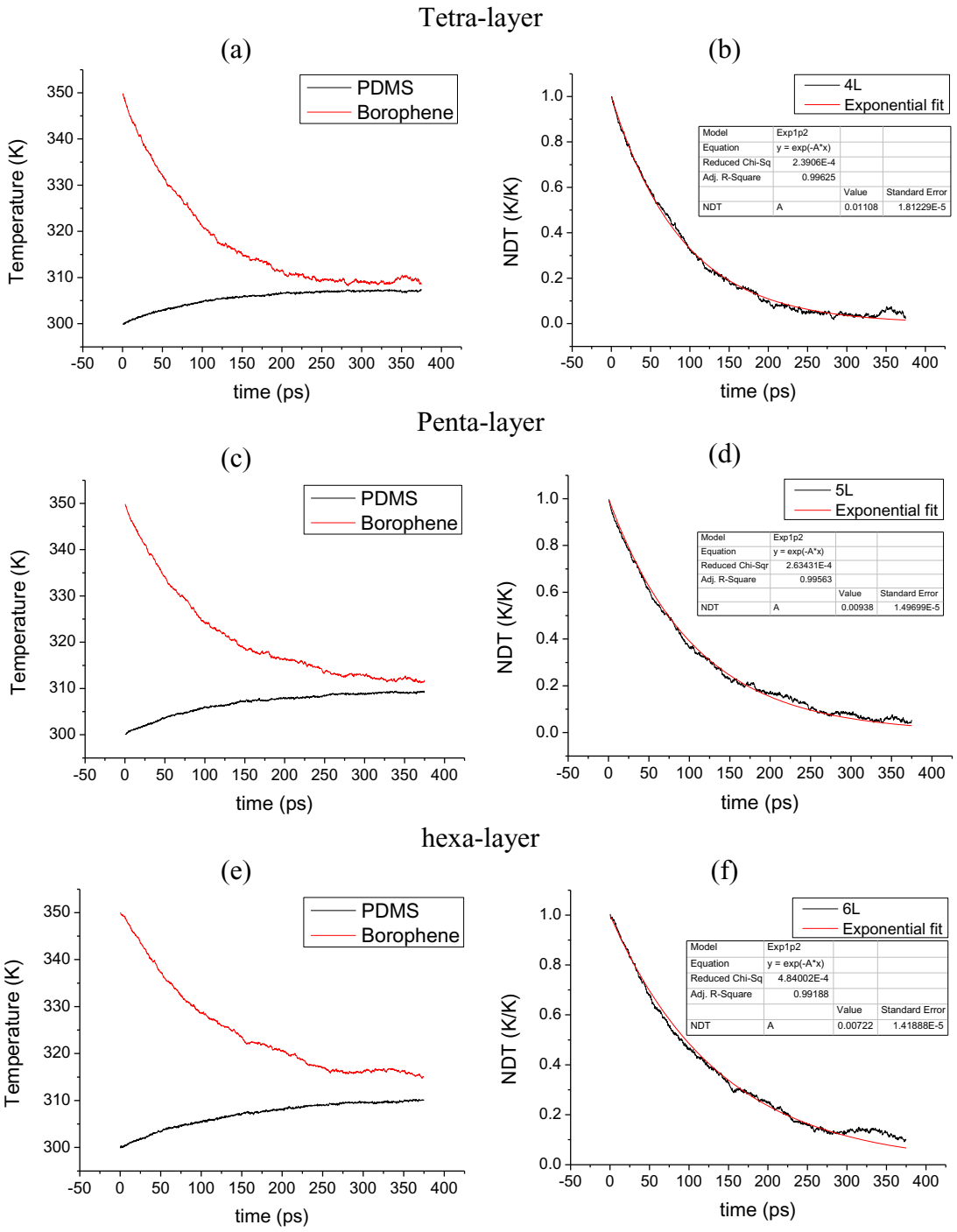

Figure 105. Temperature (left) and normalized values (NDT, right) as a function of time for PDMS-borophene interface in models made from three to six borophene layers.

Overall, the interfacial thermal conductance converged earlier than the case of graphene, just above three layers, as depicted in Figure 106. The ITC values, calculated by equation 78 are reported in Table 15. In FEM analysis, the ITC considered is the average of those within the converged range: 33 MW m^{-2} K^{-1}, which is 10% more than that of the graphene/PDMS interface.

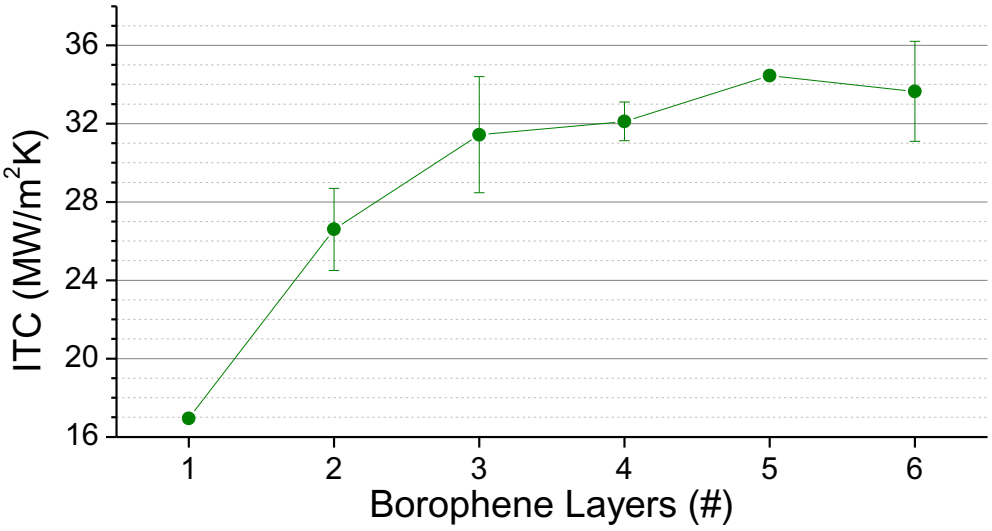

Figure 106. Borophene-PDMS ITC as a function of borophene layers, convergence starts from three layers stacked model. The line guides the eyes trough values reported in Table 15.

Table 15. Thermal conductances calculated as a function of graphene layers.

Borophene Layers	**ITC [MW m^{-2} K^{-1}]**			
#	**Batch 1**	**Batch 2**	**Average**	**Seed error** $\frac{\max - \min}{2}$
1	17.1	16.8	16.9	0.2
2	28.7	24.5	26.6	2.1
3	34.4	28.5	31.4	3.0
4	33.1	31.1	32.1	1.0
5	34.3	34.6	34.4	0.2
6	31.1	36.2	33.6	2.6

6.2. Effective thermal conductivity of composites

A series of RVEs were used for graphene and borophene fillers to calculate the effective thermal conductivity of composites, following the method described in paragraph 2.7. The parameters corresponding to the thermal properties are

summarized in Table 16, as they are known from literature. The ITC values acquired from the MD simulations discussed in the previous section were used to define the interfacial thermal conductance between the fillers and the polymer matrix.

Table 16. Parameters for composite modeling adopted in FEM analysis

Parameter	**value**	**unit**	**source**
Graphene TC	2000	$W\ m^{-1}\ K^{-1}$	[14, 15]
PDMS TC	0.15	$W\ m^{-1}\ K^{-1}$	[174]
Borophene TC	75	$W\ m^{-1}\ K^{-1}$	[192]
Graphene-PDMS ITC	30	$MW\ m^{-2}\ K^{-1}$	MD, section 6.1
Borophene-PDMS ITC	33	$MW\ m^{-2}\ K^{-1}$	MD, section 6.1

The main assumptions that have been made in the FEM analysis are as follows:

- Two materials, graphene and borophene were modelled as randomly oriented, rigid disks as described as described in paragraph 2.7.
- Three filler loadings (volume fractions), 1%, 2% and 4% were considered.
- Four aspect ratios (disc's diameter to thickness ratio), 25, 50, 75 and 100 (Figure 107) were considered.
- Three thicknesses, 1, 10 and 100 nm were considered.
- The constructed models are all periodic, meaning that if a particle path a boundary surface of the RVE it will enter from the opposite surface, so by putting the RVEs side by side all the fillers will show perfect disc geometries.

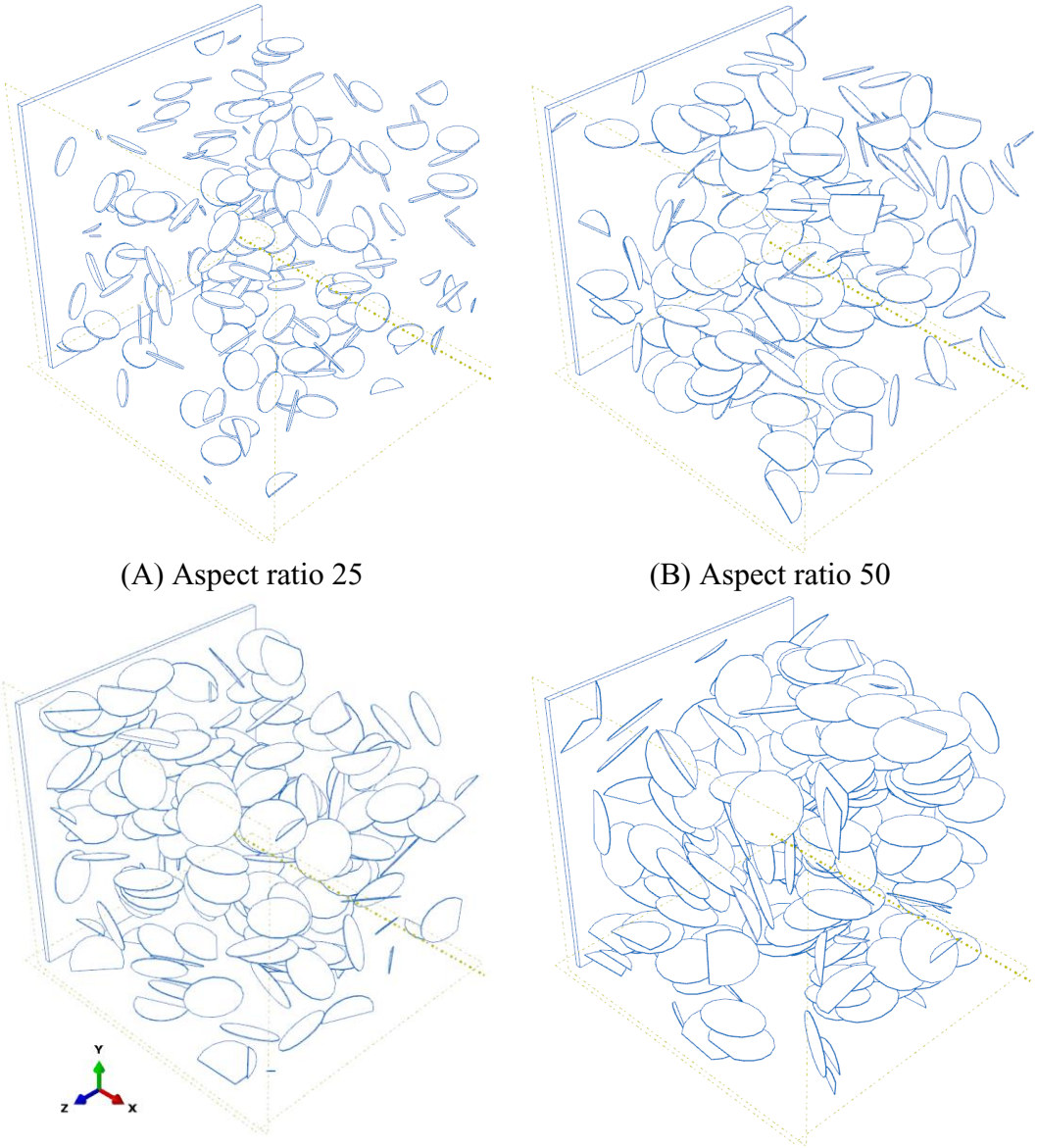

(A) Aspect ratio 25 (B) Aspect ratio 50

(C) Aspect ratio 75 (D) Aspect ratio 100

Figure 107. Conductive particles displacement inside RVE in 1% filler loading and thickness 1 for different aspect ratios. The flat surface in YZ plane drives the eye in three-dimensional representation.

Every FEM simulation reported a temperature profile as depicted in Figure 108. Such representations highlight thermal anisotropy caused by different fillers configurations inside the RVEs. The coldest (blue color) region was set with a temperature of zero, and so the red color represents the hottest zone, from which the established ΔT was calculated and was used to extract the effective thermal conductivity.

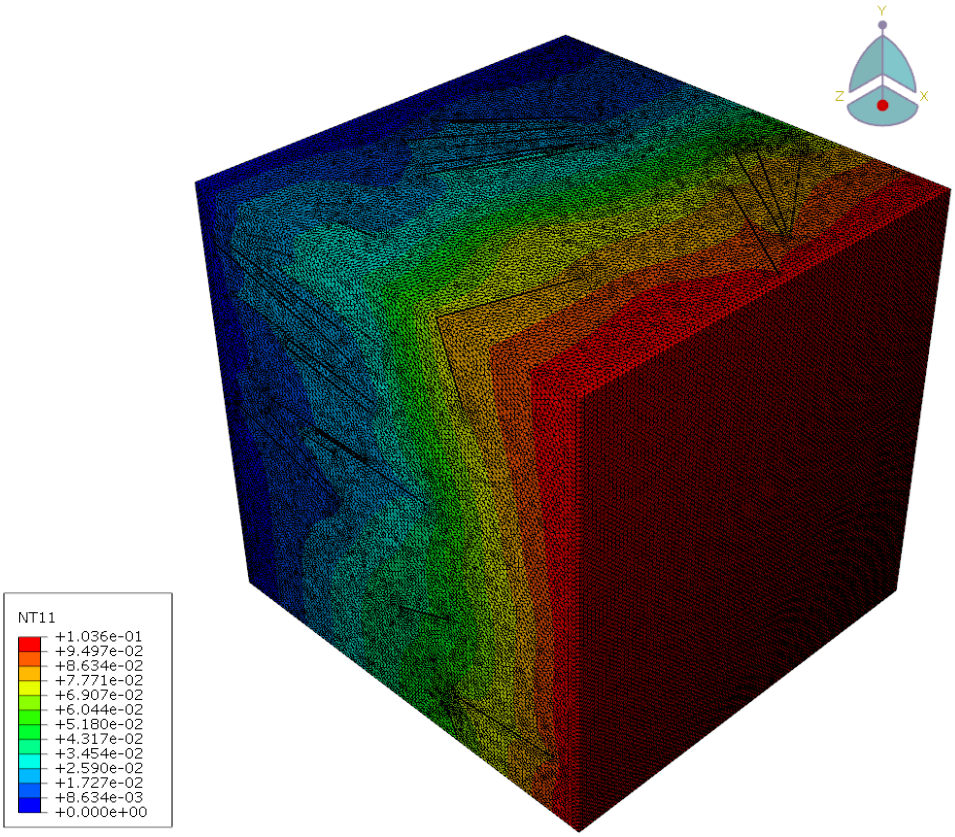

Figure 108. Temperature profile in meshed RVE for 4% graphene filler loading, thickness 1 nm and aspect ratio 100.

The following results are ordered by filler thickness and coupled for graphene and borophene to simplify the comparison between these fillers. Figure 109 and Table 17 reports values for platelets of 1 nm thickness. Figure 110 and Table 18 summarizes 10 nm thickness results while Figure 111 and Table 19 reports values for the thickest fillers of the set (100 nm).

For all the tables ΔT_{boroph} indicates the ΔT in RVE for borophene, ΔT_{graph} indicates the ΔT in RVE for graphene, and similarly, TC_{boroph} indicates the TC of borophene, TC_{graph} indicates the TC for graphene.

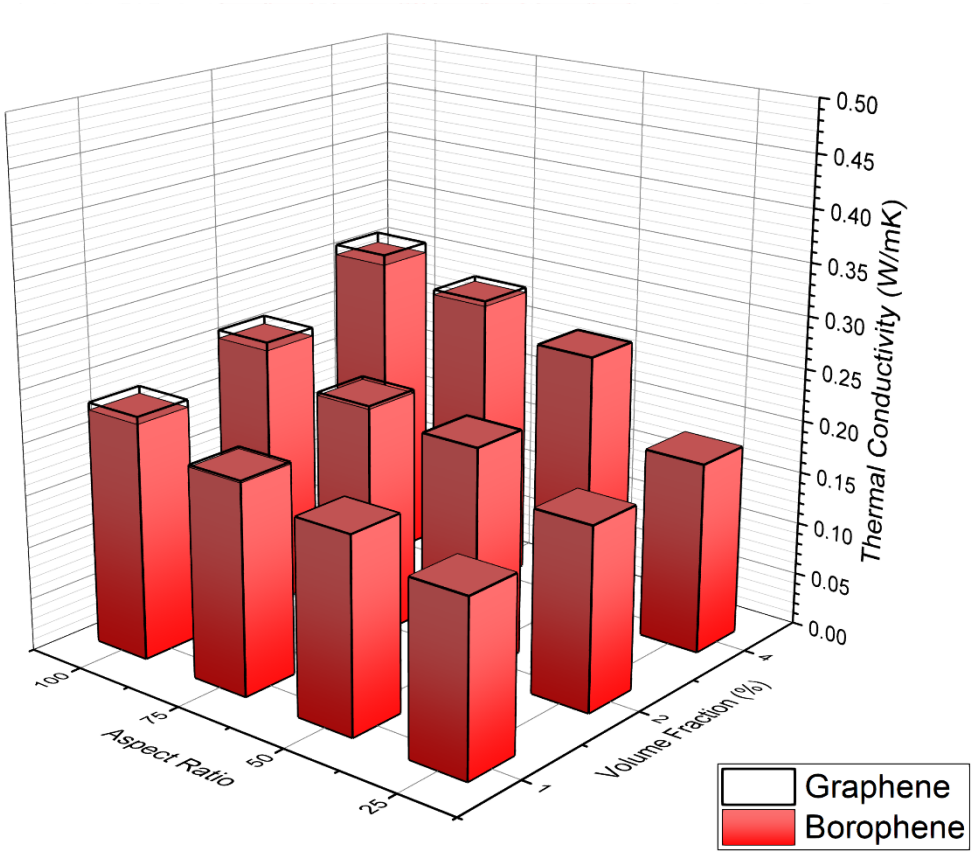

Figure 109. FEM calculated TC of PDMS composites with 1 nm filler thickness. Solid red shades for borophene and black line for graphene. Data from Table 17.

Table 17. RVE size, ΔT and TC of PDMS composites with 1 nm filler thickness calculated in FEM analysis.

Volume fraction	**Aspect Ratio**	**RVE side [nm]**	**ΔT_{boroph} [K]**	**ΔT_{graph} [K]**	**TC_{boroph} [$Wm^{-1}K^{-1}$]**	**TC_{graph} [$Wm^{-1}K^{-1}$]**
1%	25	202	0.122	0.123	0.165	0.164
	50	321	0.173	0.173	0.185	0.185
	75	420	0.210	0.208	0.200	0.202
	100	509	0.226	0.219	0.225	0.232
2%	25	160	0.091	0.092	0.175	0.174
	50	254	0.119	0.118	0.214	0.215
	75	333	0.149	0.147	0.223	0.226
	100	404	0.160	0.154	0.253	0.261
4%	25	127	0.069	0.070	0.183	0.182
	50	202	0.079	0.078	0.256	0.257
	75	265	0.093	0.092	0.282	0.287
	100	321	0.106	0.103	0.300	0.310

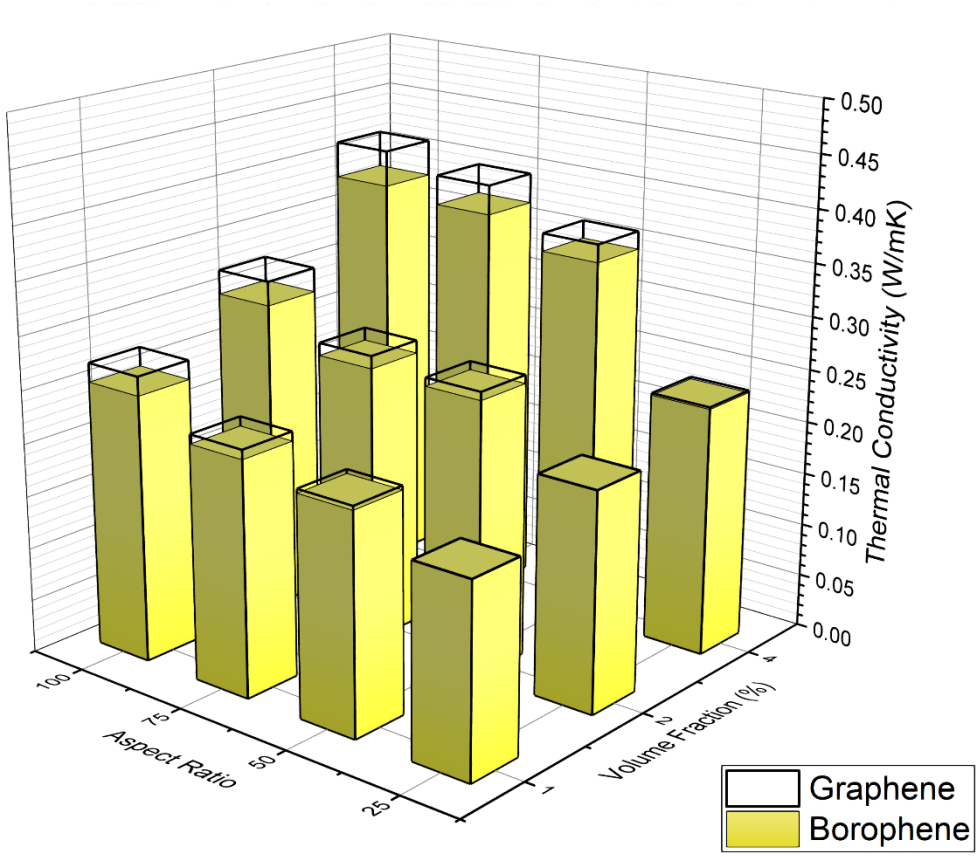

Figure 110. FEM calculated thermal conductivities of PDMS composites with 10 nm filler thickness. Solid yellow reports borophene TC while black line graphene TC. TC, ΔT and RVE size are reported in Table 18.

Table 18. FEM calculated ΔT and TC of PDMS composites with 10 nm filler thickness.

Volume fraction	**Aspect Ratio**	**RVE side [nm]**	**ΔT_{boroph} [K]**	**ΔT_{graph} [K]**	**TC_{boroph} [$Wm^{-1}K^{-1}$]**	**TC_{graph} [$Wm^{-1}K^{-1}$]**
1%	25	202	0.113	0.112	0.179	0.180
	50	321	0.155	0.152	0.207	0.211
	75	420	0.189	0.182	0.222	0.231
	100	509	0.202	0.188	0.252	0.270
2%	25	160	0.078	0.077	0.206	0.207
	50	254	0.098	0.095	0.259	0.267
	75	333	0.127	0.121	0.262	0.274
	100	404	0.136	0.126	0.297	0.320
4%	25	127	0.054	0.053	0.235	0.237
	50	202	0.058	0.055	0.347	0.364
	75	265	0.071	0.066	0.371	0.399
	100	321	0.084	0.077	0.379	0.413

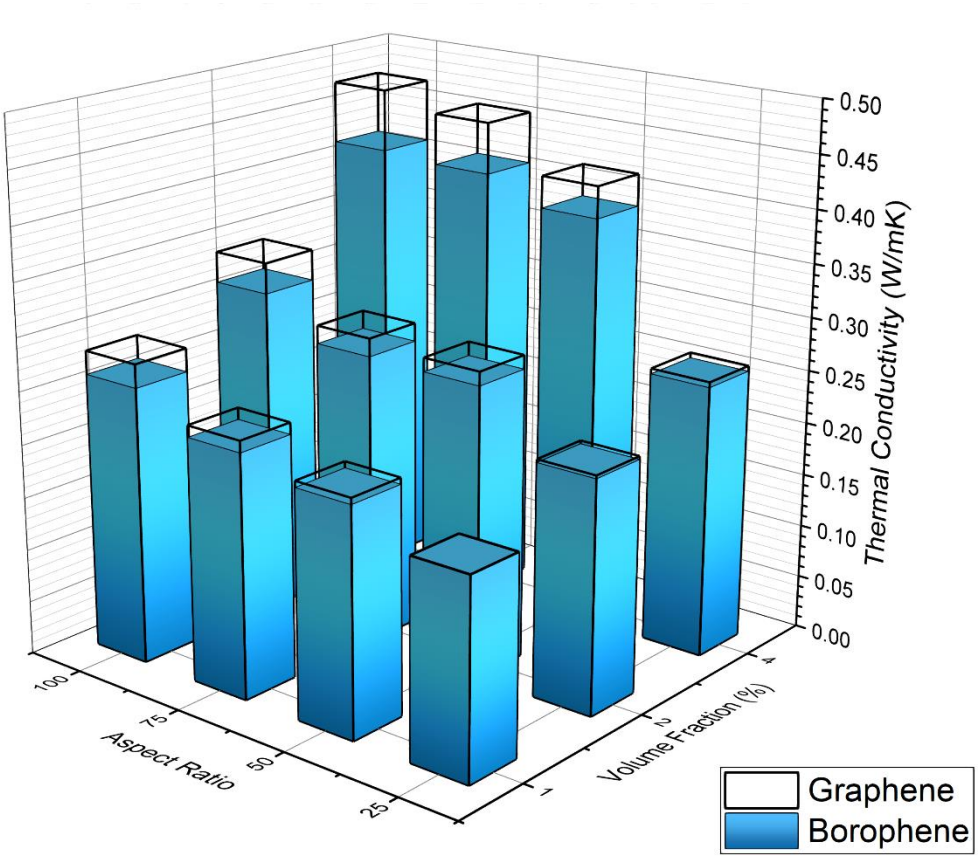

Figure 111. FEM calculated TC of PDMS composites with 100 nm filler thickness. Solid light blue represents borophene and black line for graphene. Data from Table 19.

Table 19. FEM calculated ΔT and TC of PDMS composites with 100 nm thick filler.

Volume fraction	**Aspect Ratio**	**RVE side [nm]**	**ΔT_{boroph} [K]**	**ΔT_{graph} [K]**	**TC_{boroph} [$Wm^{-1}K^{-1}$]**	**TC_{graph} [$Wm^{-1}K^{-1}$]**
1%	25	202	0.110	0.109	0.184	0.185
	50	321	0.150	0.146	0.213	0.219
	75	420	0.183	0.175	0.229	0.240
	100	509	0.196	0.180	0.260	0.282
2%	25	160	0.073	0.072	0.218	0.221
	50	254	0.093	0.089	0.273	0.286
	75	333	0.121	0.114	0.274	0.291
	100	404	0.131	0.119	0.309	0.338
4%	25	127	0.049	0.048	0.256	0.261
	50	202	0.052	0.048	0.388	0.418
	75	265	0.064	0.057	0.410	0.458
	100	321	0.077	0.068	0.414	0.472

All the simulation results reported higher thermal conductivities than the neat PDMS (0.15 W m^{-1} K^{-1}) demonstrating that all the investigated parameters contributed the thermal conductance improvement. The volume fraction of the filler, as known from literature, confirmed as the typical parameter to tune to improve heat transfer in composite materials where 4% of filler about doubles the TC compared to 1% condition.

Experimental investigation on PDMS and graphene composites were performed by Zhao and coworkers [196], with a 0.7% graphene content in weight more than doubled the TC, passing from 0.19 W m^{-1} K^{-1} of neat PDMS to about 0.45 W m^{-1} K^{-1} of graphene sheet composite. Such remarkable TC improvement was attributed to the creation of a tight percolation network of graphene platelets. Such platelets were obtained by foaming, a technique that allowed the creation of particles with length in the range of some micrometers by about 3 nm of thickness. In 2017, Tian [197] and coworkers adopted silicone rubber (SR) with three different graphene platelets concentrations obtained by mechanical blending and curing. The platelets were about 3 nm thick and about 5 by 10 micrometers in lateral size. The maximum concentration of graphene platelets, 0.72% in weight determined an increase of the TC from 0.2 W m^{-1} K^{-1} of SR to 0.3 W m^{-1} K^{-1}. The comparison between the work of Zhao [196] and Tian [197] pointed out how the particle displacement and consequently interaction between particles impacts on the composite TC. Li and coworkers [106] reviewed several works on GRM materials, featured by oriented particles, three dimensional structures or segregated particles, evidencing how the thermal conductivity enhancement in three dimensional structures is about five times than segregated structures. Despite this consideration, high TC materials made of segregated particles as the thermoplastics realized by Alam and coworkers [198] or the epoxy resin from Shahil and Balandin [199] pays the drawback of filler loadings in the order of magnitude of one tenth or more.

In the proposed RVE, no specific interaction in filler-filler contact is considered, thus the TC of the material is much closer to the segregated particles in classical nanocomposites, as deeply explained in Burger's work [11]. For thin fillers the TC more than doubled the polymer one (Table 17) and in the thickest filler, the graphene based composites improved TC by about three times (Table 19).

Overall, graphene-based composites reported higher thermal conductivities than borophene ones, as depicted in Figure 109, Figure 110 and Figure 111 where the empty columns representing graphene TC overheads the solid colored ones of borophene. This finding is not surprising because the thermal conductivity of graphene is at least one order of magnitude higher than the borophene one.

Despite this general trend, as known from literature[11], short particles featured by a low aspect ratio (25 and 50) confirmed to provide a smaller contribution than longer ones to improve thermal transport in composites. The combination of low concentration, small aspect ratio and thin samples represents the only condition when the TC of borophene and graphene fillers composites is similar (Table 17 and Table 18). Such result is particularly relevant because the TC of borophene is at least one order of magnitude lower than graphene, while ITC of borophene-PDMS is just 10% more than graphene-PDMS one.

6.3. Conclusions

The Multi-scale modeling proved to be a smart approach to simulate material properties. The Molecular Dynamics calculations by the application of thermal equilibration method were employed to calculate the interfacial thermal conductance (ITC) between the flat surfaces of PDMS polymer and two different particles, graphene (30 MW m^{-2} K^{-1}) and borophene (33 MW m^{-2} K^{-1}). These values were then employed as thermal conductances in FEM modeling.

The FEM modeling adopted a series of representative volume elements (RVE) consisting in disc-shaped particles inside a cubic volume of polymer. The disk shaped elements were tuned to simulate flakes of graphene and borophene inside PDMS matrix. Within the FEM modeling, three thicknesses, three different filler concentrations and four aspect ratios were evaluated for both graphene and borophene flakes.

The filler loading doubled the composite TC when rising from 1% to 4%. Moreover, the increased thickness of the filler determined an increase in composite TC up to about one third. Despite this finding, the parameter that affected more the composite TC was the aspect ratio. When particles with low aspect ratio are employed, the relative thick layer of polymer interposed within the particles does now allow particles to create a three dimensional path able to transport efficiently heat.

The effect of aspect ratio confirmed literature predictions, as the aspect ratio increases, the amount of flake-polymer-flake junctions that heat crosses decreases, reducing the overall thermal resistance and thus letting the filler, with its higher thermal conductivity, to better contribute within the heat transfer process. The models with higher aspect ratio, are the ones in which the composite conductivity scales more with graphene instead of borophene, confirming that the heat is transferred along the conductive flakes, depending on their intrinsic conductivity. Despite this finding, the maximum difference in term of thermal conductivity for the composite is usually lower than 15% that is significantly less than the difference in intrinsic TC for graphene (2000 W m^{-1} K^{-1}) and borophene (75 W m^{-1} K^{-1}). This finding suggests that for polymer-based composites, significant TC improvement can be reached adopting particles with TC even not even outstanding, provided that higher thermal conductance at the interface is obtained (as could be other 2D materials as silicene, germanene, or phosphorene). Therefore, on one hand, an optimal route to improve TC of composites includes the optimization of interface design to reduce thermal resistance, as could be the interface functionalization. Additionally, the possibility to manufacture an effective percolation network by the exploitations of flake-to-flake junctions represents the smartest route to improve the TC of composite.

Chapter 7

General conclusions

In the present Ph.D. dissertation, the thermal transport across graphene platelets as thermally conductive material was investigated by computational tools, with the aim to contribute to the development of polymeric composites materials with enhanced thermal properties.

Most of the efforts focused on the improvement on the thermal transport in graphene-based nanostructures by the reduction of the thermal boundary resistance within the flakes, for the ideal purpose to create a thermally conductive network of particles. The idea developed in this work relates to the adoption of chemically bound molecules between the graphene platelets, called molecular junctions, able to act as thermal bridges between the graphene platelets. Grafting molecules across the edges of graphene flakes ideally preserve the efficiency in phonon transfer inside the graphene pristine structure and improved heat transfer between the platelets.

The functionalization with species exploiting non-bonding interaction was studied via Molecular Dynamics (MD) simulations as a possible path to reduce thermal resistance among suspended nanoplatelets. Encouraging results from pending alkyl chains induced further investigations on more chemically viable functionalization, such as phenols. However, the use of phenols and other non-covalently bound junctions as thermal bridges provided overall a limited improvement of the thermal boundary conductance (TBC).

Molecular junctions exploiting covalent bond represented a significantly more efficient media to enhance TBC between suspended particles of graphene compared to non-covalent ones. Shorter species were found more efficient to drive heat than longer ones, due to diffusive mismatch of phonons between linker and graphene while a plateauing trend was found for longer chains. Overall, the TBC improvement was found to be the lowest for junctions made of aliphatic moieties, characterized by the long and flexible alkyl chain and the highest for the short and rigid polyaromatic bridging molecules. Moreover, the elastic modulus of the molecular junctions was estimated and found correlated with the TBC. The analysis of vibrational modes between molecular junctions and the adopted graphene flakes found limited overlap for aliphatic/aromatic junctions where aromatic and polyaromatic structures displayed closer vibrational spectra.

The results obtained from molecular junctions bridging suspended graphene platelets were a useful achievement to implement molecular junctions in a context closer to an actual composite. To fulfill this purpose, a polydimethylsiloxane (PDMS) polymer matrix was simulated surrounding the platelets and the molecular junctions. In this latter study, the use of molecular junctions was demonstrated to be

an efficient approach to increase the thermal conductance of the interface. In fact, for the chemical species investigated, limited to a partially aliphatic, an aromatic, and a polyaromatic with strong aromatic coupling, the TBC increased up to about 5-times the initial value.

Such improvement in thermal transfer inside the junction was attributed, on the one hand, to the length of the molecular junction that forced the flakes to keep the distance between the platelets and, on the other hand, to the chemistry of the junction, as previously observed in suspended flakes. The strongly coupled junction, based on anthracene, was find able to behave similarly to a uniform material and was thus considered a theoretical upper value for molecularly joined graphene nanocomposites.

Beside the effect of TBC between platelets (filler-filler), inside a composite material, the large area of interaction between polymer and filler is known to have an important role in the heat flux within the composite. Therefore, to investigate the thermal transport inside a composite material, an upper-scale implementation is needed.

Following this premise, MD and Finite Element Method (FEM) were then coupled in a multi-scale approach to investigate thermal transport in the continuum for novel composite materials. In MD simulations, carried out by the thermal equilibration method, the interfacial thermal conductance (ITC) between the surface of PDMS polymer and two different filler candidates, graphene and borophene were determined. The so calculated values were then fitted into FEM simulations. Overall, the graphene-based composites reported higher thermal conductivities than the counterpart made of borophene flakes did. Moreover, in the models with higher aspect ratio, thus flakes with higher lateral size, were the ones in which the composite conductivity scales more with graphene compared to borophene. Despite this finding, the much lower thermal conductivity (TC) of borophene, two orders of magnitude lower than graphene, was compensated by the slightly higher thermal conductance at the interface with polymer. This phenomenon suggested that an optimal route to improve TC of composites should include proper interface design to improve the boundary conductance, for example by chemical functionalization even at the cost of a moderate reduction of the TC. Nevertheless, the strategies to reach percolation by design of molecularly joined three-dimensional networks still represent one of the most powerful mechanism to improve the TC of composite. Within this approach, the use of molecular linkers contributes to the creation of a percolative network and thus improving composite TC by reducing thermal resistance in filler-filler contact.

The findings obtained in this Ph.D. thesis could bring to new opportunities and challenges in the rational design of materials. Future works could refine and expand some of the routes, some example follows.

The atomistic modelling of molecular junctions demonstrated how such functionalization is efficient to improve the thermal transport at the nanoscale, especially when embedded in polymer mass. From this point of view, the proposed investigation, with junctions in polymer, can be considered pioneering and thus open the route to more complex topologies, layered structures, more efficient junctions and different polymers. It is always to take account that the early findings proposed

herein, obtained by a computational approach, constitutes a precursory work to experimental studies. Despite the interesting results obtained in the early works with suspended molecules, classical MD evidenced its limit in modelling thermal transport in atomistic sized devices. To overcome this issue, the adoption of quantum mechanics tools, would certainly add value to the research of feasible molecular junctions. In addition, the encouraging finding in trends between thermal properties and mechanical properties in molecular junctions deserves further investigations.

On the FEM side, the innovative approach of multiscale modelling was found a versatile tool to upscale results. Further improvements in design proper RVEs should take account of some needs to obtain a domain capable to manage the filler-filler contact and as well capable to distinguish edge contact from planar contact would increase the accuracy in FEM modelling of composites, such as those that occurred in predictive models. Moreover, the recent growing interest for 2D materials, such as silicene, germanene or phosphorene could open new challenges to the development of thermal transport devices.

Chapter 8

Appendix (i)

8.1. Computational workload of the simulations

All the calculations presented herein were performed using the following machines:

A) Lenovo P900 Workstation equipped with dual Intel Xeon® 2620v3 – 12 physical cores and nVidia® K4000 GPU card for Cuda® support.

B) Lenovo P910 Workstation equipped with dual Intel Xeon® 2687w v4 – 24 physical cores and nVidia® M2000 GPU card for Cuda® support.

C) HP ZBook Mobile Workstation equipped with Intel i7® 4700MQ – 4 physical cores and nVidia® K5100M GPU card for Cuda® support.

D) HPC Vegas cluster nodes in Bauhaus Universität Weimar equipped with Intel Xeon® 2620v3 and 2630v3

All the machines adopted several builds of LAMMPS from February 2016 to March 2019. The workstations A, B and C worked with Ubuntu OS version 14.04 LTS, 16.04 LTS and 18.04 LTS as the Ubuntu distribution updates. Windows 10 run also on C to support Abaqus standard (FEM). The Cluster Vegas (D) workload was managed by SLURM on Unix/Linux environment.

Overall, the MD simulations for thermal calculations were the most demanding in terms of computational resources while FEM and other MD simulations required much less computational power, and could work with a good personal computer.

The unsupported non-covalent molecular junction systems were simulated on A. The typical workload for each simulation was about 23 hours and the same workload was needed by the unsupported covalently bound molecular junctions (in A and D), which eventually halved the running time on B. As stated above, all the molecular models cited above were made of about 4000 atoms. On one hand, in the case of multilayers made up to 18000 atoms, the time needed was proportional to that value, and rise up to several days of calculation time. On the other hand, small system reflected lightweight Molecular Dynamics calculations as VDOS dump run, VDOS autocorrelation and tensile testing, performed on workstation C, with workload in the range of few hours.

The polymer-embedded molecular junctions were still simulated in A and B. In this case, GPU support demonstrated to be a powerful tool to speed up vdW forces calculation and each simulation took about 100 hours each 12 physical cores and GPU.

The highest computational workload was represented by the Molecular Dynamics calculations for Borophene-PDMS layered systems. Such work took about

two months of calculations on A and each node of D. The reason of such heaviness in calculation is find in the computational weight of REAXFF, the large amount of atoms and the lack of GPU support (GPU package in LAMMPS was not compatible with that modelling). The graphene counterpart took about one week for each model on the same systems. However, the FEM calculation were much faster and needed about 35 minutes of CPU time for each simulation on workstation C.

In MD simulations, when working on local workstations, to optimize domain splitting, MPI issues, and eventually hyper threading support, the optimal number of cores and the contribution of GPU support was found by a simple benchmarking code with actual data prior to the simulation.

References

[1] A. Warshel, M. Levitt, Theoretical studies of enzymic reactions: Dielectric, electrostatic and steric stabilization of the carbonium ion in the reaction of lysozyme, Journal of Molecular Biology 103(2) (1976) 227-249.
[2] R.G. Parr, Density functional theory of atoms and molecules, Horizons of Quantum Chemistry, Springer1980, pp. 5-15.
[3] R. Car, M. Parrinello, Unified approach for molecular dynamics and density-functional theory, Phys Rev Lett 55(22) (1985) 2471-2474.
[4] M. Allen, D. Tildesley, Computer simulation of liquids, (1989).
[5] R.E. Rudd, J.Q. Broughton, Coarse-grained molecular dynamics and the atomic limit of finite elements, Physical Review B 58(10) (1998) R5893-R5896.
[6] J.H. Lienhard, A heat transfer textbook, Courier Corporation2018.
[7] J.M. Ziman, Electrons and phonons: the theory of transport phenomena in solids, Oxford university press1960.
[8] C. Kittel, P. McEuen, P. McEuen, Introduction to solid state physics, Wiley New York1996.
[9] P. Carruthers, Theory of thermal conductivity of solids at low temperatures, Reviews of Modern Physics 33(1) (1961) 92.
[10] P. Klemens, Thermal conductivity and lattice vibrational modes, Solid state physics, Elsevier1958, pp. 1-98.
[11] N. Burger, A. Laachachi, M. Ferriol, M. Lutz, V. Toniazzo, D. Ruch, Review of thermal conductivity in composites: Mechanisms, parameters and theory, Progress in Polymer Science 61 (2016) 1-28.
[12] G. Fugallo, L. Colombo, Calculating lattice thermal conductivity: a synopsis, Physica Scripta 93(4) (2018) 043002.
[13] D.D.L. Chung, Materials for thermal conduction, Applied Thermal Engineering 21(16) (2001) 1593-1605.
[14] H.Y. Chen, V.V. Ginzburg, J. Yang, Y.F. Yang, W. Liu, Y. Huang, L.B. Du, B. Chen, Thermal conductivity of polymer-based composites: Fundamentals and applications, Progress in Polymer Science 59 (2016) 41-85.
[15] Z.D. Han, A. Fina, Thermal conductivity of carbon nanotubes and their polymer nanocomposites: A review, Progress in Polymer Science 36(7) (2011) 914-944.
[16] A. Bjorneklett, L. Halbo, H. Kristiansen, Thermal-Conductivity of Epoxy Adhesives Filled with Silver Particles, International Journal of Adhesion and Adhesives 12(2) (1992) 99-104.
[17] M. Harada, N. Hamaura, M. Ochi, Y. Agari, Thermal conductivity of liquid crystalline epoxy/BN filler composites having ordered network structure, Compos Part B-Eng 55 (2013) 306-313.
[18] C.L. Choy, Thermal conductivity of polymers, Polymer 18(10) (1977) 984-1004.
[19] H. Grad, On the kinetic theory of rarefied gases, Communications on Pure and Applied Mathematics 2(4) (1949) 331-407.

[20] T. Luo, G. Chen, Nanoscale heat transfer--from computation to experiment, Phys Chem Chem Phys 15(10) (2013) 3389-412.
[21] X. Xu, J. Chen, J. Zhou, B. Li, Thermal Conductivity of Polymers and Their Nanocomposites, Adv Mater 30(17) (2018) e1705544.
[22] E.T. Swartz, R.O. Pohl, Thermal-Resistance at Interfaces, Applied Physics Letters 51(26) (1987) 2200-2202.
[23] E.T. Swartz, R.O. Pohl, Thermal boundary resistance, Reviews of Modern Physics 61(3) (1989) 605-668.
[24] G.L. Pollack, Kapitza Resistance, Reviews Of Modern Physics 41(1) (1969) 34.
[25] A. Maiti, G.D. Mahan, S.T. Pantelides, Dynamical simulations of nonequilibrium processes — Heat flow and the Kapitza resistance across grain boundaries, Solid State Communications 102(7) (1997) 517-521.
[26] ASTM C168-18.
[27] S. Shen, A. Henry, J. Tong, R. Zheng, G. Chen, Polyethylene nanofibres with very high thermal conductivities, Nat Nanotechnol 5(4) (2010) 251-5.
[28] A. Henry, G. Chen, Anomalous heat conduction in polyethylene chains: Theory and molecular dynamics simulations, Physical Review B 79(14) (2009).
[29] A. Henry, G. Chen, High thermal conductivity of single polyethylene chains using molecular dynamics simulations, Phys Rev Lett 101(23) (2008) 235502.
[30] T.F. Luo, K. Esfarjani, J. Shiomi, A. Henry, G. Chen, Molecular dynamics simulation of thermal energy transport in polydimethylsiloxane (PDMS), Journal of Applied Physics 109(7) (2011) 074321.
[31] P. Dashora, G. Gupta, On the temperature dependence of the thermal conductivity of linear amorphous polymers, Polymer 37(2) (1996) 231-234.
[32] W.N. dos Santos, J.A. de Sousa, R. Gregorio, Thermal conductivity behaviour of polymers around glass transition and crystalline melting temperatures, Polymer Testing 32(5) (2013) 987-994.
[33] K.S. Novoselov, A.K. Geim, S.V. Morozov, D. Jiang, Y. Zhang, S.V. Dubonos, I.V. Grigorieva, A.A. Firsov, Electric field effect in atomically thin carbon films, Science 306(5696) (2004) 666-9.
[34] A.K. Geim, Graphene: status and prospects, Science 324(5934) (2009) 1530-4.
[35] S. Ghosh, I. Calizo, D. Teweldebrhan, E.P. Pokatilov, D.L. Nika, A.A. Balandin, W. Bao, F. Miao, C.N. Lau, Extremely high thermal conductivity of graphene: Prospects for thermal management applications in nanoelectronic circuits, Applied Physics Letters 92(15) (2008).
[36] A. King, G. Johnson, D. Engelberg, W. Ludwig, J. Marrow, Observations of intergranular stress corrosion cracking in a grain-mapped polycrystal, Science 321(5887) (2008) 382-5.
[37] A. Bianco, H.M. Cheng, T. Enoki, Y. Gogotsi, R.H. Hurt, N. Koratkar, T. Kyotani, M. Monthioux, C.R. Park, J.M.D. Tascon, J. Zhang, All in the graphene family - A recommended nomenclature for two-dimensional carbon materials, Carbon 65 (2013) 1-6.
[38] W.J. Evans, L. Hu, P. Keblinski, Thermal conductivity of graphene ribbons from equilibrium molecular dynamics: Effect of ribbon width, edge roughness, and hydrogen termination, Applied Physics Letters 96(20) (2010) 203112.
[39] L.A. Jauregui, Y. Yue, A.N. Sidorov, J. Hu, Q. Yu, G. Lopez, R. Jalilian, D.K. Benjamin, D.A. Delkd, W. Wu, Thermal transport in graphene nanostructures: Experiments and simulations, Ecs Transactions 28(5) (2010) 73-83.
[40] A.A. Balandin, Thermal properties of graphene and nanostructured carbon materials, Nat Mater 10(8) (2011) 569-81.

[41] O. Gamayun, E. Gorbar, V. Gusynin, Gap generation and semimetal-insulator phase transition in graphene, Physical Review B 81(7) (2010) 075429.
[42] D.L. Nika, A.A. Balandin, Phonons and thermal transport in graphene and graphene-based materials, Rep Prog Phys 80(3) (2017) 036502.
[43] A.A. Balandin, S. Ghosh, W. Bao, I. Calizo, D. Teweldebrhan, F. Miao, C.N. Lau, Superior thermal conductivity of single-layer graphene, Nano letters 8(3) (2008) 902-7.
[44] G. Fugallo, A. Cepellotti, L. Paulatto, M. Lazzeri, N. Marzari, F. Mauri, Thermal conductivity of graphene and graphite: collective excitations and mean free paths, Nano letters 14(11) (2014) 6109-14.
[45] A.I. Cocemasov, D.L. Nika, A.A. Balandin, Engineering of the thermodynamic properties of bilayer graphene by atomic plane rotations: the role of the out-of-plane phonons, Nanoscale 7(30) (2015) 12851-9.
[46] X. Xu, L.F. Pereira, Y. Wang, J. Wu, K. Zhang, X. Zhao, S. Bae, C. Tinh Bui, R. Xie, J.T. Thong, B.H. Hong, K.P. Loh, D. Donadio, B. Li, B. Ozyilmaz, Length-dependent thermal conductivity in suspended single-layer graphene, Nat Commun 5 (2014) 3689.
[47] R. Saito, M. Mizuno, M.S. Dresselhaus, Ballistic and Diffusive Thermal Conductivity of Graphene, Physical Review Applied 9(2) (2018).
[48] J. Hu, X. Ruan, Y.P. Chen, Thermal conductivity and thermal rectification in graphene nanoribbons: a molecular dynamics study, Nano letters 9(7) (2009) 2730-5.
[49] W.-R. Zhong, M.-P. Zhang, B.-Q. Ai, D.-Q. Zheng, Chirality and thickness-dependent thermal conductivity of few-layer graphene: A molecular dynamics study, Applied Physics Letters 98(11) (2011) 113107.
[50] B. Mortazavi, S. Ahzi, Thermal conductivity and tensile response of defective graphene: A molecular dynamics study, Carbon 63 (2013) 460-470.
[51] J.J. Yeo, Z. Liu, T.Y. Ng, Comparing the effects of dispersed Stone-Thrower-Wales defects and double vacancies on the thermal conductivity of graphene nanoribbons, Nanotechnology 23(38) (2012) 385702.
[52] S. Colonna, O. Monticelli, J. Gomez, C. Novara, G. Saracco, A. Fina, Effect of morphology and defectiveness of graphene-related materials on the electrical and thermal conductivity of their polymer nanocomposites, Polymer 102 (2016) 292-300.
[53] B. Mortazavi, M. Potschke, G. Cuniberti, Multiscale modeling of thermal conductivity of polycrystalline graphene sheets, Nanoscale 6(6) (2014) 3344-52.
[54] N.P. Cheremisinoff, Advanced polymer processing operations, William Andrew1998.
[55] A. Seppala, Efficient method for predicting the effective thermal conductivity of various types of two-component heterogeneous materials, International Journal of Thermal Sciences 134 (2018) 282-297.
[56] K. Pietrak, T.S. Wiśniewski, A review of models for effective thermal conductivity of composite materials, Journal of Power Technologies 95(1) (2014) 14-24.
[57] Y. Su, J.J. Li, G.J. Weng, Theory of thermal conductivity of graphene-polymer nanocomposites with interfacial Kapitza resistance and graphene-graphene contact resistance, Carbon 137 (2018) 222-233.
[58] L. Gong, Y. Wang, X. Cheng, R. Zhang, H. Zhang, Thermal conductivity of highly porous mullite materials, International Journal of Heat and Mass Transfer 67 (2013) 253-259.

[59] L. Weber, R. Tavangar, Diamond-based metal matrix composites for thermal management made by liquid metal infiltration—potential and limits, Advanced Materials Research, Trans Tech Publ, 2009, pp. 111-115.
[60] S. Colonna, M.M. Bernal, G. Gavoci, J. Gomez, C. Novara, G. Saracco, A. Fina, Effect of processing conditions on the thermal and electrical conductivity of poly (butylene terephthalate) nanocomposites prepared via ring-opening polymerization, Materials & Design 119 (2017) 124-132.
[61] M. Zouari, M. Kharrat, M. Dammak, Wear and friction analysis of polyester coatings with solid lubricant, Surface and Coatings Technology 204(16-17) (2010) 2593-2599.
[62] M. Shtein, R. Nadiv, M. Buzaglo, K. Kahil, O. Regev, Thermally Conductive Graphene-Polymer Composites: Size, Percolation, and Synergy Effects, Chemistry of Materials 27(6) (2015) 2100-2106.
[63] A.P. Kumar, D. Depan, N. Singh Tomer, R.P. Singh, Nanoscale particles for polymer degradation and stabilization—Trends and future perspectives, Progress in Polymer Science 34(6) (2009) 479-515.
[64] C.Y. Zhi, Y. Bando, T. Terao, C.C. Tang, H. Kuwahara, D. Golberg, Towards Thermoconductive, Electrically Insulating Polymeric Composites with Boron Nitride Nanotubes as Fillers, Advanced Functional Materials 19(12) (2009) 1857-1862.
[65] X. Shen, Z.Y. Wang, Y. Wu, X. Liu, J.K. Kim, Effect of functionalization on thermal conductivities of graphene/epoxy composites, Carbon 108 (2016) 412-422.
[66] S. Lin, M.J. Buehler, The effect of non-covalent functionalization on the thermal conductance of graphene/organic interfaces, Nanotechnology 24(16) (2013) 165702.
[67] Y. Gao, F. Muller-Plathe, Increasing the Thermal Conductivity of Graphene-Polyamide-6,6 Nanocomposites by Surface-Grafted Polymer Chains: Calculation with Molecular Dynamics and Effective-Medium Approximation, The journal of physical chemistry. B 120(7) (2016) 1336-46.
[68] M. Wang, N. Hu, L. Zhou, C. Yan, Enhanced interfacial thermal transport across graphene–polymer interfaces by grafting polymer chains, Carbon 85 (2015) 414-421.
[69] F. Sun, T. Zhang, M.M. Jobbins, Z. Guo, X. Zhang, Z. Zheng, D. Tang, S. Ptasinska, T. Luo, Molecular bridge enables anomalous enhancement in thermal transport across hard-soft material interfaces, Adv Mater 26(35) (2014) 6093-9.
[70] V. Varshney, J. Lee, A.K. Roy, B.L. Farmer, Modeling of interface thermal conductance in longitudinally connected carbon nanotube junctions, Journal of Applied Physics 109(8) (2011).
[71] C.F. Carlborg, J. Shiomi, S. Maruyama, Thermal boundary resistance between single-walled carbon nanotubes and surrounding matrices, Physical Review B 78(20) (2008) 205406.
[72] B. Mortazavi, O. Benzerara, H. Meyer, J. Bardon, S. Ahzi, Combined molecular dynamics-finite element multiscale modeling of thermal conduction in graphene epoxy nanocomposites, Carbon 60 (2013) 356-365.
[73] Z.-Y. Ong, E. Pop, Molecular dynamics simulation of thermal boundary conductance between carbon nanotubes and SiO 2, Physical Review B 81(15) (2010) 155408.
[74] B. Mortazavi, T. Rabczuk, Multiscale modeling of heat conduction in graphene laminates, Carbon 85 (2015) 1-7.
[75] X.J. Liu, G. Zhang, Y.W. Zhang, Thermal Conduction Across Graphene Cross-Linkers, J Phys Chem C 118(23) (2014) 12541-12547.
[76] N. Yang, X.F. Xu, G. Zhang, B.W. Li, Thermal transport in nanostructures, Aip Advances 2(4) (2012) 041410.

[77] T. Meier, F. Menges, P. Nirmalraj, H. Holscher, H. Riel, B. Gotsmann, Length-dependent thermal transport along molecular chains, Phys Rev Lett 113(6) (2014) 060801.
[78] H. Han, Y. Zhang, N. Wang, M.K. Samani, Y. Ni, Z.Y. Mijbil, M. Edwards, S. Xiong, K. Saaskilahti, M. Murugesan, Y. Fu, L. Ye, H. Sadeghi, S. Bailey, Y.A. Kosevich, C.J. Lambert, J. Liu, S. Volz, Functionalization mediates heat transport in graphene nanoflakes, Nat Commun 7 (2016) 11281.
[79] A. Sinitskii, A. Dimiev, D.A. Corley, A.A. Fursina, D.V. Kosynkin, J.M. Tour, Kinetics of diazonium functionalization of chemically converted graphene nanoribbons, ACS nano 4(4) (2010) 1949-54.
[80] D.V. Kosynkin, A.L. Higginbotham, A. Sinitskii, J.R. Lomeda, A. Dimiev, B.K. Price, J.M. Tour, Longitudinal unzipping of carbon nanotubes to form graphene nanoribbons, Nature 458(7240) (2009) 872-6.
[81] M. Fang, K.G. Wang, H.B. Lu, Y.L. Yang, S. Nutt, Covalent polymer functionalization of graphene nanosheets and mechanical properties of composites, Journal of Materials Chemistry 19(38) (2009) 7098-7105.
[82] V. Georgakilas, A.B. Bourlinos, R. Zboril, T.A. Steriotis, P. Dallas, A.K. Stubos, C. Trapalis, Organic functionalisation of graphenes, Chem Commun (Camb) 46(10) (2010) 1766-8.
[83] S. Park, R.S. Ruoff, Chemical methods for the production of graphenes, Nat Nanotechnol 4(4) (2009) 217-24.
[84] X. Zhang, L. Hou, A. Cnossen, A.C. Coleman, O. Ivashenko, P. Rudolf, B.J. van Wees, W.R. Browne, B.L. Feringa, One-Pot Functionalization of Graphene with Porphyrin through Cycloaddition Reactions, Chemistry–A European Journal 17(32) (2011) 8957-8964.
[85] M. Quintana, K. Spyrou, M. Grzelczak, W.R. Browne, P. Rudolf, M. Prato, Functionalization of graphene via 1,3-dipolar cycloaddition, ACS nano 4(6) (2010) 3527-33.
[86] L.H. Liu, M.M. Lerner, M. Yan, Derivitization of pristine graphene with well-defined chemical functionalities, Nano letters 10(9) (2010) 3754-6.
[87] T.A. Strom, E.P. Dillon, C.E. Hamilton, A.R. Barron, Nitrene addition to exfoliated graphene: a one-step route to highly functionalized graphene, Chem Commun (Camb) 46(23) (2010) 4097-9.
[88] C.G. Salzmann, V. Nicolosi, M.L.H. Green, Edge-carboxylated graphene nanoflakes from nitric acid oxidised arc-discharge material, Journal of Materials Chemistry 20(2) (2010) 314-319.
[89] Z. Sun, S.-i. Kohama, Z. Zhang, J.R. Lomeda, J.M. Tour, Soluble graphene through edge-selective functionalization, Nano Research 3(2) (2010) 117-125.
[90] V. Georgakilas, M. Otyepka, A.B. Bourlinos, V. Chandra, N. Kim, K.C. Kemp, P. Hobza, R. Zboril, K.S. Kim, Functionalization of graphene: covalent and non-covalent approaches, derivatives and applications, Chem Rev 112(11) (2012) 6156-214.
[91] Y.S. Liu, J.Y. Zhou, X.L. Zhang, Z.B. Liu, X.J. Wan, J.G. Tian, T. Wang, Y.S. Chen, Synthesis, characterization and optical limiting property of covalently oligothiophene-functionalized graphene material, Carbon 47(13) (2009) 3113-3121.
[92] D. Yu, Y. Yang, M. Durstock, J.B. Baek, L. Dai, Soluble P3HT-grafted graphene for efficient bilayer-heterojunction photovoltaic devices, ACS nano 4(10) (2010) 5633-40.
[93] Z. Liu, J.T. Robinson, X. Sun, H. Dai, PEGylated nanographene oxide for delivery of water-insoluble cancer drugs, Journal of the American Chemical Society 130(33) (2008) 10876-7.

[94] S. Park, D.A. Dikin, S.T. Nguyen, R.S. Ruoff, Graphene Oxide Sheets Chemically Cross-Linked by Polyallylamine, J Phys Chem C 113(36) (2009) 15801-15804.
[95] P. Tarakeshwar, H.S. Choi, K.S. Kim, Olefinic vs. aromatic pi-H interaction: a theoretical investigation of the nature of interaction of first-row hydrides with ethene and benzene, Journal of the American Chemical Society 123(14) (2001) 3323-31.
[96] C.R. Martinez, B.L. Iverson, Rethinking the term “pi-stacking”, Chemical Science 3(7) (2012) 2191.
[97] C.A. Hunter, J.K.M. Sanders, The nature of .pi.-.pi. interactions, Journal of the American Chemical Society 112(14) (1990) 5525-5534.
[98] C.A. Hunter, M.N. Meah, J.K. Sanders, Dabco-metalloporphyrin binding: ternary complexes, host-guest chemistry and the measurement of. pi.-. pi. interactions, Journal of the American Chemical Society 112(15) (1990) 5773-5780.
[99] Q. Li, M. Strange, I. Duchemin, D. Donadio, G.C. Solomon, A Strategy to Suppress Phonon Transport in Molecular Junctions Using pi-Stacked Systems, J Phys Chem C 121(13) (2017) 7175-7182.
[100] F. Müller-Plathe, D. Reith, Cause and effect reversed in non-equilibrium molecular dynamics: an easy route to transport coefficients, Computational and Theoretical Polymer Science 9(3-4) (1999) 203-209.
[101] Y. Chalopin, K. Esfarjani, A. Henry, S. Volz, G. Chen, Thermal interface conductance in Si/Ge superlattices by equilibrium molecular dynamics, Physical Review B 85(19) (2012).
[102] L. Hu, T. Desai, P. Keblinski, Determination of interfacial thermal resistance at the nanoscale, Physical Review B 83(19) (2011).
[103] L. Hu, T. Desai, P. Keblinski, Thermal transport in graphene-based nanocomposite, Journal of Applied Physics 110(3) (2011) 033517.
[104] Y. Wang, H.F. Zhan, Y. Xiang, C. Yang, C.M. Wang, Y.Y. Zhang, Effect of Covalent Functionalization on Thermal Transport across Graphene-Polymer Interfaces, J Phys Chem C 119(22) (2015) 12731-12738.
[105] T.F. Luo, J.R. Lloyd, Enhancement of Thermal Energy Transport Across Graphene/Graphite and Polymer Interfaces: A Molecular Dynamics Study, Advanced Functional Materials 22(12) (2012) 2495-2502.
[106] Li, Zhang, Zhang, Thermal Conductivity of Graphene-Polymer Composites: Mechanisms, Properties, and Applications, Polymers 9(12) (2017) 437.
[107] W. Chen, J.C. Zhang, Y.A. Yue, Molecular dynamics study on thermal transport at carbon nanotube interface junctions: Effects of mechanical force and chemical functionalization, International Journal of Heat and Mass Transfer 103 (2016) 1058-1064.
[108] W. Zhang, T.S. Fisher, N. Mingo, The Atomistic Green's Function Method: An Efficient Simulation Approach for Nanoscale Phonon Transport, Numerical Heat Transfer, Part B: Fundamentals 51(4) (2007) 333-349.
[109] P.E. Hopkins, P.M. Norris, M.S. Tsegaye, A.W. Ghosh, Extracting phonon thermal conductance across atomic junctions: Nonequilibrium Green’s function approach compared to semiclassical methods, Journal of Applied Physics 106(6) (2009) 063503.
[110] J.C. Klockner, M. Burkle, J.C. Cuevas, F. Pauly, Length dependence of the thermal conductance of alkane-based single-molecule junctions: An ab initio study, Physical Review B 94(20) (2016) 205425.
[111] Q. Li, I. Duchemin, S.Y. Xiong, G.C. Solomon, D. Donadio, Mechanical Tuning of Thermal Transport in a Molecular Junction, J Phys Chem C 119(43) (2015) 24636-24642.

[112] J.C. Klockner, J.C. Cuevas, F. Pauly, Transmission eigenchannels for coherent phonon transport, Physical Review B 97(15) (2018).
[113] R. Gulotty, M. Castellino, P. Jagdale, A. Tagliaferro, A.A. Balandin, Effects of functionalization on thermal properties of single-wall and multi-wall carbon nanotube-polymer nanocomposites, ACS nano 7(6) (2013) 5114-21.
[114] Y.Y. Zhang, Q.X. Pei, X.Q. He, Y.W. Mai, A molecular dynamics simulation study on thermal conductivity of functionalized bilayer graphene sheet, Chemical Physics Letters 622 (2015) 104-108.
[115] L. Verlet, Computer "experiments" on classical fluids. I. Thermodynamical properties of Lennard-Jones molecules, Physical review 159(1) (1967) 98.
[116] W.C. Swope, H.C. Andersen, P.H. Berens, K.R. Wilson, A Computer-Simulation Method for the Calculation of Equilibrium-Constants for the Formation of Physical Clusters of Molecules - Application to Small Water Clusters, Journal of Chemical Physics 76(1) (1982) 637-649.
[117] G.J. Martyna, M.L. Klein, M. Tuckerman, Nosé–Hoover chains: The canonical ensemble via continuous dynamics, The Journal of chemical physics 97(4) (1992) 2635-2643.
[118] M. Parrinello, A. Rahman, Polymorphic transitions in single crystals: A new molecular dynamics method, Journal of Applied Physics 52(12) (1981) 7182-7190.
[119] F. Müller-Plathe, A simple nonequilibrium molecular dynamics method for calculating the thermal conductivity, The Journal of chemical physics 106(14) (1997) 6082-6085.
[120] R. Kubo, The fluctuation-dissipation theorem, Reports on progress in physics 29(1) (1966) 255.
[121] K.R. Hahn, C. Melis, L. Colombo, Structural, Vibrational, and Thermal Properties of Nanocrystalline Graphene in Atomistic Simulations, J Phys Chem C 120(5) (2016) 3026-3035.
[122] C. Melis, R. Dettori, S. Vandermeulen, L. Colombo, Calculating thermal conductivity in a transient conduction regime: theory and implementation, The European Physical Journal B 87(4) (2014).
[123] D.W. Brenner, O.A. Shenderova, J.A. Harrison, S.J. Stuart, B. Ni, S.B. Sinnott, A second-generation reactive empirical bond order (REBO) potential energy expression for hydrocarbons, J Phys-Condens Mat 14(4) (2002) 783-802.
[124] D.W. Brenner, Empirical Potential for Hydrocarbons for Use in Simulating the Chemical Vapor-Deposition of Diamond Films, Physical Review B 42(15) (1990) 9458-9471.
[125] J. Tersoff, Modeling solid-state chemistry: Interatomic potentials for multicomponent systems, Phys Rev B Condens Matter 39(8) (1989) 5566-5568.
[126] J. Tersoff, New empirical approach for the structure and energy of covalent systems, Phys Rev B Condens Matter 37(12) (1988) 6991-7000.
[127] M.R. Weismiller, A.C. van Duin, J. Lee, R.A. Yetter, ReaxFF reactive force field development and applications for molecular dynamics simulations of ammonia borane dehydrogenation and combustion, J Phys Chem A 114(17) (2010) 5485-92.
[128] A.C.T. van Duin, S. Dasgupta, F. Lorant, W.A. Goddard, ReaxFF: A Reactive Force Field for Hydrocarbons, The Journal of Physical Chemistry A 105(41) (2001) 9396-9409.
[129] P. Dauber-Osguthorpe, V.A. Roberts, D.J. Osguthorpe, J. Wolff, M. Genest, A.T. Hagler, Structure and energetics of ligand binding to proteins: Escherichia coli dihydrofolate reductase-trimethoprim, a drug-receptor system, Proteins: Structure, Function, and Bioinformatics 4(1) (1988) 31-47.

[130] H. Sun, S.J. Mumby, J.R. Maple, A.T. Hagler, An Ab-Initio Cff93 All-Atom Force-Field for Polycarbonates, Journal of the American Chemical Society 116(7) (1994) 2978-2987.
[131] H. Sun, COMPASS: An ab Initio Force-Field Optimized for Condensed-Phase ApplicationsOverview with Details on Alkane and Benzene Compounds, The Journal of Physical Chemistry B 102(38) (1998) 7338-7364.
[132] J.R. Maple, M.J. Hwang, T.P. Stockfisch, U. Dinur, M. Waldman, C.S. Ewig, A.T. Hagler, Derivation of class II force fields. I. Methodology and quantum force field for the alkyl functional group and alkane molecules, Journal of Computational Chemistry 15(2) (1994) 162-182.
[133] M.J. Hwang, T.P. Stockfisch, A.T. Hagler, Derivation of Class-Ii Force-Fields .2. Derivation and Characterization of a Class-Ii Force-Field, Cff93, for the Alkyl Functional-Group and Alkane Molecules, Journal of the American Chemical Society 116(6) (1994) 2515-2525.
[134] J.R. Maple, U. Dinur, A.T. Hagler, Derivation of force fields for molecular mechanics and dynamics from ab initio energy surfaces, Proceedings of the National Academy of Sciences 85(15) (1988) 5350-5354.
[135] J.-H. Lii, N.L. Allinger, The MM3 force field for amides, polypeptides and proteins, Journal of Computational Chemistry 12(2) (1991) 186-199.
[136] J. Delhommelle, P. MilliÉ, Inadequacy of the Lorentz-Berthelot combining rules for accurate predictions of equilibrium properties by molecular simulation, Molecular Physics 99(8) (2001) 619-625.
[137] D. Boda, D. Henderson, The effects of deviations from Lorentz–Berthelot rules on the properties of a simple mixture, Molecular Physics 106(20) (2008) 2367-2370.
[138] M. Waldman, A.T. Hagler, New combining rules for rare gas van der Waals parameters, Journal of computational chemistry 14(9) (1993) 1077-1084.
[139] A.K. Rappe, W.A. Goddard, Charge Equilibration for Molecular-Dynamics Simulations, Journal of Physical Chemistry 95(8) (1991) 3358-3363.
[140] A.K. Rappe, C.J. Casewit, K.S. Colwell, W.A. Goddard, W.M. Skiff, UFF, a full periodic table force field for molecular mechanics and molecular dynamics simulations, Journal of the American Chemical Society 114(25) (1992) 10024-10035.
[141] L. Lindsay, D.A. Broido, Optimized Tersoff and Brenner empirical potential parameters for lattice dynamics and phonon thermal transport in carbon nanotubes and graphene, Physical Review B 81(20) (2010).
[142] J.H. Zou, Z.Q. Ye, B.Y. Cao, Phonon thermal properties of graphene from molecular dynamics using different potentials, The Journal of chemical physics 145(13) (2016) 134705.
[143] L. Lindsay, D.A. Broido, N. Mingo, Flexural phonons and thermal transport in graphene, Physical Review B 82(11) (2010).
[144] D.L. Nika, S. Ghosh, E.P. Pokatilov, A.A. Balandin, Lattice thermal conductivity of graphene flakes: Comparison with bulk graphite, Applied Physics Letters 94(20) (2009) 203103.
[145] H. Sun, D. Rigby, Polysiloxanes: ab initio force field and structural, conformational and thermophysical properties, Spectrochimica Acta Part A: Molecular and Biomolecular Spectroscopy 53(8) (1997) 1301-1323.
[146] H. Sun, Force field for computation of conformational energies, structures, and vibrational frequencies of aromatic polyesters, Journal of Computational Chemistry 15(7) (1994) 752-768.
[147] H. Sun, Ab initio calculations and force field development for computer simulation of polysilanes, Macromolecules 28(3) (1995) 701-712.

[148] X. Shen, X. Lin, N. Yousefi, J. Jia, J.-K. Kim, Wrinkling in graphene sheets and graphene oxide papers, Carbon 66 (2014) 84-92.
[149] X.F. Wu, T.F. Luo, The importance of anharmonicity in thermal transport across solid-solid interfaces, Journal of Applied Physics 115(1) (2014) 014901.
[150] N. Mingo, Anharmonic phonon flow through molecular-sized junctions, Physical Review B 74(12) (2006).
[151] J. Zhang, X. He, L. Yang, G. Wu, J. Sha, C. Hou, C. Yin, A. Pan, Z. Li, Y. Liu, Effect of tensile strain on thermal conductivity in monolayer graphene nanoribbons: a molecular dynamics study, Sensors (Basel) 13(7) (2013) 9388-95.
[152] S.J. Stuart, A.B. Tutein, J.A. Harrison, A reactive potential for hydrocarbons with intermolecular interactions, Journal of Chemical Physics 112(14) (2000) 6472-6486.
[153] G. Barbarino, C. Melis, L. Colombo, Effect of hydrogenation on graphene thermal transport, Carbon 80 (2014) 167-173.
[154] G. Barbarino, C. Melis, L. Colombo, Intrinsic thermal conductivity in monolayer graphene is ultimately upper limited: A direct estimation by atomistic simulations, Physical Review B 91(3) (2015).
[155] C.H. Diao, Y. Dong, J. Lin, Reactive force field simulation on thermal conductivities of carbon nanotubes and graphene, International Journal of Heat and Mass Transfer 112 (2017) 903-912.
[156] J.E. Flaherty, Finite element analysis, (2000).
[157] B. Pentenrieder, Finite element solutions of heat conduction problems in complicated 3d geometries using the multigrid method, Degree thesis, Technical University of Munich (2005).
[158] K. Ramani, A. Vaidyanathan, Finite element analysis of effective thermal conductivity of filled polymeric composites, Journal of Composite Materials 29(13) (1995) 1725-1740.
[159] M.R. Islam, A. Pramila, Thermal conductivity of fiber reinforced composites by the FEM, Journal of Composite Materials 33(18) (1999) 1699-1715.
[160] K. Sanada, Y. Tada, Y. Shindo, Thermal conductivity of polymer composites with close-packed structure of nano and micro fillers, Composites Part A: Applied Science and Manufacturing 40(6-7) (2009) 724-730.
[161] R. Nayak, D.P. Tarkes, A. Satapathy, A computational and experimental investigation on thermal conductivity of particle reinforced epoxy composites, Computational Materials Science 48(3) (2010) 576-581.
[162] B. Mortazavi, M. Baniassadi, J. Bardon, S. Ahzi, Modeling of two-phase random composite materials by finite element, Mori–Tanaka and strong contrast methods, Composites Part B: Engineering 45(1) (2013) 1117-1125.
[163] B. Mortazavi, F. Hassouna, A. Laachachi, A. Rajabpour, S. Ahzi, D. Chapron, V. Toniazzo, D. Ruch, Experimental and multiscale modeling of thermal conductivity and elastic properties of PLA/expanded graphite polymer nanocomposites, Thermochimica Acta 552 (2013) 106-113.
[164] B. Mortazavi, A. Dianat, O. Rahaman, G. Cuniberti, T. Rabczuk, Borophene as an anode material for Ca, Mg, Na or Li ion storage: A first-principle study, Journal of Power Sources 329 (2016) 456-461.
[165] B. Mortazavi, O. Rahaman, S. Ahzi, T. Rabczuk, Flat borophene films as anode materials for Mg, Na or Li-ion batteries with ultra high capacities: A first-principles study, Applied Materials Today 8 (2017) 60-67.
[166] B. Mortazavi, H. Yang, F. Mohebbi, G. Cuniberti, T. Rabczuk, Graphene or h-BN paraffin composite structures for the thermal management of Li-ion batteries: A multiscale investigation, Applied Energy 202 (2017) 323-334.

[167] B. Mortazavi, L.F.C. Pereira, J.-W. Jiang, T. Rabczuk, Modelling heat conduction in polycrystalline hexagonal boron-nitride films, Scientific reports 5 (2015) 13228.
[168] S. Plimpton, Fast parallel algorithms for short-range molecular dynamics, Journal of computational physics 117(1) (1995) 1-19.
[169] LAMMPS website. <http://lammps.sandia.gov>).
[170] W.M. Brown, P. Wang, S.J. Plimpton, A.N. Tharrington, Implementing molecular dynamics on hybrid high performance computers – short range forces, Computer Physics Communications 182(4) (2011) 898-911.
[171] A. Khan, I. Navid, M. Noshin, H. Uddin, F. Hossain, S. Subrina, Equilibrium Molecular Dynamics (MD) Simulation Study of Thermal Conductivity of Graphene Nanoribbon: A Comparative Study on MD Potentials, Electronics 4(4) (2015) 1109-1124.
[172] A. Cao, Molecular dynamics simulation study on heat transport in monolayer graphene sheet with various geometries, Journal of Applied Physics 111(8) (2012) 083528.
[173] S.T. Huxtable, D.G. Cahill, S. Shenogin, L. Xue, R. Ozisik, P. Barone, M. Usrey, M.S. Strano, G. Siddons, M. Shim, P. Keblinski, Interfacial heat flow in carbon nanotube suspensions, Nat Mater 2(11) (2003) 731-4.
[174] T.M. Madkour, J. Mark, Polymer data handbook, Oxford University Press New York, 1999.
[175] T. Tohei, A. Kuwabara, F. Oba, I. Tanaka, Debye temperature and stiffness of carbon and boron nitride polymorphs from first principles calculations, Physical Review B 73(6) (2006) 064304.
[176] B. Peng, H. Zhang, H. Shao, Y. Xu, R. Zhang, H. Zhu, The electronic, optical, and thermodynamic properties of borophene from first-principles calculations, Journal of Materials Chemistry C 4(16) (2016) 3592-3598.
[177] A.P. Thompson, S.J. Plimpton, W. Mattson, General formulation of pressure and stress tensor for arbitrary many-body interaction potentials under periodic boundary conditions, The Journal of chemical physics 131(15) (2009) 154107.
[178] D.M. Heyes, Pressure tensor of partial-charge and point-dipole lattices with bulk and surface geometries, Physical Review B 49(2) (1994) 755-764.
[179] H.F. Zhan, Y.T. Gu, Theoretical and numerical investigation of bending properties of Cu nanowires, Computational Materials Science 55 (2012) 73-80.
[180] H.A. Wu, Molecular dynamics study on mechanics of metal nanowire, Mechanics Research Communications 33(1) (2006) 9-16.
[181] H. Kurata, S. Isoda, T. Kobayashi, Quantitative Elemental Distribution Image of a Carbon
Nanotube, Microscopy Microanalysis Microstructures 6(4) (1995) 405-413.
[182] W. Humphrey, A. Dalke, K. Schulten, VMD: visual molecular dynamics, J Mol Graph 14(1) (1996) 33-8, 27-8.
[183] M.M. Bernal, A. Di Pierro, C. Novara, F. Giorgis, B. Mortazavi, G. Saracco, A. Fina, Edge-Grafted Molecular Junctions between Graphene Nanoplatelets: Applied Chemistry to Enhance Heat Transfer in Nanomaterials, Advanced Functional Materials 28(18) (2018) 1706954.
[184] D. Segal, A. Nitzan, P. Hanggi, Thermal conductance through molecular wires, Journal of Chemical Physics 119(13) (2003) 6840-6855.
[185] J.C. Duda, C.B. Saltonstall, P.M. Norris, P.E. Hopkins, Assessment and prediction of thermal transport at solid-self-assembled monolayer junctions, The Journal of chemical physics 134(9) (2011) 094704.

[186] A. Di Pierro, G. Saracco, A. Fina, Molecular junctions for thermal transport between graphene nanoribbons: Covalent bonding vs. interdigitated chains, Computational Materials Science 142 (2018) 255-260.
[187] C.S. Boland, U. Khan, G. Ryan, S. Barwich, R. Charifou, A. Harvey, C. Backes, Z. Li, M.S. Ferreira, M.E. Mobius, R.J. Young, J.N. Coleman, Sensitive electromechanical sensors using viscoelastic graphene-polymer nanocomposites, Science 354(6317) (2016) 1257-1260.
[188] S. Deng, V. Berry, Wrinkled, rippled and crumpled graphene: an overview of formation mechanism, electronic properties, and applications, Materials Today 19(4) (2016) 197-212.
[189] F. Liu, S. Song, D. Xue, H. Zhang, Folded structured graphene paper for high performance electrode materials, Adv Mater 24(8) (2012) 1089-94.
[190] J. Zhang, J. Xiao, X. Meng, C. Monroe, Y. Huang, J.M. Zuo, Free folding of suspended graphene sheets by random mechanical stimulation, Phys Rev Lett 104(16) (2010) 166805.
[191] H. Wang, H. Tian, S. Wang, W. Zheng, Y. Liu, Simple and eco-friendly solvothermal synthesis of luminescent reduced graphene oxide small sheets, Materials Letters 78 (2012) 170-173.
[192] B. Mortazavi, M.-Q. Le, T. Rabczuk, L.F.C. Pereira, Anomalous strain effect on the thermal conductivity of borophene: a reactive molecular dynamics study, Physica E: Low-dimensional Systems and Nanostructures 93 (2017) 202-207.
[193] Z.-Y. Ong, Thickness-dependent Kapitza resistance in multilayered graphene and other two-dimensional crystals, Physical Review B 95(15) (2017) 155309.
[194] F. Menges, H. Riel, A. Stemmer, C. Dimitrakopoulos, B. Gotsmann, Thermal transport into graphene through nanoscopic contacts, Phys Rev Lett 111(20) (2013) 205901.
[195] P. Yuan, C. Li, S. Xu, J. Liu, X. Wang, Interfacial thermal conductance between few to tens of layered-MoS2 and c-Si: Effect of MoS2 thickness, Acta Materialia 122 (2017) 152-165.
[196] Y.-H. Zhao, Z.-K. Wu, S.-L. Bai, Study on thermal properties of graphene foam/graphene sheets filled polymer composites, Composites Part A: Applied Science and Manufacturing 72 (2015) 200-206.
[197] L. Tian, Y. Wang, Z. Li, H. Mei, Y. Shang, The thermal conductivity-dependant drag reduction mechanism of water droplets controlled by graphene/silicone rubber composites, Experimental Thermal and Fluid Science 85 (2017) 363-369.
[198] F.E. Alam, W. Dai, M. Yang, S. Du, X. Li, J. Yu, N. Jiang, C.-T. Lin, In situ formation of a cellular graphene framework in thermoplastic composites leading to superior thermal conductivity, Journal of Materials Chemistry A 5(13) (2017) 6164-6169.
[199] K.M. Shahil, A.A. Balandin, Graphene–multilayer graphene nanocomposites as highly efficient thermal interface materials, Nano letters 12(2) (2012) 861-867.